BORE WAVINESS MEASUREMENT USING AN IN-PROCESS GAGE

A Dissertation
Presented to
The Academic Faculty

By

Kristian Wolfgang Krueger

In Partial Fulfillment
Of the Requirements for the Degree
Doctor of Philosophy in Mechanical Engineering

Georgia Institute of Technology

December 2005

BORE WAVINESS MEASUREMENT USING AN IN-PROCESS GAGE

Approved by:

Dr. Thomas R. Kurfess, Advisor
Department of Mechanical Engineering
Clemson University

Dr. Steven Y. Liang
School of Mechanical Engineering
Georgia Institute of Technology

Dr. Shreyes N. Melkote
School of Mechanical Engineering
Georgia Institute of Technology

Dr. Paul M. Griffin
School of Industrial and Systems Engineering
Georgia Institute of Technology

Dr. Chen Zhou
School of Industrial and Systems Engineering
Georgia Institute of Technology

Date Approved: November 22, 2005

ACKNOWLEDGEMENTS

The author would like to take this opportunity to thank his advisor and dissertation committee chair, Dr. Thomas R. Kurfess. He has provided the guidance and resources to make this research possible. In addition to Dr. Kurfess, the author is grateful to the other members of the committee for their valuable comments and feedback on this dissertation.

The author would also like to thank the engineers and staff at the Timken Manufacturing Development Center. Without their support and resources this research could not have been completed. Most of all, the author would like to thank Darren Averett for his continuous support from the very beginning to the end of this project. The author is also thankful for the contributions of Bernie Ulmer, Cres Ferrell, and Ian Harrison, who were involved in different stages of this project.

This work was partially funded by a grant from The Timken Company. Any opinions, findings, and conclusions or recommendations are those of the author and do not necessarily reflect the views of The Timken Company.

TABLE OF CONTENTS

LIST OF TABLES

LIST OF FIGURES

LIST OF SYMBOLS

The following formatting is used for symbols:

- Numbers and indices are printed in *italicized* lower or upper case letters. Examples: f, t, V.
- Vectors and matrices are printed in **boldfaced** lower or upper case letters. Examples: $\mathbf{B}$, $\mathbf{H}$, $\mathbf{m}$.
- Standard functions are printed in plain lower or upper case letters. Examples: $\sin(\alpha)$, $\mathrm{E}[X]$, $\mathrm{Cov}(X,Y)$.
- Units are printed in plain lower or upper case letters. Examples: nm, Hz, mV.

$\mathbf{A}$	Matrix
$A(k)$	Amplitude of the *k*-th frequency in the spectrum
A_0	Amplitude
A_{crit}	Critical maximum profile amplitude
A_G	Maximum profile amplitude measured with the grinding machine
A_{GF}	Maximum profile amplitude in the grinding machine with the spindle off
A_{GN}	Maximum profile amplitude in the grinding machine with the spindle on
A_P	Maximum profile amplitude measured with the post-process machine
ΔA_P	Maximum profile amplitude error of the post-process machine
A_R	Maximum profile amplitude measured with the roundness machine

$\bar{A}_R$	Average maximum profile amplitude of the roundness machine
ΔA_R	Maximum profile amplitude error measured with the roundness machine
$\mathbf{B}$	Magnetic flux density
B	Bandwidth
b_j	Least square estimators of a regression coefficient β_j
$\mathrm{Cov}(X,Y)$	Covariance of the random variables X and Y
d_φ	Amount of eccentricity of the fingers in the y-direction
$E_x(k)$	k-th harmonic of the error movement in the x-direction
$E_y(k)$	k-th harmonic of the error movement in the y-direction
$\boldsymbol{\mathcal{E}}_x(k)$	Random variable of the k-th harmonic of the error motion in x-direction
$\boldsymbol{\mathcal{E}}_y(k)$	Random variable of the k-th harmonic of the error motion in y-direction
$\mathrm{E}[X]$	Expected value of the random variable X
e	Natural constant
$e(\theta)$	Error movement as a function of the rotational angle θ
e_i	Residuals of the i-th observation in a regression model
e_i	i-th sample of the error movement
$e_x(\theta)$	Error movement in the x-direction as a function of the rotational angle θ
$e_y(\theta)$	Error movement in the y-direction as a function of the rotational angle θ
f	Frequency
f_n	Undamped natural frequency in Hz
Δf	Frequency resolution

$f(t)$	Arbitrary function
$f(x)$	Probability density function
$g(x)$	Arbitrary function
$\mathbf{H}$	Magnetic field
H_0	Null hypothesis
H_a	Alternative hypothesis
H_{LP}	Transfer function of a low-pass filter
H_S	Transfer function of the measurement system
h_{crit}	Critical profile height
h_G	Profile height measured in the grinding machine
h_{GF}	Profile height in the grinding machine with the spindle turned off
h_{GN}	Profile height in the grinding machine with the spindle turned on
h_P	Profile height measured with the post-process machine
Δh_P	Profile height error measured with post-process machine
$\Delta h_{P,rel}$	Relative profile height error measured with post-process machine
h_R	Profile height measured with the roundness machine
$\overline{h}_R$	Average profile height measured with the roundness machine
Δh_R	Profile height error measured with the roundness machine
$\Delta h_{R,rel}$	Relative profile height error measured with the roundness machine
I	Electrical current
$I_{1/f}$	Noise current due to $1/f$ noise

I_{DC}	DC component of a current
I_{sh}	RMS noise current due to shot noise
i	Index variable
j	Imaginary unit
k	Index variable
k	Number of undulations per revolution
$k_{1/f}$	Constant for 1/*f* noise
k_B	Boltzmann's constant
k_C	Clipping value
k_{GG}	Gage voltage gain
k_{In}	Intercept of the voltage-finger displacement relationship
k_{SG}	Signal conditioning card voltage gain
k_{Sl}	Slope of the voltage-finger displacement relationship
k_{SZ}	Zero-adjust of the signal conditioning card voltage
$M_A(k)$	Fourier transform of the measurement at finger A
$\boldsymbol{\mathcal{M}}_A(k)$	Random variable of the *k*-th harmonic of the measurement at finger A
$M_B(k)$	Fourier transform of the measurement at finger B
$\boldsymbol{\mathcal{M}}_B(k)$	Random variable of the *k*-th harmonic of the measurement at finger B
$M_C(k)$	Fourier transform of the combined measurement of several probes
$M_W(k)$	Harmonic weighting function of the radius
$M_{W,E_x}(k)$	Harmonic weighting function of the horizontal error motion

$M_{W,E_y}(k)$	Harmonic weighting function of the vertical error motion
m	Index variable
$\mathbf{m}$	Vector of the sampled measurements
$\bar{m}(\theta)$	Average of several measurements
$m_A(\theta)$	Measurement at finger A
$m_B(\theta)$	Measurement at finger B
$m_C(\theta)$	Combined measurement of several probes or fingers
$m_i(\theta)$	Measurement of the *i*-th probe or *i*-th repetition
N	Number of samples
$N_A(k)$	*k*-th harmonic of the lumped noise at finger A
$\mathcal{N}_A(k)$	Random variable of the *k*-th harmonic of the lumped noise at finger A
N_B	Number of bits
$N_B(k)$	*k*-th harmonic of the lumped noise at finger B
$\mathcal{N}_B(k)$	Random variable of the *k*-th harmonic of the lumped noise at finger B
N_b	Number of observations
N_E	Number of ensembles
N_m	Number of measurements in multi-orientation methods
N_P	Number of predictor variables in a regression model
N_R	Number of data points per revolution
$\bar{N}_R$	Average number of data points per revolution
N_S	Number of samples

N_W	Window size
n	Index variable
$n_A(\theta)$	Lumped noise at finger A
$n_B(\theta)$	Lumped noise at finger B
p	Probability
p_k	*k*-th pole of a transfer function
Q	Least square criterion
q_E	Charge of an electron
R	Electrical resistance
$R(k)$	Fourier transform of the radius
$\tilde{R}(k)$	Estimated *k*-th harmonic of the radius
$\hat{R}_{AMDF}$	Average magnitude difference function
$\hat{R}_{ASDF}$	Average square difference function
$\tilde{R}_D(k)$	Estimated *k*-th harmonic of the radius using the difference of the signals
$\hat{R}_{DCF}$	Direct correlation function
$\hat{R}_{HS}$	Hybrid sign estimator
$\hat{R}_{NAMDF}$	Normalized average magnitude difference function
$\hat{R}_{NDCF}$	Normalized direct correlation function
$\hat{R}_{PC}$	Polarity coincidence estimator
$\tilde{R}_{PS}(k)$	Estimated *k*-th harmonic of the radius using the phase-shifted sum

$\tilde{R}_S(k)$	Estimated *k*-th harmonic of the radius using the sum of the signals
r	Vector of the radii
$\overline{r}$	Average radius
$r(\theta)$	Radius as a function of the rotation θ
r_i	*i*-th sample of the radius
s	Complex variable in the Laplace Transform
s	Standard deviation
t	Time
t_0	Instant in time
T	Time or time period
T	Absolute temperature
T	Test statistic with a *t*-distribution
$T(\mu_\varphi)$	Performance index for the optimal eccentricity angle
$T_H(\mu_\varphi)$	Heuristic based performance index for the optimal eccentricity angle
V	Voltage
$V(t)$	Time-varying voltage
V_G	Voltage between different grounds
V_M	Measured voltage
V_R	Voltage of the gage fingers
V_{RMS}	RMS value of a time-varying voltage
V_S	Voltage of a signal source

V_T	RMS voltage due to thermal noise
ΔV_{res}	Resolution of the discretized voltage
$\mathrm{Var}(X)$	Variance of the random variable X
w_i	Weight of the i-th expression or i-th observation in weight least squares
X	General real random variable
X_{ij}	i-th observation of the j-th predictor variable
x_d	Displacement of a finger
$x(k)$	k-th observation of a sample
$\Delta x(k)$	Profile difference
$\Delta x_G(k)$	Profile difference measured with the grinding machine
$\Delta x_{GF}(k)$	Profile difference in the grinding machine with the spindle off
$\Delta x_{GN}(k)$	Profile difference in the grinding machine with the spindle on
$\Delta x_{mag}(k)$	Magnitude of the profile differences on the post-process machine
$x_P(k)$	Profile measured with the post-process machine
$\Delta x_P(k)$	Profile difference measured with the post-process machine
$x_R(k)$	Profile measured with the roundness machine
$\overline{x}_R(k)$	Average profile measured with the roundness machine
$\Delta x_R(k)$	Profile difference of the roundness machine measurements
$\overline{x}$	Arithmetic mean of a sample
Y	General real random variable
Y_i	i-th observation of the response variable in a regression model

$\hat{Y}_i$	Fitted value of the *i*-th observation in a regression model
$y(k)$	Output of a digital filter
Z	General complex random variable
α	Angle
β	Angle
β_0	Intercept term in a regression model
β_j	Coefficient of the *j*-th parameter in a regression model
ε_i	Random error term of the *i*-th observation in a regression model
$\varepsilon_S(n)$	Error of the sampling location
κ	Small constant
κ_C	Critical amplification value for the vibration separation heuristic
μ	Expected value
μ_0	Permeability of free space
μ_n	*n*-th central moment of a random variable
μ_r	Relative permeability of a ferromagnetic material
μ_X	Expected value of the real random variable X
μ_Y	Expected value of the real random variable Y
μ_Z	Expected value of the complex random variable Z
μ_Φ	Expected value of the eccentricity angle
Φ	Random variable of the eccentricity angle

φ	Eccentricity angle
$\Delta\varphi$	Variation of the eccentricity angle or finger angle
λ	Wavelength
σ	Standard deviation
σ^2	Variance
$\sigma_{E_x}^{\ 2}$	Variance of the horizontal error motion harmonics
$\sigma_{E_y}^{\ 2}$	Variance of the vertical error motion harmonics
$\sigma_{N_A}^{\ 2}$	Variance of the random noise harmonics of finger A
$\sigma_{N_B}^{\ 2}$	Variance of the random noise harmonics of finger B
$\sigma_{\mu}^{\ 2}$	Variance of the eccentricity angle
θ	Rotational angle
θ	Phase angle
$\Delta\theta$	Angular increment
π	Mathematical constant, area of the unit circle
ω	Angular velocity
ω_c	Cutoff frequency
ω_n	Undamped natural frequency in radians/s
ζ	Damping ratio

LIST OF ABBREVIATIONS

AC	Alternating current
ACH	Analog input channel signal
ADC	Analog-to-digital converter
AE	Acoustic emission
AIGND	Analog input ground signal
AISENSE	Analog input sense signal
AMDF	Average magnitude difference function
ASDF	Average square difference function
BNC	Bayonet Neill Concelman or Bayonet nut connector
CCF	Combined correlation function
DAQ	Data acquisition
DC	Direct current
DCF	Direct correlation function
DIFF	Differential mode
DSP	Digital signal processor
EMI	Electromagnetic interferences
FFT	Fast Fourier transform
FM	Frequency modulation
IC	Integrated circuit
ID	Inner diameter
LSB	Least significant bit

MA	Moving average
NRSE	Nonreferenced single ended mode
LTI	Linear time-invariant
LVDT	Linear variable differential transformer
OD	Outer diameter
PCI	Peripheral component interface
PGIA	Programmable gain instrumentation amplifier
PLC	Programmable logic controller
PWM	Pulse width modulation
RFI	Radio-frequency interferences
RMS	Root-mean-square
RSE	Referenced single ended mode
UPR	Undulations per revolution

SUMMARY

Profile waviness is one of the main causes for scrapped parts in precision bore grinding. Although efforts have been made to reduce its occurrence, the problem has not been eliminated completely. In production, the identification of a few scrapped parts in a lot of several thousands often requires expensive manual processes. Grinding machines used to produce these parts are usually equipped with measurement gage heads having tactile probes. Until now, these in-process gages have been used to measure only the average diameter of the part.

This research focused on the use of these tactile probes to measure bore waviness in precision-ground parts. The first objective was to develop a post-process machine that performs automated measurement of the bore profile and is capable of detecting waviness. The machine was built using the same measurement system and the same roll-shoe centerless fixture as the grinding machines used for the production of the parts. The machine was designed and set up such that disturbances of the measurement are minimized. It was shown that the machine reaches accuracies close to those obtained by manually operated roundness machines. The cycle time is approximately 4 seconds per part compared to several minutes for manually operated roundness machines.

As a second objective, the possibility of measuring waviness directly in the grinding machine was evaluated. Feasible design modifications to reduce the effect of disturbances are very limited in grinding machines, since interference with the grinding process must be avoided. Therefore, analytical methods were developed to reduce these effects and partly restore the original profile. The main disturbances that were addressed are errors due to irregular sampling of the profile, to the frequency response behavior of

the gage heads, and to motion of the workpiece center relative to the gage heads. The post-process machine was used as a development and test platform for the analytical methods. To further verify these methods, tests were also conducted in an industrial grinding machine.

CHAPTER 1 – INTRODUCTION

1.1 Motivation

Today's engineering applications face the challenge of providing products with increased efficiency, longer product lifetime, and higher quality. These requirements lead to a growing demand for high-precision parts. Examples can be found in all engineering areas. One specific example is the bearing industry. Manufacturing processes have to keep up with this trend by providing parts with tighter tolerances and higher surface finish. On the other hand, competition requires manufacturing costs and cycle times to be continuously reduced. In mass production, the machining time can be as low as a few seconds per part for a specific machining operation. As a result of these requirements, a shift from conservative towards more aggressive machining strategies is fostered. In this setting, constant quality monitoring is critical.

1.2 Problem Statement

The raceways of high precision bearings are usually finished by a grinding process. Potential defects in the raceway surface, such as waviness patterns, result in unwanted vibration, increased bearings noise, and premature failure of the bearing. Depending on the function of the bearing, its failure can have catastrophic results and may lead to costs much higher than the cost of replacing the bearing itself. To prevent this, manufacturers define strict specifications for the raceway surfaces. To assure the specifications are meet, continuous monitoring of the grinding result is necessary.

A procedure commonly used in industry is to monitor the process by taking sample parts from the production at defined intervals and testing them on a roundness machine. If defective parts are found, the machine that produced the part is halted and the problem is remedied. In addition, it is necessary to sort out all parts in the lot not meeting the specifications. Currently, testing and sorting parts involves a high degree of manual labor. With lot sizes of several thousands parts, this is a time consuming and therefore expensive process. Since the inspection is a very repetitive task, it leads to fatigue and the reliability and repeatability of this process is therefore not guaranteed. Thus, it is highly desirable to improve the efficiency and reliability of the part inspection by automating this process.

The parts to be inspected are the outer rings of the bearings. The bearings are used for automotive components. The automation of the raceway inspection is a challenging task due to the small size of the bore.

1.3 Objectives

The objectives of this research are twofold. The first objective is to develop a machine that is capable of automatic profile measurement and part testing according to the specifications. It can be utilized as an independent post-process machine to sort the parts. It is desirable to obtain high measurement accuracy and a low cycle time within certain financial and development time constraints.

A second objective of this research is to evaluate the possibility of in-process part inspection directly in the grinding machine. This poses a bigger challenge than the

development of a post-process system since detrimental effects, such as mechanical vibration, are expected. While the post-process machine can be solely designed for the purpose of precision measurement, the technical modifications of the grinding machine for accuracy improvement are very limited.

In pursuing these objectives, special emphasis is put on the industrial implementation of the results. Owing to this requirement and the two research objectives, the post-process machine is built as a partial replication of a grinding machine by using the same workpiece fixture for part rotation and the same measurement system as in a grinding machine. The grinding machines are usually equipped with measurement gage heads having tactile probes. Until now, the probes are used to measure only the average diameter.

Using components of the grinding machine for the design of the post-process machine has several benefits. The workpiece fixture and the measurement system are proven to work reliably in a harsh manufacturing environment. Maintenance of the post-process machine is simplified since the machine shares spare parts with a grinding machine. In addition, operators do not have to be trained with the setup and maintenance of new hardware. The workpiece fixture has the advantage of short loading and unloading times which helps reducing the cycle time of the post-process machine. With respect to the second objective, due to the similarity of the two machines, the post-process machine will serve as a test platform for in-process measurements in the grinding machine.

1.4 Research Plan and Dissertation Outline

The dissertation outline is depicted in Figure 1-1. Chapter 2 gives some background on grinding and in-process measurement in grinding. It concludes by fitting the systems developed here into the framework of existing process monitoring systems.

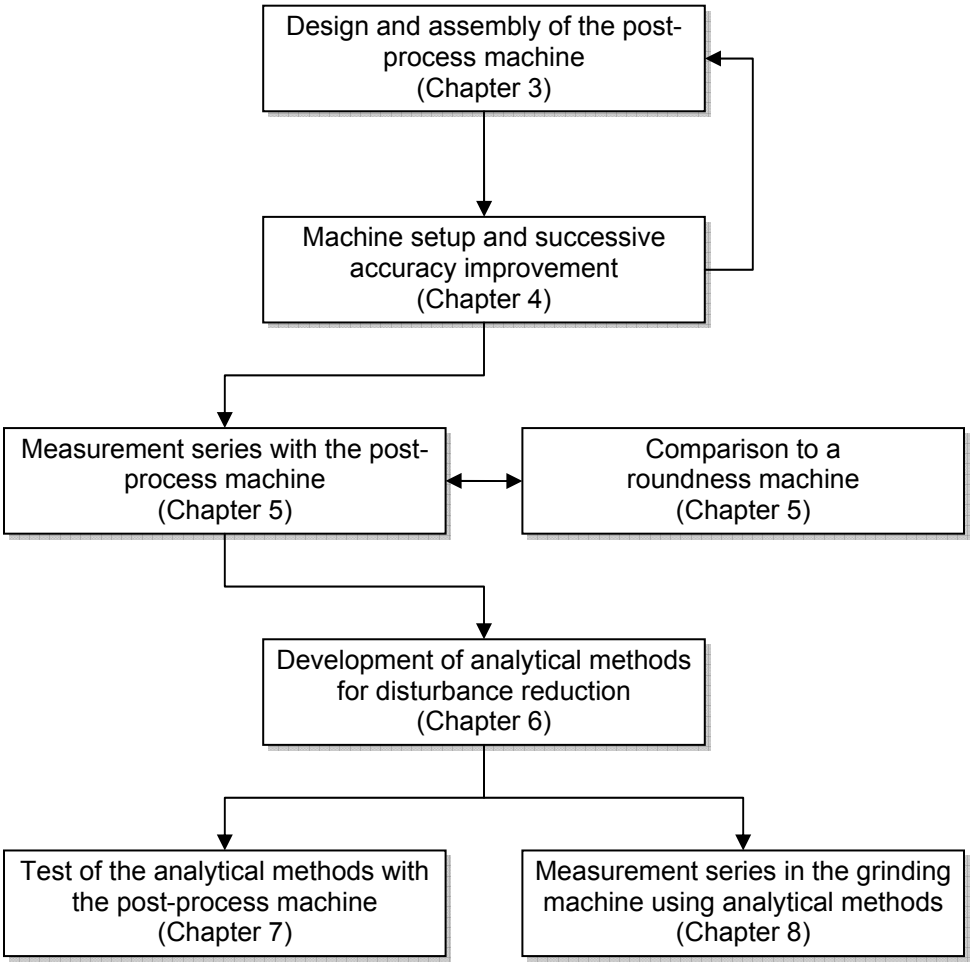

Figure 1-1: Dissertation outline

Chapter 3 and Chapter 4 deal with the development of the post-process machine. The development involves several steps of successive accuracy improvements and design

revisions. Chapter 3 presents the hardware components that were chosen for the final design along with their specifications. Chapter 4 gives an overview of the disturbances that affect the measurement and explains the setup of the hardware for measurement. Chapter 5 evaluates the performance of the post-process machine as it would be used in an industrial environment. A measurement series is conducted with a set of test parts and is compared to measurements taken with a roundness machine. In Chapter 6, analytical methods are developed to partially filter the effect of disturbances from the measurement signal. The methods are developed based on the data obtained with the post-process machine. However, they are targeted mainly for the grinding machine to improve the measurement accuracy when technical modifications are not feasible. Chapter 7 tests the developed methods with the post-process machine and Chapter 8 presents tests performed on a grinding machine. Chapter 9 concludes the dissertation by summarizing the results and giving directions for further development.

CHAPTER 2 – BACKGROUND

2.1 Fundamentals of Grinding

Grinding is a machining process that utilizes hard abrasive particles of random shape to remove material. Its cutting mechanisms allow surface finishes and tolerances far superior to other cutting processes to be achieved. In addition, it is the most suitable process for machining hardened materials. Because of these two properties, grinding is ideal for the production of high precision parts such as bearing rings. Precision grinding is usually used as the last of several manufacturing steps, therefore making it the quality defining finishing process [Lezanski, Rafalowicz 1993].

Despite its advantages, grinding is on the other hand also the least understood machining process. The abrasive process itself is very complex. Besides cutting, it involves rubbing and plowing. Due to the high number and the random geometry of the abrasive particles, modeling is more difficult for grinding than for other machining processes. The grinding process is also highly transient. Both, the cutting ability and the shape of the grinding wheel change during the operation. A third difficulty is the high number of setup and process parameters that affect the process [Hahn, Lindsay 1971a, Hahn, Lindsay 1971b]. Some examples are the elastic deformation of the machine [Kaliszer, Webster 1982] and the tool [Tanaka et al. 1975], setup of the dressing process and frequency of the redressing [Inasaki 1985a], wear of the dressing tool, condition of the coolant, or wheel-to-wheel variation of the cutting properties. The influence of these parameters on the grinding result is still not understood as well as other manufacturing

processes [Kegg 1983]. Due to the sensitivity of the grinding process to its parameters, reproducibility remains a critical issue.

2.2 Internal Centerless Grinding

Cylindrical grinding is a special grinding setup for manufacturing cylindrical workpieces. During the material removal, both the grinding wheel and the workpiece are rotating. Depending on the orientation of the machined surfaces, it is further categorized into internal and external grinding. Internal grinding refers to the machining of inner workpiece surfaces such as bores. The process requires the grinding wheel to be smaller than the diameter of the bore. For small bores, as they are considered here, this presents a special challenge, since the wheel wears even faster and requires more dressing cycles. As a result, the transient nature of the grinding process is aggravated by the small wheel size making the process even less predictable.

A common workholding mechanism for internal grinding is the centerless setup. With this setup, the workpiece is held in place by contact at three points. The workpiece center however can float. In Figure 2-1, the principle of the roll-shoe centerless fixture is shown. The three contact points are provided by two rolls and a stationary shoe. The two rolls rotate the workpiece during the grinding process. Two face plates hold the workpiece in the axial direction. The angles between the three contact points are an important characteristic of the setup. The centerless workholding method eliminates the step of workpiece centering, thus allowing very short loading and unloading times. Because of this, the centerless fixture is ideal for mass production. Unfortunately, due to

the floating workpiece center, the roundness generation process is more complex than with other workholding methods and can be an additional source for errors [Nakkeeran, Radhakrishnan 1988], [Hashimoto et al. 2000]. The possibilities for adapting research results from the field of external grinding to internal grinding are therefore limited [Tönshoff et al. 1980].

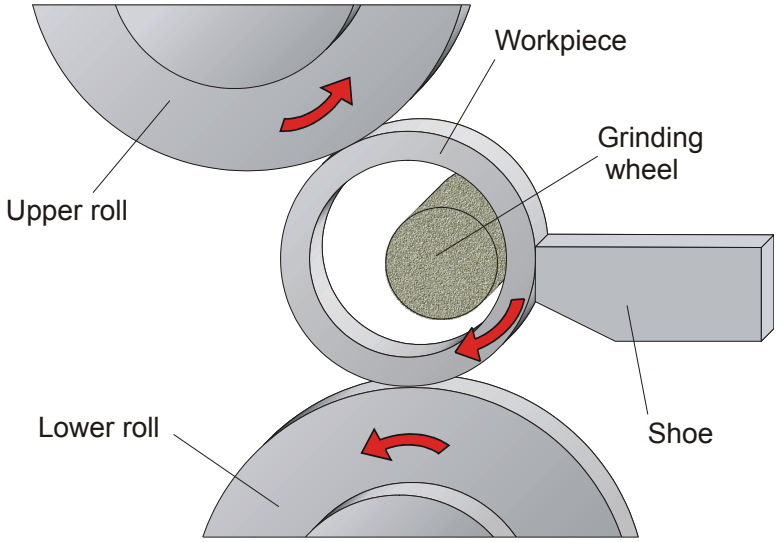

Figure 2-1: Principle of the roll-shoe centerless fixture

2.3 Classification of Geometrical Errors

The quality of the grinding process is usually evaluated based upon three characteristics of the finished parts: the geometrical error, the surface finish, and the subsurface material condition, which may for example be adversely affected by grinding burn. The geometrical error, in its most general sense, is regarded as any departure of the true workpiece shape from the desired three-dimensional shape. Based on functional

requirements, the geometric deviations can be broken down into three types: form error, waviness, and roughness [Whitehouse 1994]. Examples of profile shapes along with their potential causes are shown in Table 2-1. It should be mentioned that there are no clear boundaries between the different error types. A wave pattern may be regarded as a long-wavelength form of waviness or a short-wavelength form of a form error. The same applies for the boundary between waviness and roughness. The boundaries are therefore usually defined by the size of the workpiece or by functional properties.

Table 2-1: Classification of geometrical errors (adopted from [DIN 4760])

Error type	Profile shape	Potential cause
Form Error		Workholding mechanism, error in slideways
Waviness		Vibration of the machine or the tool
Roughness		Type and condition of tool, tool feed rate

This research is concerned with the measurement of waviness. The definition of waviness is made based on the company specification for the workpieces. Waviness is here defined as any wave pattern on the inner bore that exhibits 10 to 250 undulations per revolution (UPR). Patterns with less than 10 undulations are regarded as a form error.

2.4 Waviness and Chatter in Grinding

Profile waviness is caused by a vibration of the tool relative to the workpiece. In machining processes, this vibration is referred to as *chatter*. A lobing pattern can built up on both the workpiece and the grinding wheel. Workpiece waviness due to chatter can be severe enough to be visible to the human eye. A significant amount of work has been devoted to understanding the underlying mechanisms that lead to chatter [Tobias 1961]. It is caused by two different types of vibrations: forced vibrations and self-excited vibrations [Malkin 1989], [Inasaki 2001].

Forced vibrations are any vibrations that are not created by the abrasive process itself. The most common source of forced vibrations is spindle or wheel unbalance [Nikulkin 1970], [Rubinchik, Soloveichik 1970]. Other sources are bearings, hydraulic components [Nakano et al. 1986], mechanical or electrical unbalance of electromotors [Peters, Vanherck 1971], driving V-belts [Arantes, Cunha 1970] or even the environment. Elimination of forced vibrations usually begins with the measurement of the vibration frequency. Once the frequency is known, it is usually easy to identify the source of the vibration. In a subsequent step, technical modifications can be made to eliminate or reduce the vibration, such as using vibration-isolating material in the hub of the grinding wheel [Grazen 1983], [McFarland et al. 1999].

Self-excited vibrations are caused by the abrasive process itself and lead to regenerative chatter [Hahn 1954]. Random disturbances in the grinding process result in short transient vibrations of the grinding wheel relative to the workpiece which leave a wave train in the part profile (Figure 2-2). After one part revolution, the wheel passes the

wave train again and the varying depth of cut excites the system another time. If the system is stable, the wave train will be ground out gradually with each successive pass. In the unstable case, the vibrations are intensified during each pass and lead to chatter.

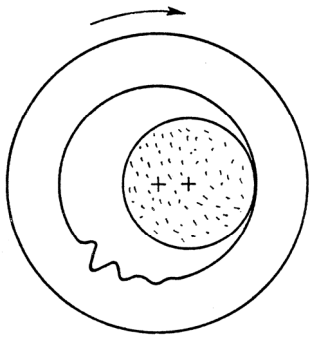

Figure 2-2: Workpiece with a random wave pattern [Hahn 1954]

Whether vibrations are intensified or attenuated depends on several factors such as the geometry of the workholding mechanism [Furukawa et al. 1970], [Zhou 1996], [Hashimoto et al. 2000], the contact zone stiffness, and the wear characteristics of the wheel [Hashimoto et al. 1984], [Hashimoto et al. 1985], [El-Wardani et al. 1987]. Internal centerless grinding is more prone to chatter than other grinding processes since the grinding wheel is usually less rigid and the workpiece center is floating [Hahn 1954], [Zhou 1996], [Udupa et al. 1988].

To avoid regenerative chatter, several approaches are used. They involve careful setup of the workholding mechanism, modification of the wheel or workpiece rotational speed, selection of the wheel type and the dressing technique, and frequent dressing of the wheel. Another important factor is the static and dynamic stiffness of the system, since the chatter frequencies are usually close to the natural frequency of the setup.

Improving static and dynamic stiffness and increasing damping helps reducing the occurrence of chatter. This can be accomplished by a variety of technical methods such as the use of dynamic dampers [Nakano et al. 1988], wheels with flexible hub [McFarland et al. 1999], vacuum-preloaded hydrostatic shoe [Yang et al. 1999] or the injection of high-viscosity coolant into the wedge area between wheel and workpiece to create hydrodynamic pressure [Maksoud, Mokbel 2002].

Despite the progress that has been made in understanding the causes of chatter and its prevention, it still remains a problem in industrial grinding, especially in the internal centerless grinding of small parts. Due to the complexity of the grinding process and its sensitivity to setup and process parameters, chatter can be caused in a number of different ways. In a high-volume industrial production its occasional occurrence is therefore unavoidable.

2.5 Process Monitoring

Process monitoring is used since reliable prediction of the workpiece quality is not possible due to the complex transient nature of the grinding process. Monitoring systems are designed to fulfill certain tasks such as observing the workpiece profile waviness. This can be accomplished either directly by measuring the workpiece geometry during the grinding operation or indirectly by measuring process variables such as grinding forces, vibration, or acoustic emission and drawing conclusions on the expected profile based on these signals [Tönshoff et al. 2002].

2.5.1 Criteria for a Process Monitoring System

During the last 30 years, a variety of systems have been developed to monitor workpiece geometry utilizing different types of sensors. Although most approaches yielded satisfactory results in a lab environment, applications in industry are limited to a very few different methods. To evaluate and compare process monitoring systems with respect to their information content and their applicability in a manufacturing environment, the following criteria can be used:

- How detailed is the information that the process monitoring system yields about the workpiece geometry? Does it yield only a single value characterizing the total amount of waviness in the profile across a wide frequency band or does it yield a profile trace sampled at certain angular increments? What is the highest frequency in the profile that the system can measure?

- How accurate is the measurement, i.e. what is the average deviation between the measured geometry and the true geometry?
- How much space does the sensor system require on the work piece? Is it suitable for internal grinding of small parts or do the sensors interfere with the grinding wheel?
- Is the sensor system able to maintain its accuracy even in presence of coolant or swarf?
- Is the setup of the system for specific a grinding task complicated and time consuming or can it be done by a skilled machine operator?
- What costs are associated with the implementation of the system?

2.5.2 Monitoring Systems Using Indirect Methods

Process monitoring systems for the workpiece geometry can be grouped into direct and indirect methods. Direct process monitoring methods have the advantage of retrieving the desired quantity directly, thus achieving a higher accuracy. However, direct geometry measurement during the grinding process is often technically difficult to implement. Therefore, indirect methods are often used, utilizing quantities that can be more easily measured. The downside is a loss in information content and accuracy since the measured quantity has to be related to the workpiece geometry.

The most common sensors for indirect measurement are acoustic emission (AE) sensors. AE sensors have been successfully applied for detection of grinding wheel contact with the workpiece and therefore grinding cycle start [Inasaki 1985a]. It was found that they are also capable of detecting excessive vibration in the grinding system.

Therefore, AE sensors are used for roughness estimation or chatter detection [Inasaki 1991]. For a pure contact detection between grinding wheel and workpiece, the location of the AE sensor is not very critical and the sensor can for example be placed on the tailstock of the machine [Inasaki 1985a]. For waviness and chatter detection the sensor has to be placed in close proximity to the grinding zone to be effective. In [Matsumoto et al. 1993], [Inasaki 1997], and [Inasaki 1999] an AE sensor including a battery and a FM transmitter was incorporated into the grinding wheel. The disadvantage of this method is that a clear signal is obtained only once per wheel revolution when the sensor passes the grinding zone. This method also requires the grinding wheel to be large enough so that the sensor can be incorporated into the wheel hub. Inasaki [1991] used a stationary AE sensor and supplied a continuous stream of fluid from the grinding zone to the sensor to provide a stable path for transmission. The quality of the signal is highly susceptible to contaminations of the fluid.

To relate the AE signal to the amount of waviness in the profile, characteristic values are computed from the AE data. In the time-domain, the root-mean-square (RMS) value is traditionally used [Webster et al. 1994], [Webster et al. 1996], [Kim et al. 2001]. It is implemented as a continuous filter. Its main disadvantage is that due to its averaging operation, sharp impulses in the signal are smoothed out discarding valuable information. More powerful methods to process the signal are based on the spectral decomposition of the data. Since no acceptable analytic models exist for the relationship between AE and surface profile, most models rely on empirical models. The most common empirical models are artificial neural networks [Inasaki 1997], [Inasaki 1999]. The various neural network implementations differ in the network architecture and in the type of information

that is passed to the input layer of the network. In [Kwak, Song 2001] and [Kwak, Ha 2004] characteristic time-domain and frequency-domain values such as the RMS value, the standard deviation or the maximum amplitude in the spectrum are used as inputs. Karpuschewski et al. [2000] normalizes the spectrum with respect to the highest amplitude in the considered frequency range and utilizes the amplitudes of selected frequencies as inputs. Further differences between neural network implementations can be found in the number of hidden layers [Kwak, Ha 2004] or the type of learning [Susič, Grabec 2000]. The outputs of the neural networks are usually values indicating the estimated likelihood of a faulty state such as workpiece waviness. Neural networks proved to have good predictive capabilities for unusual grinding states and also adequate speed due to their parallel nature. Their main disadvantage is that they are highly specific to the grinding setup. To adapt a network to a different setup, representative training data has to be generated, the network has to be trained, and threshold values have to be defined for the network outputs. To overcome the disadvantage of time consuming training processes, Gradišek et al. [2003] proposed to use the entropy of the power spectrum as a characteristic value. The entropy is an indicator for the amount of randomness in the spectrum. It is low if the total power in the spectrum is concentrated on a few distinct frequencies, and it is high if it is distributed over a wide frequency band.

Closely related to AE monitoring methods are monitoring systems based on vibration. Vibration signals are acquired by accelerometers that are mounted for example on the tailstock [Mori et al. 1992] or on a shoe in centerless grinding [Lacey 1990a], [Lacey 1990b]. Similar to AE signals, vibration is capable of estimating workpiece quality [Lacey 1990b]. Chen et al. [1996] used a neural network to indicate the existence

of chatter. Each input neuron is supplied with the acceleration density of a frequency band in the spectrum. With this approach the number of inputs could be kept low, resulting in a high processing speed. Mori et al. [1992] employed a network with 106 inputs, each representing a discrete frequency. The higher number of inputs allowed the distinction between six different types of vibration such as workpiece chatter, wheel chatter or different structural vibrations. In [Fu et al. 1994], the neural network is replaced by the entropy function. Based upon the entropy value, a classification of the vibration into normal, wheel regenerative chatter, or workpiece regenerative chatter can be made. The spectrum is filtered by a three-point-moving-average filter to smooth out irregularities. This filter is simple to implement but comes with the side effect of reduced vibration amplitudes at the peaks. In [Fu et al. 1996] a morphological filter is therefore used instead of the moving-average filter.

Besides acoustic emission and vibration, some systems exist that utilize the grinding forces. In [Govekar et al. 2002] an application is presented that is based on the entropy rate of the normal grinding force. Another approach is documented by Tönshoff et al. [1985]. Opposite to most of the other indirect methods which rely on empirical relationships, this approach is based on a theoretical model between the grinding normal force and the resulting workpiece waviness.

2.5.3 Monitoring Systems Using Direct Methods

Direct methods can be grouped into contact and non-contact methods [Osborne 1993]. Systems with contacting probes usually utilize two or more probe fingers that trace the surface of the workpiece. The finger motion is in most cases converted into an electrical signal by inductive sensors [Knyazhitskii et al. 1989], [Gao, Jones 1992]. Other designs based on capacitive sensors are also reported [Kaliszer et al. 1979]. Application of tactile probes is wide spread in industry and can be considered standard for precision grinding systems [WMSW 1969], [TP 1978], [Scholz 2002]. The probes are primarily used to measure the average diameter of the workpiece and to terminate the grinding process when the required target value is reached [Tönshoff et al. 1980]. Since for average diameter measurements higher frequencies are irrelevant, most commercially available gages possess a relatively low cutoff frequency between 200 and 400 Hz [Longanbach, Kurfess 2001]. Foth [1989] developed an in-process system for external grinding. The used probes have a cutoff frequency of more than 1000 Hz and therefore allow waviness measurement of more than 100 UPR at 600 RPM workpiece rotational speed. The probes are used in addition to an existing gage for average diameter measurement. This system is therefore not suitable for internal grinding of small parts because of its space requirements. Commercial probes have nowadays achieved accuracies of 0.5 μm or better with resolutions down to 0.025 μm. The overall measurement accuracy is limited by machine vibration and inaccuracies in the workpiece rotation that are superimposed on the workpiece profile. In [Longanbach, Kurfess 1998], spindle rotational errors are separated from the workpiece profile by applying a high-pass filter with a 10 UPR cutoff frequency. This approach has the disadvantage that workpiece

profile information below 10 UPR may be discarded as well. Tönshoff and Chen [1989] presented a solution using two probes, one tracing the workpiece and the other tracing the workpiece holder as a reference. Subtracting the signals yields the workpiece profile without vibration. Other in-process systems combine the information from multiple probes on the workpiece to overcome this problem. With three probes the disturbances and workpiece profile can be separated even if they occur at the same frequencies [Foth 1989], [Li et al. 1991]. A more detailed review of vibration separation methods will be presented in section 6.6.

Non-contacting probes have the advantage that they are virtually wear-free. A simple class of non-contacting probes are pneumatic sensors. They utilize the fact that the pressure inside a precision air nozzle depends on the distance of the nozzle to a surface such as the workpiece. Trumpold and Mack [1975] presented a pneumatic sensor that has a measurement range of 250 μm and a linearity error of 7.5 μm. Hydraulic sensors are similar to pneumatic sensors except that oil or an emulsion is used instead of air [Suzuki 1984]. The strength of fluid based sensors is their robustness and their insensitivity to coolant and swarf. They fall short in terms of accuracy compared to most tactile probes. In addition, instead of measuring the distance from the sensor to a small point on the workpiece, they tend to measure the average distance to a small area on the workpiece. They are therefore not suitable for measuring waviness of the workpiece surface.

The largest class of non-contacting probes are optical sensors. They consist of a light source emitting either white light or laser light and one or more light detectors. Several in-process systems measure the distance between the sensor and the workpiece using the triangulation method [Lee et al. 1987], [Matsuo et al. 1993], [Drew et al. 1999].

This method projects a laser beam on the workpiece with a certain angle of inclination. The reflected beam is projected onto a photodiode array through a lens. The exact location of the reflection point on the array depends on the distance between the sensor and the workpiece. By evaluating the light intensity of the different photodiodes in the array, the distance of the workpiece can be estimated. Systems based on this method have a relatively large measurement range of several millimeters [Drew et al. 1999]. As a consequence, the resulting measurement error is relatively large as well. Lee et al. [1987] found it to be about 20 μm. The most important limiting factor of the accuracy is the diameter of the laser beam which should be ideally as small as possible. Novak [1981] developed a system that measures the workpiece diameter by partially screening two laser beams. The beams touch the workpiece tangentially and are partially screened by the workpiece. A DC motor adjusts the position of the beams to maintain a constant screening of 50 % as the diameter of the workpiece changes. The distance between the beams is measured by an encoder. The presented system has an accuracy of 10 μm. Since the measurement requires constant positioning of the beams, it is relatively slow and not capable of detecting high undulation wave patterns. Optical methods are also used to measure the surface roughness. Optical surface roughness measurement systems make use of the fact that the light scattering behavior depends on the roughness of the surface [Brodmann et al. 1984], [Inasaki 1985b], [Brodmann et al. 1986]. All optical systems have the disadvantage of a high susceptibility to cooling fluid or swarf. This limitation has restricted their use to lab environments or post-process quality control systems. In addition, the discussed optical systems are developed for external grinding processes.

They are not suitable for internal grinding operations, where access to the machined surface is very limited.

In [Lee et al. 1997] and [Lee et al. 2000] an eddy current sensor is used for diameter measurement. The measurements are sampled at 250 Hz. Since the sensor is highly affected by noise, the samples are combined into a single diameter reading using a Kalman filter. The measurement range of the sensor was 1 mm and the error for the averaged diameter value was within 4 μm.

Tönshoff et al. [1980] presented a sensor that was specifically designed for the measurement of small parts in internal grinding. To avoid possible interference with the grinding wheel, the sensor is placed on the outer diameter of the workpiece and measures wall thickness using ultrasonic impulses. The sensor head contains both the impulse transmitter and receiver. When a sound impulse is sent, a part of it is reflected by the outer diameter surface and a part by the inner diameter surface of the workpiece. The receiver records the time difference between the two reflected waves and, given the sonic speed, can estimate the wall thickness. The sensor head is sufficiently compact to be used for small parts. To avoid abrasion, the sensor is coupled to the workpiece by means of a fluid film. The accuracy of the developed system is within 2 μm.

2.5.4 Comparison of Methods

The strengths and weaknesses of the discussed process monitoring system are summarized in Table 2-2. The table evaluates the systems according to the criteria outlined in section 2.5.1. The information detail is the type of information that the methods yield. A value of “1” means the method yields only an indicator value

characterizing the amount of waviness on a certain scale, without any physical meaning. "2" means the method yields the average diameter of the part and "3" means the method yields a trace of the profile sampled at certain angular increments.

Table 2-2: Comparison of Process Monitoring Systems

Method	Principle	Relevant Publications	Information Detail	Approximate Accuracy [µm]	Frequency response	Robustness against coolant, swarf	Space Requirement	Setup Time
Indirect	Acoustic emission	[Inasaki 1991], [Webster el al. 1994]	1	–	++	+	++	--
	Vibration	[Mori et al. 1992], [Lacey 1990a]	1	–	++	++	++	--
	Force signal	[Govekar et al. 2002], [Tönshoff et al. 1985]	1	–	++	++	++	--
Direct	Tactile probes	[Kaliszer et al. 1979], [Foth 1989],	3	0.5	o	+	o	++
	Pneumatic sensor	[Trumpbold, Mack 1975]	3	2-10	-	+	-	++
	Hydraulic sensor	[Suzuki 1984]	3	2-10	-	+	-	++
	Laser triangulation	[Lee et al. 1987], [Matsuo et al. 1993], [Drew et al. 1999]	3	10-30	++	--	--	++
	Laser beam screening	[Novak 1981]	2	10	--	o	-	++
	Eddy current sensor	[Lee et al. 1997], [Lee et al. 2000]	2	5	--	o	--	++
	Ultrasonic sensor	[Tönshoff et al. 1980]	3	2	o	+	+	++
very good (++), good (+), average (o), poor (-), very poor (--) Information detail: good/bad indication (1), average diameter (2), profile trace (3)								

Since the indirect methods yield only an indicator value, no accuracy can be stated for them. Their complicated setup and therefore inflexibility towards different machine or grinding parameters limits their application for in-process monitoring in an industrial environment. The main disadvantage of optical methods is that they are prone to cooling fluid or swarf. They are therefore as well not suitable for robust industry applications.

Tactile probes have been used in industry for a while and the commercially available probes provide an accuracy that is superior to the other measurement methods. Their main problem is their relatively low cutoff frequency so that they have been used in industry mainly for the measurement of the average workpiece diameter. Another potential difficulty is the space requirement, which is however less critical than with other direct measurement methods. In addition, most industrial systems for precision grinding are already equipped with these probes, so that it is reasonable to investigate if they can also be used to measure the workpiece waviness.

2.6 Purpose of this Work

Figure 2-3 shows how the two systems developed here are expected to fit into the existing inspection methods. Manually operated roundness machines provide the highest accuracy and are considered state-of-the art for roundness measurement. Inspection costs are high since an operator is needed to perform the measurement. Therefore, they are used only for sample measurements.

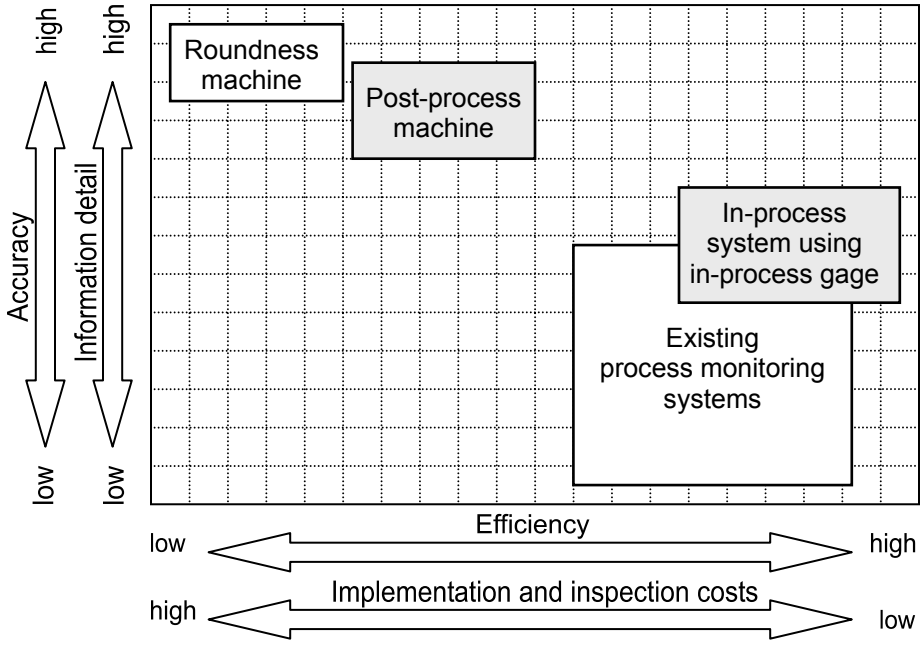

Figure 2-3: Present work in the context of existing work

The process monitoring systems discussed in the previous sections are highly efficient since they are fully automated and do not affect cycle time but come with the disadvantage of significantly lower accuracy.

The goal of this work is to present two additional methods that fall in between roundness machines and the existing process monitoring systems. The post-process machine will be designed as a fully automated measuring machine with a high throughput while sacrificing some accuracy compared to a roundness machine. In-process measurement using an in-process gage is expected to provide accuracies higher than a lot of other monitoring systems. The implementation costs may also be lower than that of other monitoring systems since it uses equipment that is already present in most high-precision grinding machines.

CHAPTER 3 – EQUIPMENT AND MACHINE DESIGN

3.1 Predator NTS Grinding Machine

The grinding machine that this research is based on is a Predator NTS grinding machine as shown in Figure 3-1. It was designed and built by the Timken Company. The machine is an internal cylindrical grinding machine for the machining of small high-precision parts at high output rates. Hydrostatic slides with integral servo motors are used for positioning. The 6 sigma repeatability of the feed axis is less than 0.51 μm. The machine uses a Bosch open architecture controller.

Figure 3-1: Predator NTS grinding machine

During the grinding process, the cylindrical parts are held and rotated by a roll-shoe centerless fixture. The schematic of the fixture is shown in Figure 3-2. The axis of the lower roll is fixed, while the upper roll is attached to an arm with a pivot bearing.

During the grinding cycle, the upper roll is pressed down to generate sufficient friction for the rotation of the workpiece. The grinding wheel is inserted into the part from one side and touches the workpiece at the 3 o'clock position. The feed direction points towards the stationary shoe. The rotational speed of the workpiece ranges between 750–800 RPM (12.5–13.3 rev/s). The speed of the grinding wheel varies between 65000 and 90000 RPM.

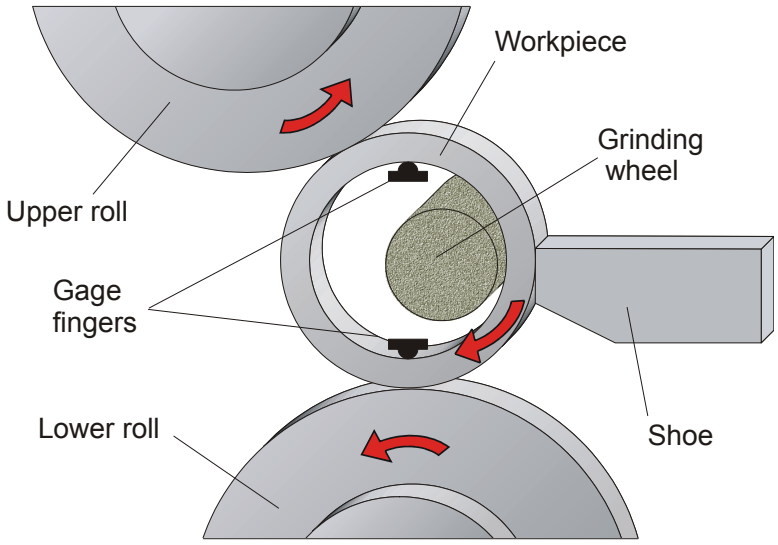

Figure 3-2: Setup of the roll-shoe centerless fixture with gage fingers

The average diameter of the workpiece during the grinding cycle is measured with a Marposs Mini Thruvar 5 in-process gage head. The gage head traces the bore of the workpiece with two fingers. The fingers are inserted into the part from the opposite side as the grinding wheel. The fingers touch the part at the 12 o'clock and 6 o'clock position to avoid interferences with the grinding wheel. The diameter information of the gage head is used to indicate the end of the finishing cycle when the target diameter is reached.

3.2 Components of the Post-Process Machine

3.2.1 Mechanical Components

The post-process machine is built using the same workpiece fixture and measurement gage head as its key components as the grinding machines, therefore partly resembling a grinding machine. The workpiece fixture of the post-process machine is an earlier design revision of the roll-shoe centerless fixture currently employed in the grinding machines. Its features and operational principle however are the same. A detailed overview of its components is given in Figure 3-3 and Figure 3-4.

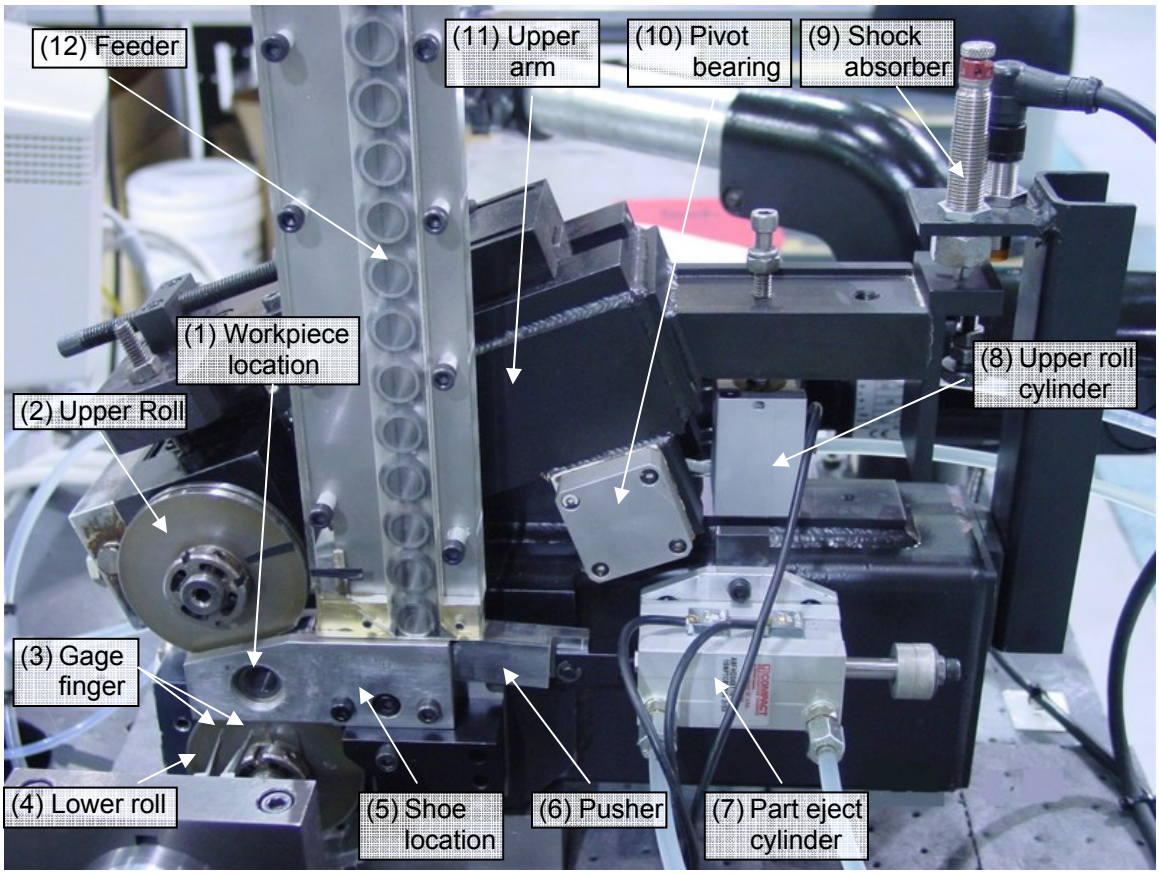

Figure 3-3: Workpiece fixture of the post-process machine

The workpiece (1) is held by the upper roll (2), the lower roll (4), and the stationary shoe (5). The two rolls are precision-ground to minimize their roundness error. The axis of the lower roll is fixed whereas the upper roll can pivot around a bearing (10) in the upper arm (11) of the fixture. During the measurement, a hydraulic cylinder (8) pushes the upper roll down to provide sufficient friction between the rolls and the part. The gage fingers (3) are inserted into the part and measure the profile. Once the measurement is completed, a second hydraulic cylinder pulls the gage (15) out of the part and the upper roll cylinder (8) retracts. A pusher (6) moved by a third hydraulic cylinder (7) ejects the part and pushes a new part into place. During ejection of the part, the upper roll falls down on the new part. A shock absorber (9) softens the impact to prevent part damage from the roll. Through the feeder (12), new parts are supplied.

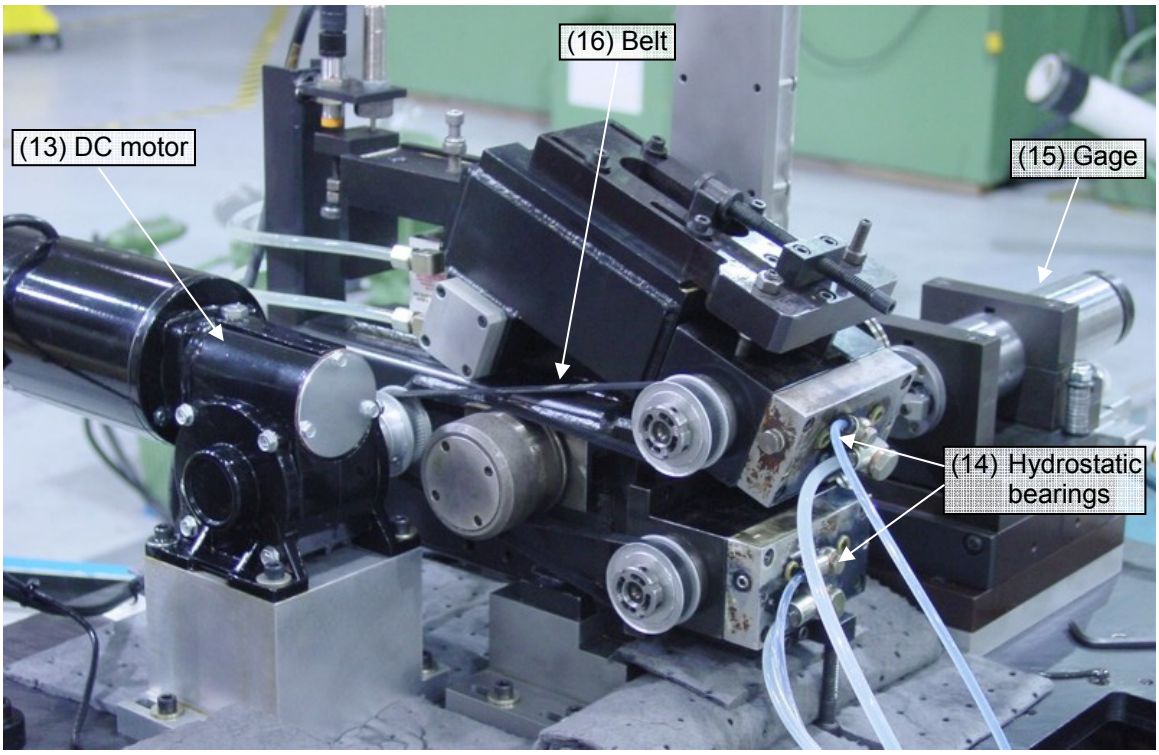

Figure 3-4: Driven side of the workpiece fixture

The spindles of the upper and lower roll run in hydrostatic bearings (14) to provide a precise low-vibration rotation while maintaining high stiffness. The spindles are driven by a Bodine permanent magnet DC motor (13). A pulse width modulation drive (PWM-drive) is used for the speed control of the motor. The PWM-drive achieves the speed control by changing the duty cycle of a 16 kHz square wave. Due to the inertia of the motor, the high modulation frequency leads to a smooth rotation of the motor shaft with low vibration. With the PWM-drive, the motor shaft can run at a maximum speed of 1900 RPM. A gearbox integrated into the motor reduces the maximum speed of the output shaft to 95 RPM. A worm gear was chosen to minimize the backlash in the system. The motor provides a power of 0.093 kW (0.125 HP) and is rated for a torque of 4.2 Nm. The torque is transmitted from the motor shaft to the roll spindles by a belt (16). To prevent slipping, the belt is toothed with a 2 mm pitch. The pulleys of the motor output shaft and the roll spindle both have 60 grooves.

The acquisition of the profile data is triggered by a rotary motion encoder that is mounted on the shaft of the motor spindle. The motor shaft is not the optimal location for the encoder since it does not allow accurate estimation of the workpiece rotation. It was chosen here for reasons of simplicity. Currently, the roll spindles do not provide any possibility to mount an encoder without modifications. Besides that, due to the gear ratio, a relatively inexpensive motor encoder with a low resolution can be chosen. The selected encoder generates 360 pulses per motor spindle revolution. With the given pulleys, this results in 7200 pulses per roll revolution and approximately 1930 pulses per part revolution.

3.2.2 Hydraulic Components

The hydraulic components of the machine are the three hydraulic cylinders and the two hydrostatic bearings of the roll spindles. The cylinders and the bearings are divided into two independent circuits. They are powered by a hydraulic unit made by Hydropa (Figure 3-5) which is equipped with two gear pumps. The gear pump for the hydrostatic bearings has 12 teeth, a maximum flow rate of 9.2 L/min and a maximum pressure of 210 bar. The pump for the cylinder circuit has 9 teeth, a maximum flow rate of 5 L/min and a maximum pressure of 180 bar. Both pumps are driven by a single motor with 2.5 kW at approximately 1715 RPM. To reduce the pressure and flow rate of the unit for the hydraulic components of the machine, pressure reducing valves and flow control valves are included in both circuits.

Figure 3-5: Hydraulic unit of the post-process machine

The hydrostatic bearings contain both radial and thrust bearings. The pressure in the radial part is set to 20 bar and in the thrust part to 7 bar. Through the flow control valve, the flow rate for both bearings combined is set to 3.8 L/min. The hydraulic cylinders are controlled by solenoid actuated directional control valves. The force of the cylinders is adjusted by the pressure reducing valves and the actuation speed by the flow control valves. Proximity switches are used to sense the position of the cylinders.

To reduce vibration due to the strokes of the gear pumps, two HYDAC accumulators are added to the circuits for pulsation dampening (Figure 3-6). The accumulators are diaphragm type accumulators with a welded housing. The accumulators have a gas volume of 0.32 L and are charged to 20 bar.

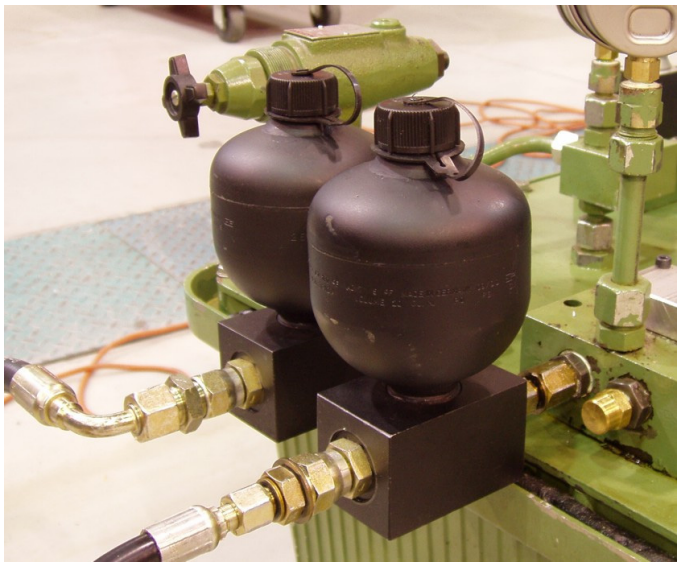

Figure 3-6: Hydraulic accumulators

3.2.3 Electrical Components

The main power connection of the machine is 480V/3 phase with ground. This voltage is needed for the hydraulic unit. Lower voltages for the other electrical components of the machine are provided by a transformer and two power supplies. Most of the components are mounted inside the main electrical cabinet. They are shown in Figure 3-7.

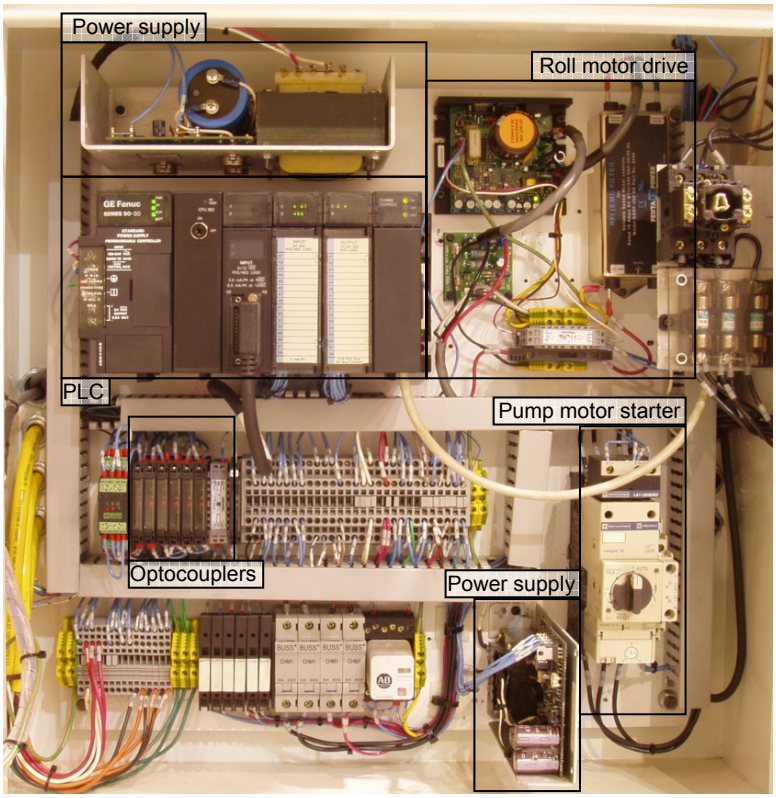

Figure 3-7: Electrical cabinet of the post-process machine

The control diagram is shown in Figure 3-8. In the center is a GE Fanuc 90-30 programmable logic controller (PLC). Through a 24 V output module, the PLC controls the components of the machine such as the solenoid valves for the hydraulic cylinders,

the pump motor and the roll motor. When needed, relays are used to match the voltage and current requirements of the controlled component. Through optocouplers, the output module also signals certain states to the PC. A 24 V input module allows the PLC to receive signals back from components such as the position of the cylinders from the proximity switches. A 5 V input module allows the PC to signal certain conditions back to the PLC, such as the outcome of a measurement.

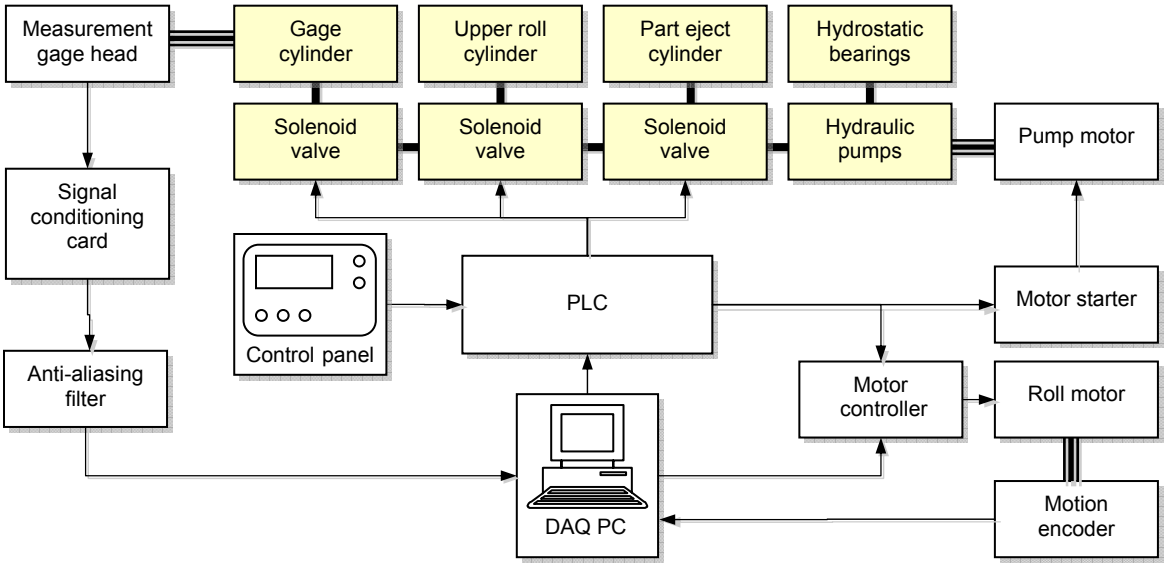

Figure 3-8: Control diagram of the machine

An additional module of the PLC is used to communicate with the user control panel of the machine (Figure 3-9). Through the control panel, the machine can be operated in manual or automatic mode. In manual mode, the cylinders, the pumps, and the roll motor can be actuated or switched on and off manually through the panel. The PLC assures that the machine cannot be damaged by for example trying to eject a part while the fingers are still inserted for measurement. In automatic mode, the PLC automatically actuates the

cylinders to load and eject parts. Once a part is in place, the PLC sends a signal to the data acquisition card of the PC and the PC launches the part measurement and performs the necessary analysis of the data. Once the measurement is completed, the data acquisition card signals the completion of the measurements with one signal and the outcome of the measurement (part passed or part failed) with a second signal.

Figure 3-9: User control panel

3.2.4 Vibration Isolation System and Base Plate

To minimize relative motion between the gage head and the workpiece fixture, the components shown in Figure 3-3 and Figure 3-4 are mounted on a 100 mm thick honeycomb base plate made by Newport. The plate is an engineered steel structure with a honeycomb like core (Figure 3-10). Due to the structure of the core, the static stiffness of the plate is almost the same as solid steel, while its weight is only a fraction of that of solid steel. The combination of high stiffness and low weight results in a dynamic stiffness that is superior to both solid steel and granite. Aluminum pads inside the structure provide increased damping at the natural frequencies and improved frequency response characteristics.

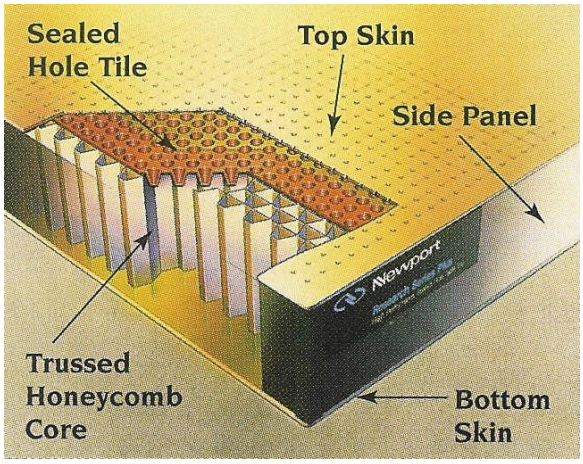

Figure 3-10: Honeycomb base plate [Newport 2004]

The honeycomb base plate with its components is supported by four isolators. For this purpose, outriggers are attached to the base plate to achieve a cradle like design (Figure 3-11). The benefit of this configuration is that the center of gravity of the plate with

components is lower with respect to the supporting surface of the isolator. A lower center of gravity stabilizes the system and prevents rocking modes.

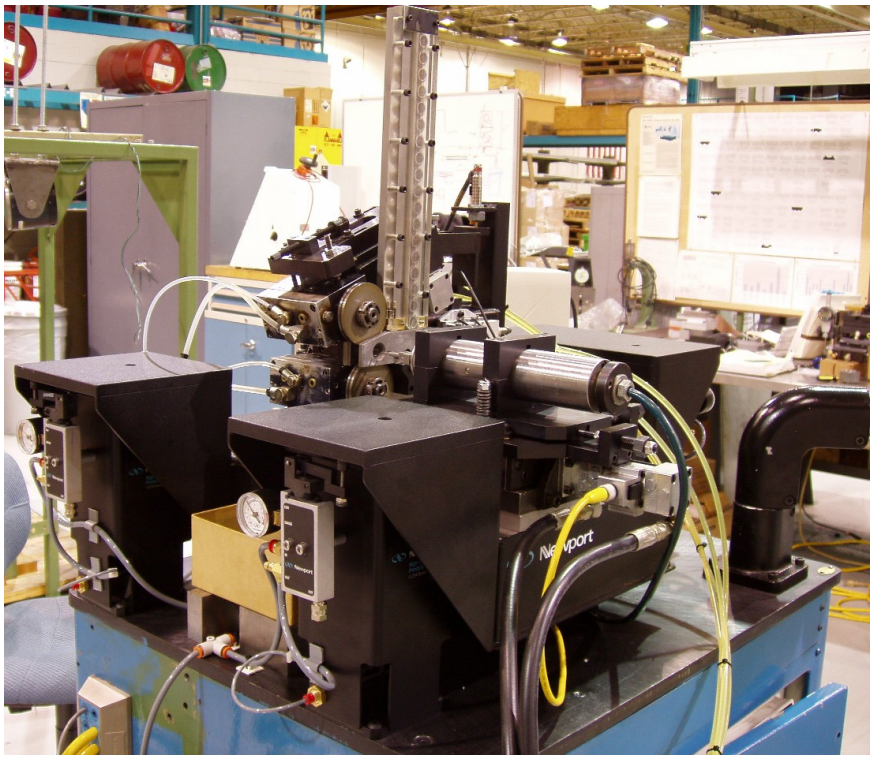

Figure 3-11: Vibration isolation system

The isolators are pneumatic isolators which can support a total weight of 225 kg. Leveling valves are attached to the cylinders to allow repositioning after a disturbance. The natural frequency of the isolators is specified with 1.8 Hz and 1.3 Hz in the vertical and horizontal direction, respectively. Laminar flow damping in the isolators reduces the amplitude at the resonance frequency and improved the settling time.

3.3 Measurement System

3.3.1 Overview

The measurement system converts a geometric quantity into a sequence of digitized values that can be processed by a computer for further analysis. The components involved in this task are displayed in Figure 3-12.

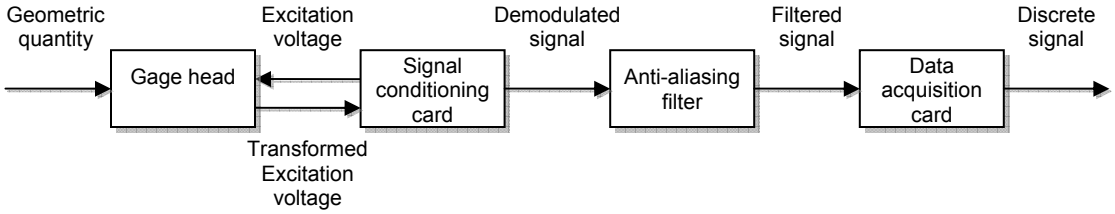

Figure 3-12: Components of the measurement system

The specifications of the components and their principle of operation is important to tune the measurement system optimally for the given measurement task. Each of the components is therefore discussed in the following sections.

3.3.2 Fundamentals of LVDTs

To fulfill the measurement task, the gage head is equipped with two fingers that trace the part profile while the part is being rotated. The movement of the gage fingers is converted into an electrical signal by means of an LVDT (linear variable differential transformer). An LVDT is essentially a variable voltage transformer consisting of a primary coil and two secondary coils. The displacement of the LVDT probe is converted

into a proportional voltage at the secondary coils by means of variable inductance. The typical design of an LVDT is shown in Figure 3-13.

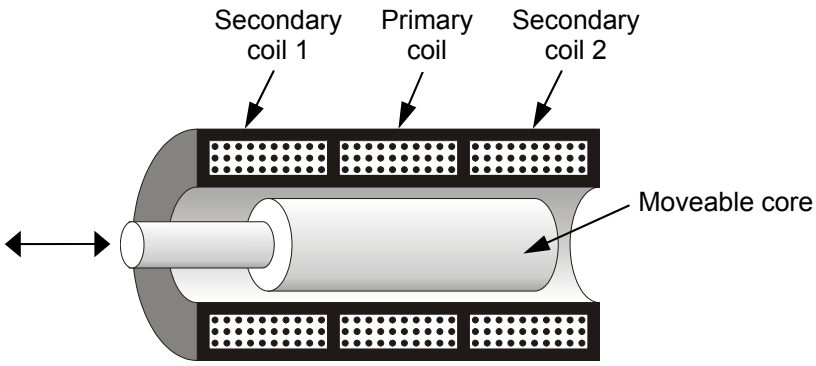

Figure 3-13: Cut-away of a linear variable differential transformer

The primary coil is wound over the middle of a hollow nonmagnetic tube. Two identical secondary coils are symmetrically and coaxially aligned to the primary coil. A rod-shaped magnetic core can move freely in the hollow tube. When the primary coil is excited by an AC voltage, the core provides a path for the magnetic flux so that an AC voltage is induced in the secondary coils. The amplitude of the induced voltages depends on the position of the core. The two secondary coils are connected in series but with opposite orientation, so that the induced voltages have opposite polarity. The output of the LVDT is therefore the difference of the secondary coil voltages. If the core is in the center position, the voltages add to zero, which marks the null position. If the core is moved towards one secondary coil, the amplitude of the voltage in that coil increases while the amplitude in the other coil decreases. Moving the core through the null-position is marked by a sudden phase shift of 180º in the output signal. If the core movement is within its nominal range around the null position, the voltage-displacement relationship is

fairly linear. Outside the nominal range, the linearity deteriorates (Figure 3-14). Severe non-linearity occurs if the core is not kept within the secondary coils.

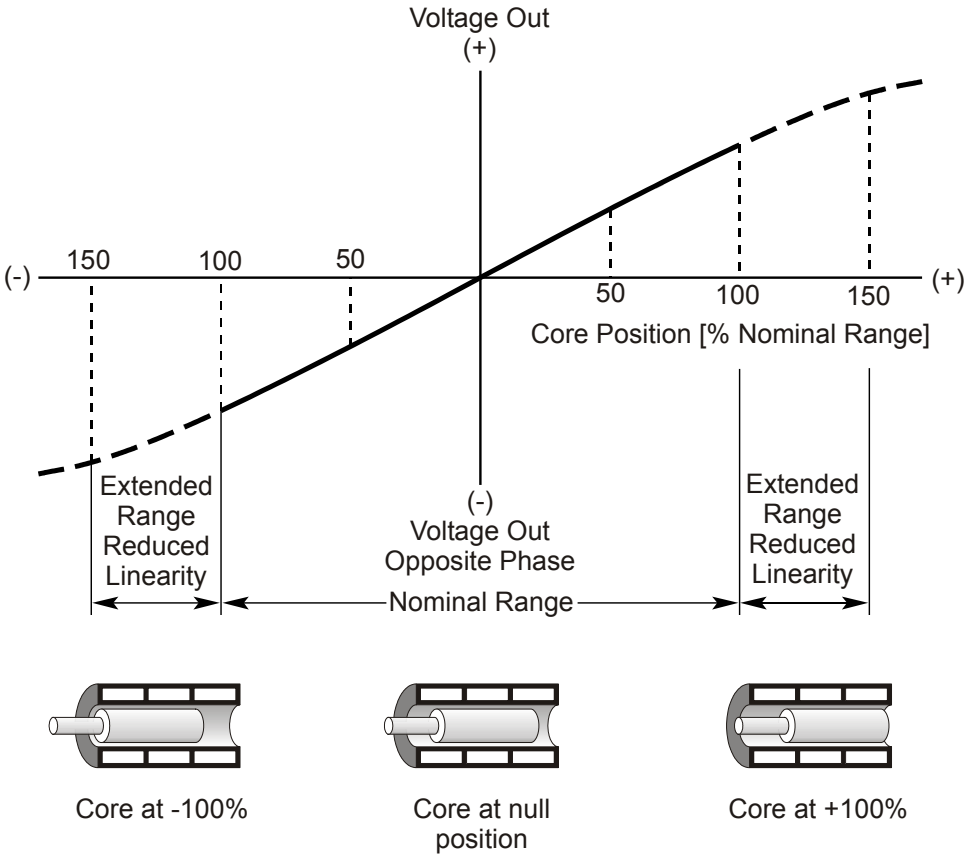

Figure 3-14: Nominal range of an LVDT

LVDTs have several properties that are advantageous for use in the post-process machine [Herceg 1972]:

- Since no physical contact is required between the core and the coils, the measurement is basically frictionless. In the gage head, friction only occurs to convert the finger motion into a core motion.

- The main components for the measurement are the coils and the core. Due to the absence of friction, their lifetime essentially infinite.
- Because the displacement-voltage conversion is based on the principle of inductance, the resolution of an LVDT is theoretically infinite.
- Due to its principle of operation, an LVDT exhibits a very stable and repeatable null position.
- LVDTs are characterized by a high ruggedness and durability. Exposure to occasional shocks or vibration does not affect their accuracy permanently. They are therefore ideal for employment in rough manufacturing environments.

The most important factors that limit the accuracy of LVDT are temperature fluctuations and distortions in the excitation waveform. A temperature rise causes an increase of the copper coil resistance. As a result, the primary coil current and the induced secondary currents are reduced. Similarly, variations in the excitation waveform affect the output signal of the secondary coils. Several design variation of LVDTs exist that attempt to compensate these effects [Herceg 1972], [Ara 1972], [Saxena and Seksena 1989].

3.3.3 Marposs Thruvar 5 Gage Head Family

As a sensor, gage heads from the Marposs Thruvar 5 family are used. The family consists of three gage heads, the standard Thruvar 5, the mini Thruvar 5, and the micro Thruvar 5. All gage heads possess two fingers and two LVDTs. The main difference between the models is their size to allow their application even in space constrained

setups. The smaller size of the mini Thruvar and micro Thruvar compared to the standard design has to be compromised with slightly reduced accuracies. In addition, only the standard Thruvar 5 and the mini Thruvar 5 feature a DC motor to adjust the radial position of the gage fingers to accommodate them to different internal diameters of the workpiece. With the micro Thruvar, the finger position has to be adjusted by setscrews.

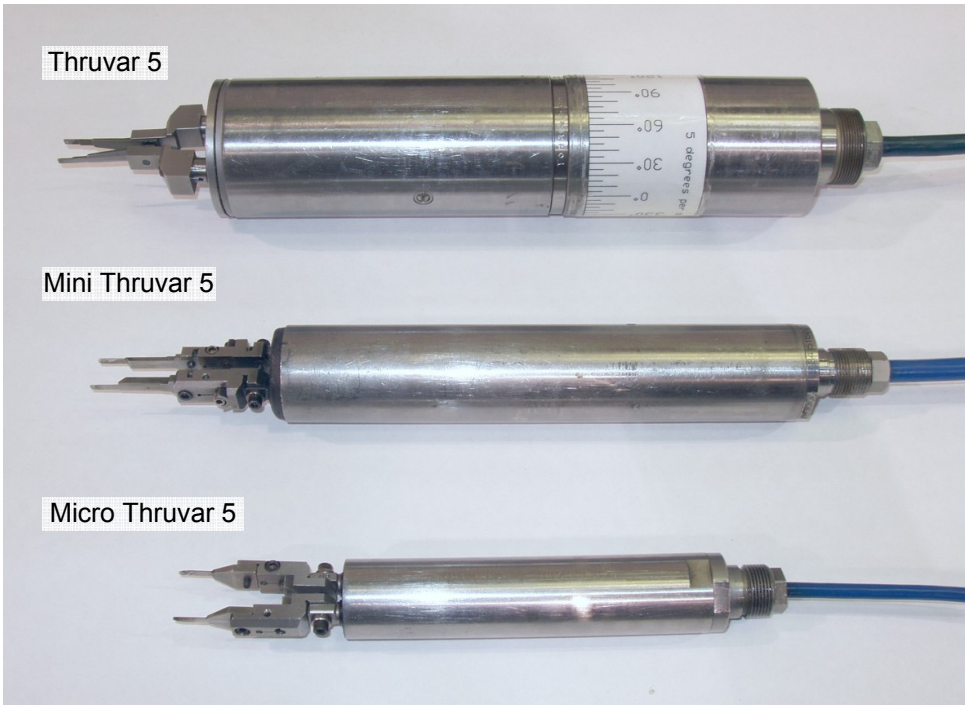

Figure 3-15: Marposs Thruvar 5 Gage Head Family

In the Predator grinding machine, the mini Thruvar 5 is used, since the gage head has to be fed from the left side of the fixture through the housings of the upper and lower spindles. In the post-process machine, the gage head is inserted into the workpiece from the right side where no space restrictions exist. Therefore, the standard Thruvar 5 gage head is used for the post-process machine.

The pin connections of the gage connector and the corresponding circuits are displayed in Figure 3-16. The connector is equipped with two variable resistors to adjust the gains of the two secondary outputs before the induced voltage enters the signal conditioning unit. The DC motor moves both finger A and finger B simultaneously in the same direction. A pin on the gage connector signals, when the fingers are completely closed. The gage head is mounted on a bracket that allows the head to be swiveled in the horizontal *xz*-plane and pivoted in the *yz*-vertical plane (Figure 3-17). In combination with the finger adjustment provided by the motor, this allows an arbitrary placement of the fingers in the *xy*-plane relative to the workpiece.

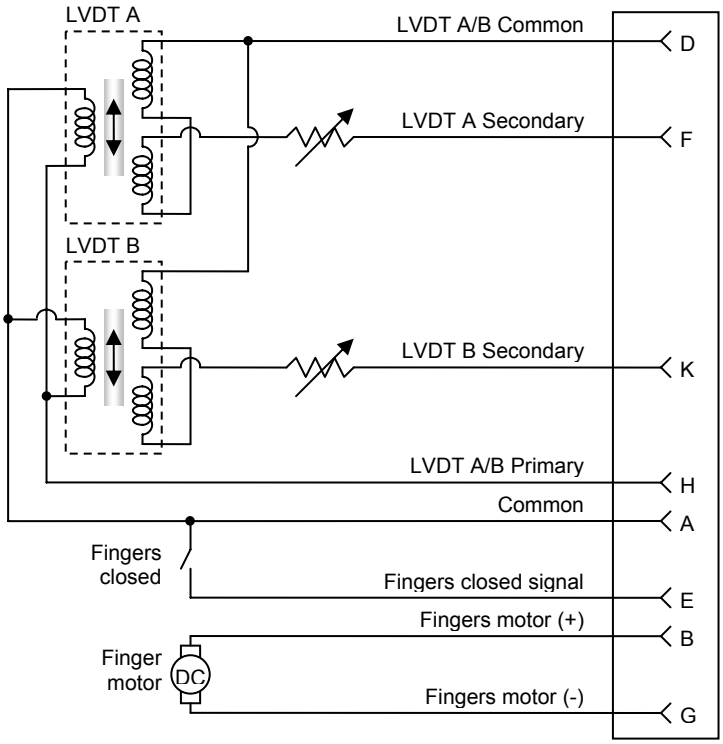

Figure 3-16: Schematics of the Marposs Thruvar 5 Gage Head

The fingers of the gage head are tipped with a diamond. The approximate probe tip radius is 0.46 mm (Figure 3-18). The gage head is filled with oil to provide damping of the fingers.

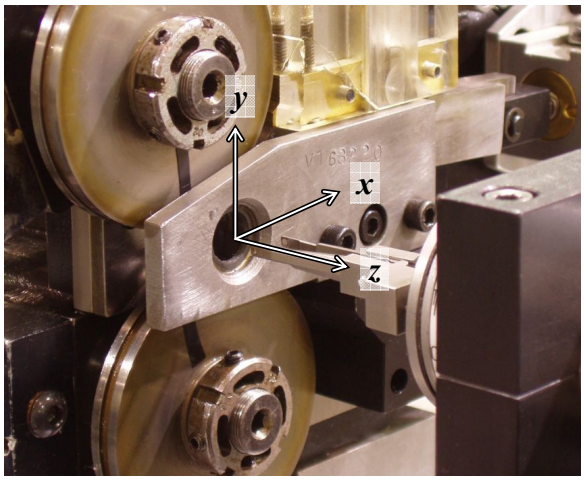

Figure 3-17: Coordinate system

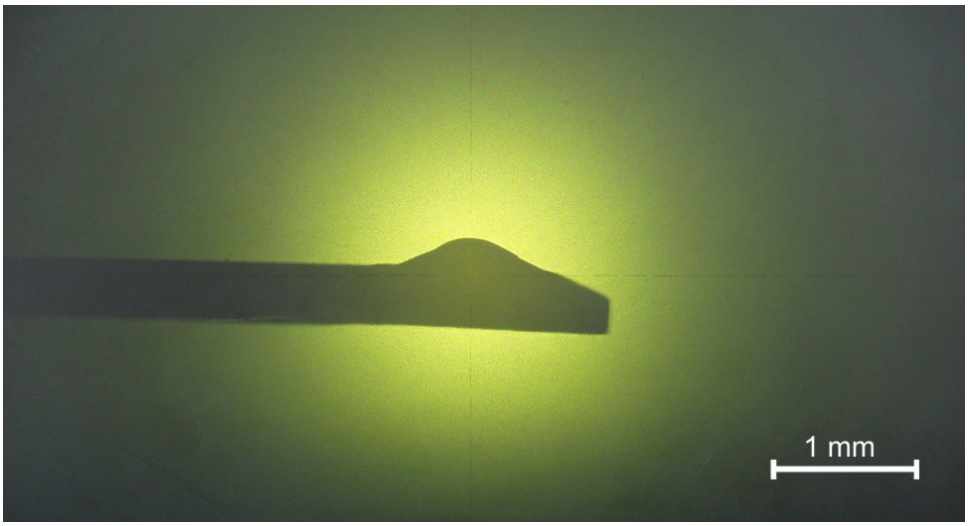

Figure 3-18: Finger tip geometry

3.3.4 LVDT Signal Conditioning

Most LVDTs, such as the Marposs Thruvar 5, require a separate signal conditioning unit. LVDT signal conditioning comprises two tasks: supplying the excitation voltage of the primary coil and demodulating the excitation frequency from the secondary coil outputs to obtain a DC signal proportional to the displacement. The circuitry to accomplish theses tasks is available as space saving ICs [Gray 1987], [Sylvan 1990]. Traditionally, the demodulation is carried out with the analog signal. In recent publications however, the secondary signal is first converted into a digital signal and then demodulated with the aid of a digital signal processor (DSP). [Yassa, Garverick 1990], [Crescini et al. 1998], [Weissbach et al. 2000], [Ford et al. 2000], [Ford et al. 2001].

3.3.5 Signal Conditioning Card

To energize the LVDTs and to convert the LVDT output to a DC voltage, a Solartron CAH-8D signal conditioning card is used. The card has two channels for the two LVDTs of the Marposs gage head. The schematics of the card are depicted in Figure 3-19.

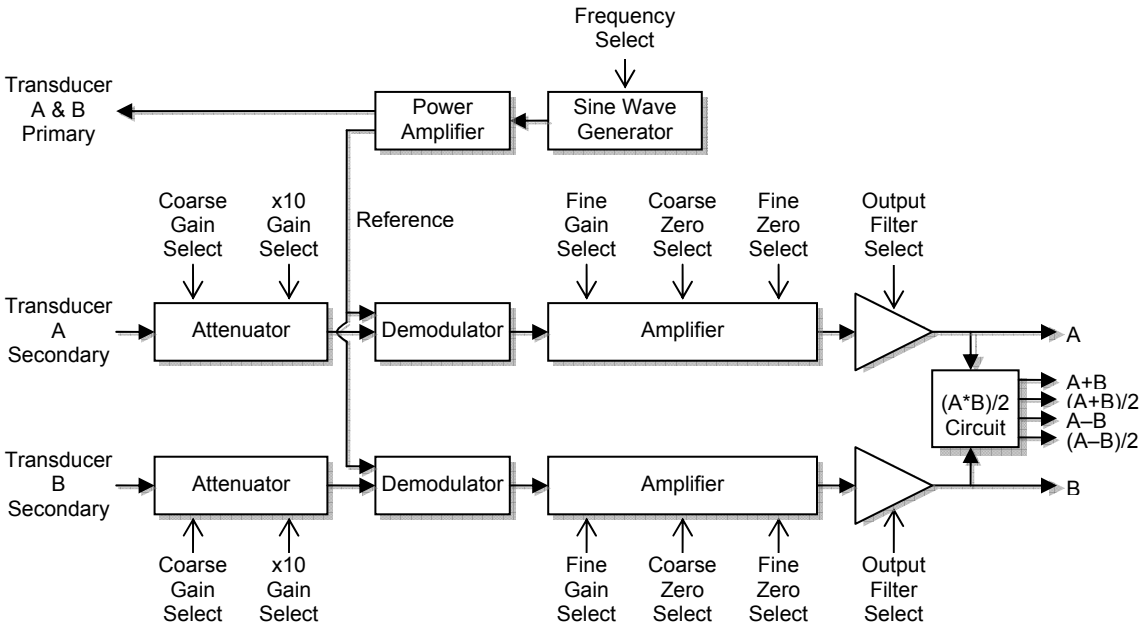

Figure 3-19: Schematics of the Solartron signal conditioning card

The sine wave generator provides a 5 V excitation voltage for the primary coils with selectable excitation frequencies of 5 kHz or 10 kHz. As a general rule, the excitation frequency should be at least 10 times higher than the highest frequency to be measured with the LVDT. For the given application, a 10 kHz excitation voltage is chosen allowing theoretically to measure waveforms up to 1 kHz. The sensitivity of the two channels is adjustable to allow for different measurement ranges of the transducer.

One of nine sensitivity ranges can be chosen with the coarse gain (Table 3-1). A potentiometer provides fine adjustment of the sensitivity within the selected range. The gains in Table 3-1 are expressed as the equivalent sensitivity of the transducer for which an output between –5 V and +5 V is obtained. In addition to the gain adjustment, coarse and fine zero adjustment of the channels is provided as well. For the initial setup of the gage head, the gains are selected according to company specifications for the internal grinding system. The resulting measurement range is 635 μm which corresponds to a voltage output from –10 V to + 10 V. In section 4.4, the gage setup is optimized and the gains are adjusted to achieve optimal performance of the measurement system.

Table 3-1: Signal conditioning card coarse gains

Range	Equivalent transducer sensitivity [mV/V]	Gain
1	250-750	Low
2	100-300	↑
3	50-150	
4	25-75	
5	10-30	
6	5-15	
7	2.5-7.5	↓
8	1-3	
9	0.5-1.5	High

The output of the channels is passed through a low-pass filter with cutoff frequencies of either 500 Hz or 1 kHz to reduce ripple in the signal. For the given application, the 1 kHz cutoff frequency is chosen to retain higher frequency components in the signal. The filter is a third order filter. The filter type is not further specified in the card manual.

3.3.6 Anti-Aliasing Filter

The purpose of the anti-aliasing filter is to prevent aliasing of frequencies above the Nyquist frequency to frequencies below the Nyquist frequency during the sampling of the analog signals. For this purpose, a 4 channel Krohnhite 3384 filter is employed. The filter can perform low-pass filtering with selectable frequencies using 8-pole filters. As a filter type, Butterworth or Bessel is available for each channel. The advantage of a Butterworth filter is that the magnitude of the frequency response is maximally flat in the passband therefore providing the best amplitude preservation below the cutoff frequency. Bessel filters are characterized by an almost constant group delay in the passband frequency range therefore introducing less phase distortion to the signal below the cutoff frequency. For the work discussed here, amplitude preservation is more critical than phase preservation so that Butterworth filters are employed for low-pass filtering. Depending on the sampling rate during the measurements, different cutoff frequencies between 400 Hz and 1 kHz are chosen.

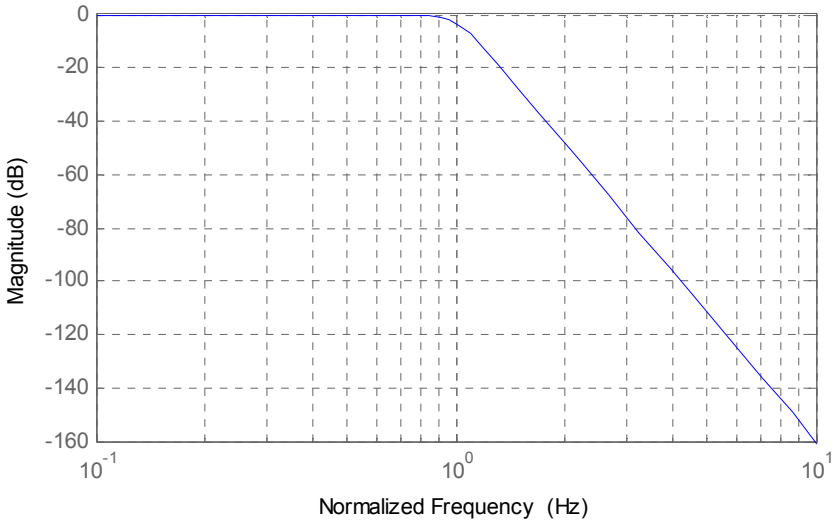

Figure 3-20: Frequency response of an 8-pole low-pass Butterworth filter

3.3.7 Data Acquisition System

The analog output of the low-pass filters is converted into a digitized discrete-time signal by a National Instruments NI PCI-6031 E data acquisition card. The card features a total of 64 analog inputs. The inputs are configured for a bipolar range from –10 to +10 V, matching the output range of the signal conditioning card. The card uses 16 bit analog-to-digital converters so that the resolution expressed in volts ΔV_{Res} is given by

$$\Delta V_{Res} = \frac{\Delta V_{Range}}{2^{N_B}} = \frac{20\,\mathrm{V}}{2^{16}} = 0.305\,\mathrm{mV}\,, \tag{3.1}$$

where ΔV_{Range} is the full voltage range and N_B is the number of bits. Due to the finite resolution, a quantization error of the same value is induced in the measurement.

Acquisition of a voltage sample can either be triggered by the encoder of the roll motor, corresponding to a constant angular movement of the workpiece, or by the internal clock of the data acquisition card, corresponding to a sampling rate that is constant in time. The maximum sampling rate for single channel acquisition is specified with 100 kSamples/s. In addition to the analog inputs, the data acquisition card features two analog outputs and eight digital channels that can be configured as either input or output. One analog output is connected to the roll motor controller for speed control. The digital inputs and outputs are used for communication with the PLC.

The data acquisition card is installed in a standard desktop PC and communicates with the PC hardware through a PCI bus. The PC is equipped with an Intel Pentium 3 processor with 600 MHz.

3.4 Software

The software for the machine is developed to perform measurements, carry out analysis of the data, and aid in the setup of the machine. Microsoft Visual Basic 6 is used as a programming language. To interface with the data acquisition hardware, the National Instruments Component Works add-on for Visual Basic 6 is used.

The main window (Figure 3-21) of the software provides access to several other windows that fulfill certain tasks.

Figure 3-21: Main window of the machine software

The signal setup window allows configuring the signals that are acquired by the data acquisition card. By default, the signals for the two fingers are entered. For diagnostic purposes, additional sensors can be connected to the data acquisition card and their signals can be recorded by the software. The type of the signal corresponds to the physical quantity of the sensor and can be voltage, displacement, force, acceleration, or frequency. For each signal, calibration information, a preferred unit, and the DAQ channel have to be entered.

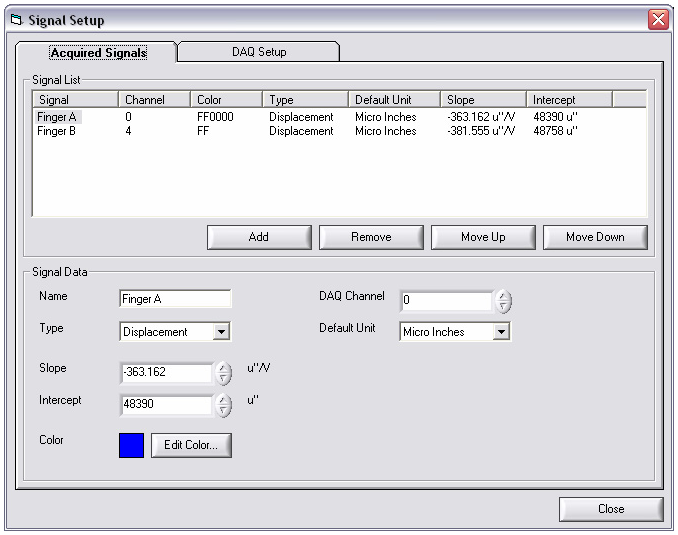

Figure 3-22: Signal setup window

With the gage finger positioning window, the position of the gage fingers can be adjusted using the built-in motor of the Marposs Thruvar 5 or mini Thruvar 5 gage head.

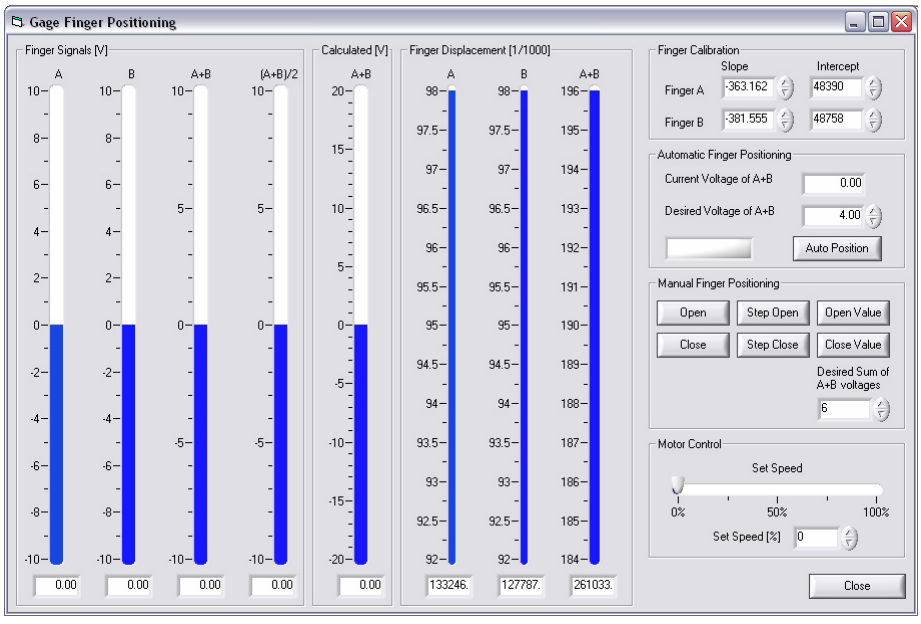

Figure 3-23: Gage finger positioning window

The fingers move inward or outward as long as the "Open" or "Close" buttons are pressed. For finer adjustment, they can also be moved in small increments. In addition, the desired sum of the voltages from the two fingers can be entered and the fingers are automatically positioned to achieve this value.

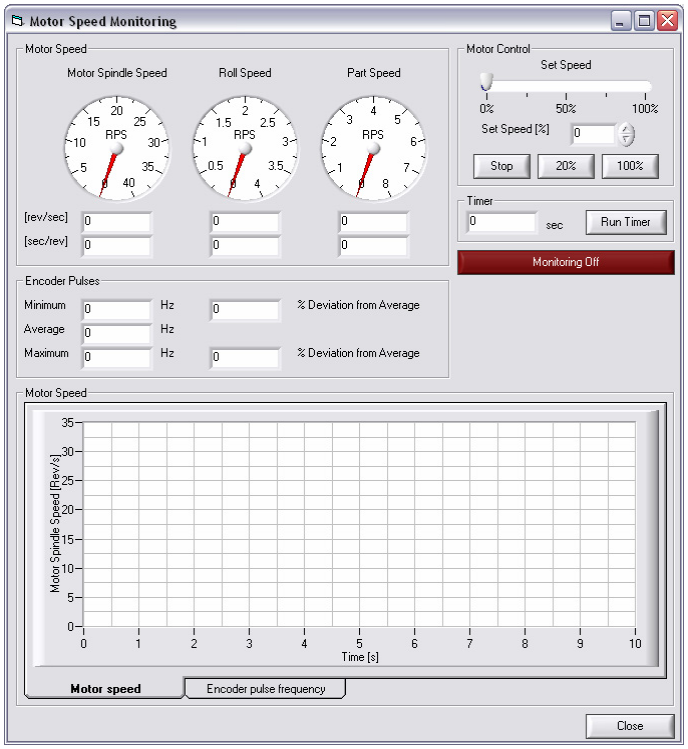

Figure 3-24: Motor speed monitoring window

The motor speed window allows monitoring the rotational speed of the main motor spindle and the resulting roll and part speed. The speed of the motor can be adjusted by a slider and is specified as the percentage of the maximum speed that is send to the motor controller. Using the plots of the speed versus time, fluctuations in the motor speed can be observed.

The roundness measurement window is the main window for acquiring measurements of the selected signals. Several parameters for the measurements can be chosen such as the number of data points or the number of workpiece revolutions to acquire, the roll motor speed, or the method of triggering the data acquisition. When the data acquisition is triggered by the motor encoder, the software also records the exact time of the trigger events which allows determining the momentary motor speed between two trigger events.

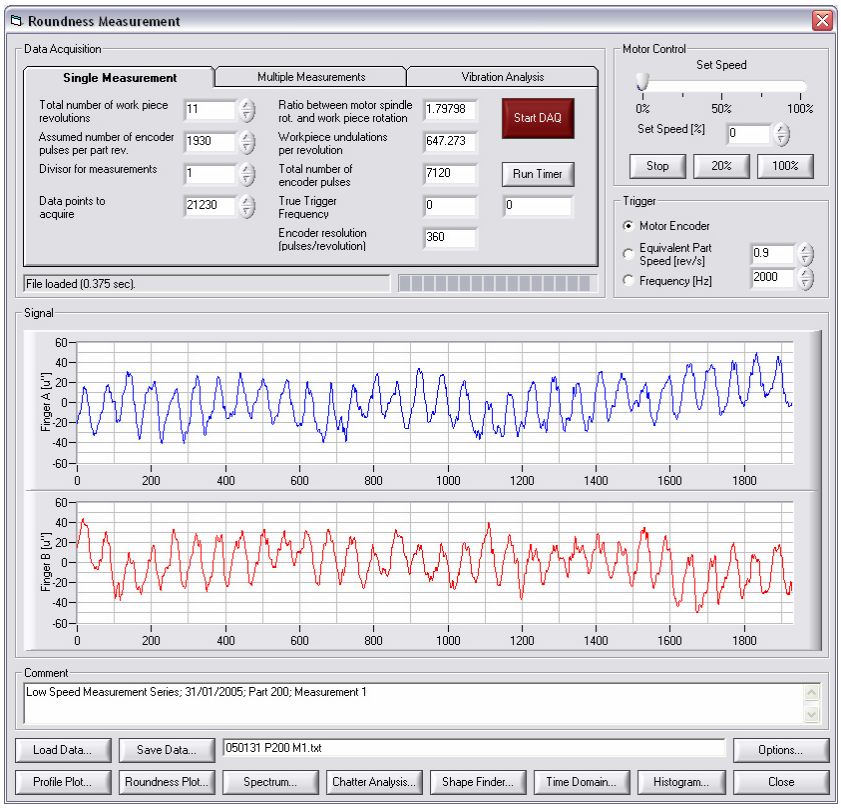

Figure 3-25: Roundness measurement window

The software can acquire either measurements of a single part or a measurement series of several parts where the parts are automatically loaded and ejected after

completion of the measurements. All measured data can be saved in a file and loaded into the software again for latter analysis. Comments describing the measurement can be entered and are saved with the data. The data files are space delimited text files which can easily be imported into Microsoft EXCEL or MATLAB.

To display the measured signals, two time-domain plots are available. The window includes additional buttons for further analysis such as time and frequency-domain analysis, calculation of the profile height, and search for distinct shapes in the signals.

Additional modules included in the software, such as the gage finger calibration and the dynamic calibration, are explained in the later sections.

3.5 Part Specifications

3.5.1 Part Geometry

The parts that are inspected here are the outer rings of bearings. The dimensions of the rings relevant for this work are shown in Figure 3-26.

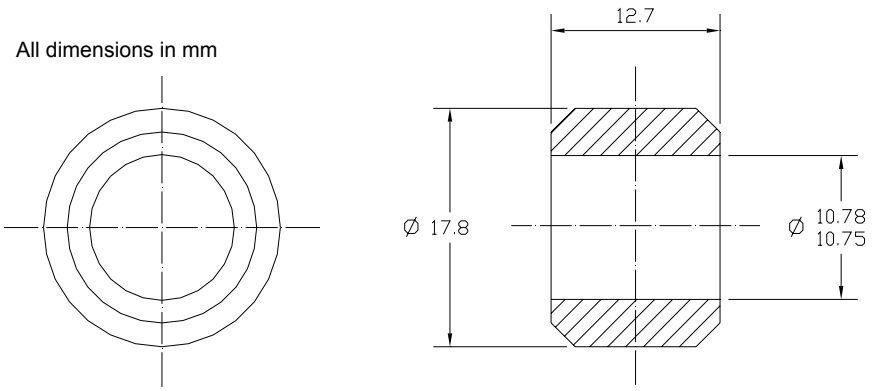

Figure 3-26: Geometry of the parts

3.5.2 Profile Waviness Specifications

The requirements for the part bore with respect to waviness are defined in a separate specification. To decide whether a part meets the specifications, the raw profile of the bore is measured (Figure 3-27) and a rectangular digital band-pass filter with a passband from 10–250 UPR is applied (Figure 3-28). Subsequently, the radial difference of the highest peak and the lowest valley in the profile is calculated. This difference is referred to as the *profile height* and is denoted to by h_P and h_R depending on whether it is measured with the post-process machine or a roundness machine. For a part to pass the

test criterion, the profile height has to be less or equal than the critical profile height h_{crit}, which is 1.270 µm (50 µinch).

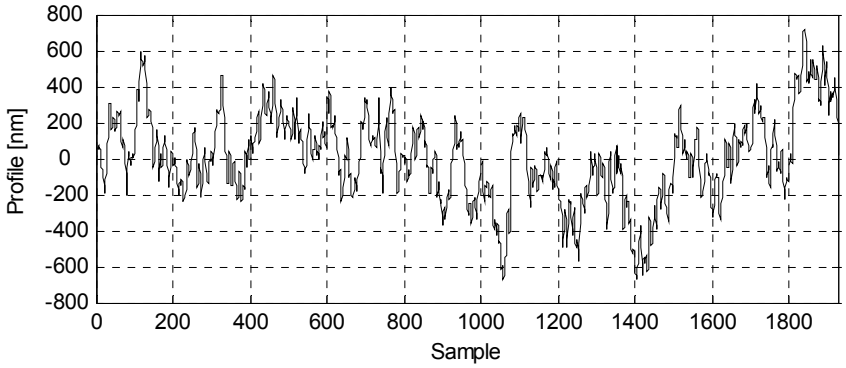

Figure 3-27: Unfiltered part profile

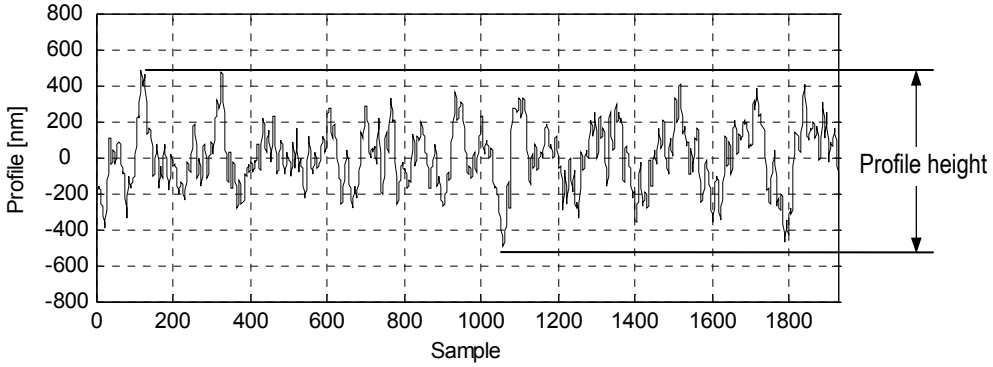

Figure 3-28: Filtered part profile

The work discussed here will focus exclusively on the measurement of profile waviness. Measurement of the average absolute part diameter is the traditional application of in-process gages like the Marposs Thruvar 5. Since it has been employed successfully in industry for many years, it will not be considered here further. For waviness measurement, only the relative radial distance of the sampled data points from the workpiece center is important and not the absolute distance. For the waviness analysis of the data, it is therefore convenient to remove the mean of the profile.

CHAPTER 4 – SETUP AND ANALYSIS OF THE MACHINE

4.1 Identification of Potential Noise Sources

One of the main requirements of the post-process machine is to achieve the highest possible measurement accuracy while taking time constraints and financial constraints into account. Therefore, careful consideration has to be given to potential noise sources that may limit the achievable accuracy. In the subsequent sections, the main disturbances in the system and their expected effect on the measurement are discussed. The methods for eliminating or reducing the noise discussed here are limited to technical methods. In Chapter 6, analytical methods are developed to improve the accuracy further than what is achievable by technical methods alone. Some of the hardware listed in Chapter 3 was selected with potential noise sources in mind.

Due to the similarity between the post-process machine and the grinding machine, it is expected that the discussed noise sources occur with both machines. The machines differ with respect to possible remedies to the disturbances. Technical modifications of the grinding machine for noise reduction are very limited. This necessitates the analytical methods in Chapter 6 in addition to technical methods for noise reduction.

4.1.1 Electrical Noise

Since part of the post-process machine is an electrical system, the machine is subject to electrical noise. Electrical noise is unavoidable and cannot be eliminated. Through proper shielding and grounding techniques however, it can be minimized to a

level where it is tolerable for the given application. Section 4.2 and 0 discuss the sources of electrical noise and the employed methods for its reduction.

4.1.2 Forced Vibrations

Forced vibrations cause a movement of the gage head relative to the workpiece fixture and therefore also relative to the measured workpiece (Figure 4-1). The relative motion is superimposed on the measured profile. Forced vibrations can originate from a variety of sources. The most obvious one are moving machine components. Examples are the roll motor and the components driven by it, transient vibrations caused by the actuation of hydraulic cylinders, or the grinding wheel in the grinding machine. Additional sources are the pulsation of the hydraulic fluid due to the strokes of the gear pumps. Mechanical vibrations at multiples of the power frequency caused by the buzzing of the transformer and other electrical components were also found. Finally, vibrations can also enter the system from the environment.

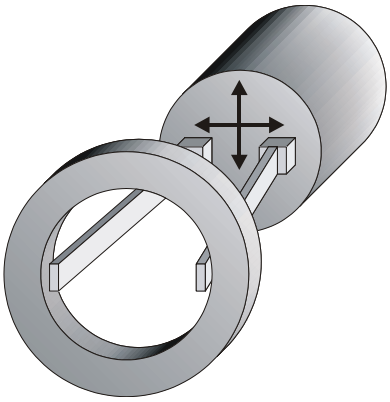

Figure 4-1: Effect of forced vibration

By installing a vibration isolation system and by mounting as many machine components as possible on the non-vibration isolated part of the machine, vibration from the environment or the buzzing of electrical components is minimized. The roll motor remains as a vibration source in the isolated part of the machine. Using the PWM drive for speed control reduces the introduced vibration to a minimum. Vibration of the hydraulic fluid remains as well since the tubing of the hydraulic components bypasses the vibration isolation system. The hydraulic accumulators help reducing the pulsation of the fluid. Long and flexible tubes prevent vibration from the tubes themselves.

4.1.3 Centerless Fixture

One advantage of the roll-shoe centerless fixture is that parts are loaded quickly for measurement. Time consuming centering of the part, as it is required for the three-jaw chuck of conventional roundness measurement machines, is not necessary.

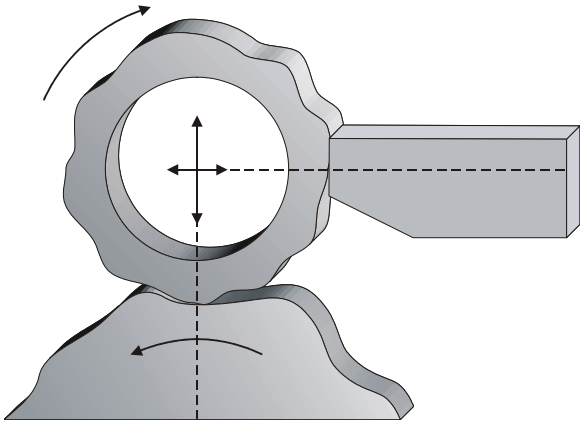

Figure 4-2: Effect of the centerless fixture

The disadvantage of the centerless design is that the workpiece center is floating. Its location is defined by the contact points of the workpiece outer diameter with the stationary shoe and the lower roll (Figure 4-2). Variations in the part outer diameter cause a movement of the part center in the horizontal direction since the stationary shoe traces the diameter. In the vertical direction, the part center movement is caused by the combination of the variations in the part outer diameter and the roundness error of the lower roll. It is therefore assumed that the movement in the vertical direction is higher than in the horizontal direction. For this reason, the gage fingers are placed horizontally at the 3 o'clock and 9 o'clock position opposite to the configuration in the grinding machine where the fingers measure at the 12 o'clock and 6 o'clock position.

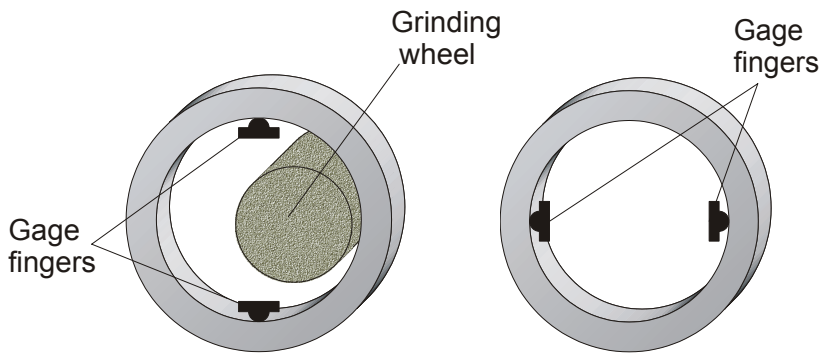

Figure 4-3: Finger configuration in the grinding machine and post-process machine

4.1.4 Gage Head

As a key component of the measurement system, the gage head introduces errors to the measurement. An obvious source of inaccuracies are errors in the calibration of the gage head. Depending on the method of calibration, errors can also be introduced by misaligning the gage head with respect to the part, i.e. the measurement direction of the

fingers is not normal to the part surface. Calibrating the machine using master parts usually avoids this problem. The calibration of the gage head is discussed in section 4.4. In addition, the gage head may exhibit small nonlinearities in the conversion of the finger movement into an electrical signal.

Tracing the workpiece surface with the gage fingers introduces an error since the movement of the gage fingers does not exactly follow the profile of the workpiece. The deviation is caused by the finite radius of the finger tip which acts as a mechanical filter [Radhakrishnan 1970], [McCool 1984], [Mendeleyev 1997], [Wu 1999], [Pawlus 2004]. Small details in the profile will not be represented properly in the finger movement. Steep slopes may cause the finger to temporarily loose contact with the workpiece [Damir 1973], [Kaliszer et al. 1986], [Song, Vorburger 1996]. This misrepresentation is tolerable since the goal is to measure profile waviness and not surface roughness. Steep slopes are also not expected in the workpiece profile.

Another source of error stems from the fact that the fingers trace the part on axially slightly different planes of the part. Since the exact part surface depends on the axial measurement position, the fingers measure slightly different part profiles. Small profile details may not be captured with both fingers.

Since waviness for a range of frequencies is measured, the frequency response of the gage head has to be considered. The highest undulation to be measured has to be below the cutoff frequency of the gage head to prevent amplitude attenuation. Depending on the damping, the amplitudes of frequencies close to the natural frequency may be amplified. To minimize distortion of the amplitudes, the parts therefore have to be rotated sufficiently slowly. Longanbach and Kurfess [2001] measured the frequency response of

several industrial in-process gages including Marposs Thruvar gage heads. The frequency response measurements were replicated here with the gage heads used in this dissertation and the results were found to be very similar to the ones published in Longanbach and Kurfess [2001]. In Chapter 6, a method is presented to account for the dynamic behavior of the gage head.

Since the stiffness of the gage fingers is finite, they may deflect during the measurement. A distinction has to be made between static stiffness and dynamic stiffness. The deflection due to finite static stiffness should be accounted for during the calibration of the fingers since it is expected that the deformation is the same during the calibration and the part measurement. The calibration however does not account for the dynamic stiffness. It is assumed though that because of the relatively low weight of the gage fingers, their natural frequency is located above the cutoff frequency of the gage head.

4.1.5 Signal Sampling

Errors are also associated with the sampling of the analog signal. Conversion of the continuous output voltage of the gage head into discrete states introduces a quantization error. The maximum quantization error depends on the number of bits of the analog-to-digital converters of the card. With 16 bits, it is expected that the resulting quantization error is sufficiently small. Its exact value will be determined in section 4.4.3.

The sampling of the data points is subject to an error due to the location of the rotary encoder that triggers the sampling. Since it is mounted on the rotor spindle of the roll motor, the pulses do not resemble accurate angular increments of the workpiece rotation. The deviations result in small phase errors in the measurement. They are caused

by inaccuracies in the worm gear of the motor, elasticity of the belt, and roundness errors in the outer diameter of the part and the rolls. The errors in the angular increments are relatively small. Larger errors can occur, when the part is rotated between the rolls for a high number of revolutions. Since the upper and lower roll have slightly different perimeters, tension builds up in the belt, because the different perimeters force the rolls to rotate at different angular velocities. After several revolutions, one or both rolls slip with respect to the part and the built-up tension releases. This effect does not occur when parts are measured for only a few revolutions. In this case, tension in the belt is released whenever a part is ejected. After how many revolutions parts start to slip, is difficult to determine since it depends on the friction between the part and the rolls which can for example be affected by thin fluid films on the part or the roll. Since parts in the post-process are at most rotated for a few revolutions, part slipping is not considered to be critical here.

4.1.6 Other Sources

Besides the sources mentioned above, the workpiece itself may distort the measurement to a small extent. The measurement of the profile requires the workpiece to act like a perfectly rigid body which may not be the case. Vibrations in the system can cause the workpiece to vibrate in a certain mode. Due to the preload of the gage fingers, the workpiece may deform locally in the contact zone with the finger tip.

Finally, mechanical creep and thermal expansion due to temperature changes may affect the measurement [Tan et al. 1993]. For waviness measurements, only the variation of the radius about its mean value is important, the mean value itself is not. Since

mechanical creep and thermal expansion progress slowly and the measurement time of a workpiece is short, their effect is not expected to have a significant impact on the measurement.

4.1.7 Overview of Technical Improvements

The technical methods used to improve the measurement accuracy are summarized in Table 4-1. Most of them can only be implemented in the post-process machine. Improvements for the grinding machine and mostly limited to analytical methods which will be discussed in Chapter 6.

Table 4-1: Overview of technical improvements

Source	Post-process machine	Grinding machine
Electrical noise	Shielding, grounding, and cabling techniques	
Forced vibrations	Low vibration motor drive Vibration isolation system Hydraulic accumulators Flexible hydraulic tubing	
Centerless fixture	Horizontal finger placement	
Gage head	Slow part rotation	

4.2 Measurement of the Electrical Noise

To improve the accuracy by reducing electrical noise, a procedure has to be found to measure and quantify this type of noise. For this purpose, the electrical noise is defined as the fluctuation of the digitized measurement signal when the fingers of the gage are fixed and cannot move. If the fingers are undeflected, noise measurement is not possible since in this case the analog inputs of the data acquisition card saturate and read a constant value of 10 V. The fingers are therefore displaced by a small distance so that the signal is within the -10 V to 10 V input range of the data acquisition card. The displacement is achieved by clamping the gage head down in a fixture and letting the fingers rest against two small steel blocks that are mounted on the fixture. The amount of displacement is adjusted by positioning the fingers with the motor in the gage head. Although the fixture is very rigid, it is susceptible to vibration from the environment, which may be measured by the gage head due to its high sensitivity. The fixture is therefore placed on the base plate of the vibration isolation system. The roll motor and the hydraulic unit are turned off during the measurements to further reduce mechanical vibration.

To obtain a measurement, the electrical signal of both fingers is measured for a duration of 60 seconds. The analog signals are sampled at a frequency of 2 kHz since this is approximately the sampling frequency when parts are measured. The time domain signals of the two fingers are shown in Figure 4-4 for a duration of 0.5 seconds.

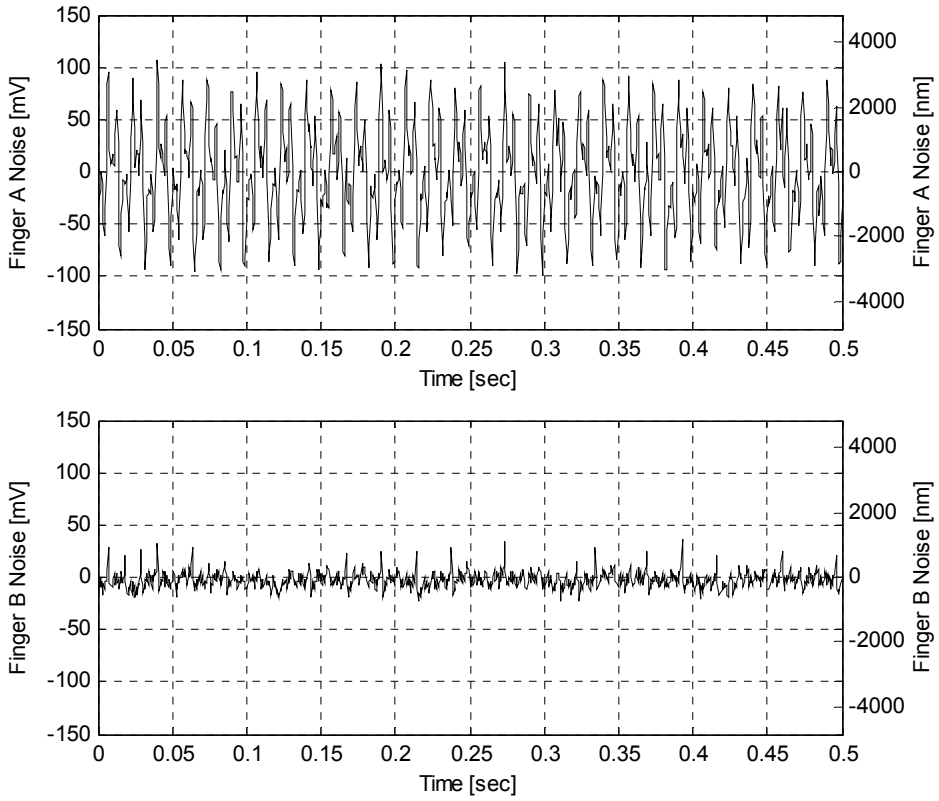

Figure 4-4: Electrical noise of finger A and B before noise reduction

The noise levels reflect the noise of the original measurement system prior to any optimization of the circuits. The axes of the plots show the noise in both millivolts and also in nanometers for the selected calibration. It can be seen that the noise level for finger A is significantly higher than for finger B. In addition, the noise for finger B appears to be more random than for finger A. The noise of finger A seems to contain harmonic components at a few distinct frequencies.

For the optimization of the circuits it is convenient to use a characteristic value that quantifies the amount of noise in the signal. Traditionally, the root-mean-square (RMS) value is used in electrical engineering [Davidson 1961]. The RMS value of an AC voltage is the corresponding voltage of a DC voltage that contains the same amount of

energy. After removal of the DC or constant part of the electrical signal, the RMS value is the energy contained in the fluctuation of the signal. The concept of the RMS value of an AC current in electrical engineering is similar to the concept of the sample standard deviation of a random process. The RMS voltage V_{RMS} of a time-varying continuous signal $V(t)$ over the time period T is given by

$$V_{RMS} = \sqrt{\frac{1}{T}\int_0^T V^2(t)\,dt}\ . \tag{4.1}$$

If the voltage is only known as N samples $V(k)$, $k = 0,...,N-1$, the integral can be approximated by

$$V_{RMS} \approx \sqrt{\frac{1}{N}\sum_{k=0}^{N-1} V^2(k)}\ . \tag{4.2}$$

This equation is very similar to the definition of the sample standard deviation s of N observations $x(k)$, $k = 0,...,N-1$

$$s = \sqrt{\frac{1}{N-1}\sum_{k=0}^{N-1}(x(k)-\bar{x})^2} \tag{4.3}$$

if the mean $\bar{x}$ of the sample is zero. For the further analysis it is more convenient to regard the sampled voltages as a random process and use the standard deviation as a measure of noise rather than the RMS value.

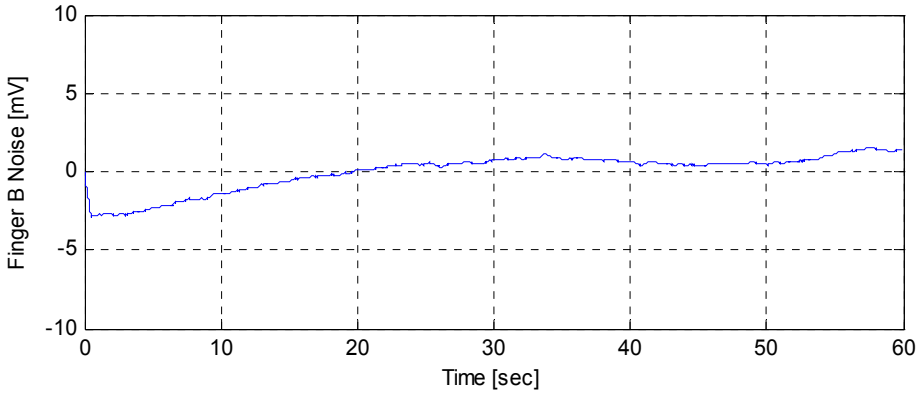

Figure 4-5: Electrical noise after application of a 1000-point MA filter

Depending on the electrical configuration it was found that the mean value of the signal exhibits a slow fluctuation over time. This is depicted in Figure 4-5 which shows the electrical noise of finger B for the full time period of 60 seconds. The signal in the diagram is smoothed by applying a moving average (MA) filter with 1000 points given by

$$y(k) = \frac{1}{1000}\sum_{n=0}^{999} x(k-n)\,, \tag{4.4}$$

where $y(k)$ is the filter output. The random process is therefore nonstationary with a time-varying mean value [Bendat, Piersol 1986]. Calculating the standard sample deviation as given by equation (4.3) over the full length of 60 seconds therefore yields a value that is too high since it also includes the variation of the mean. To account for that, the measurement data is divided into $N_E = 60$ non-overlapping ensembles with a length of 1 second or $N_S = 2000$ observations each. It is assumed that the variation of the mean is small enough so that the signal can be considered as piecewise stationary over the

ensemble length. The overall standard deviation is then calculated as the mean of the standard deviations of the individual ensembles.

$$s = \frac{1}{N_E}\sum_{n=0}^{N_E-1}\sqrt{\frac{1}{N_S-1}\sum_{k=0}^{N_S-1}\left[x\left(k+N_S n\right)-\bar{x}(n)\right]^2}\,, \tag{4.5}$$

where $\bar{x}(n)$ are the arithmetic ensemble means

$$\bar{x}(n) = \frac{1}{N_S}\sum_{k=1}^{N_S} x(k+N_S n)\,. \tag{4.6}$$

To gain information about the physical causes of the noise, the spectral decomposition of the signal is an important tool. For this purpose, the averaged periodogram is calculated as described in [Tretter 1976]. The data set is divided into the same ensembles as for the standard deviation. For each of the N_E ensembles, the periodogram is calculated and the averaged amplitudes $A(m)$ are calculated from the ensemble amplitudes

$$A(m) = \frac{1}{N_E}\frac{1}{N_S}\sum_{n=0}^{N_E-1}\left|\sum_{k=0}^{N_S-1} x(k+N_S n)e^{-j\omega_0 km}\right| \quad \text{for } m = 0,\ldots,N_S-1\,, \tag{4.7}$$

with $\omega_0 = 2\pi / N_S$. The averaged periodograms for finger A and B of the original not optimized system are shown in Figure 4-6. As already seen in the time domain plots in Figure 4-4, the noise is significantly higher for finger A than for finger B. The highest amplitude in the spectrum of finger A is about 20 times larger than in the spectrum of finger B. The 60 Hz and 180 Hz frequencies are dominant in the spectrum of finger A. Oscillations occurring at a multiple of the 60 Hz power frequency are a quite common

phenomenon in electrical systems. By revising and optimizing the electrical circuits, their amplitudes can often be reduced.

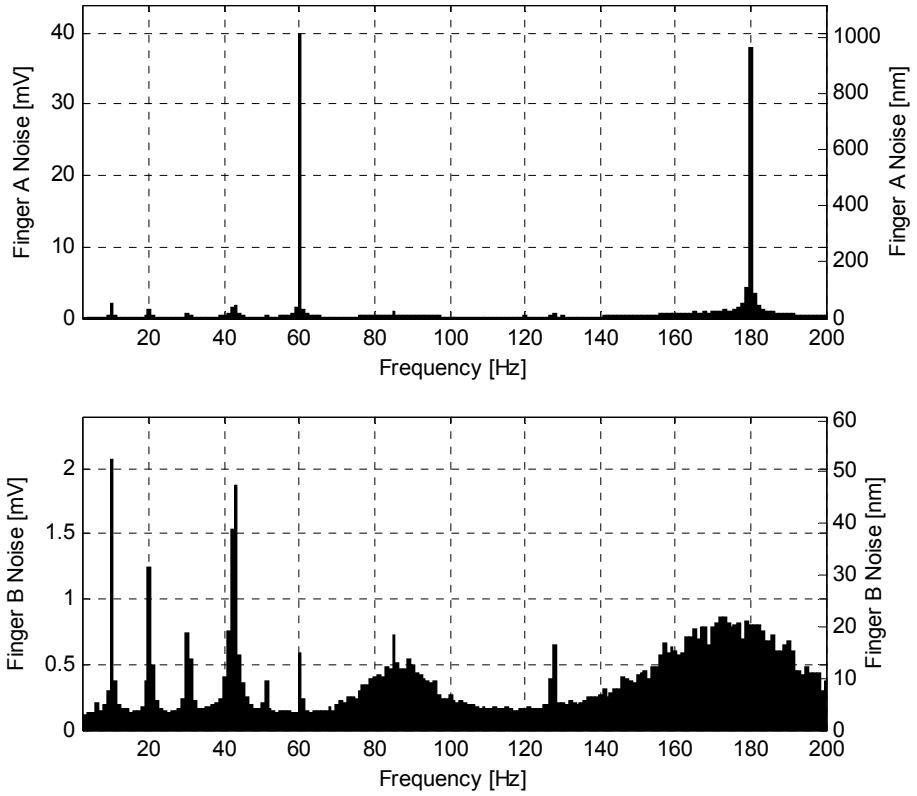

Figure 4-6: Spectral decomposition of the electrical noise before noise reduction

Table 4-2: Electrical noise of the original system

	Standard deviation	
	[mV]	[nm]
Finger A	43.4	1402
Finger B	7.70	248

The noise of the original system is summarized in Table 4-2. It is expressed in millivolts and in equivalent nanometers for the given calibration.

4.3 Reduction of Noise Interferences in the Electrical Circuits

4.3.1 Basic Methods for Interference Reduction

In this section, the methods for noise interference reductions are discussed. *Noise interference* is here defined as any undesirable effect of noise [Ott, 1988]. In most practical cases, the interferences due to noise can only be reduced but not be eliminated completely.

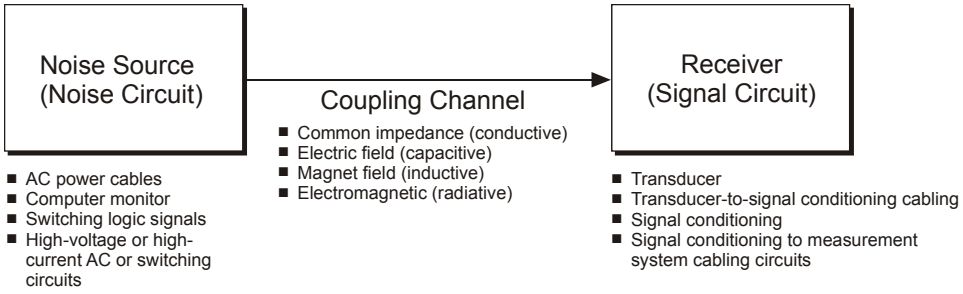

Figure 4-7: Typical noise path [Shah 2001]

The typical mechanism for noise interferences is shown in Figure 4-7. Three components are involved in this process: a noise source, a noise receiver, and a common coupling channel between them through which the noise can be transmitted. Typical examples for the noise source are AC power cables, motors, or transformers. The receiver can be any component of the signal circuit. A coupling channel can exist through a common conductor or through a field, which can be electric, magnetic or electromagnetic.

Several methods exist to reduce interferences. The methods employed here for the given system can be grouped into four categories:

- Shielding of components (section 4.3.2)
- Grounding techniques (section 4.3.3)
- Improvement of the signal-to-noise ratio (section 4.4)
- Filtering of the signal (section 4.3.5)

This section is primarily concerned with the design of the electrical circuits. Therefore, the main emphasis is on the shielding of components and grounding techniques. Filtering of the signal is only briefly discussed in 4.3.5. Section 4.4 addresses the signal-to-noise ratio.

4.3.2 Shielding

Shielding reduces interferences by obstructing the coupling channel. It is an important method for noise reduction whenever AC signals exist. Shielding can be done at the source to reduce its noise emission or at the receiver to lower its susceptibility. The selection of the shield depends mainly on the type of field involved in the interference and the frequency of the field.

Electric fields cause interferences by capacitive coupling. They are relatively easy to shield. Enclosing a component completely with a conducting material provides sufficient shielding, since the electric field inside the enclosure is independent from the field outside the enclosure. The enclosure should be grounded at one point. Common materials for shielding electric fields are copper or aluminum.

Magnetic fields couple on the receiver by induction. They are more difficult to attenuate than electric fields. In a lot of cases the magnetic fields can only be reduced but

not eliminated. For adequate shielding, high permeability alloys are used. They are known under brand names such as Permalloy, Mu-Metal, or Supermalloy. High permeability alloys protect the target by redirecting the magnetic flux [Morrison 1998]. Magnetic shields should enclose a component as completely as possible and holes or gaps should be minimized. Grounding of the shield is not required.

Electromagnetic waves affect the receiver by radiation. Depending on the type of waves, such interferences are referred to as electromagnetic interferences (EMI) or radio-frequency interferences (RFI). Whereas electric or magnetic fields only exist in the near field, electromagnetic fields can also exist in the far field. Shields that are effective against electric and magnetic fields usually also provide sufficient protection against electromagnetic fields. Electromagnetic shields attenuate a wave through reflection on its surface and through absorption inside the material. An enclosure can contain holes or gaps as long as their dimensions are smaller than half of the wavelength. Common materials for electromagnetic shielding are aluminum or copper.

In the post-process machine, shielded cables were used for the transmission of the measurement signal to provide protection against electric fields. The cable shields were grounded at one end. Grounding at several points is only recommended for high frequency signals, where the signal wavelength is in the same order of magnitude as the cable length. For low frequencies, multiple ground connections should be avoided. Otherwise ground currents can flow in the shield causing interferences with the signal.

The BNC cables connecting the anti-aliasing filter to the system displayed a slight susceptibility to magnetic fields. The magnetic fields stemmed from the computer monitor and the power supply of the low-pass filter. Since the noise level was not severe,

sufficient attenuation was obtained by routing the BNC cables further away from the two noise sources.

Tests also revealed a high sensitivity of the signal conditioning card to magnetic fields. In the electrical cabinet, the signal conditioning card is mounted close to the power supply of the measurement system. With a Gaussmeter, magnetic fields originating from the power supply were measured at 60 and 180 Hz. These fields couple on the measurement signal. In the spectrum for finger A (Figure 4-6), they are visible as two sharp peaks. In addition to the power supply, magnetic fields from relays affected the signal conditioning card as well.

To protect the card, it was decided to shield it rather than to move it away from the sources of the fields. For this purpose, a shielded enclosure was designed (Figure 4-8). The outside of the enclosure consists of 4.7 mm thick aluminum. Aluminum was chosen because of its good reflection and absorption of electromagnetic waves. Therefore, the enclosure provides protection against EMI and RFI. To achieve also protection against electric fields, the enclosure was connected to the ground. The magnetic fields, however, were attenuated by the aluminum alone by only a factor of 2. To achieve further attenuation, a high permeability alloy was added. The alloys tested were CO-NETIC and NETIC made by the Magnetic Shield Corporation. They are alloys with high nickel content and have similar properties as Permalloy or Mu-Metal. When exposed to a magnetic field of strength $\mathbf{H}$, they produce a magnetic flux density $\mathbf{B}$ given by

$$\mathbf{B} = \mu_0 \mu_r(\mathbf{H})\mathbf{H}, \tag{4.8}$$

where $\mu_0 = 4\pi \times 10^{-7}\ \mathrm{N\,A^{-2}}$ is the permeability of free space and μ_r is the permeability of the alloy which is a function of $\mathbf{H}$. Plotting $\mathbf{B}$ against $\mathbf{H}$ shows the typical shape of a

magnetic hysteresis curve of a ferromagnetic metal. For an unmagnetized metal, the magnetic flux density **B** increases at first linear with the field strength **H** until the metal starts to saturate. At this point, the curve levels off. Increasing **H** does not yield any further increase in **B**, since the metal is fully magnetized. The two alloys CO-NETIC and NETIC have slightly different magnetic properties. CO-NETIC has a maximum permeability of $\mu_r = 450000$ but saturates at $|\mathbf{B}| = 0.8$ Tesla. The maximum permeability of NETIC is only $\mu_r = 4000$, but saturation occurs at $|\mathbf{B}| = 2.14$ Tesla. CO-NETIC is therefore the preferred alloy to shield weak fields. If the fields are strong, a combination of NETIC and CO-NETIC is usually used. For the application discussed here, CO-NETIC provided better shielding than NETIC. This indicates that the magnetic fields were not strong enough to cause a saturation of the CO-NETIC sheets. For the given application, CO-NETIC is therefore the better choice.

High permeability alloys, such as CO-NETIC, are usually annealed to achieve their high permeability. Often, they are exposed to a magnetic field during this process. As a result, they can loose their shielding properties during machining operations such as forming, bending, punching or drilling [Barnes 1987]. To minimize machining operations, metal sheets were cut to size to cover each wall of the enclosure. No bending of the sheets was necessary. Each of the six walls was covered by two layers of 0.76 mm thick CO-NETIC sheets. The final design of the enclosure with the high permeability alloys resulted in an attenuation of the magnetic fields by a factor of approximately 80.

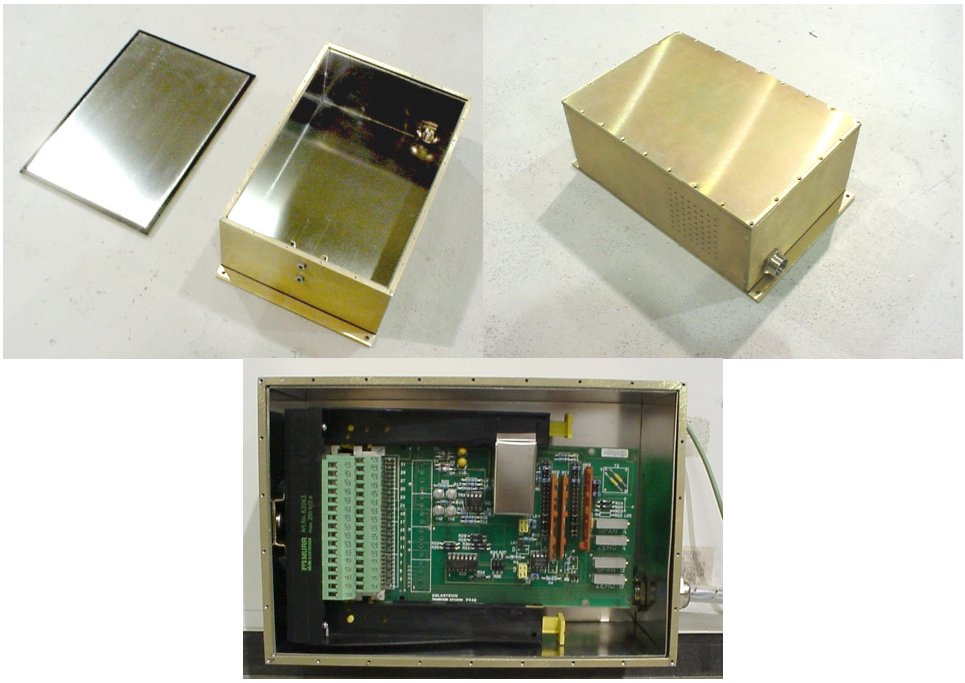

Figure 4-8: Shielded enclosure of the signal conditioning card

4.3.3 Grounding

Proper grounding is important for interference reduction especially when the electrical system consists of components that operate at very different voltage and power levels. The grounding of components should be made with respect to two main goals:

1. Minimization of common ground impedance
2. Avoidance of ground loops

A common ground impedance exists whenever two or more electrical components are connected to the ground through a common impedance. In general, there are two different methods to ground several components in a system. In multipoint systems

(Figure 4-9) different electrical components have completely separate connections to the ground. Single point systems (Figure 4-10) are connected to the ground at only one point.

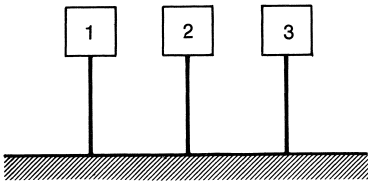

Figure 4-9: Multipoint grounding connections

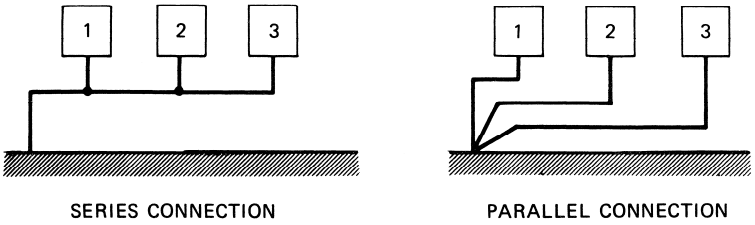

Figure 4-10: Single point grounding connections

The electrical circuits of the machine have only a single connection to the power line and the ground. Therefore, multipoint systems are not further considered here. In a single point system, the components can be connected in series or in parallel. Series connections are practical since they reduce cable length and simplify wiring. However, their disadvantage is that components share a common ground impedance. Whenever a common ground impedance exists, the voltage drop between the component and the ground depends on the sum of the currents flowing through the common ground impedance. Therefore, ground currents of one components cause a fluctuation of the ground voltage of all other components connected through the common ground impedance. A parallel connection of components, in which the common ground

impedance is minimized, is therefore favorable. It is particularly important to separate components that operate at voltage and power levels (Figure 4-11).

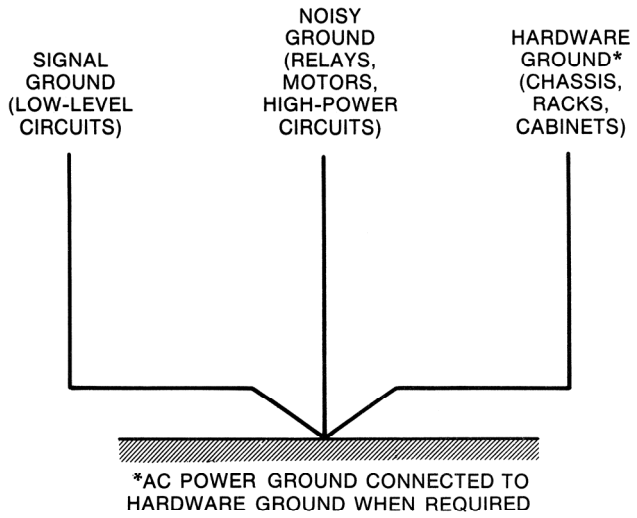

Figure 4-11: Optimal configuration for low frequency grounding [Ott 1988]

The grounding of the post-process machine is done according to Figure 4-11. The grounds of the measurement system components, which are the gage head, the signal conditioning card with its power supply, and the DAQ card, are directly connected by a wire. The ground connections of all other electrical devices are separated from the measurement system ground as much as possible. This is especially necessary for higher voltage components such as the motor of the hydraulic pumps or the roll motor. For other electrical equipment it is not always obvious if they introduce noise into the ground. One example is the roll motor drive. The drive is equipped with a positive (+) and negative (-) connection for speed regulation of the motor. In the original configuration, the positive (+) terminal was connected to one of the analog outputs of the DAQ card and the negative (-) terminal to the DAQ card ground. Tests showed however that the motor drive introduces

noise through the negative (-) connection which entered the measurement system through the DAQ card. The noise disappeared after connecting the negative terminal to the same ground as the roll motor. The improvement of the measurement signal justifies the potential small loss of motor speed accuracy due to slight ground potential differences between the drive and the DAQ card.

Ground loops occur whenever two different grounds are connected by a conductor. This is exemplified in Figure 4-12 by a grounded signal source connected in referenced single ended (RSE) mode to a grounded instrument amplifier.

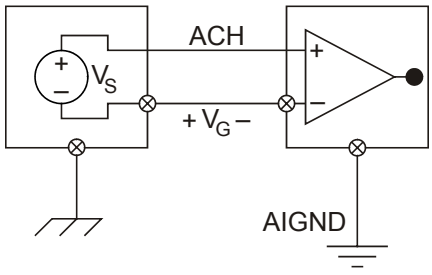

Figure 4-12: Grounded signal source connected in single ended mode

A ground loop exists through the wire connecting the negative (-) terminals of the two components. Since two grounds practically never have the same potential, a voltage drop V_g is observed between the two grounds causing a small current in the conductor. As a result, the amplifier measures $V_S + V_g$ as the voltage of the signal source. The configuration as shown in Figure 4-12 is therefore not recommended. To overcome this problem, the DAQ card offers two alternative wiring modes. In nonreferenced single ended mode (NRSE), all inputs are measured with the AISENSE connection of the DAQ card as a reference (Figure 4-13). AISENSE is connected to the ground of the signal

sources. Any difference V_G in the ground potentials appears at both inputs of the amplifier and therefore cancels out in the measured voltage V_M.

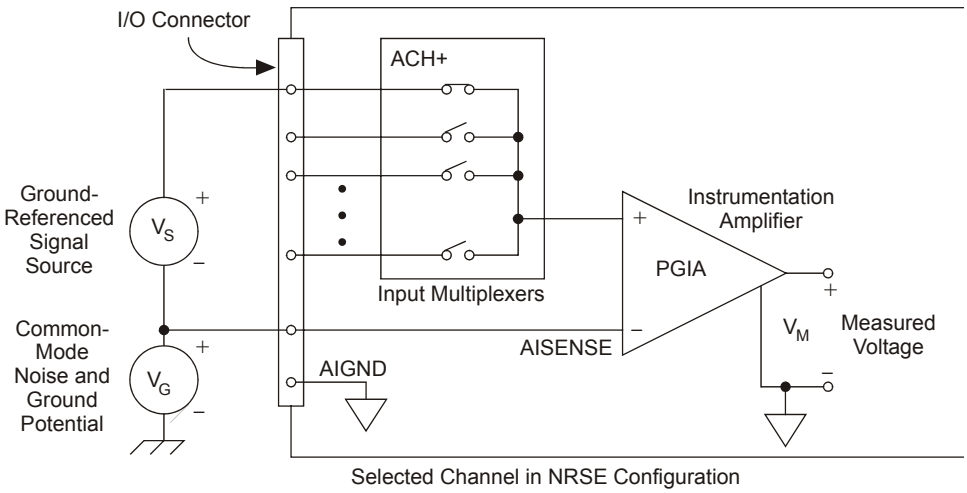

Figure 4-13: Nonreferenced single ended mode [National Instruments 2002]

In addition to the NRSE mode, the DAQ card allows connecting signal sources in differential (DIFF) mode (Figure 4-14). In this configuration, a separate analog input is used for the ground of every signal source. Similar to the NRSE configuration, any difference in the ground potential is rejected from the measurement. In addition, the DIFF configuration can also eliminate noise that couples on the cables between the signal source and the DAQ card, assuming the same voltage adds to the positive (+) and the negative (-) leads. In electrical systems, where cables are long or run through a noisy environment, the DIFF configuration is preferable over the NRSE mode. If noise coupling on the cables is not an issue and a common reference can be used for all signal sources, the NRSE configuration is often more convenient since it reduces the number of cables.

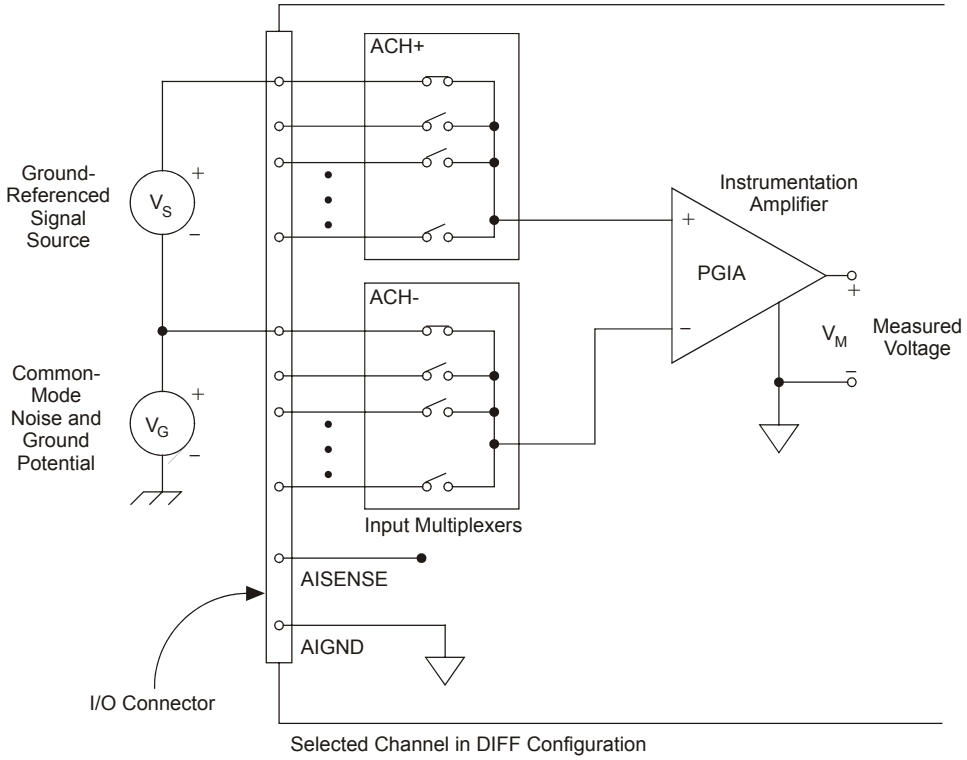

Figure 4-14: Differential configuration mode [National Instruments 2002]

For the post-process machine, the DIFF configuration was used due to its superior noise rejection. It should be noted though that no significant difference was observed compared to the NRSE configuration. The reason may be that the shielding of the cables is already adequate in which case the DIFF mode does not offer much improvement.

4.3.4 Intrinsic Noise Sources

Intrinsic or *internal noise sources* mark a special type of noise as the interference is produced within a component. Almost every electrical device is prone to this type of

noise. Electrical circuits are usually designed based upon fundamental laws in electrical engineering such as Kirchhoff's' laws or Ohm's law. These laws assume that an electrical current is a uniform and continuous flow of charge. When working with very low voltages levels, this assumption does not agree very well with practical observations. Instead, a current is better modeled as the movement of discrete charges whose behavior is governed by probabilities. Deviations of the charge flow from the assumed uniform and continuous behavior appear as intrinsic noise.

The three main types of intrinsic noise are *thermal noise*, *shot noise* and *1/f noise*. Thermal noise results from thermal agitations of electrons within a resistance. It is also referred to as *Johnson noise*, named after its discoverer J. B. Johnson [Johnson 1928]. Nyquist [1928] derived on a theoretical basis that the RMS voltage V_T of thermal noise is given by

$$V_T = \sqrt{4k_B TRB}\,, \tag{4.9}$$

where $k_B = 1.38 \times 10^{-23}\,\mathrm{JK}^{-1}$ is Boltzmann's constant, T the absolute temperature, R the resistance of the conductor under consideration, and B is the bandwidth of the system. In the spectrum, thermal noise appears as white noise.

Shot noise is caused by the random emission of electrons in a current which causes a fluctuation of the current about its mean value. Schottky [1918, 1922] showed that the RMS noise current I_{sh} is given by

$$I_{sh} = \sqrt{2q_E I_{DC} B}\,, \tag{4.10}$$

where q_E is the charge of an electron and I_{DC} is the DC component of the current. Like thermal noise, shot noise appears as white noise in the spectrum.

1/*f* noise is also called *contact noise* or *excess noise*. It results from the fluctuating conductivity due to imperfect contacts between materials. The noise current $I_{1/f}$ can be approximated by

$$I_{1/f} \approx k_{1/f} I_{DC} \sqrt{\frac{B}{f}}, \tag{4.11}$$

where $k_{1/f}$ is a constant depending on the material and its geometry and f is the frequency. The name 1/*f* noise stems from the fact that its power spectrum is frequency dependent and decays with $1/f$.

As can be seen from equations (4.9) to (4.11), the intrinsic noise depends on quantities that cannot be influenced by the circuit design. The only exception is the bandwidth *B*. Therefore, the purpose here is not to attempt a reduction of the intrinsic noise but to consider it as the base line for the electrical noise in the system. Once it is believed that the major amount of the noise is caused by intrinsic sources, no further methods for electrical noise reduction are pursued.

4.3.5 Filtering of the Signal

Filtering can be used to remove noise that cannot be eliminated by other methods. The idea is to reduce the signal bandwidth to the frequency range that contains the desired information. All other frequencies should be filtered out by low-pass, high-pass or band-pass filters. The post-process machine contains two analog low-pass filters, the signal conditioning card filter and the anti-aliasing filter, which both reduce the bandwidth. In addition, the measurement software allows applying a digital band-pass filter whose passband can be flexibly configured. The determination of the profile height requires the passband to be set to 10-250 UPR. Even for other measurement tasks, the passband should be limited to a reasonable frequency range to reduce the noise in the measurement signal. For Gaussian white noise, the standard deviation σ of the signal is proportional to the square root of the bandwidth B

$$\sigma \sim \sqrt{B} \,. \tag{4.12}$$

4.4 Gage Head and Signal Conditioning Card Setup

4.4.1 Gage and Signal Conditioning Card Gains

Both the gage head and the signal conditioning card provide adjustable gains to influence the relationship between finger displacement and output voltage. The output voltage at the signal conditioning card as a function of the finger displacement is depicted in Figure 4-15 and Figure 4-16 for finger A and B respectively. The different curves show the effect of different gage gains. The gain of the signal conditioning card was set to the lowest value (250-750 mV/V equivalent transducer sensitivity) to prevent saturation of the DAQ card inputs. The zero of the signal conditioning card was set to yield 0 V at the null position of the LVDTs.

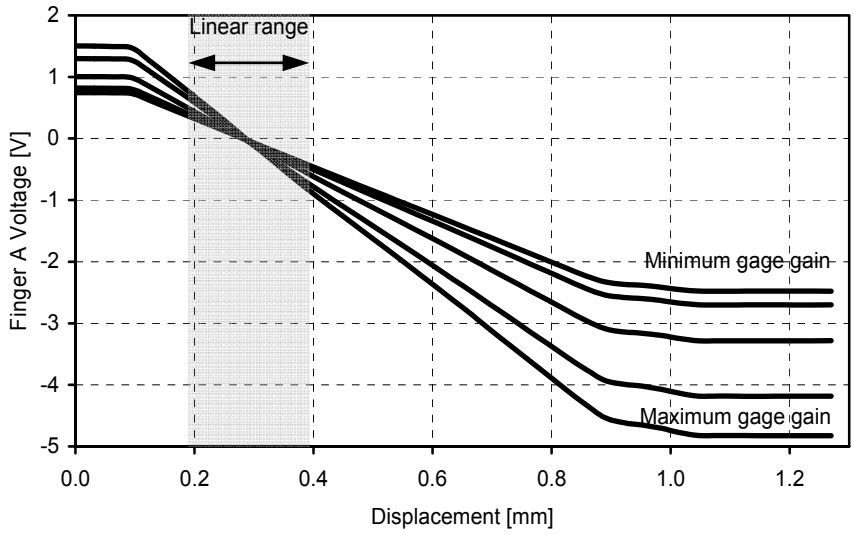

Figure 4-15: Effect of gage gains for finger A

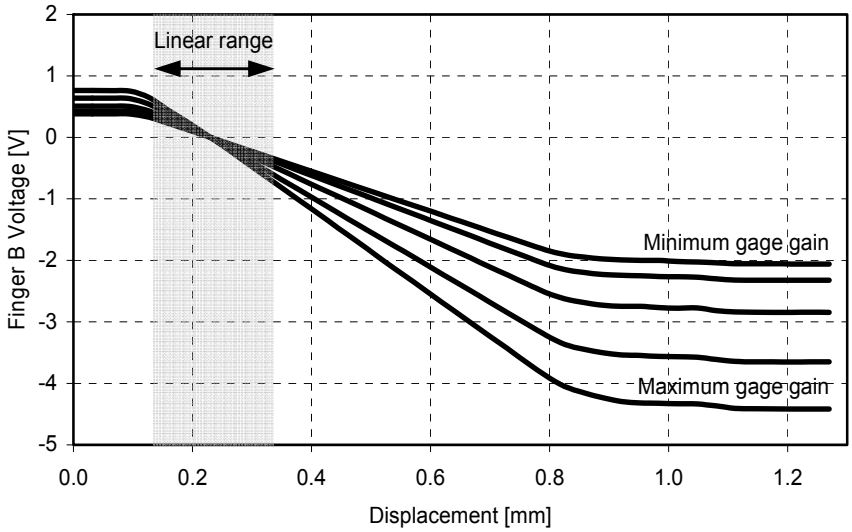

Figure 4-16: Effect of gage gains for finger B

The plots show the linear range of the gage head. It can be seen that an initial displacement of the fingers is necessary to operate within the linear range. LVDTs usually have the best linearity around their null position. They should therefore be calibrated to operate close to this point. The usable range for the fingers is shown as a shaded area in the figures. To utilize the complete input range of the DAQ card, the gains of the signal conditioning card can be increased. Within the linear range of the LVDTs, the output voltage V_R is given by

$$V_R = k_{SG}(k_{GG}x_d + k_{SZ}), \tag{4.13}$$

where x_d is the finger displacement, k_{GG} the gage gain, k_{SG} the gain, and k_{SZ} the zero adjust of the signal conditioning card.

For the specific gage head used here, a small degree of cross talk between the two fingers was detected, which is not accounted for in equation (4.13). With one finger fixed and the other finger deflected the signal of the fixed finger experiences approximately 5 % of the voltage change of the deflected finger. To simplify the calibration, this effect is ignored.

4.4.2 Selection of the Measurement Range

Several considerations should be made when adjusting the gains to setup the gage head for a certain measurement range:

- Generally, a large measurement range is practical for several reasons. To setup the gage for a specific part diameter, the fingers have to be positioned so that their displacement falls into the measurement range. The positioning is done with the finger motor and the set screw that swivels the gage head. If the measurement range is very small and the sensitivity is high, positioning becomes a difficult task, since the motor and the set screw do not provide a very accurate motion. In addition, a wider measurement range allows varying the initial displacement of the fingers and therefore the preload of the fingers.
- The minimum of the measurement range is given by the requirement that no saturation occurs during the measurement. The total range of finger displacement is given by the total variability of the workpiece diameter plus any noise or disturbances. The total allowable diameter variability according to Figure 3-26 is 30 μm. If the fingers are setup in a certain position, this variability can occur in

the positive or negative direction, so that the measurement range has to cover twice the variability. In presence of additional noise, the measurement range should be at least 100 μm to prevent saturation.

- With respect to electrical noise, the measurement range should be only as large as necessary to achieve a high signal-to-noise ratio. High gains usually ensure that the signal voltage is high compared to the voltage due to electrical noise. On the other hand, any noise that is introduced into the circuits prior to the amplification is increased in the same way as the signal is increased, thus not yielding any improvement of the signal-to-noise ratio.

The gage head was calibrated so that the output voltage is 0 V at the null position of the LVDTs. Therefore, no zero adjustment was undertaken. To achieve a certain gain, different combinations of gage and signal conditioning card gains can be chosen, since both the gage and signal conditioning card gains can be set independently. It was found that the electrical noise is lower, when the gage gains are high and the signal conditioning card gains are low than vice versa. Therefore, the gage gains were set to the maximum value. Subsequently, different coarse gain settings of the signal conditioning card were tested. The lowest electrical noise was obtained, when using the 5-15 mV/V setting (Table 3-1). The noise was measured using the standard deviation as given by equation (4.5) expressed as the equivalent displacement in nm. The fine gains of the signal conditioning card were adjusted so that both fingers have approximately the same gain. With this gain setting, the measurement range was large enough to prevent saturation during measurements.

4.4.3 Calibration Procedure

The previous section established the approximate relationship between finger displacement and voltage. In this section the exact relationship is determined through calibration of the gage head. This relationship can be expressed by

$$x_d = k_{Sl} V_R + k_{In}\,, \tag{4.14}$$

where k_{Sl} is the calibration slope and k_{In} the intercept.

The two most common calibration methods are calibration with master parts or direct calibration. Master parts are a set of highly precise parts with different nominal diameters. They are often used to calibrate in-process gages in grinding machines. A series of them are loaded in the machine and measured with the gage head. Comparison of the known master diameters with the gage voltages yields the displacement-voltage relationship. The advantage of this method is that the gage is calibrated to measure the absolute radial deviation rather than a relative deviation. In addition, geometric misalignments between the gage head axis and the part axis are compensated.

In the application considered here the gage fingers are calibrated directly. For this purpose, the fingers are displaced by a micrometer head while the output voltage of the gage is measured. Direct calibration is chosen here, since it provides a greater flexibility than a set of masters with fixed diameters.

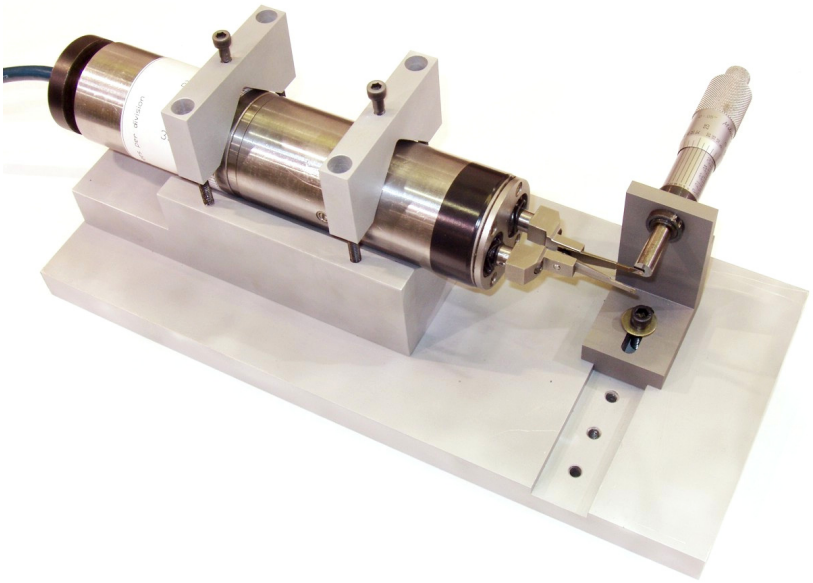

Figure 4-17: Calibration setup for the gage head

The setup is shown in Figure 4-17. The gage head is clamped down and held securely by a bracket. A Mitutoyo micrometer head is used to displace the fingers. The micrometer head has a total range of 1.27 mm (0.05 inch) and a resolution of 0.127 μm (0.000005 inch). One complete revolution of the screw moves the measuring face by 31.75 μm (0.00125 inch). The manufacturer specifies the accuracy with ±1.905 μm (±0.000075 inch) per revolution and ±6.35 μm (±0.00025 inch) overall. The setup as shown in Figure 4-17 allows the fingers to be calibrated only for relative radial measurements. For the measurement of surface profile waviness, this is sufficient since the absolute value of the radial distance is unimportant. The intercept k_{In} in equation (4.14) can therefore be chosen arbitrarily.

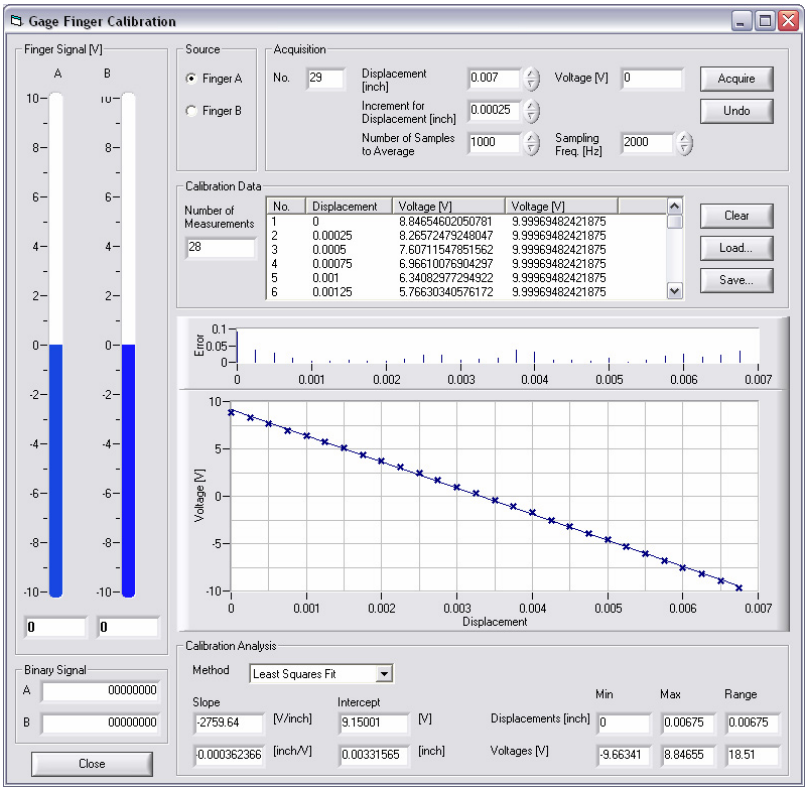

Figure 4-18: Software interface for gage finger calibration

To simplify the calibration, the calibration module of the software is used. The corresponding dialog is displayed in Figure 4-18. At the beginning of the calibration procedure, the tip of the micrometer spindle is brought into contact with the gage finger to be calibrated. An arbitrary initial displacement is entered into the software and recorded together with the output voltage of the finger. Subsequently, the finger is displaced in 6.35 µm (0.00025 inch) increments and for each step the output voltage is measured simultaneously. To minimize the effect of disturbances due to electrical noise or mechanical vibration, the average of 1000 samples of the voltage sampled at a frequency of 2000 Hz is taken as the corresponding voltage for a displacement. With the chosen displacement increments, 28 displacement-voltage pairs were taken. The slope of

the displacement-voltage relationship was obtained by fitting a straight line through the data points using a least squares fit. The calibration procedure was repeated three times for each finger and the average of the three slopes was used as the calibration slope k_{Sl}. The values for k_{Sl} are shown in Table 4-3 together with the measurement range of the fingers. In addition, the resolution expressed in finger displacement resulting from the 16 bit sampling of the output voltage is stated.

Table 4-3: Calibration data for finger A and B

	Finger A	Finger B
Slope	9.224 µm/V	9.691 µm/V
Measurement range	184.5 µm	193.8 µm
Resolution	2.815 nm	2.957 nm

4.5 Electrical Noise Budget

4.5.1 Electrical Noise in the Optimized System

After optimization of the electrical circuits and calibration of the gage head, the electrical noise is measured again following the same procedure outlined in section 4.2. The averaged periodograms for finger A and B are shown in Figure 4-19.

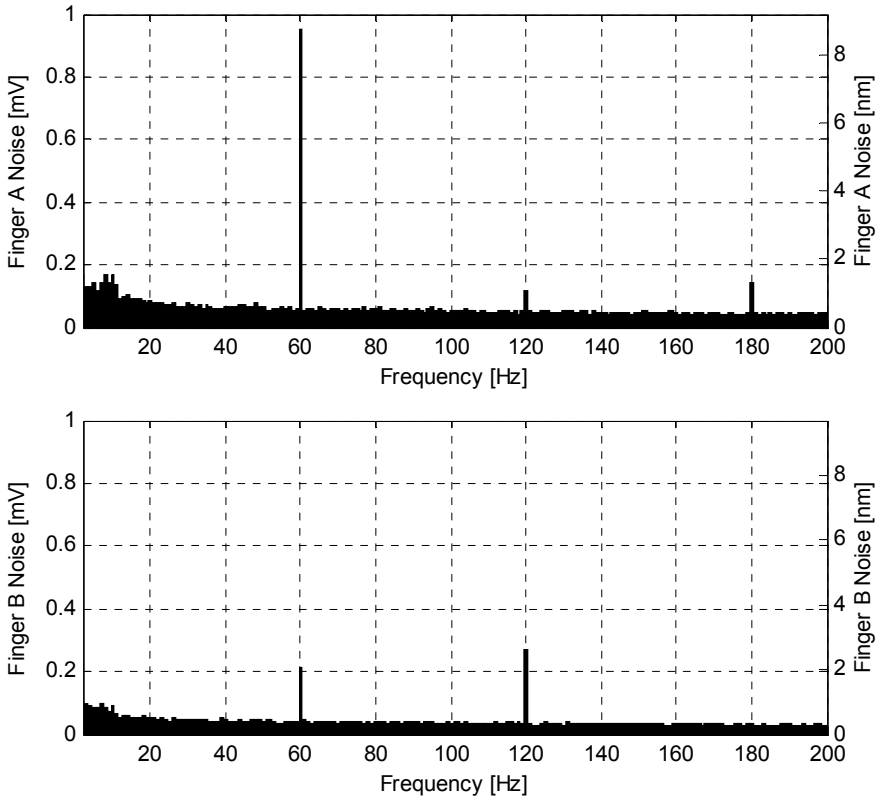

Figure 4-19: Spectral decomposition of the electrical noise after noise reduction

It can be seen that the noise has been greatly reduced compared to the original system depicted in Figure 4-6. Most of the noise still occurs at multiples of the 60 Hz power frequency but with significantly lower amplitudes. Similar to the original system,

the noise for finger A remains higher than for finger B. The results of the noise reduction are summarized in Table 4-4. Besides the standard deviation of the time domain signal, the amplitudes for the three highest peaks and the noise floor are listed. The noise floor is the average amplitude of the white noise that exists in addition to distinct peaks in the spectrum. The amplitude of the noise floor is estimated by calculating the median of all amplitudes for frequencies from 1 to 400 Hz. The median is used instead of the arithmetic average since it is not influenced by peaks in the spectrum.

Table 4-4: Results of the noise reduction

	Parameter	Original system		Optimized system		Factor of reduction	
		[mV]	[nm]	[mV]	[nm]	[mV]	[nm]
Finger A	Standard deviation	43.4	1402	1.12	10.3	39	136
	Noise floor	0.305	9.85	0.0429	0.395	7.1	25
	60 Hz noise	39.9	1289	0.953	8.79	42	147
	120 Hz noise	0.308	9.93	0.117	1.08	2.6	9.2
	180 Hz noise	38.0	1227	0.142	1.31	268	937
Finger B	Standard deviation	7.70	248	0.646	6.26	12	40
	Noise floor	0.270	8.72	0.0307	0.298	8.8	30
	60 Hz noise	0.591	19.1	0.212	2.05	2.8	9.3
	120 Hz noise	0.165	5.32	0.270	2.62	0.6	2.0
	180 Hz noise	0.807	26.0	0.036	0.349	22	74

The redesign of the circuits and the calibration of the gage head yielded a reduction of the standard deviation by a factor of 136 and 40 for finger A and B. The noise at 180 Hz could be decreased by a factor of even 937. As an important result it can be stated that the standard deviation of the noise at finger A is 10.3 nm and 6.26 nm at finger B.

4.5.2 Design of Experiments for Electrical Noise Budget

It is desired to gain evidence about the contribution of the electrical components to the noise budget and also examine the susceptibility of the system to additional disturbances. The components of the measurement system are depicted in Figure 4-20.

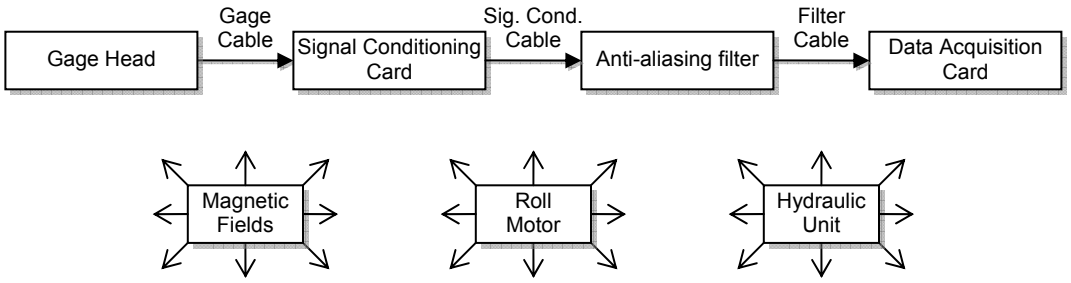

Figure 4-20: Components and disturbances of the measurement system

The system consists of four electrical devices (gage head, signal conditioning card, low-pass filter, and data acquisition card) and three cables connecting them. The analog signal generated in the gage head therefore has to pass seven devices until it is digitized. Each of the seven components can contribute to the total electrical noise. In addition to these components, three external disturbances are considered. The first disturbance are magnetic fields to which the gage cable, the signal conditioning card, and the signal conditioning cable are exposed to. Since a high susceptibility of the signal conditioning card to magnetic fields was found, it is desirable to examine whether the card is still susceptible after shielding it by an enclosure. The other two disturbances are the roll motor and the hydraulic unit. Turning these devices on may cause small ground loops which can affect the measurement signal.

For the design of experiments, each of the seven components is regarded as a factor or an independent variable. Each factor can take on two levels: component removed from the system (0) or component included in the system (1). Likewise, the disturbances are treated as factors. Each disturbance factor can take two levels: disturbance not applied to the system (0) and disturbance applied to the system (1). The factors with their levels are listed in Table 4-5.

Table 4-5: Factors for the design of experiment

Factors		Levels	
		0	1
F1	Data acquisition card	Removed	Included
F2	Filter cable	Removed	Included
F3	Low-pass filter	Removed	Included
F4	Signal conditioning cable	Removed	Included
F5	Signal conditioning card	Removed	Included
F6	Gage cable	Removed	Included
F7	Gage head	Removed	Included
F8	Magnetic fields	Not applied	Applied
F9	Roll motor	Not applied	Applied
F10	Hydraulic unit	Not applied	Applied

Due to the nature of the system, meaningful noise measurement cannot be obtained for all possible combination of levels for the factors F1-F7. For example, the noise cannot be measured when the signal conditioning card alone is removed from the system or when all cables are removed. The only way to vary factor levels is to remove components one by one starting from F7 down to F1. For the first treatment, all components are included. In the second treatment, the gage head is disconnected from the cable and the leads of the cable are shortened to close the electrical circuit. For the third treatment the gage cable is removed and the connections on the signal conditioning card

are shortened. This procedure is continued until only the data acquisition card is left in the system. For the case that all factors F1-F7 assume the level 0, the noise is by definition zero. This 2^7 fractional factorial design produces seven different treatments for the factors F1-F7. Opposite to F1-F7, the disturbance factors F8-F10 can be varied arbitrarily and a 2^3 full factorial design can be employed, resulting in 8 treatments. Combined with the treatments of the factors F1-F7, this results in $7 \cdot 8 = 56$ treatments compared to 1024 treatments for a 2^{10} full factorial design.

As a result of the low number of experiments compared to the full design, some information is lost. More specifically, the effect of any factor interaction between the factors F1-F7 cannot be distinguished from the effect of a single factor. This is known as effect aliasing [Christensen 1996]. For example, the effect of the factor interaction F1*F2 will be aliased to the factor effect of F2. It is assumed here that no significant interaction occurs between the components represented by the factors F1-F7 so that the loss of information on the interactions can be tolerated. Since a full factorial design is used for the factors F8-F10, all information about interactions between these factors is preserved.

The measured noise may to a small extend depend on environmental conditions such as temperature fluctuations and variations of the ground potential. In addition, the experiments require rewiring of the components. Since several noise sources exist, the measured noise can depend on the exact route of the cables. To gain a higher confidence in the results, three replications are performed on different days. This results in a total number of 168 experiments.

For each experiment, the noise is measured for 60 seconds with a sampling frequency of 2000 Hz. The measured data is divided into 60 non-overlapping ensembles

of 2000 observations each. For each ensemble, the five parameters are computed that were used in the previous section to characterize the noise (standard deviation, amplitudes of the noise floor, 60, 120, and 180 Hz peak). The values of the individual ensembles are averaged over all ensembles. The goal of the data analysis is to estimate the effect of the factors F1-F10 on the five parameters for both finger A and B.

4.5.3 Analysis of the Data

To analyze the effects of the factors, a multiple linear regression model is used. The model is given by

$$Y_i = \beta_0 + \sum_{j=1}^{N_P} \beta_j X_{ij} + \varepsilon_i , \qquad i = 1,...,N_b . \tag{4.15}$$

In this model, Y_i is the dependent variable or response variable. The response variable can be any of the five noise parameters of one of the two fingers. X_{ij} denotes the *i*-th observation of the *j*-th independent variable or predictor variable. The predictor variables are single factors or factor interactions. Since each variable X_{ij} can take on only the value 0 or 1, they are also called indicator or binary variables. Since all predictor variables are binary, the model is equivalent to an analysis of variance model. β_0 is the intercept which is by definition zero. β_j is the coefficient of the *j*-th predictor variable. It denotes the increase of the noise when the factor or factor interaction associated with the *j*-th predictor variable is applied to the system. ε_i is the random error term.

As predictor variables, the seven component factors F1-F7 are included in the model. As discussed earlier, interactions between the factors F1-F7 cannot be included

due to the fractional design of the experiment. The disturbance factors F8-F10 by itself are not used as predictors since in absence of any electrical component the noise in the system is by definition zero. The disturbance factors are only used in interactions with a component factor. This results in 21 interaction terms. The effect of these interactions can be interpreted as the noise that the disturbance introduces in the specific component. To keep the number of predictor variables down, no interactions with more than two factors are considered. Thus, the total number of initial predictor variables included in the model is 28.

When fitting a regression model to the data, the coefficients β_j are estimated by least square estimators b_j. The linear regression model makes the following assumptions about the error term ε_i, which affect the estimates:

1. Zero mean: $\mathrm{E}[\varepsilon_i] = 0$ (4.16)
2. Constant variance: $\mathrm{Var}(\varepsilon_i) = \sigma^2$ (4.17)
3. Error terms are uncorrelated: $\mathrm{Cov}(\varepsilon_i, \varepsilon_j) = 0$ for $i \neq j$ (4.18)

Under these conditions, the Gauss-Markov theorem states that the least square estimators b_j are unbiased estimators and efficient estimators, i.e. they have minimum variance among all unbiased estimators. [Neter et al. 1996] Fitting the model to the measured data reveals that the variance of the error term is not constant. Instead, it increases with the value of the response variable. This is shown in Figure 4-21, where the residuals e_i are plotted against the fitted values $\hat{Y}_i$. The fitted values and the residuals are given by

$$\hat{Y}_i = \sum_{j=1}^{N_P} b_j X_{ij} \tag{4.19}$$

$$e_i = Y_i - \hat{Y}_i, \tag{4.20}$$

respectively. The nonconstant variance is known as heteroscedasticity. In a heteroscedastic model, the least square estimators are still unbiased but have no longer minimum variance. Furthermore, variance estimators are biased, so that test statistics for the significance of a predictor yield incorrect results.

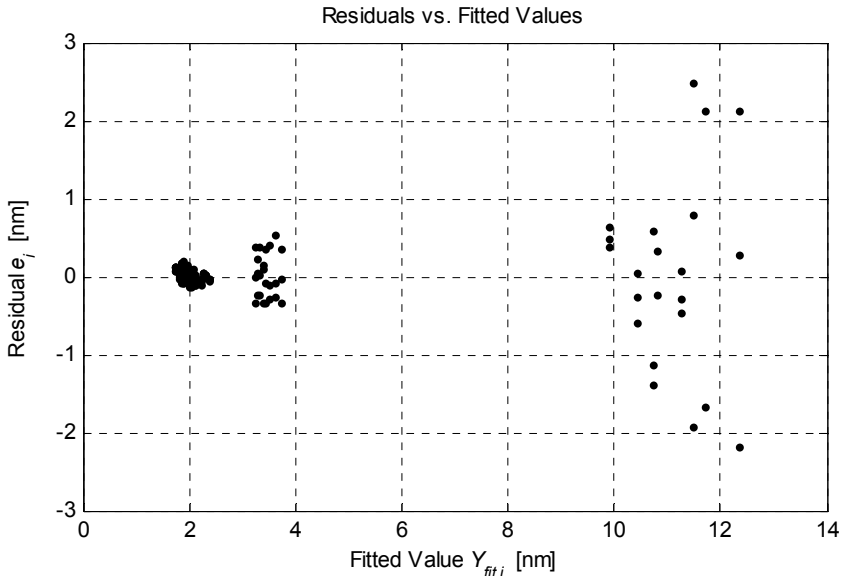

Figure 4-21: Residuals vs. fitted values for the standard deviation of finger A

A possible remedy is to transform the response variable. However, this results in an unwanted nonlinear relationship between the response variable and the predictors. Another solution to this problem is to employ weighted least squares. Carroll and Ruppert [1988] suggest as a rule of thumb that weighted least squares should be used if the standard deviations differ by a factor of 3 or more. Therefore, this approach is selected

here. The regression equation with zero intercept term for a heteroscedastic dataset is given by

$$Y_i = \sum_{j=1}^{N_P} \beta_j X_{ij} + \varepsilon_i \ , \ \ \mathrm{Var}(\varepsilon_i) = \sigma_i^{\,2} \, . \tag{4.21}$$

Defining weighting coefficients $w_i = 1/\sigma_i$ and multiplying both sides of equation (4.21) with w_i yields

$$w_i Y_i = \sum_{j=1}^{N_P} w_i \beta_j X_{ij} + w_i \varepsilon_i \ , \quad \mathrm{Var}(w_i \varepsilon_i) = 1 . \tag{4.22}$$

The estimates b_j of β_j are computed by minimizing the equation

$$\begin{aligned} Q &= \sum_{i=1}^{N_b} \left(w_i Y_i - \sum_{j=1}^{N_P} w_i b_j X_{ij} \right)^2 \\ &= \sum_{i=1}^{N_b} w_i^{\,2} \left(Y_i - \sum_{j=1}^{N_P} b_j X_{ij} \right)^2 \end{aligned} \ , \tag{4.23}$$

which is the weighted least square equation.

Initially, the regression models for the 10 parameters are developed with all 28 predictor variables included. To remove predictors that are not statistically significant, a formal t-test is used. The t-test tests the following null hypothesis H_0 against the alternative hypothesis H_a

$$H_0 : \ \beta_j = 0 \, \text{(predictor is not significant)}$$

$$H_a : \ \beta_j \neq 0 \, \text{(predictor is significant).}$$

For each predictor, the P-value of the t-test is calculated. The P-value is the smallest probability of a type I error (mistakenly concluding H_a) for which H_a is still concluded that means it is the probability that an as significant identified predictor is actually insignificant. A stepwise backward elimination procedure is used to remove insignificant predictors by eliminating the predictor with the highest P-value and refitting the reduced model. This procedure is repeated until the P-value for all predictors is smaller than 0.01. The predictors that remain in the model are therefore significant with a probability of 99% . The procedure is applied to all 10 regression models in the same manner.

4.5.4 Results

The results of the 10 regression models are summarized in Figure 4-22. The bars indicate the amount of the specific noise for finger A and finger B. Every predictor that was found to be significant in at least one of the 10 regression models is included. The diagrams of the noise floor, the 60, 120, and 180 Hz noise have two y-axes. The right axis shows the amplitude of the respective type of noise. The left axis quantifies the equivalent standard deviation of the specific noise type. This allows assessing how much each noise type contributes to the total standard deviation. The calculations of the equivalent standard deviations are explained in the following paragraphs. It should be noted though that the standard deviations of the different noise types cannot be added arithmetically to yield the overall standard deviation.

The 60, 120, and 180 Hz noise are mathematically described by a sinusoid. A sinusoid X with amplitude A_0, frequency f, phase angle θ at time t_0

$$X = A_0 \sin(2\pi f_0 t_0 + \theta) \tag{4.24}$$

can be regarded as a random variable if θ is assumed to be a random variable. If θ is uniformly distributed over the interval $[0, \pi]$, then the probability density function of X is given by [Bendat, Piersol 1993]

$$p(X = x) = \begin{cases} \dfrac{1}{\pi\sqrt{A_0{}^2 - x}} & \text{if } |x| < A_0 \\ 0 & \text{if } |x| \geq A_0 \end{cases} \tag{4.25}$$

and the standard deviation is

$$\sigma = \frac{A_0}{\sqrt{2}}. \tag{4.26}$$

The standard deviation of the noise floor can be obtained if the noise floor is regarded as a sum of independent sinusoids as defined in (4.24) with the common amplitude A_0 but different frequencies. With a sampling frequency of 2 kHz, the bandwidth B of the signal is 1 kHz and the frequency resolution Δf is 1 Hz. Knowing the standard deviation from equation (4.26), the standard deviation for the noise floor with bandwidth B becomes

$$\sigma_{Sum} = \sqrt{\sum_{i=1}^{B/\Delta f} \sigma^2} = \sqrt{\frac{B}{2\Delta f}}\,\sigma. \tag{4.27}$$

Observing the plots, it can be easily seen that the largest share of the noise is produced in the gage head with the noise for finger A being more than twice as high as for finger B. The second largest contributor to the total noise budget is the DAQ card. Its noise can be mainly attributed to the dither inherent in the analog-to-digital converter (ADC) and the PGIA of the card which cause the least significant bit (LSB) to fluctuate between two values. Modeling the dither as a discrete random variable X with two

equally likely values x_0 and $x_0 + 1$, the expected value and the standard deviation of X are given by

$$\mu = E[X] = (x_0 + 0.5) \tag{4.28}$$

$$\sigma = 0.5\,. \tag{4.29}$$

Expressed in nanometers, this results in a standard deviation of 1.408 nm for finger A and 1.479 nm for finger B. In the experiments, the measured standard deviation for finger A and B were 1.863 nm and 1.942 nm, respectively, which is slightly higher than the dither alone.

While the gage head and the DAQ card account for the majority of the noise, to a small extend the filter cable, the signal conditioning card, and the signal conditioning card cable also contribute to the noise. In addition to these components, three interactions between components and external disturbances were found to have a significant effect on the overall noise. The signal conditioning card is affected by both the roll motor and the hydraulic unit. The interference may be due to ground currents in common impedances. An increase of the noise floor was recognized when the measuring system was exposed to these two disturbances while the amplitudes of the power frequencies showed no or only a very little increase. An important result is that no susceptibility of the signal conditioning card to magnetic fields could be detected. This indicates that the shielding of the card seems to be sufficient. Interferences were also found between the roll motor and the gage cable. The power cable of the roll motor and the gage cable are routed next to each other for a certain distance. The interference may stem from magnetic fields coupling on the gage cable.

For some disturbances, it can be observed that certain noise types decrease when the measurement system is exposed to them. For example, the 120 Hz noise in the gage head decreases slightly when the roll motor is turned on. However, despite this decrease, a reduction in the overall noise cannot be observed. In general, harmonic noise at certain frequencies does not necessarily affect the standard deviation of the overall noise. One example for this is the interaction between magnetic fields and the gage head. In presence of this disturbance, the amplitude of the 180 Hz frequency increases by 6 nm and the standard deviation of the corresponding sinusoid by itself is 4 nm while the overall standard deviation is not affected. A potential explanation is that the 180 Hz noise is highly correlated to the 60 and 120 Hz noise so that it does not influence the overall variability.

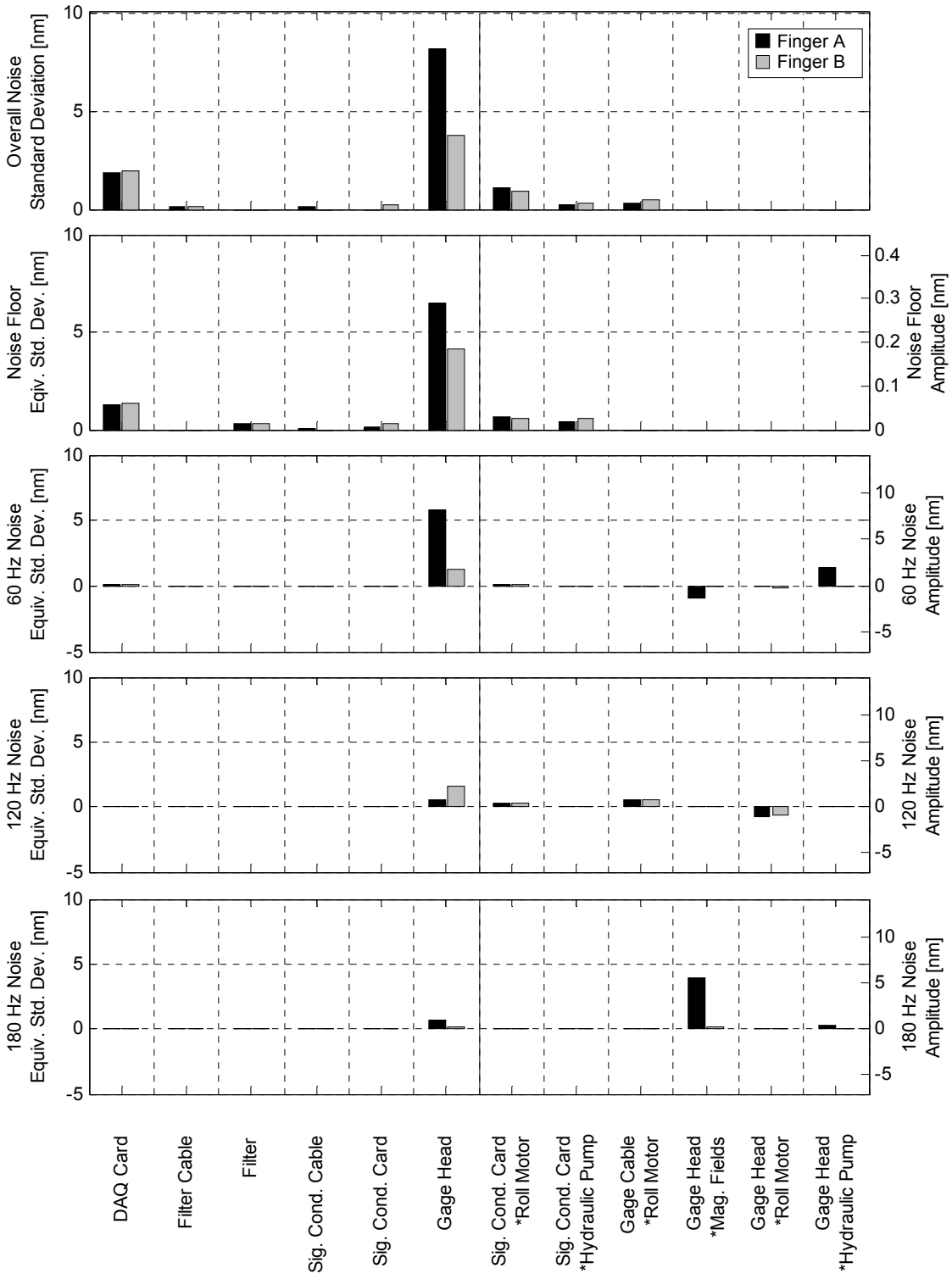

Figure 4-22: Noise budget of the measurement system

CHAPTER 5 – EXPERIMENTAL RESULTS

5.1 Measurement with the Roundness Machine

Before measurements are taken with the post-process machine, a benchmark for the measurements has to be established. For this purpose, a sample of test parts is selected and measured on a manually operated roundness measuring machine. For the remainder of this dissertation these measurements will be used as the reference measurements.

5.1.1 Methodology

The machine used for the reference measurements is a Rondcom 30C desktop roundness measuring machine made by Carl Zeiss/Tokyo Seimitsu (Figure 5-1). It is a table rotating type machine opposite to a transducer rotating machine. The table is supported by a high-precision air bearing to provide high rotational accuracy.

Figure 5-1: Roundness machine used for the reference measurements

The machine is installed in a temperature controlled metrology lab and is certified for an accuracy of 50 nm or better. The transducer readout is transmitted to a standard PC which allows saving the raw data to a file.

As a sample for the measurements, 138 test parts were chosen. The parts were selected so that approximately one third of the parts exhibit waviness with even UPR, one third waviness with odd UPR, and one third are considered to be free of defects. On the sidewalls, every part was engraved with a number for identification. In addition to that, one sidewall was marked so that the two different part orientations can be distinguished.

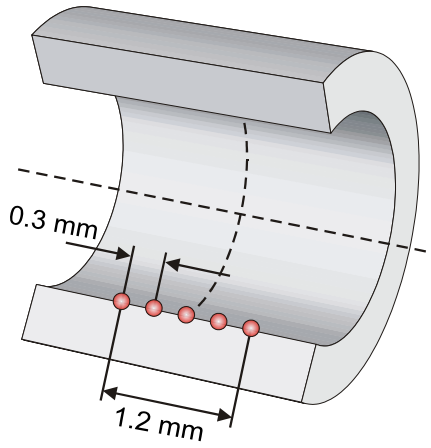

Figure 5-2: Measurement positions on the workpiece

To set the axial position for the measurement, a reference part was machined with a narrow groove in the dead center. The probe of the roundness machine was positioned so that the probe stylus hits the center groove. This reference part was also used to position the probe of the post-process machine. During pretests it was found that the measured profile can depend to a certain degree on the axial measurement position. Since even with the reference part, the exact measuring position of the roundness machine

stylus cannot be found with the post-process machine, is has to be ensured that measurements between the roundness machine and the post-process machine remain comparable. Therefore, five measurements per part at slightly different axial positions were taken with the roundness machine. The positions are spaced by 0.3 mm and are axially centered covering a total distance of 1.2 mm (Figure 5-2). The positions were stored in the memory of the roundness machine so that the probe stylus could automatically be positioned at the predefined locations.

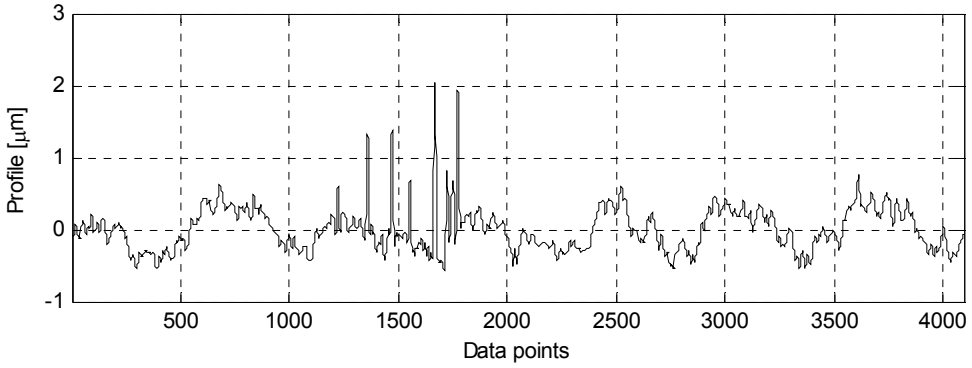

Figure 5-3: Profile of a part with contamination

All test parts were cleaned with alcohol to remove particles from the measured surface since any contaminations produces highly unrepeatable results. Despite careful cleaning, some parts displayed peaks in the profile as shown in Figure 5-3, indicating contamination of the surface. If this occurred, the part was cleaned again and the measurements were repeated. If the peaks persisted, the part was dropped from the sample set. A total of 12 parts were removed for this reason, so that the final sample set consisted of 126 parts, resulting in 630 measurements.

5.1.2 Results

The spectrum of a part with strong waviness is displayed in Figure 5-4 as an example. A high peak can be observed at the 32 UPR frequency. In addition to the fundamental frequency, the spectrum also shows peaks at higher order harmonics of the fundamental frequency which can be observed at 64, 96, 128 and 160 UPR. This is typical for parts that exhibit waviness with a high amplitude.

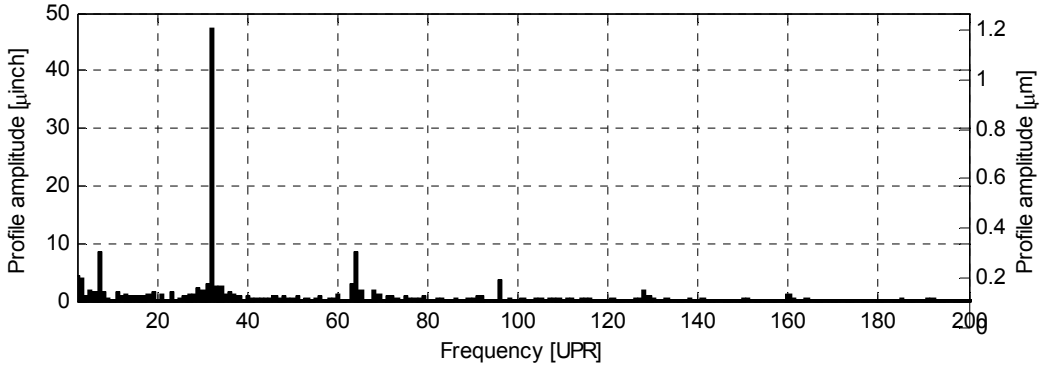

Figure 5-4: Spectrum of a sample part measured on the roundness machine

The distribution of the profile height as defined in section 3.5.2 for the 126 sample parts is displayed in Figure 5-5. The histogram shows the average profile height $\overline{h}_R(n)$ from the five measurements for each part *n*

$$\overline{h}_R(n) = \sum_{m=1}^{5} h_R(n,m), \quad n = 1,2,...,126, \tag{5.1}$$

where $h_R(n,m)$ is the profile height for the *m*-th measurement of the *n*-th part measured on the roundness machine. The bin size of the histogram is 0.254 µm (10 µinch). The lowest average profile height of the parts in the test sample was 0.46 µm (18.1 µinch) and

the highest 3.71 µm (146.1 µinch) while most parts had an average profile height between 0.51 and 2.03 µm (20 and 80 µinch). For the further analysis, the average profile height $\overline{h}_R(n)$ is used as the reference value for the profile height of each part.

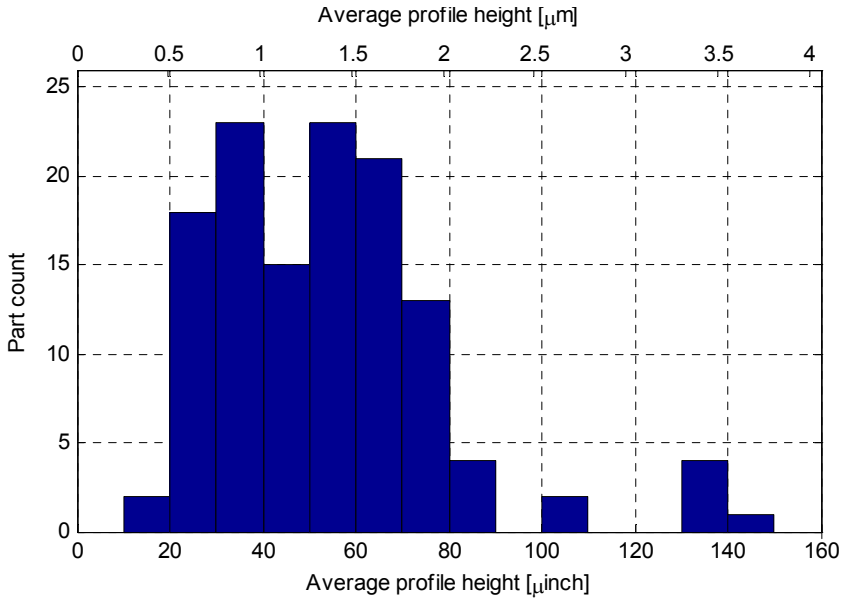

Figure 5-5: Distribution of the average profile height on the roundness machine

The classification of the sample parts according to the allowable profile height is listed in Table 5-1. The classification takes differences in the five measurements per part into account. Since the five measurements of a part may yield contradictory results, three categories are established as an outcome: "good" in all five measurements, "bad" in all five measurements, or "good" in at least one measurement and "bad" in at least one measurement. Table 5-1 shows that 27 % of the parts fall into the last category.

Table 5-1: Classification of parts obtained from the roundness machine

Roundness Machine		
Classification	Quantity	Percentage
Good	44	(35%)
Good/bad	34	(27%)
Bad	48	(38%)
Sum	126	(100%)

The variability of the measurements can be assessed from Figure 5-6 and Figure 5-7. Figure 5-6 shows the profile height error Δh_R of each measurement. Δh_R is defined as the deviation of the profile height from the average profile height, i.e.

$$\Delta h_R(n,m) = h_R(n,m) - \overline{h}_R(n),\ n = 1,2,...,126,\ m = 1,2,...,5. \tag{5.2}$$

The sample standard deviation of Δh_R is 0.176 μm (6.943 μinch) and the sample mean is 0 by definition of the profile height error. In Figure 5-7 the relative profile height error $\Delta h_{R,rel}$ given by

$$\Delta h_{R,rel}(n,m) = \frac{h_R(n,m) - \overline{h}_R(n)}{\overline{h}_R(n)},\ n = 1,2,...,126,\ m = 1,2,...,5, \tag{5.3}$$

is plotted. It can be seen that while for most measurements the relative error is within ±10 %, for a few measurements a relative error exceeding ±40 % was found. The variation observed in the plots is the result of two effects. The first effect is the limited precision of the roundness machine. The second effect is the different axial positions at which measurements were taken, which is assumed to contribute to a far greater extent to the total variation than the limited precision of the roundness machine.

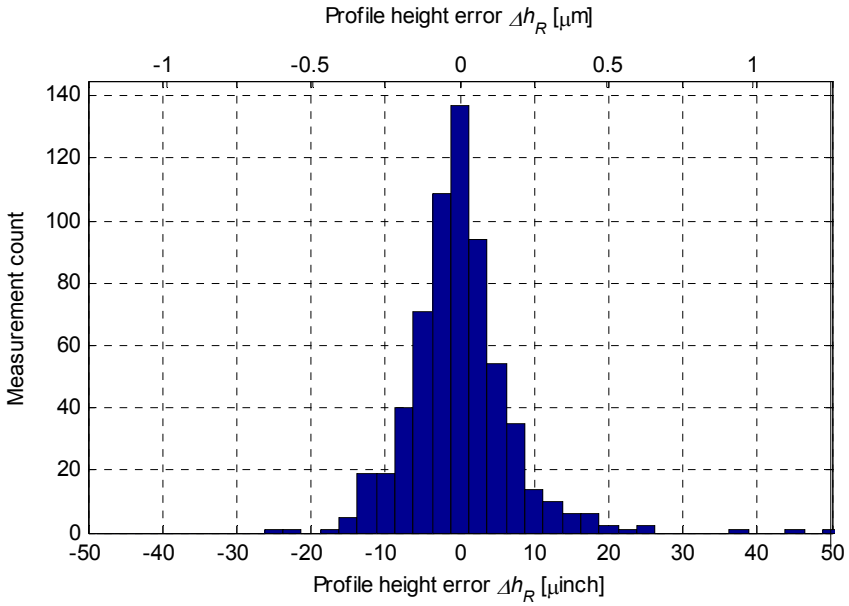

Figure 5-6: Distribution of the profile height error on the roundness machine

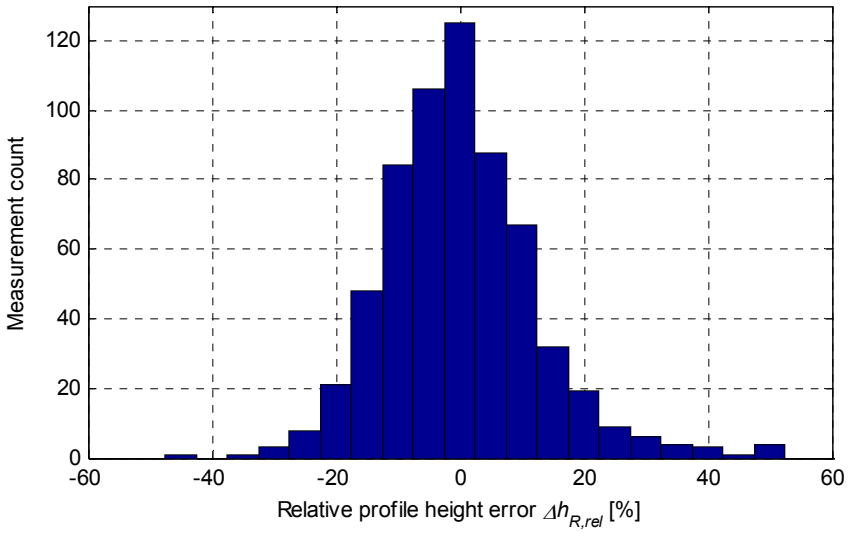

Figure 5-7: Distribution of the relative profile height error on the roundness machine

5.2 Measurement with the Post-Process Machine at Low Speed

5.2.1 Methodology

To set up the post-process machine for measurement, the gage fingers were first aligned with the part. The axial position (*z*-position) was adjusted using the reference part with the center groove. The vertical position (*y*-position) was set so that the connecting line between the two fingers passes through the workpiece center. The gage head was swiveled and the fingers were positioned using the built-in motor, so that the initial displacement of the fingers was in the middle of the measurement range.

The parts were cleaned before the measurements following the same procedure as for the roundness machine. During the measurement with the post-process machine however, all 126 parts were used and no additional parts were removed from the sample set. It was found experimentally that the gage head has its national frequency around 240 Hz. The parts were therefore rotated at a rotational speed of 0.9 rev/s (54 RPM) to ensure that the 250 UPR harmonic remains below the natural frequency. For this part speed, the cutoff frequency of the anti-aliasing filter was set to 400 Hz. Every part was measured for 10 revolutions. For the comparison with the roundness machine, only the first revolution was used. The additional revolutions were measured to have extra data for analysis in the later chapters.

After the 126 parts were loaded into the machine and were measured, the procedure was repeated and a second measurement series was taken. The second measurement series was taken on a different day to include the potential effect of

environmental factors on the measurements. For the comparison with the roundness machine, the average of the profile heights obtained from the two fingers is used.

5.2.2 Results

As an example, the spectrum measured with the post-process machine of the part from Figure 5-4 is depicted in Figure 5-8. Visual comparisons of the spectra measured with the two machines shows good agreement. The post-process machine measured the amplitude of the 32 UPR frequency correctly and also detected higher order harmonics. The smaller peaks at the 64, 96 and 128 UPR frequency can be clearly seen. In addition, very small peaks can be recognized at 160 and 196 UPR as well. This indicates that the post-process machine is capable of measuring waviness at least up to 128 UPR and possibly to 196 UPR or higher. Since none of the test parts exhibited waviness with a high amplitude at these frequencies, reliable statements about the measurement capability at frequencies of 200 UPR or higher could not be made.

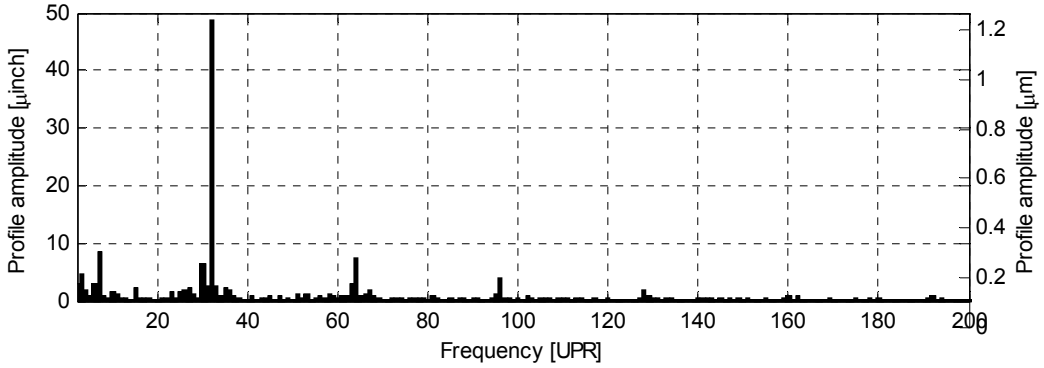

Figure 5-8: Spectrum of the sample part measured on the post-process machine

The distribution of the profile heights $h_P(n,m)$ of the m-th measurement ($m=1,2$) of the n-th part ($n=1,2,...,126$) measured with the post-process machine is shown in Figure 5-9. The histogram uses the same bin size as Figure 5-5 for better comparison. Opposite to the roundness machine, no part was measured with a profile height of less than 0.51 µm (20 µinch) and only very few parts were measured between 0.51 µm and 1.01 µm (20 and 30 µinch).

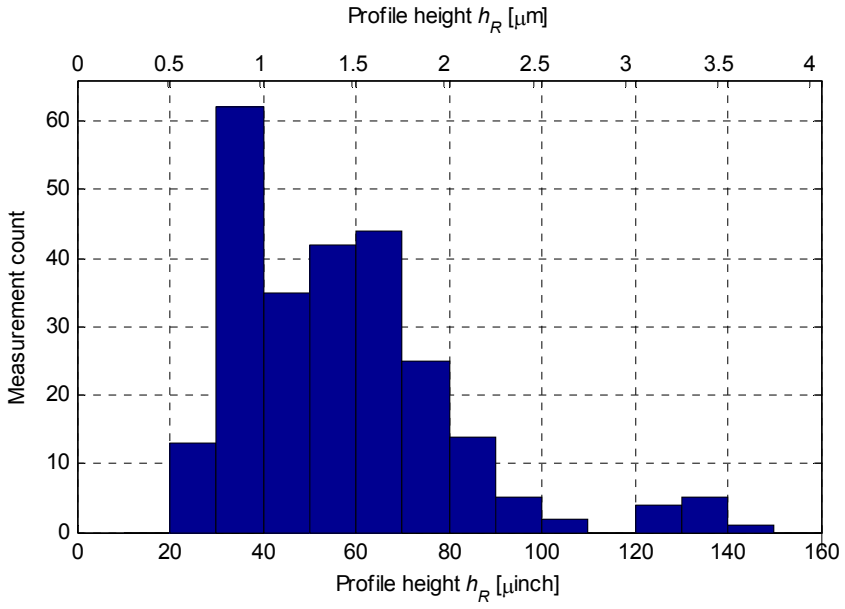

Figure 5-9: Distribution of the profile height of the post-process machine

Table 5-2 gives evidence about the capabilities of the post-process machine to identify bad parts. The table shows how the parts in the three groups ("good," "good/bad," and "bad" on the roundness machine) were measured on the post-process machine. Of the 48 "bad" parts from the roundness machine, all parts were also measured as "bad" in both measurements with the post-process machine. Thus, the post-process

machine did not let as single bad parts pass. On the other hand, of the 44 "good" parts from the roundness machine all except one were also measured as "good." The one part that was measured "bad" was consistently measured as "bad" in both measurements. For the parts that yielded inconsistent results on the roundness machine, i.e. which fell into the "good/bad" category, the post-process machine is more likely to detect them as "bad."

Table 5-2: Classification of the parts obtained from the post-process machine

Roundness Machine		Post-process machine		
		Good	Good/Bad	Bad
Classification	Quantity	Quantity	Quantity	Quantity
Good	44 (100%)	43 (97.7%)	0 (0.0%)	1 (2.3%)
Good/bad	34 (100%)	10 (29.4%)	4 (11.8%)	20 (58.8%)
Bad	48 (100%)	0 (0.0%)	0 (0.0%)	48 (100%)

Defining a null hypothesis and alternative hypothesis as follows

$$H_0: \text{the part is good} \tag{5.4}$$

$$H_a: \text{the part is bad,} \tag{5.5}$$

measuring a "good" part as "bad" constitutes a type 1 error (overpicking) and measuring a "bad" part as "good" represents a type 2 error (underpicking). For the given measurements, a type 1 error occurred for one part whereas a type 2 error never occurred. As a summary, it can be stated that the post-process machine does not miss bad parts but tends towards a type 1 error, i.e. has a slight tendency to detect good parts as bad.

The profile of the "good" part that was mistakenly detected as bad in both measurements on the post-process machine is plotted in Figure 5-10. The plots show the

profiles measured by finger A and finger B for two complete part revolutions. The solid line at 1930 data points marks the end of the first revolution. The profile show peaks at 1420 data points and at 3350 data points. From the fact that they occur at the same time at finger A and B but in opposite directions, it can be concluded that a rigid body motion of the part in the measurement direction took place. The direction of the peaks indicates that the part moved away from the fixed shoe by a distance of approximately 1 μm. Since the peak repeated itself after exactly one revolution later, the rigid body motion is attributed to a defect in the outer diameter (OD) of the part. Due to the centerless fixture of the post-process machine, this defect affects the measurement of the inner bore.

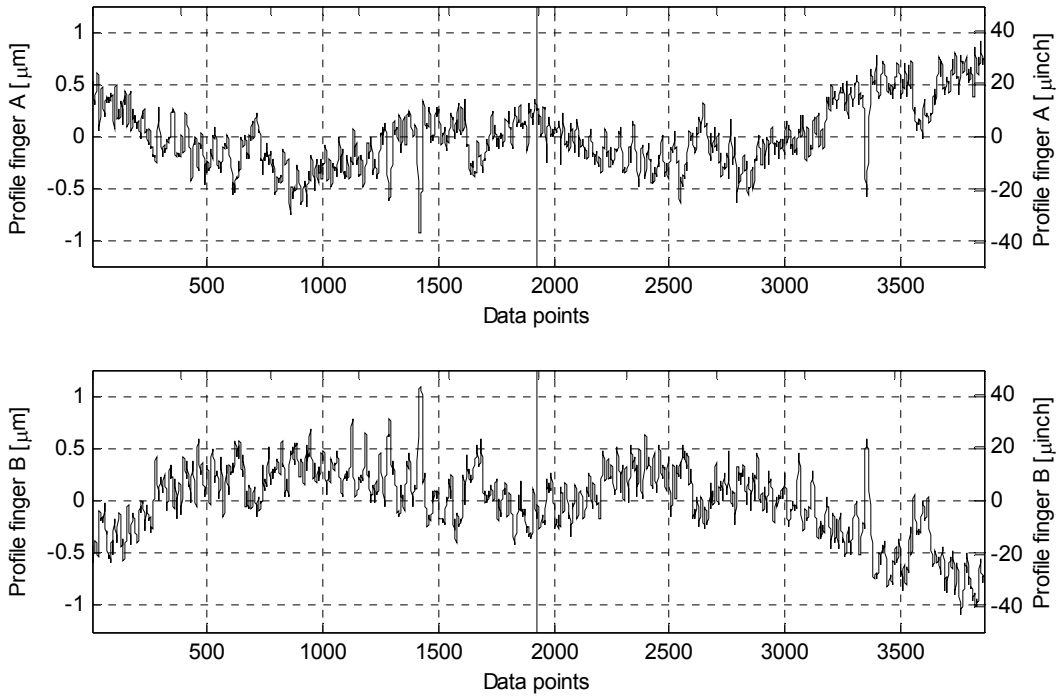

Figure 5-10: Profiles of the good part mistakenly detected as bad

Figure 5-11 and Figure 5-12 shows the variation of the error Δh_P and the relative error $\Delta h_{P,rel}$ of the profile height measured with the post-process machine. The error Δh_P is defined as the deviation of the profile height from the average profile height on the roundness machine

$$\Delta h_P(n,m) = h_P(n,m) - \overline{h}_R(n),\ n = 1,2,...,126,\ m = 1,2, \tag{5.6}$$

and the relative error $\Delta h_{P,rel}$ is defined as the relative deviation given by

$$\Delta h_{P,rel}(n,m) = \frac{h_P(n,m) - \overline{h}_R(n)}{\overline{h}_R(n)},\ n = 1,2,...,126,\ m = 1,2. \tag{5.7}$$

In Figure 5-12 it can be seen that the profile height of one part was by 148 % higher than the reference profile height. This part was the previously discussed part with the OD defect.

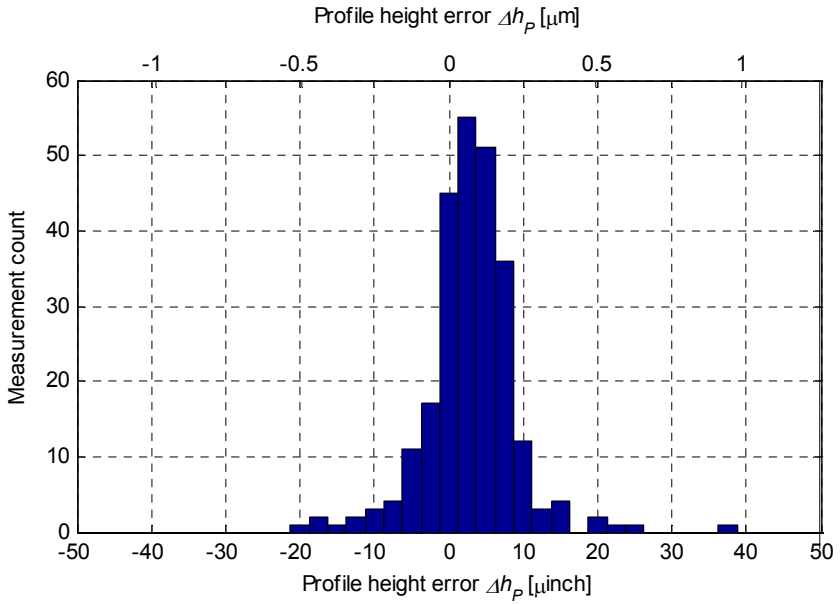

Figure 5-11: Distribution of the profile height error on the post-process machine

Figure 5-11 shows that the variation of the absolute error is not centered at 0. Instead, the distribution has its mean at 0.076 µm (2.979 µinch). This supports the earlier remark that the post-process machine tends to overpick parts and measures a profile height slightly higher than the true value. The standard deviation of the absolute error is 0.156 µm (6.140 µinch). The mean and the standard deviation are listed in Table 5-3 for comparison with the roundness machine. The standard deviation of the error distribution can also be interpreted as a measure of repeatability and the mean can be interpreted as the measurement bias. The terms repeatability and bias are also often referred to as precision and accuracy, respectively.

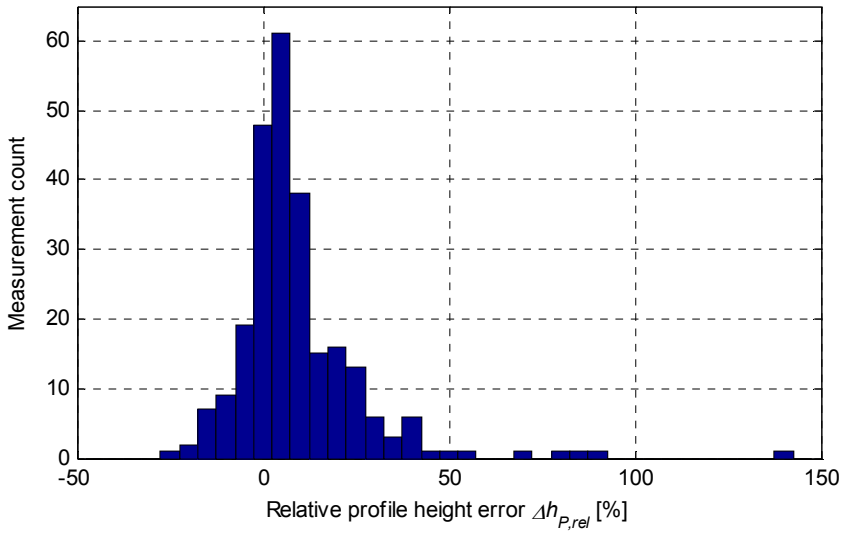

Figure 5-12: Distribution of the relative profile height error on the post-process machine

Comparing the values in Table 5-3, it can be stated that the post-process machine has a similar repeatability as the roundness machine when the measurements are taken at slightly different axial positions over a range of 1.2 mm with the roundness machine. The

profile heights measured with the post-process machine are biased. The reason is noise originating from the different sources outlined in chapter 4.1 that couples onto the true profile and causes the measured profile height to increase.

Table 5-3: Bias and repeatability of the post-process machine

	Profile height error Δh_P			
	Mean / bias		Standard deviation / repeatability	
	nm	(μinch)	nm	(μinch)
Roundness machine	0	(0)	176	(6.943)
Post-process machine	76	(2.979)	156	(6.140)

Besides the measurement accuracy, the measurement speed is an important criterion for evaluating the performance of the post-process machine. With a part speed of 0.9 rev/s, the measurement of a part for one revolution takes 1.1 s. Retracting the gage head after the measurement, ejecting the measured part, loading a new part, and reinserting the gage head takes approximately 3 s. The time for processing the data and determining the profile height is negligible with a standard PC. This results in a cycle time of 4 s or a throughput of 15 parts per minute. The long time for loading and unloading parts is caused by the low actuation speed of the cylinders and a stroke of the gage head for the insertion/retraction motion that is longer than necessary. With minor technical modifications the loading time can be reduced. In the grinding machine used for production, the loading time is reduced to less than 1 s with the same workpiece fixture. This indicates that cycling times of 2 s or throughputs of 30 parts per minute are achievable with the post-process machine.

With a manually operated roundness machine, the following steps are necessary for the measurement of a part: securing the part in the three-jaw chuck, bringing the probe tip in contact with the part, centering the part in the chuck to prevent probe saturation, starting the rotation and measurement of the part, retracting the probe from the part and removing the part from the three-jaw chuck. The total time for these steps is approximately 3 min.

5.3 Vertical Finger Placement

In section 4.1.3 it was decided to place the fingers horizontally at the 3 o'clock and 9 o'clock position. It was assumed that with this configuration the measurements are less influenced by the roundness error of the lower roll. To verify this assumption, tests were performed with the fingers placed vertically at the 12 o'clock and 6 o'clock position. A test sample of 10 parts was chosen, consisting of five "good" parts and five "bad" parts.

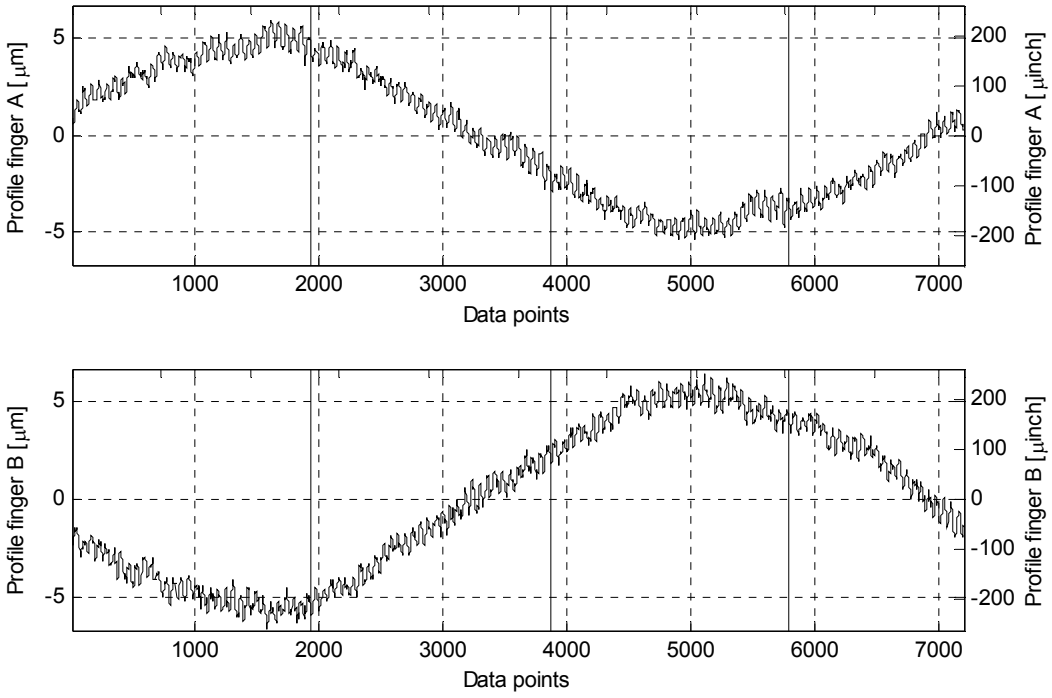

Figure 5-13: Measurement with the fingers placed vertically

The profile plot of a part for finger A and B is shown in Figure 5-13. The part profile is plotted for 7200 data points which is equivalent to one complete revolution of the rolls and 3.73 revolutions of the part. The solid vertical lines mark complete part

revolutions. For comparison, the profile of the same part for horizontally placed fingers is plotted in Figure 5-14. The same scaling of the *y*-axis is used in the plots to visualize the difference.

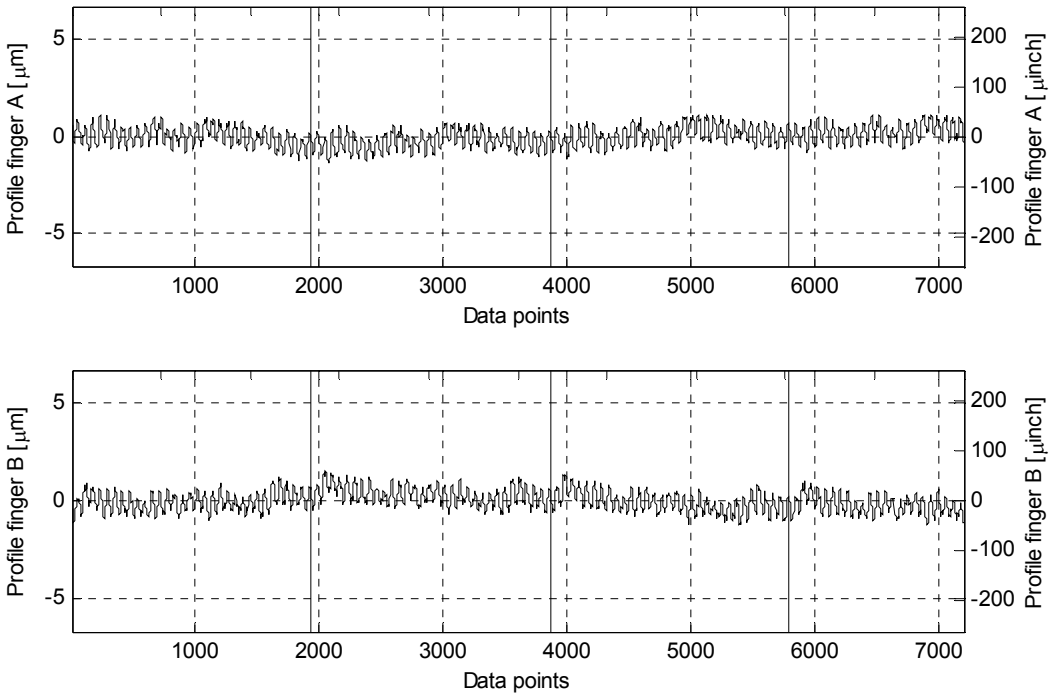

Figure 5-14: Measurement with the fingers placed horizontally

In Figure 5-13, the eccentricity of the lower roll is clear visible. The fact that the two fingers move in the opposite direction indicates that the workpiece center moves during the measurement. On average, the test parts moved 10.0 µm (394 µinch) in the vertical direction.

CHAPTER 6 – ANALYTICAL METHODS

6.1 Overview of Noise Sources

Chapter 4 explored technical methods for accuracy improvement and Chapter 5 presented experimental results based on these methods. In this chapter, the attention is turned to analytical methods to increase the accuracy. While the methods can also be applied to improve the results of the post-process machine, they are targeted at the grinding machine. An overview of the noise sources with the technical methods as they were discussed in section 4.1 is given in Table 6-1. The table is extended by the analytical methods that are developed in this chapter.

Analytical methods are necessary, since the technical modifications proposed in Chapter 4 are infeasible in the grinding machine or the particular noise source is expected to be more severe in a grinding system.

To reduce electrical noise in the grinding machine, simple filtering techniques such as notch filters are used to remove for example multiples of the power frequency from the measurement. Redesigning the circuits of the grinding machine to obtain a low noise measurement system is beyond the scope of this research. The considerations and procedures explained in section 0 for noise reduction in the post-process machine can be used as guidelines to improve the grinding system.

The errors in the sampling of the signal and potential remedies are discussed in section 6.1. A dynamic gage model to compensate the frequency response function of the gage head and to allow higher rotational speeds of the workpiece is presented in section 6.5.

Table 6-1: Overview of technical and analytical improvements

Source	Post-process machine	Grinding machine
All random noise	Averaging over multiple revolutions	
Electrical noise	Shielding, grounding, and cabling techniques	
	Notch filter at multiples of the power frequencies	
Forced vibrations	Low vibration motor drive	
	Vibration isolation system	
	Hydraulic accumulators	
	Flexible hydraulic tubing	
	Separation of workpiece center motion from part profile	
Centerless fixture	Horizontal finger placement	
Gage head	Slow part rotation	
	Gage response compensation	
Signal sampling	Profile length correction	
		High frequency sampling

☐ = technical method ☐ = analytical method

A model for the separation of the workpiece center movement from the part profile is developed in section 6.6. It can help to reduce both the effect of forced vibrations and of the centerless fixture. Section 6.3 introduces and averaging method that combines multiple measurements of the same workpiece into a single measurement reducing random noise. In section 6.4, methods for benchmarking are derived that are more exact than the profile height.

6.2 Sampling Error Compensation

As stated in section 4.1.5, the sampling of the signal is subject to two errors. The first one is the quantization error, which results from the conversion of the continuous signal into one with a limited number of discrete states. This error can be reduced by utilizing the dither of the analog-to-digital converter (ADC) that affects the least significant bit (LSB). Dither is Gaussian white noise that causes the LSB to fluctuate randomly between two states. The expected value of the fluctuation is approximately the true continuous value. By sampling at a high frequency and subsequent low-pass filtering of the digital signal, the quantization error is reduced and the resolution improved [Loewenstein 2000], [National Instruments 2002]. In the grinding machine, the quantization error is higher than in the post-process machine since the measurement range of the gage head is wider. By using a high sampling rate in combination with the 16 bit ADC, it is expected that the quantization error is sufficiently small.

The second error stems from the fact that the angular increments of the workpiece rotation are nonconstant between adjacent samples. In the post-process machine, this is due to the inconsistency between the part revolution and the encoder revolution. In the grinding machine, time based triggering has to be used since no rotary encoder is present. Fluctuations in the roll speed increase this error considerably compared to the post-process machine. The result is a varying number of data points that constitute one complete part revolution. Compensating this error is critical for the correct calculation of the harmonics. In addition, averaging of the profile over multiple revolutions is only possible if the individual revolutions are aligned since otherwise harmonics of the

averaged profile are distorted or can even be cancelled. The following sections discuss potential remedies for the irregular sampling.

6.2.1 Irregular Sampling

Irregular or *nonuniform sampling* distorts the original signal in the time- and frequency domain. The type of the distortion depends on the nature of the irregularity. Offsetting the sample locations by uniformly distributed jitter smears the peaks in the spectrum. Harmonic modulation of the sampling frequency produces sidebands that are symmetrically placed around their parent peaks and spaced from them by the modulation frequency [Learner et al. 1996]. Figure 6-1 and Figure 6-2 show the spectrum of a simulated profile consisting of a 32 UPR harmonic with an amplitude of 1. The profile was sampled at irregular angular increments $\Delta\theta + \varepsilon_S(n)$, where $\Delta\theta$ is the constant angular increment and $\varepsilon_S(n)$ is the error. In Figure 6-1 the error $\varepsilon_S(n)$ is uniformly distributed on the interval $(0.5\Delta\theta, 1.5\Delta\theta)$. Figure 6-2 shows the spectrum, when $\varepsilon_S(n)$ is deterministic and follows a sinusoid with amplitude $0.1\Delta\theta$ and a frequency of 4 UPR.

The question arises, whether the original signal can be reconstructed from its irregular samples. It is well known that for the case of *regular* or *uniform sampling* at equidistant points, a bandlimited signal $r(\theta)$ can be completely reconstructed from its samples $r(n\Delta\theta)$ if the sampling frequency is above the Nyquist frequency [Whittaker 1935], [Shannon 1949], [Shannon 1998]. A reconstruction formula is given by [Whittaker 1915]

$$r(\theta) = \sum_{n=-\infty}^{\infty} r(n\Delta\theta)\,\mathrm{sinc}\left(\theta/\Delta\theta - n\right), \tag{6.1}$$

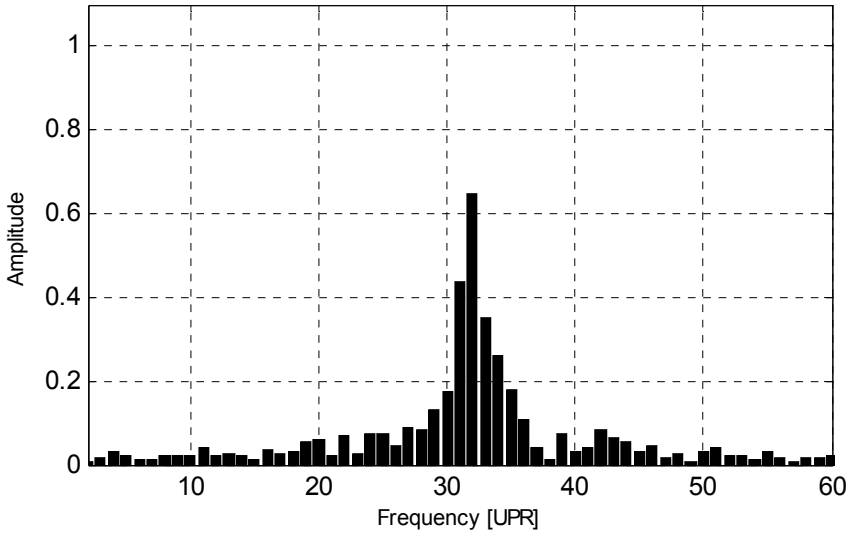

Figure 6-1: Signal sampled with uniform jitter of the sampling locations

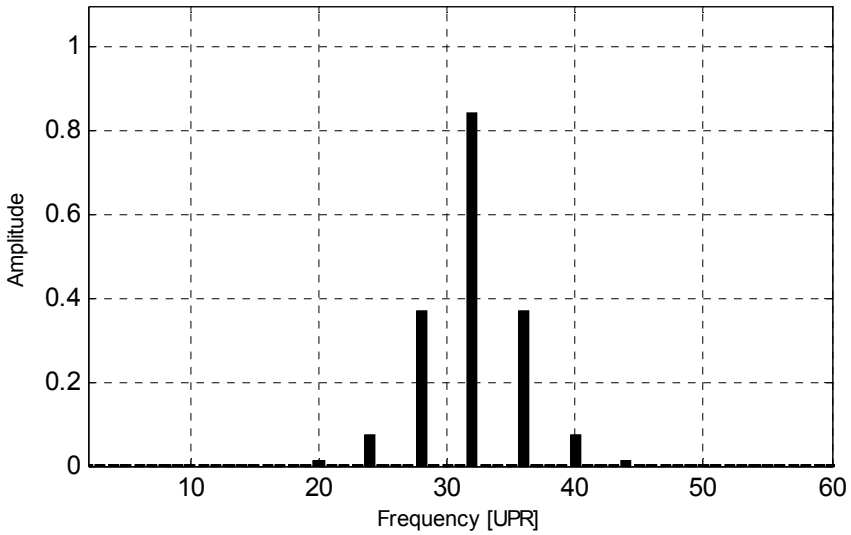

Figure 6-2: Signal sampled with frequency modulation

where

$$\mathrm{sinc}(\theta) = \begin{cases} \dfrac{\sin \pi\theta}{\pi\theta} & \theta \neq 0 \\ 1 & \theta = 0 \end{cases}. \tag{6.2}$$

It can be shown that the sampling theorem even holds for the case of irregular sampling. More specifically, a bandlimited signal $r(\theta)$ can be completely reconstructed from its irregular samples $r(\theta(n))$ as long as the average sampling rate is higher than the Nyquist rate [Beutler 1966], [Beutler 1970], [Marvasti 1993], [Higgins 1996]. The reconstruction method given by equation (6.1) however, no longer holds.

For signal reconstruction, two different cases of irregular sampling are distinguished, one in which the sampling is irregular but the sampling locations are known and one where sampling locations are irregular and unknown. In case of known sampling locations, several methods exist such as iterative methods [Marvasti et al. 1991], [Marvasti 1996], [Feichtinger 1995] low-pass filtering of an oversampled signal with regular resampling [Brault 1996], [Palchetti, Lastrucci 2001], interpolation methods [Rawn 1989], and mapping of an irregularly sampled function into a regularly sampled function [Papoulis 1966].

For the sampling of the workpiece profile, the sampling locations are unknown and therefore the above mentioned methods are not applicable. In case of unknown sampling locations, the solution of the problem becomes less tangible. A special case of the problem, where the sampling error occurs only as integer multiples of a small increment is discussed in Marzilliano and Vetterli [1999, 2000]. The problem is treated as an optimization problem. Three different methods are used to find the minimum: an exhaustive method, which tests all possible permutations of the sample locations, and two iterative descent methods, the random search method and the cyclic coordinate method [Bazaraa et al. 1993]. A variation of the solution algorithm utilizing evolutionary programming is presented by Kalluri et al. [2001]. The more general case of a continuous

sampling error is treated in Tian [2004]. Again, the solution is found by employing evolutionary algorithms. All of the proposed solution methods are computationally intensive. The exhaustive search method may even be infeasible for larger data sets. The optimization methods have the disadvantage that they may converge to a local minimum and therefore may not find the optimal solution.

For the application discussed here, it is critical that the reconstruction method is computationally efficient and yields a reliable solution. Therefore, a different approach than the ones explained above is chosen to solve the problem. Instead of adjusting the location of every single sample, the number of samples is estimated that constitutes one complete part revolution. With this information, the profile can be resampled to a certain fixed number of equidistant data points. This approach can be implemented significantly more efficient than the above discussed reconstruction methods. As long as workpiece slipping between the rolls is prevented, the expected deviation in the individual sampling locations is assumed to be small compared to the length of the profile. In this case, it is expected that the chosen approach reduces the error due to irregular sampling sufficiently.

6.2.2 Overview of Period Estimation Methods

Determining the exact beginning and end of one complete part revolution can be accomplished by acquiring data for more than one revolution and searching for the reoccurrence of the profile in the data stream. The reoccurrence is detected by calculating a suitable metric for the similarity between the beginning of the signal and parts of the signal delayed by certain numbers of data points. The task can therefore also be regarded as the estimation of the signal period. Due to noise superimposed on the true profile, the signal never exactly repeats itself which hinders exact period estimation.

The problem of comparing different parts of a signal and estimating their similarity arises in many different fields of science and engineering. One of the areas that has received most attention is speech recognition [Sondhi 1968], [Rabiner et al. 1976], [Rabiner 1978], [Furui 2001]. To detect vowels and consonants in human speech and to identify speakers, the pitch period of the speech has to be determined. Interactions between the vocal tract and the glottal excitation adversely affect the period estimation. Another application is the velocity measurement of rail-guided vehicles [Fritsche, Mesch 1973], [Zimmer et al. 1976], [Massen 1983], [Bohmann et al. 1984], [Salt et al. 1993]. Two optical sensors on the vehicle measure the reflected light from the rails at slightly different positions. The reflected light is random, but the same for both sensors except for a small time delay proportional to the distance between the sensors. Estimation of the time delay allows computation of the vehicle speed. In medicine, applications are the detection of the fetal heart rate [Park et al. 1992], [Lee 1998] or time delay estimation in ultrasound signal processing [Viola, Walker 2003]. Another application is the scene matching for missile guidance systems [During 1997].

The available methods for period and delay estimation can be roughly categorized into three groups [Rabiner et al. 1976]: time-domain methods, frequency-domain methods, and hybrid-methods which utilize both time- and frequency-domain properties of the data. The most common time-domain methods are correlation methods. One correlation estimator is the *direct correlation function* (DCF) [Gabriel 1983], [Jacovitti, Scarano 1993]. For two signals $x_1(k)$ and $x_2(k)$, the direct correlation function $\hat{R}_{DCF}$ is given by

$$\hat{R}_{DCF}(n) = \frac{1}{N_W}\sum_{k=1}^{N_W} x_1(k)x_2(k+n)\,, \tag{6.3}$$

where n is the delay and N_W the window size in data points. Large positive values of $\hat{R}_{DCF}$ suggest a high agreement between two compared signals. The direct correlation function can be normalized to the interval [–1,1] by

$$\hat{R}_{NDCF}(n) = \frac{\sum_{k=1}^{N_W} x_1(k)x_2(k+n)}{\sqrt{\sum_{k=1}^{N_W}\left(x_1(k)\right)^2\sum_{k=1}^{N_W}\left(x_2(k)\right)^2}}. \tag{6.4}$$

Variations of the direct correlation estimator are the *hybrid-sign estimator* $\hat{R}_{HS}$ [Hertz 1982]

$$\hat{R}_{HS}(n) = \frac{1}{N_W}\sum_{k=1}^{N_W} x_1(k)\,\mathrm{sign}\left(x_2(k+n)\right) \tag{6.5}$$

and the *polarity-coincidence estimator* $\hat{R}_{PC}$ [Jespers et al. 1962], [Wolff et al. 1962]

$$\hat{R}_{PC}(n) = \frac{1}{N_W} \sum_{k=1}^{N_W} \operatorname{sign}\left(x_1(k)\right) \operatorname{sign}\left(x_2(k+n)\right), \tag{6.6}$$

where the sign function is given by

$$\operatorname{sign}(x) = \begin{cases} -1 & \text{for } x < 0 \\ 0 & \text{for } x = 0 \\ 1 & \text{for } x > 0 \end{cases}. \tag{6.7}$$

The advantage of the hybrid-sign and polarity coincidence estimator over the direct correlation function is the higher computational efficiency and the easy implementation as digital circuits. However, the two alternative methods, especially the polarity-coincidence method, have the disadvantage of a larger variance [Fertner, Sjölund 1986]. In the simulations performed by Gabriel [1983], the two methods required three to four times the number of samples to achieve the same variance as the direct correlation method. In certain cases, efficient computational implementations can calculate the direct correlation with slightly more than half of the multiplications required for equation (6.3) [Blankinship 1974].

A method that is based on additions instead of multiplications is the *average magnitude difference function* (AMDF) [Ross et al. 1974], [Un, Yang 1977]

$$\hat{R}_{AMDF}(n) = \frac{1}{N_W} \sum_{k=1}^{N_W} \left| x_1(k) - x_2(k+n) \right|. \tag{6.8}$$

Here, low values of $\hat{R}_{AMDF}$ indicate high agreement between the signals. The AMDF is almost as accurate as the direct correlation but requires less computational efforts [Fertner, Sjölund 1986]. A normalized version of the AMDF yielding values between zero and one is given by [Kim et al. 2002]

$$\hat{R}_{NAMDF}(n) = \frac{\sum_{k=1}^{N_W} \left| x_1(k) - x_2(k+n) \right|}{\sum_{k=1}^{N_W} \left| x_1(k) \right| + \left| x_2(k+n) \right|} . \tag{6.9}$$

For the *average square difference function* (ASDF) [Jacovitti, Scarano 1993]

$$\hat{R}_{ASDF}(n) = \frac{1}{N_W} \sum_{k=1}^{N_W} \left(x_1(k) - x_2(k+n) \right)^2 , \tag{6.10}$$

the square of the difference is taken instead of the magnitude. The direct correlation and the AMDF are both independent statistics, where the former indicates good correlation by large positive values and the later by small positive values. Therefore, the peaks of the correlation functions can be sharpened by using the quotient of the direct correlation and the AMDF [Kobayashi, Shimamura 2000], [Shimamura, Kobayashi 2001], [Hasan et al. 2003], [Nazrul et al. 2004]

$$\hat{R}_{DCF,AMDF}(n) = \frac{\hat{R}_{DCF}(n)}{\hat{R}_{AMDF}(n) + \kappa} , \tag{6.11}$$

where κ is a small constant to prevent a singularity if $\hat{R}_{AMDF}$ is zero.

In speech recognition, the performance of the correlation methods is often improved by nonlinear preprocessing of the signal [Rabiner 1977]. The *center clipping* method retains only the portion of the signal that is outside a certain clipping value $+/-k_C$. If the amplitude is within $+/-k_C$, the output of the center clipper is zero [Sondhi 1968]. The output of the *binary clipper* is $+1$, whenever the input signal exceeds a clipping value $+k_C$, the output is -1 whenever the input is below $-k_C$ and the output is zero in all other cases [Dubnowski et al. 1976]. Other methods preprocess the signal in

the frequency domain. The methods are based on the idea that the periodicity of the signal becomes more pronounced if the amplitudes in the spectrum of the periodic signal are normalized to one. The *spectrum flattener* [Sondhi 1968] accomplishes this by passing the signal through a bank of band-pass filters and normalizing the amplitudes for each passband. In addition, the *minimum phase spectrum flattener* synchronizes the phases of the filters to sharpen the peaks of the correlation function even more. Other variations of the correlation method use windows other than a rectangular window such as a Hamming window [Sondhi 1968] or an exponential window [Fette et al. 1980]. Ying et al. [1996] improved the results of the period estimation with a probabilistic approach. Instead of a single period, several candidates for the period estimates are determined and the final period is picked based on a previously determined distribution of period lengths.

Besides correlation functions, other techniques operate on the time-domain data of the signal. The *data reduction method* [Miller 1975], [Rabiner et al. 1976] utilizes the zero crossings of the signal to divide it into *excursion cycles*. Each excursion cycle is characterized by its length, amplitude and energy. The period is determined by recognizing the repetition of excursion cycles based on their features and by taking information about the allowable period length into account. *Parallel processing methods* pass the signal simultaneously through a set of different filters [Gold, Rabiner 1969], [Rabiner et al. 1976], [Prezas et al. 1986]. From each filter output, a period estimate is obtained. By using pattern recognition techniques the final period is picked from the individual estimates.

In speech recognition and earth quake science, methods can be found that work on the frequency-domain data of the signal. In the same manner in which the difference of

time-domain data is calculated with the AMDF, a difference metric can be calculated for the frequency-domain data. The difference can be calculated for all harmonics in the spectrum individually, or for several spectrum bands by using band-pass filter banks [Furui 2001]. With the *cepstrum method* [Noll 1967], [Schafer, Rabiner 1970], [Rabiner et al. 1976], the cepstrum of signal segments is calculated and the location of the highest peak is used as the period length. Charpentier [1986] presented a method based on the phase information of the short-time Fourier spectrum. The fundamental period of the signal can be estimated from the instantaneous frequency distribution, which is the time derivative of the short-time phase spectrum. Schimmel proposed a method called the *phase cross-correlation* [Schimmel 1999], [Schimmel and Paulsen 1997]. The method generates a complex trace by taking the real signal and adding its Hilbert transform as a complex part to it and subsequently normalizes the amplitude to unity. The resulting signals are matched by minimizing the absolute difference between them.

Examples of hybrid period estimation methods are the *simplified inverse filter tracking algorithm* [Markel 1972] and the *spectral equalization LPC method* [Rabiner et al. 1976]. Both methods are specific for speech recognition and therefore not further considered here.

6.2.3 Selection of a Correlation Method

Among the techniques discussed in the previous section, the time-domain correlation methods are the ones with the widest variety of successful applications. Other methods may have proven to be useful for a certain type of signals such as human voice, but may be of very limited use for other type of signals. The correlation methods

therefore seem to be the most promising techniques for profile length estimation. An important requirement is the computational efficiency of the algorithm. The algorithm also has to be able to handle a variety of different profiles. These include profiles of good parts as well as profiles with different types of defects. Methods that require additional parameters like the clipping value for the center clipping method and the binary clipper are avoided since they tend to be less flexible. If their parameters are not chosen carefully, a method can easily become useless [Dubnowski et al. 1976]. The methods that appear to be most suitable for this application are the direct correlation function (DCF)

$$\hat{R}_{DCF}(n) = \frac{1}{N_W} \sum_{k=1}^{N_W} x_1(k) x_2(k+n) \,, \tag{6.12}$$

and the average magnitude difference function (AMDF)

$$\hat{R}_{AMDF}(n) = \frac{1}{N_W} \sum_{k=1}^{N_W} \left| x_1(k) - x_2(k+n) \right| . \tag{6.13}$$

In addition, the ratio of the two, hereafter referred to as the *combined correlation function* (CCF), is considered as well

$$\hat{R}_{DC,AMDF}(n) = \frac{\hat{R}_{DCF}(n)}{\hat{R}_{AMDF}(n) + \kappa} . \tag{6.14}$$

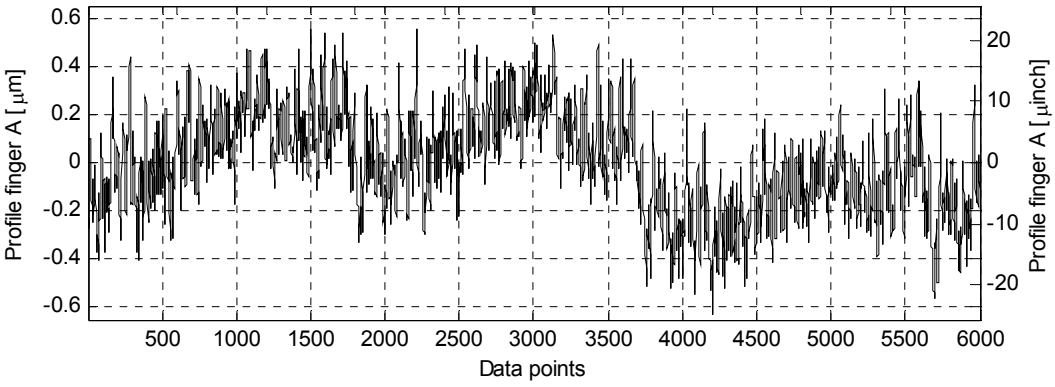

Figure 6-3: Profile of a good part

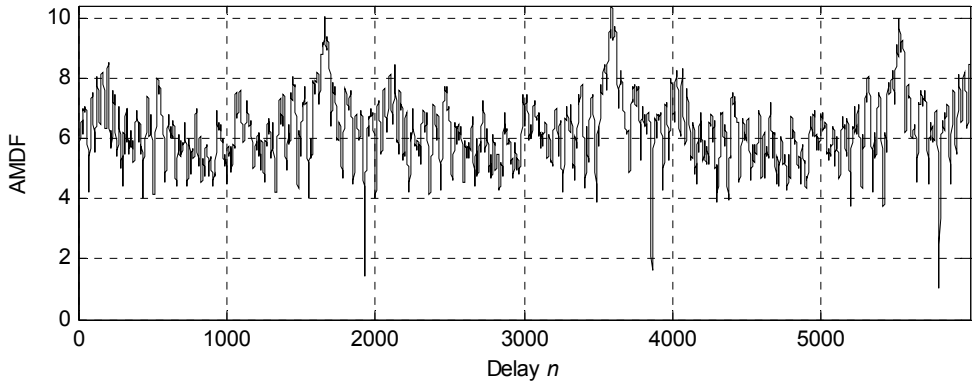

Figure 6-4: Average magnitude difference function for a good part

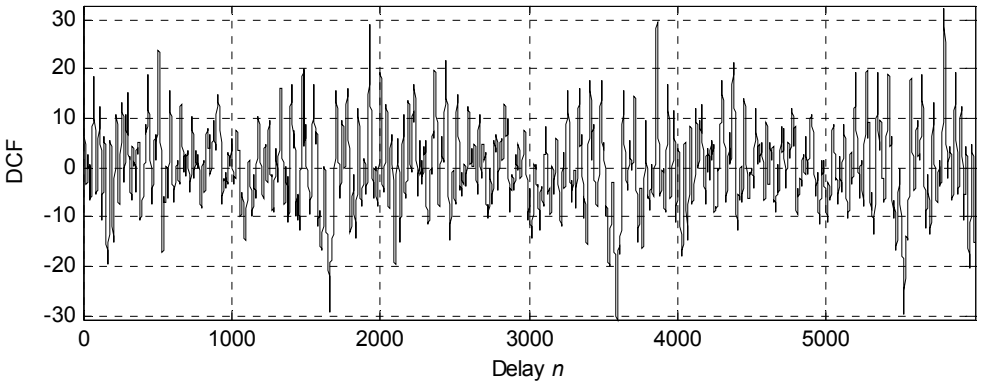

Figure 6-5: Direct correlation function for a good part

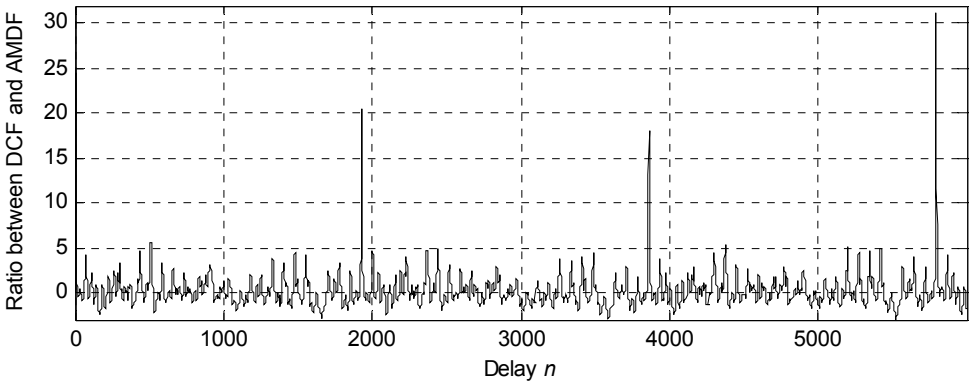

Figure 6-6: Combined correlation function for a good part

In Figure 6-3, the profile of a good part is shown for a length of slightly more than three revolutions. Figure 6-4 to Figure 6-6 show the DCF, the AMDF, and the CCF as a function of the delay n. In equation (6.12) to (6.14), $x_2(k) = x_1(k)$, since the signal is compared to itself. The window size N_W is chosen arbitrarily to be 200 data points which is approximately the first 10 % of the profile. The data sequences $x_1(1)...x_1(N_W)$ and $x_1(n+1)...x_1(n+N_W)$ are normalized to a zero mean before the computation of the correlation. The constant κ is set to 0.1.

The number of data points per revolution is approximately 1930. In the plot of the AMDF, the completion of one revolution is clearly indicated by the minima. It can be observed that at the same location where the AMDF assumes a minimum, the DCF and the CCF assumes a maximum. For all three functions, the minima or maxima corresponding to the completion of a revolution are also the global extrema within the revolution. Therefore, all three methods are suitable with the CCF giving the clearest and the DCF the least clear indication.

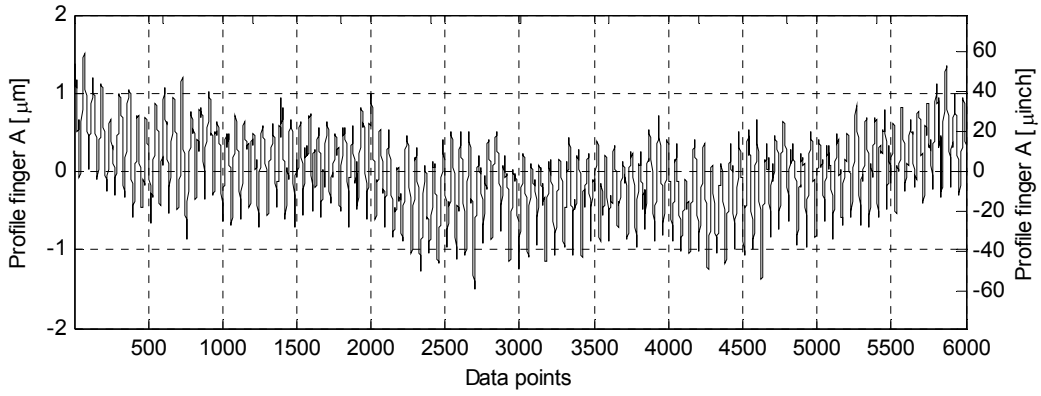

Figure 6-7: Profile of a part with waviness at 32 UPR

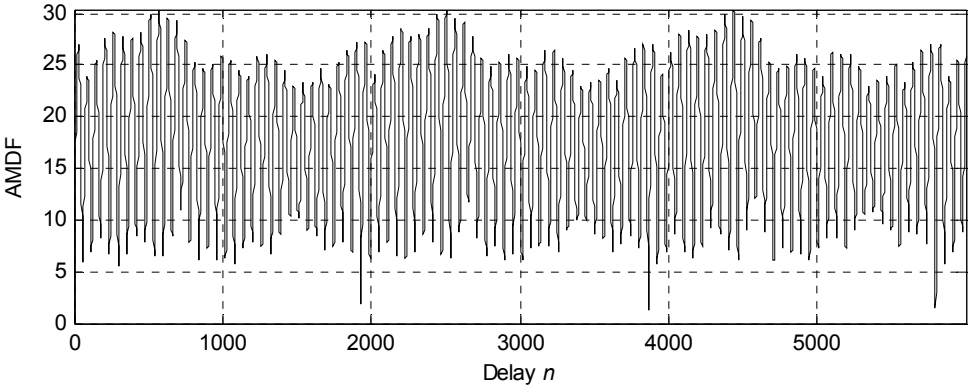

Figure 6-8: Average magnitude difference function for a part with waviness

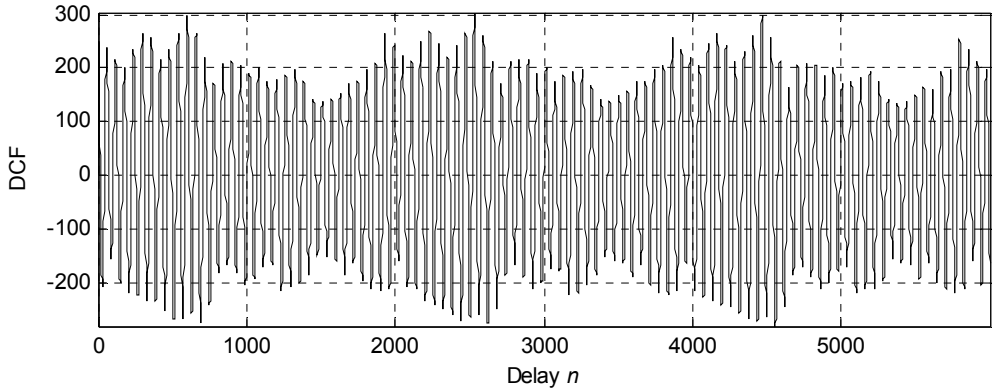

Figure 6-9: Direct correlation function for a part with waviness

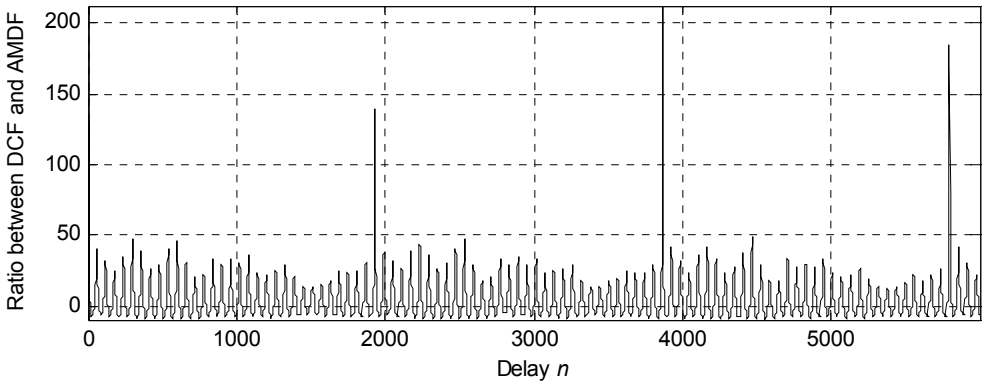

Figure 6-10: Combined correlation function for a part with waviness

The performance of the correlation functions depends highly on the analyzed profile. In Figure 6-7, approximately three revolutions of a part with waviness at 32 UPR are shown. Figure 6-8 to Figure 6-10 show the correlation functions for the part. Due to the existence of a dominant harmonic in the profile, the correlation functions exhibit oscillation at the same frequency as the part profile. In the AMDF and especially the CCF plot, the completion of a revolution can still be easily identified by the global minima and maxima, respectively. The DCF however, yields ambiguous information. The maxima corresponding to the completion of a revolution are not necessarily global maxima within one revolution anymore. Therefore, for the profile analyzed here, only the AMDF and the CCF yield reliable results while the CCF appears to be even more robust than the AMDF.

To obtain a more general comparison, the three correlation functions are applied to the full measurement data acquired with the post-process machine in Chapter 5. All 126 test parts were used, with two measurements per part. For each measurement, the length of the first 10 revolutions was computed. The possible length of the profile was confined to the range 1930 ± 50 data points. It is not expected that the true profile length

is outside this range. Restricting the allowable range to a reasonable interval significantly speeds up the computations and prevents the algorithms from yielding erroneous values.

Assuming that the unknown true profile length and the error of the correlation functions can be regarded as independent random variables, the correlation function with the lowest standard deviation of the estimated profile length should also be the function with the lowest standard deviation of the error. The histograms of the profile length distribution for the three correlation functions are shown in Figure 6-11 to Figure 6-13. The values of the most important distribution statistics are also shown in Table 6-2. The correlation functions yield a similar mean and standard deviation for the number of data points per revolution. While the profile length estimates of the AMDF and the CCF fall into a range of 12 data points, the DCF yields a few estimates that deviate considerably from the average profile length.

The estimates of the DCF cover a range of 98 data points, which is almost the complete range to which the allowable number of data points was confined. This supports the earlier observation that the DCF is not as suitable for profile length estimation as the AMDF and the CCF. The difference between the AMDF and the CCF is so small that both methods can be regarded as equally suitable. In this case, the preference is given to the AMDF since it requires less mathematical operations than the CCF.

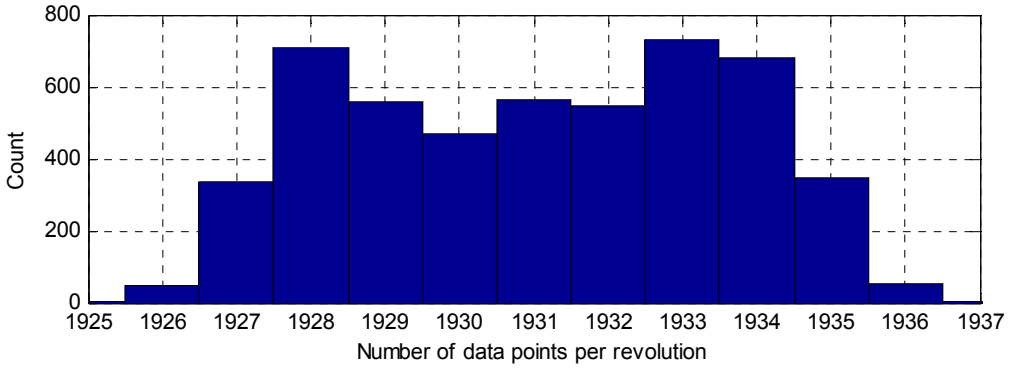

Figure 6-11: Profile length distribution of the average magnitude difference function

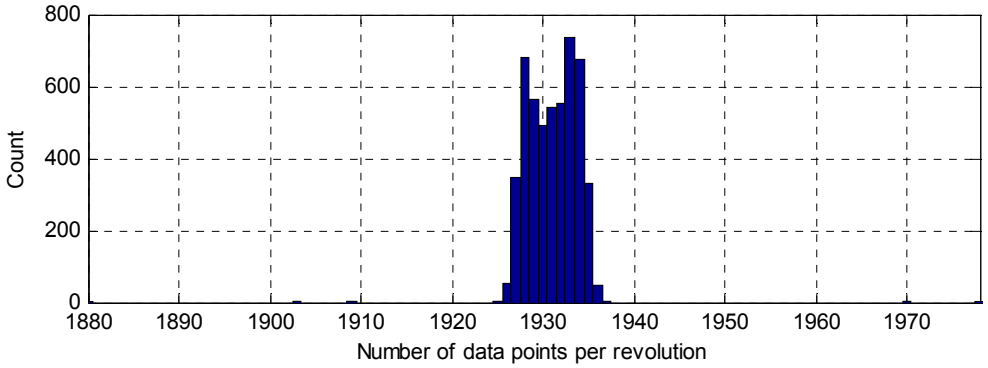

Figure 6-12: Profile length distribution of the direct correlation function

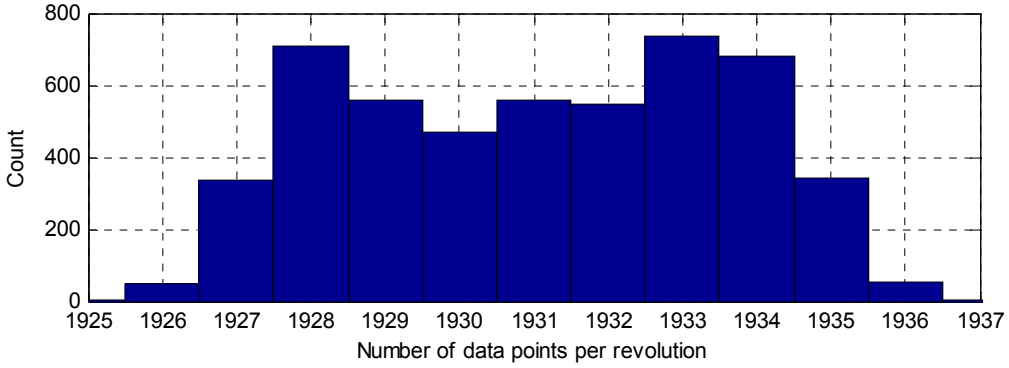

Figure 6-13: Profile length distribution of the combined correlation function

Table 6-2: Distribution of the number of data points per revolution for the correlation methods

Correlation method	Minimum	Maximum	Average	Standard deviation
AMDF	1925	1937	1931.08	2.5291
DCF	1880	1978	1931.06	2.8053
CCF	1925	1937	1931.08	2.5278

Throughout this analysis, the window size N_W was kept at the initially chosen value of 200 data points. It is therefore examined, what influence the variation of the window size has on the profile length estimates. A short window length is desirable since it reduces the number of mathematical operations. However, the accuracy of the estimation should be as high as possible. Again, the standard deviation of the computed profile lengths is used as a performance criterion. Figure 6-14 shows the standard deviation as a function of the window length for the AMDF.

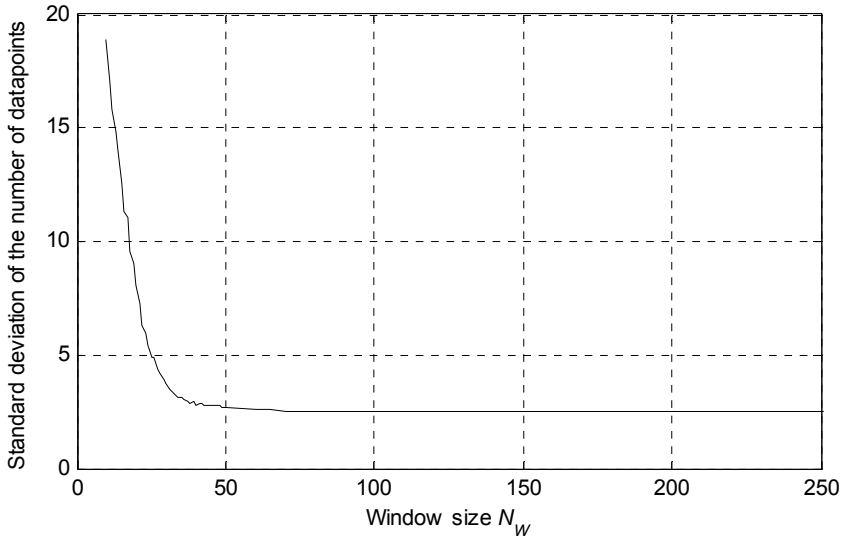

Figure 6-14: Dependence of the standard deviation of the profile length on the window size

The graph shows a steep descent until a window size of 50 is reached. For window sizes above 100 data points, it remains virtually constant. It is therefore sufficient to use a window size of 100 instead of 200.

Once the profile length has been determined, the first revolution is defined as the data point sequence ranging from the center of the fixed window to the center of the shifted window. More specifically, if n_L is the estimated length of the profile, the data that represents the first revolution is the sequence $x_1(N_W/2)...x_1(N_W/2+n_L)$.

6.3 Averaging of Profiles

Averaging multiple measurements of the same part into a single averaged profile reduces the random component of noise and disturbances regardless of the source. It is of importance since it can be applied even when no other technical or analytical method is available to reduce noise from a particular source. Practically, averaging is accomplished by measuring a part continuously for several revolutions. Using the length estimation methods outlined in the previous section, the data stream is divided into the individual revolutions. It has to be stated though that averaging can only be applied if the part geometry does not change during the measurements. This is truly the case for measurements taken with the post-process machine, but not for in-process measurement during the grinding process. For in-process measurement, the method as it is outlined here is not applicable.

A problem arises, since the individual revolutions of the part constitute a full 360° rotation but may comprise different numbers of data points. It is therefore necessary to interpolate the profiles so that the samples of the individual revolutions occur at the same angular positions. A variety of different algorithms exist to interpolate discrete data points. Some of the most common ones are Lagrange interpolation formulas [Davis 1975], cubic splines, or Bezier curves [De Boor 2001]. These algorithms however, are approximation methods, i.e. they induce an error in the interpolated profile. As mentioned in the previous section, the sampling theorem states that a bandlimited signal can be reconstructed without error from its discrete samples by

$$r(\theta) = \sum_{n=-\infty}^{\infty} r(n\Delta\theta)\,\mathrm{sinc}\left(\theta/\Delta\theta - n\right). \tag{6.15}$$

The equation allows evaluating $r(\theta)$ at arbitrary locations and can therefore theoretically be used for error-free resampling of the profile with a different number of data points per revolution. Practically, $r(\theta)$ can only be approximated, since the infinite sum in equation (6.15) has to be truncated for numerical evaluation. Using the fact that $r(\theta)$ is 2π-periodic and some algebra, a special case of (6.15) for periodic functions can be derived [Stark 1979], which is referred to as the *circular sampling theorem* [La Rivière, Pan 1998]. For an odd number N of data points per revolution, it is given by

$$r(\theta) = \sum_{n=0}^{N-1} r(n\Delta\theta)\frac{\sin\left[\frac{N}{2}\left(\theta - n\Delta\theta\right)\right]}{N\sin\left[\frac{1}{2}\left(\theta - n\Delta\theta\right)\right]} \tag{6.16}$$

and for an even number of data points by

$$r(\theta) = \sum_{n=0}^{N-1} r(n\Delta\theta)\frac{\sin\left[\frac{1}{2}\left(N-1\right)\left(\theta - n\Delta\theta\right)\right]}{N\sin\left[\frac{1}{2}\left(\theta - n\Delta\theta\right)\right]}. \tag{6.17}$$

The circular sampling theorem provides an exact representation using a finite summation. A shortcoming is that it is computationally inefficient for large numbers of data points N, since the required number of operations is proportional to N^2. A faster way to interpolate the data points is to use *zero-padding* in the frequency domain. Zero-padding in the time-domain is a well-known method to interpolate the spectrum. Because of the duality property of the Fourier transform, zero-padding in the frequency-domain can be used to

interpolate the time-domain data [Prasad, Satyanarayana 1986], [Brigham 1988]. Let $R_N(k)$, $k = 1,...,N-1$ be the spectrum of the time-domain signal with N data points, then for N odd, the zero-padded spectrum $R_M(k)$, $k = 1,...,M-1$, $M > N$ is given by [Fraser 1989]

$$R_M(k) = \begin{cases} \frac{M}{N} R_N(k) & \text{for} \quad 0 \le k \le \frac{N-1}{2} \\ 0 & \text{for} \quad \frac{N-1}{2} + 1 \le k \le M - \frac{N-1}{2} - 1 \\ \frac{M}{N} R_N(k-M+N) & \text{for} \quad M - \frac{N-1}{2} \le k \le M-1 \end{cases} \tag{6.18}$$

and for N even

$$R_M(k) = \begin{cases} \frac{M}{N} R_N(k) & \text{for} \quad 0 \le k \le \frac{N}{2} - 1 \\ \frac{M}{2N} R_N(k) & \text{for} \quad k = \frac{N}{2} \\ 0 & \text{for} \quad \frac{N}{2} + 1 \le k \le M - \frac{N}{2} - 1, \\ \frac{M}{2N} R_N^*(k-M+N) & \text{for} \quad k = M - \frac{N}{2} \\ \frac{M}{N} R_N(k-M+N) & \text{for} \quad M - \frac{N}{2} + 1 \le k \le M-1 \end{cases} \tag{6.19}$$

where $R_N^*(k)$ is the complex conjugate of $R_N(k)$. Taking the inverse FFT of $R_M(k)$ yields the interpolated time-domain profile. It can be shown that the result is the same as the one obtained with the circular sampling theorem [Cavicchi 1992], [La Rivière, Pan 1998], However, the zero-padding method takes advantage of the efficiency of the FFT. In the literature, several techniques are described to improve the speed even further. FFT pruning algorithms can compute the inverse FFT more efficiently if the spectrum contains zeros [Holm 1987]. The interpolation can also be accomplished by using

alternatives to the fast Fourier transform such as the fast Hartley transform [Hsu, Lin 1988] or other transforms [Wang 1990], [Wang 1993]. For this work, the standard FFT based on the Cooley-Tukey algorithm is used [Cooley, Tukey 1965]. The average of the profiles is calculated in the frequency domain after the spectrum has been zero-padded. The inverse FFT is then calculated from the averaged spectrum. This has the advantage that only one inverse FFT has to be calculated while the result remains the same due to the linearity property of the Fourier transform. It is also convenient to choose a power of two for the number of data points of the interpolated profile since this increases the speed of the inverse FFT.

6.4 Benchmarking Methods

In Chapter 5, the profile height was used to compare the measurements of the post-process machine to measurements taken with a roundness machine. The profile height is a suitable quantity to assess the quality of a workpiece. However, it is not necessarily an appropriate metric to compare data from the post-process machine with data from a roundness machine. Its main shortcoming is that it is calculated from only two points, the minimum and the maximum of the profile. It is therefore insensitive to the agreement between the remaining data points of the compared profiles. Two very different profiles can appear to be similar, as long as the distance between the respective maximum and the minimum are the same. To solve this problem, section 6.4.1 introduces a metric that yields more accurate comparisons of two profiles. It is strongly based on the period estimation methods discussed in section 6.2. In section 6.4.2, the *maximum profile amplitude* is defined, which will be used in the further comparisons in addition to the profile height.

6.4.1 Profile Difference

To obtain a more accurate way of comparing two profiles $x_1(k)$ and $x_2(k)$, the difference $\Delta x(k)$ between the samples of the profiles is used

$$\Delta x(k) = x_1(k) - x_2(k) . \tag{6.20}$$

This quantity is referred to as the *profile difference* and is denoted by $\Delta x_P(k)$ or $\Delta x_R(k)$ depending on whether it refers to measurements of the post-process machine or the

roundness machine. In the general case, two profile measurements $x_1(k)$ and $x_2(k)$ of the same part usually start at different angular part positions. It is therefore necessary to align the profiles prior to the computation of the profile differences. This is accomplished by using the AMDF

$$\hat{R}_{AMDF}(n) = \frac{1}{N_W} \sum_{k=1}^{N_W} \left| x_1(k) - x_2(k+n) \right| \tag{6.21}$$

as discussed in section 6.2, since it has proven to be suitable for shape comparison. For the profile alignment, the window size N_W is set to the entire length of the profile. The delay *n* assumes all values from 0 to $N-1$, with *N* being the number of data points of the profile. The delay is implemented as a circular shift of the profile, i.e.

$$x_2(k+n) = \begin{cases} x_2(k+n) & \text{for } k+n < N \\ x_2(k+n-N) & \text{for } k+n \geq N \end{cases}. \tag{6.22}$$

If the profiles have a different number of data points, interpolation is used as described in section 6.3. After alignment of the two profiles, they are normalized to zero mean such that

$$\bar{x}_1 = \frac{1}{N} \sum_{k=0}^{N-1} x_1(k) = 0\,, \quad \bar{x}_2 = \frac{1}{N} \sum_{k=0}^{N-1} x_2(k) = 0\,. \tag{6.23}$$

From the profile differences $\Delta x(k)$ for a single part or a sample of parts, the underlying distribution can be obtained and several statistics can be estimated. The sample mean of the profile differences is zero, because of equations (6.23). The sample mean of the magnitude of the profile differences $\Delta x_{mag}(k)$

$$\Delta x_{mag}(k) = \left| x_1(k) - x_2(k) \right|, \tag{6.24}$$

however, is generally nonzero. The sample mean of $\Delta x_{mag}(k)$ is given by the AMDF. Another statistic is the standard deviation of the profile differences which will be used subsequently to assess the similarity of the two compared profiles.

6.4.2 Maximum Profile Amplitude

The *maximum profile amplitude* is the highest amplitude of the harmonics in the frequency range form 10 to 250 UPR. It is denoted by A_P or A_R depending on whether it refers to measurements of the post-process machine or the roundness machine. Most of the test parts in Chapter 5, that were classified as "bad," failed because of the existence of a single strong harmonic in the profile. For these parts, the maximum profile amplitude can be used as an alternative criterion to the profile height. The advantage of the maximum profile amplitude is that it is more robust against noise since it is calculated from all data points in the profile and not just from two of them as the profile height. However, it is not suitable as a quality criterion, since it can detect only one type of defect but is insensitive to other defects such as dents and flat spots in the part profile. Nevertheless, because of its robustness and the fact that it detects the most common part defect, it is used in addition to the profile height.

In Figure 6-15 and Figure 6-16, the maximum profile amplitude is plotted against the profile height for the measurements taken on the roundness machine and on the post-process machine. It can be seen that for the used test parts a weak linear relationship exists between the two quantities. The critical profile height h_{crit} of 1.270 μm (50 μinch), which categorizes the test parts into "good" or "bad," is marked by a solid vertical line.

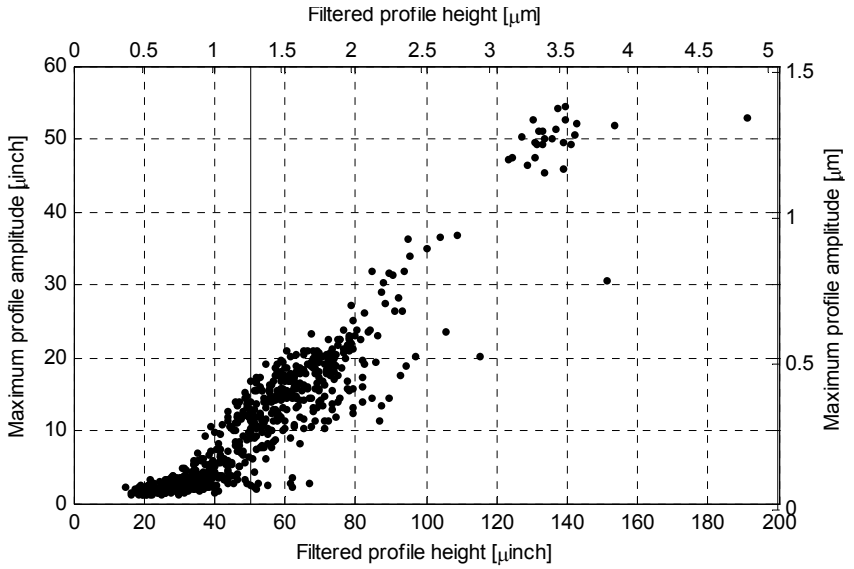

Figure 6-15: Plot of the max. profile amplitude vs. the profile height for the roundness machine

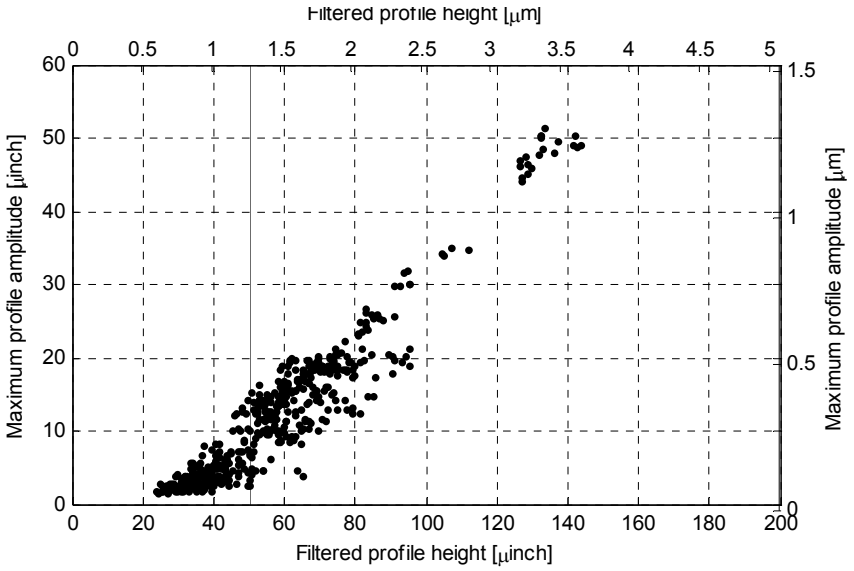

Figure 6-16: Plot of the max. profile amplitude vs. the profile height for the post-process machine

The relationship between the two quantities suggests that an equivalent critical maximum profile amplitude A_{crit} can be defined that results in a similar classification of the test measurements as using the profile height criterion. To find an equivalent value, the

classification errors as a function of the critical maximum profile amplitude are plotted in Figure 6-17.

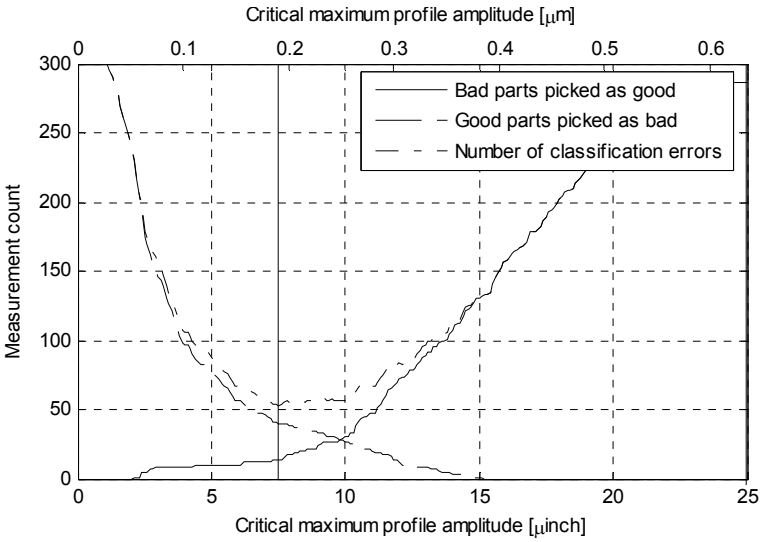

Figure 6-17: Classification errors as a function of the critical maximum profile amplitude

The total number of "good" and "bad" measurements was 300 and 330, respectively resulting from the five measurements of the 126 parts. As the critical value increases, the number of rejected "good" measurements decreases but at the same time more "bad" measurements are passed as "good." Besides these two classification errors, the total number of classification errors is plotted as a third curve. The total number of errors assumes its minimum for a critical maximum profile height of 0.191 μm (7.5 μinch). It is therefore reasonable to choose this value as an equivalent to the critical profile height of 1.270 μm (50 μinch). With this value, 13 of the 330 "bad" measurements were mistakenly passed as "good" and 40 of the 300 "good" measurements were mistakenly rejected as "bad." For the further discussion, this value is used as the critical maximum profile amplitude.

6.5 Dynamic Gage Model

6.5.1 Purpose of the Model

This section aims at developing a model of the dynamic behavior of the measurement system based on the frequency response of the system. This information allows predicting important characteristics of the dynamic behavior such as the amplitude at the resonant frequency and the amplitude attenuation at frequencies above the resonant frequency. Assuming that the system behaves like a linear time-invariant (LTI) system, the true profile, which would be obtained for an ideal system with constant frequency response, can be restored from the measured profile.

6.5.2 Measurement System and Methodology

The components that contribute the most to the overall frequency response are the gage head, the low-pass filter of the signal conditioning card, and the anti-aliasing filter (Figure 3-1).

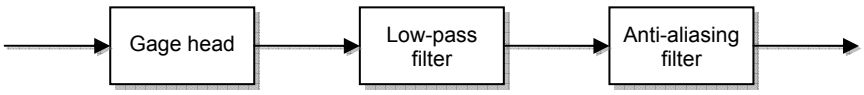

Figure 6-18: Components affecting the frequency response of the system

Among the three components, the gage head has the biggest influence on the frequency response curve, since it has the lowest natural frequency. This is attributed to the inertia and the limited stiffness of its internal mechanisms. The gage head can therefore be

regarded as a mechanical low-pass filter. The other two components in the system are electrical low-pass filters. The filter of the signal conditioning card is a 3-pole filter with a fixed cutoff frequency of 1 kHz. The cutoff frequency of the anti-aliasing filter is set to 1 kHz here as well. Due to the low-pass filters, a very step roll-off is expected for frequencies above 1 kHz. The measurement of the frequency response is therefore restricted to the range from 0 to 1 kHz, since no useable information of the profile can be obtained above 1 kHz.

The model of the measurement system is based on experimentally collected frequency response data. To collect the data, a part that exhibits a high amplitude at a certain dominant frequency is rotated in the machine at different speeds while the amplification or attenuation at the dominant frequency is recorded. Measuring the frequency response directly in the machine has several advantages over the more common offline approach [Longanbach, Kurfess 2001] where the gage is clamped down in a fixture and a force is applied to the fingers by an actuator. The main disadvantage of the offline method is that it only partly resembles the actual measurement system. For example, the results of the measurement may be affected by the frequency response of the actuator or the clamping fixture. On the other hand, measurements directly in the machine may also account for properties of the measurement system which were not explicitly considered in Figure 6-18. Examples are the frequency response of the gage fingers or local deformation of the workpiece in the contact zone. Besides that, no additional hardware is needed. The frequency response measurement can easily be implemented as a fully automated procedure which requires only inserting a master part with a strong dominant harmonic.

6.5.3 Measurement of the System Transfer Function

To measure the frequency response, a Visual Basic module is written. The corresponding dialog window is shown in Figure 6-19. It can be started from the main window by clicking on "Dynamic Calibration."

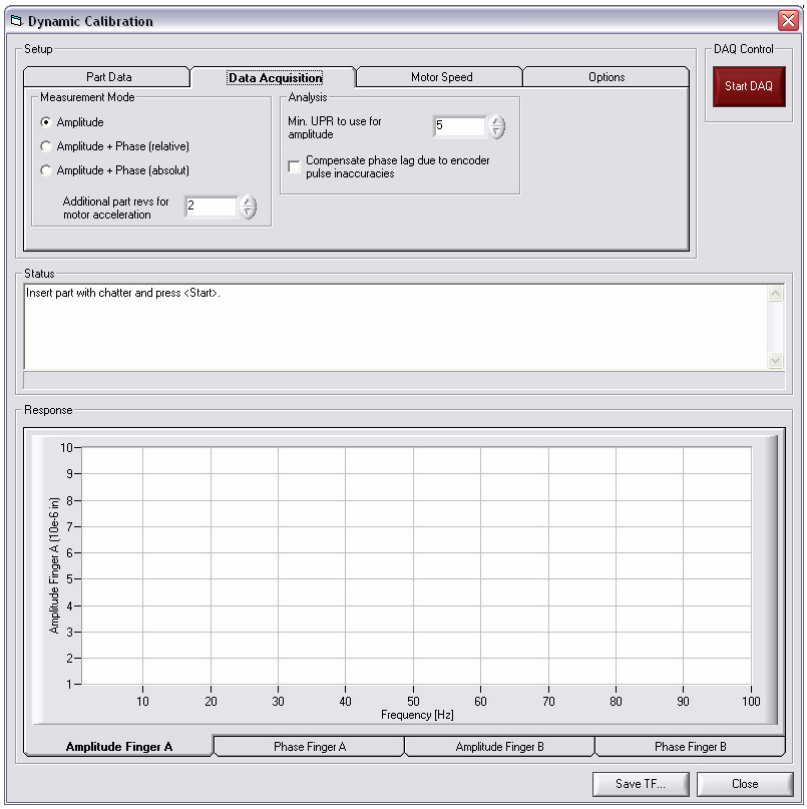

Figure 6-19: Dynamic finger calibration window

To retrieve the frequency response, the program measures both the amplitude and the phase shift of the fingers. Prior to the measurement, several parameters can be set such as the minimum roll motor speed, the maximum speed and the speed increment. Pressing the "Start DAQ" button launches the automatic measurement. As a first step, the program takes a single measurement of the part at minimum speed to determine the

frequency with the highest amplitude in the spectrum. The subsequent measurement of amplitude and phase is based on this frequency alone, since this frequency provides the best signal-to-noise ratio. Measurement of the phase requires that the part goes through several cycles of acceleration and deceleration as illustrated in Figure 6-20.

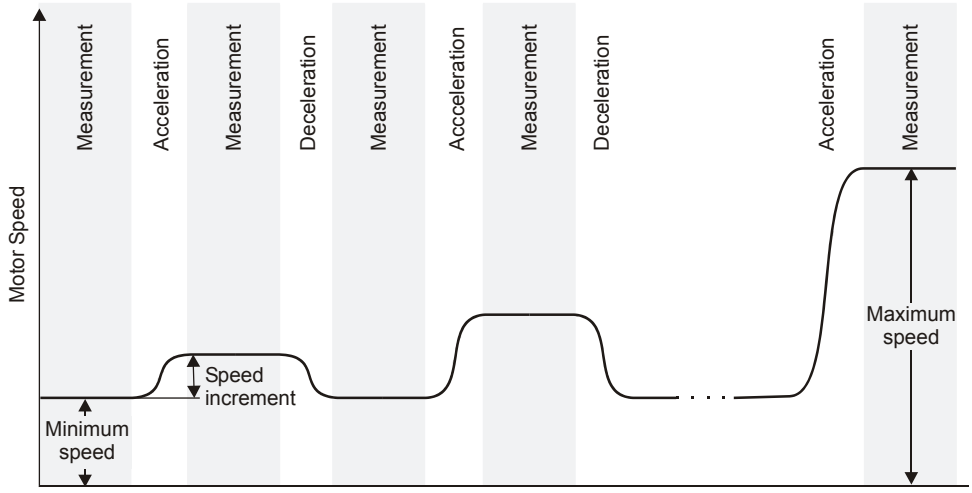

Figure 6-20: Motor speed for frequency response measurement

At the beginning of the cycles, the part is rotated at the specified minimum speed and the profile is measured. After a certain number of revolutions, the part is quickly accelerated by the specified speed increment while the measurement continues. It is then measured for several revolutions at the accelerated speed and then again decelerated to the minimum speed. In addition to the finger signals, the time of each encoder pulse is recorded. This allows the program to determine when the acceleration phase is completed by comparing the time difference between consecutive pulses. For the part of the measurement where the part speed is constant, the amplitude of the dominant frequency is measured. Comparison with the amplitude at minimum speed allows determining the attenuation. The phase shift is obtained by comparing the phase of the dominant

frequency at minimum speed and at the accelerated speed. From the time data of the encoder pulses, the part speed can be calculated and used to convert the dominant frequency from UPR into Hz. One acceleration and deceleration cycle yields one amplitude and phase datum for a certain frequency. To obtain amplitude and phase curves, several cycles have to be completed. In each cycle, the accelerated speed is increased by the speed increment from the accelerated speed in the previous cycle until it reaches the specified maximum speed.

To improve the accuracy, the amplitudes and phases are averaged over several part rotations in each cycle. This procedure yielded a fairly high accuracy for the amplitude measurements. The phase measurements on the other hand are highly contaminated by noise which can be attributed to two reasons. The first is the discrepancy between the encoder pulses and the actual part rotation due to elasticity in the belt and varying roll and part diameter. This effect is partly compensated by averaging over several part revolutions. The second reason is the part slipping due to differences in the average diameter of the upper and lower roll. Part slipping is inevitable, since a part can be rotated for more than 1000 revolutions during the measurements. Even with averaging, part slipping causes significant errors in the phase measurements. This has to be considered when analyzing the data.

The frequency range covered with this method depends on the minimum and maximum motor speed and the dominant frequency of the part profile. It therefore does not necessarily cover the full frequency range considered here from 0 to 1 kHz. For this reason, the amplitude attenuation and phase shift cannot be expressed relative to 0 Hz but only relative to the minimum frequency in the covered frequency range.

6.5.4 Measurement Results

To perform the measurements, a part with waviness at 32 UPR with amplitude of approximately 1.5 μm was used. At minimum part speed, 32 UPR corresponded to a frequency of 51 Hz and at maximum speed to 547 Hz. These frequencies define the range in which the frequency response can be measured with the used part. The amplitude and phase measurements for the two fingers of the Marposs Thruvar 5 are shown in Figure 6-21 and Figure 6-22. In Figure 6-21, the amplitudes are shown as the absolute amplitudes as they were measured with the part without scaling. The phase in Figure 6-22 is plotted so that an imaginary extension of the curve towards 0 Hz corresponds to approximately 0°.

The amplitude curves reveal that both fingers have the same natural frequency. The difference of the amplitude between the two fingers at 51 Hz results from the fact that the fingers measure on slightly different planes of the workpiece. Finger A seems to have a slightly lower damping coefficient than finger B which can be seen from the higher ratio of the resonant peak values to the values at minimum frequency.

The phase curve shows a lag of approximately 400° in the measured frequency range. As expected, the curves display fluctuations especially in the higher frequency range and the accuracy of the phase measurement is low. While the fluctuations appear to be random with respect to frequency, they are highly correlated between the two fingers indicating that the same noise source is the reason for the fluctuations. This further supports the previous assumption that the low accuracy of the phase angle measurement is caused by workpiece slipping.

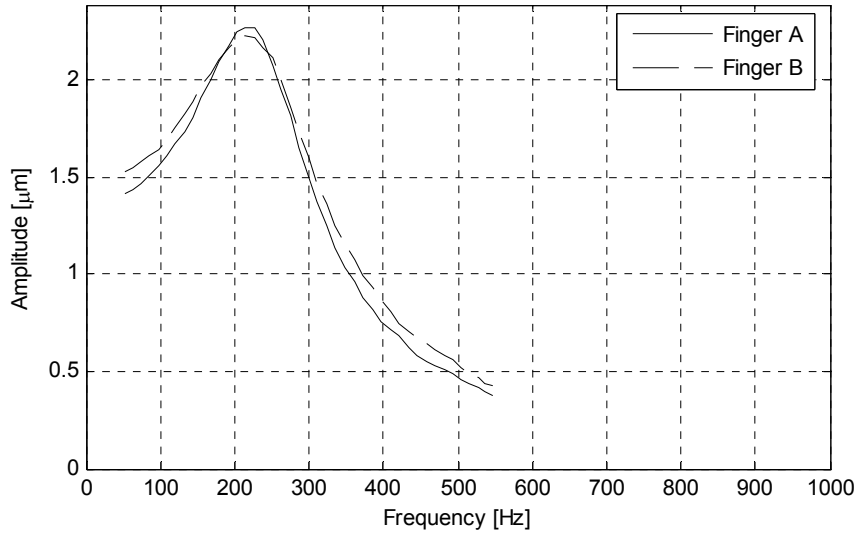

Figure 6-21: Amplitude as a function of the frequency

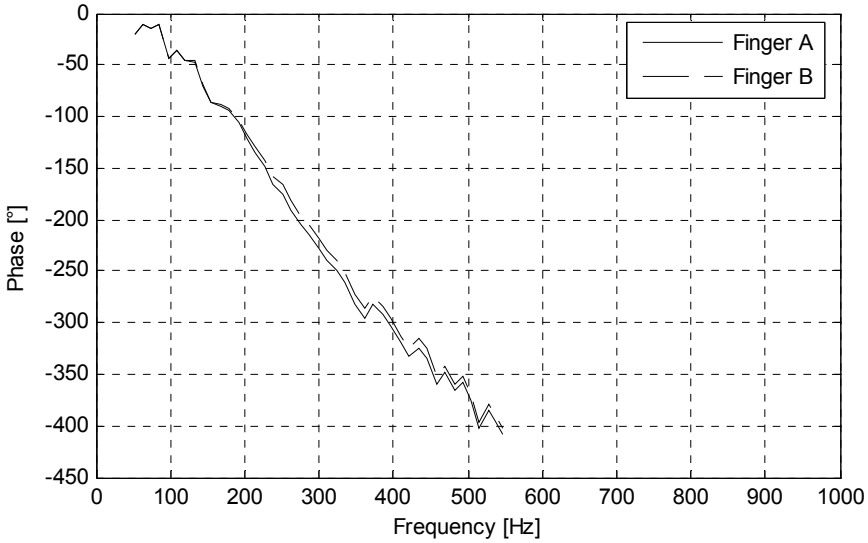

Figure 6-22: Phase shift as a function of the frequency

6.5.5 System Model

For system identification purposes it is convenient to use a logarithmic scaling of the frequency axis and to plot the magnitude in decibels instead of the absolute amplitude.

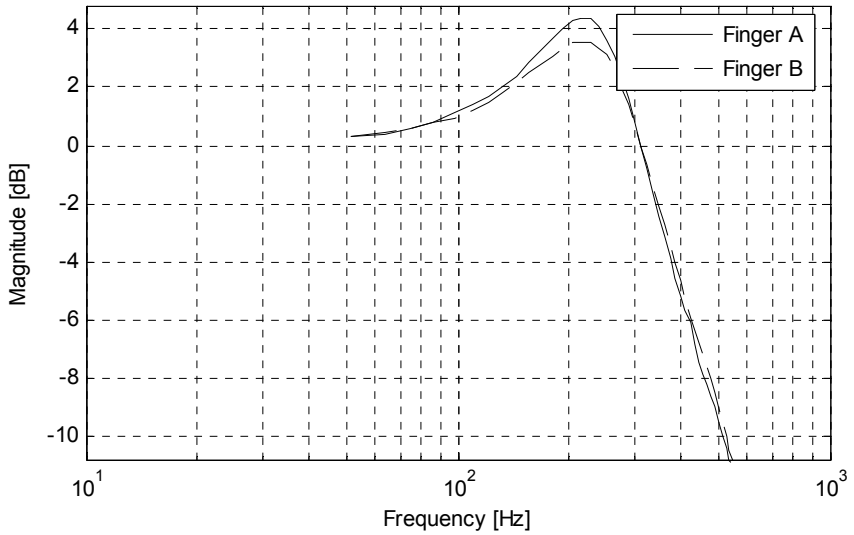

Figure 6-23: Magnitude as a function of the frequency

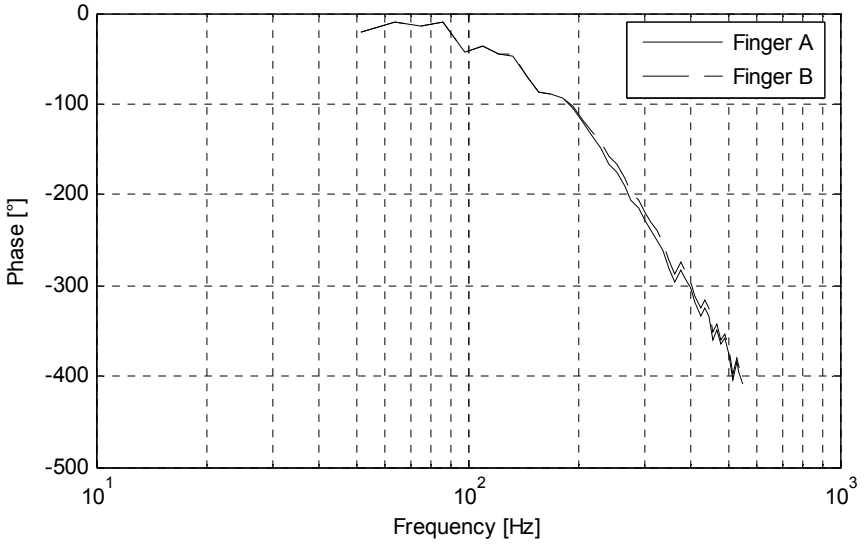

Figure 6-24: Phase shift as a function of frequency

This is done in Figure 6-23 and Figure 6-24. In Figure 6-23, the magnitude is normalized so that the imaginary extension of the curve towards 0 Hz converges to 0 dB.

The magnitude curve shows a resonant frequency around 220 Hz and has a slope of approximately –40 dB/decade above this frequency which is characteristic for a second order system. The descent of the phase is larger than that of a second order system which can be explained by the two low-pass filters with 1 kHz cutoff frequency. It therefore seems that the experimental data can be well enough described if spring-mass-damper model is assumed for the gage head and the two low-pass filters are expressed by the appropriate transfer function for their filter type, order, and cutoff frequency. Using a theoretical rather than an empirical model allows extrapolation of the frequency response curve. This is important, since the experimental data acquired with the selected part does not cover the full frequency range from 0 to 1 kHz.

The signal conditioning card low-pass filter is a third order filter. Its type, however, is unknown. It is therefore assumed that it is a third order Butterworth filter, since this is the most common filter type for applications like this. The magnitude squared function of a Butterworth low-pass filter with order N is given by

$$\left|H_{LP}(s)\right|^2 = \frac{1}{1+\left(\frac{s}{j\omega_c}\right)^{2N}}. \tag{6.25}$$

The N poles p_k in the factorized transfer function representation of the filter

$$H_{LP}(s) = \frac{1}{\prod_{k=0}^{N-1}(s - p_k)} \tag{6.26}$$

can be obtained by solving

$$1+\left(\frac{p_k}{j\omega_c}\right)^{2N}=0. \tag{6.27}$$

Using only the solutions of (6.27) that lie in the left half of the complex plane, the poles p_k are given by

$$p_k=-\sin\frac{(2k+1)\pi}{2N}\omega_c+j\cos\frac{(2k+1)}{2N}\omega_c, \qquad k=0,...,N-1. \tag{6.28}$$

The second order transfer function of the gage head is given by

$$H_{GH}(s)=\frac{1}{\left(\frac{s}{\omega_n}\right)^2+2\zeta\left(\frac{s}{\omega_n}\right)+1}, \tag{6.29}$$

where ω_n is the undamped natural frequency and ζ the damping ratio. The overall transfer function of the system is therefore given by the second order transfer function of the gage head, a third order Butterworth filter, and an eighth order Butterworth filter, both with a cutoff frequency of 1 kHz.

$$H_S(s)=\frac{1}{\left(\frac{s}{\omega_n}\right)^2+2\zeta\left(\frac{s}{\omega_n}\right)+1}\cdot\frac{1}{\prod_{k=0}^{2}(s-p_{3k})}\cdot\frac{1}{\prod_{k=0}^{7}(s-p_{8k})}. \tag{6.30}$$

The undamped natural frequency ω_n and the damping ratio ζ are unknown and have to be determined based on the measured frequency response. System identification methods offer a systematic approach to do this. The methods usually weigh the amplitude and phase information equally. This may not yield optimal results since the amount of noise in the amplitude and the phase measurements is very different. Therefore, the values of

the parameters ω_n and ζ are chosen manually, so that a good fit between the measured response and the model response is achieved. The goodness of the fit is assessed by visual comparison of the response curves. The chosen values are listed in Table 6-3.

Table 6-3: Dynamic parameters of the Thruvar 5 gage head

	Finger A	Finger B
Undamped natural frequency in Hz f_n	244 Hz	251 Hz
Undamped natural frequency in rad/s ω_n	1533 rad/s	1577 rad/s
Damping ratio ζ	0.32	0.35

The agreement between the experimental data and the model is shown in Figure 6-25 and Figure 6-26 for finger A. The curves for finger B are very similar and are therefore omitted here. At about 900 Hz, the onset of the steep amplitude roll-off due to the two low-pass filters can be observed.

With the knowledge of the system transfer function H_S, the measurement can be compensated for the frequency response by dividing the measured signal by H_S in the frequency domain

$$M_{RC}(k) = \frac{M(k)}{H_S(j\omega)} = \frac{M(k)}{H(2\pi kj)}, \tag{6.31}$$

where $M(k)$ is the measured signal and $M_{RC}(k)$ is the frequency response compensated signal. Taking the inverse Fourier transform of $M_{RC}(k)$ yields the compensated signal in the time-domain.

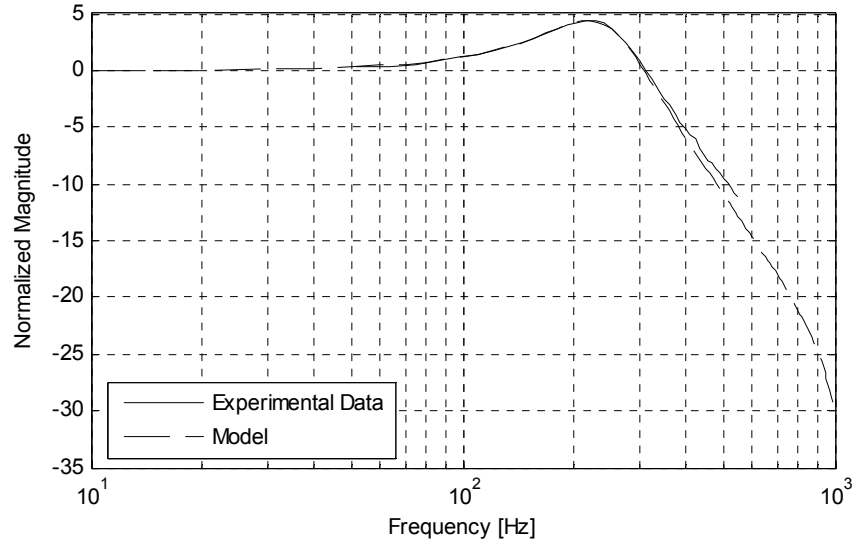

Figure 6-25: Magnitude of experimental data and model for finger A

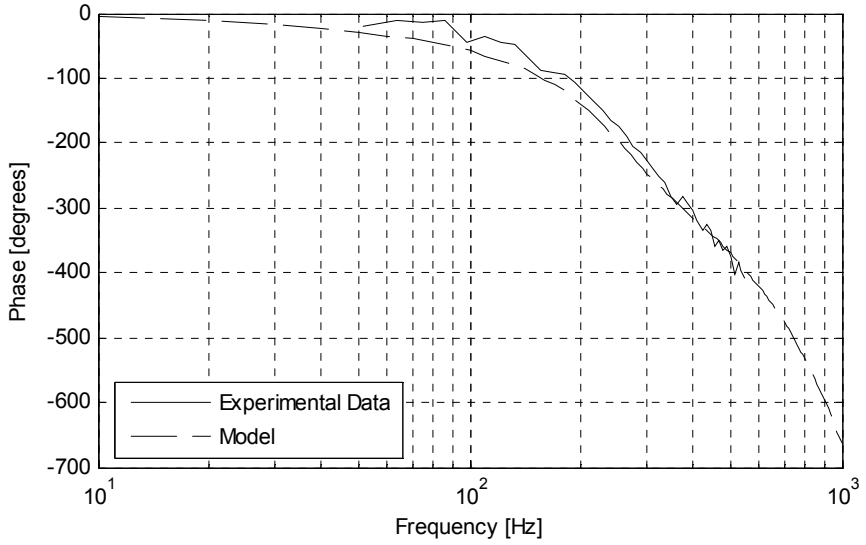

Figure 6-26: Phase shift of experimental data and model for finger A

A drawback of the compensation is that for the higher frequencies any random noise in the system is severely amplified. Unless a very high signal-to-noise ratio is obtained, the method requires averaging of several measurements to achieve an acceptable accuracy.

6.6 Vibration Separation

6.6.1 Classification of Methods

The task of separating the workpiece profile from the relative movement between the workpiece and the gage head belongs to a class of problems frequently encountered in high-precision metrology. This class is characterized by problems where the measurement is the sum of two quantities: the geometric variation of a rigid body and a relative motion between the body and the measuring probe. In most problems, one of the two quantities is the desired quantity and the other one is considered the disturbance or error which is to be removed from the measurement. One example is the measurement of a circular workpiece in presence of vibration or spindle error. In this case the geometry of the workpiece is the desired quantity. Another example is the measurement of spindle runout using a master ball. Here, the relative motion between the master ball and the probe is the desired quantity and variations in the geometry of the master ball are treated as the disturbance. Owing to the application discussed here, the workpiece geometry is regarded as the desired quantity and the relative motion as the disturbance or error.

The methods for error separation can be classified according to certain criteria. A classification is given in Figure 6-27. With respect to the measured geometry, roundness or straightness measurements can be distinguished. For most straightness measuring methods, an equivalent method exists for roundness measurement so that methods referring to straightness are not further discussed here. With respect to the separable error, a classification can be made into a systematic error that repeats itself with every workpiece revolution or a variable error that is non-repeatable during multiple workpiece revolutions [Whitehouse 1976]. The common principle of all separation methods is to

acquire multiple measurements of the same workpiece. The idea is to combine the redundant information in an appropriate way so that the error is reduced or canceled. Depending on the way multiple measurements are obtained, the methods can be grouped into multi-orientation methods and multi-probe methods [Whitehouse 1976].

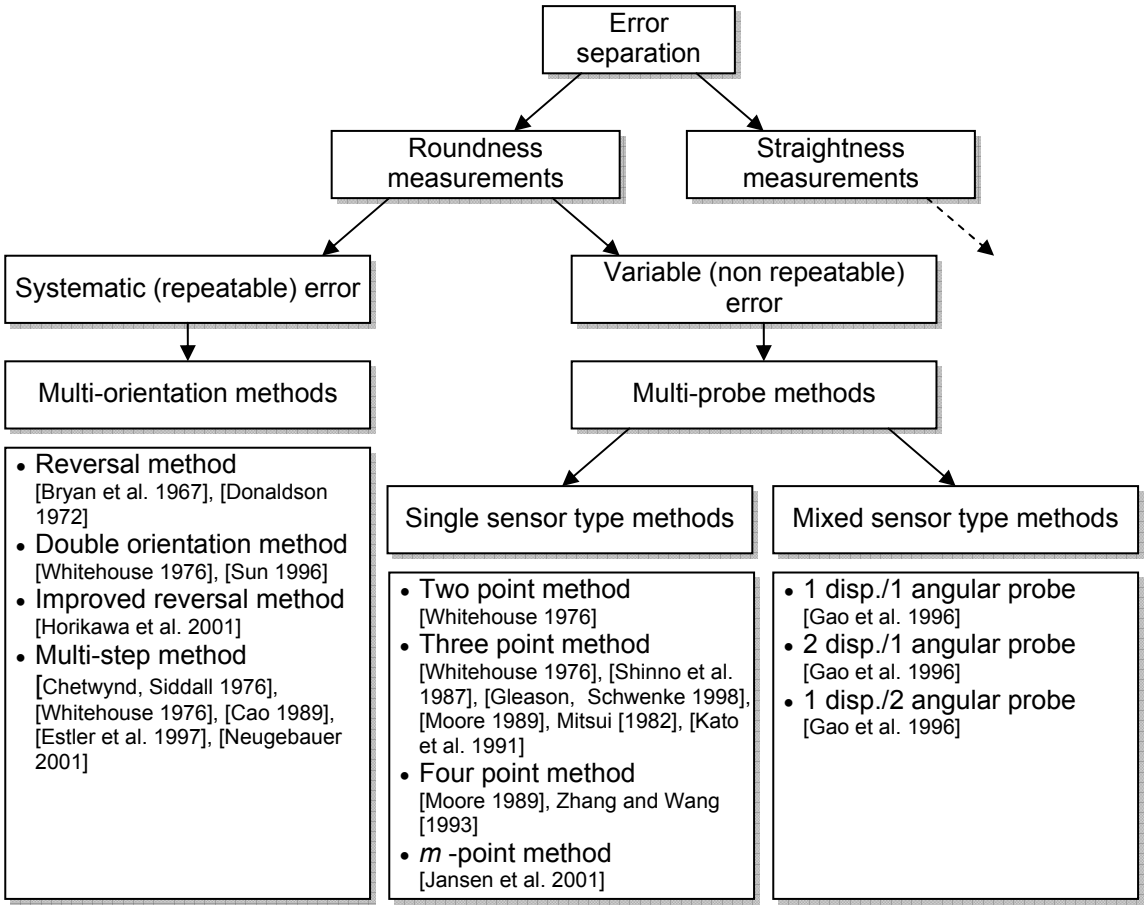

Figure 6-27: Classification of error separation methods

6.6.2 Multi-Orientation Methods

Multi-orientation methods use a single probe and sequentially take multiple measurements while the orientation of the probe with respect to the part is changed after each measurement. They are applicable only when the error is systematic. A simple but well-known multi-orientation method is the reversal method [Bryan et al. 1967], [Donaldson 1972]. It is usually used to separate the spindle error from the part roundness error. With the setup shown in Figure 6-28, a measurement is taken for one complete part revolution. The measurement of the probe is given by

$$m_1(\theta) = r(\theta) + e(\theta)\,, \tag{6.32}$$

where $m_1(\theta)$, $r(\theta)$, and $e(\theta)$ are the measurement signal, the workpiece radius and the spindle error, respectively and θ is the angle of rotation. After the first measurement, both the probe and the workpiece are rotated by 180° with respect to the spindle and a second measurement is taken which is given by

$$m_2(\theta) = r(\theta) - e(\theta)\,. \tag{6.33}$$

Adding the measurements yields twice the workpiece radius, subtracting them twice the spindle error

$$m_1(\theta) + m_2(\theta) = 2r(\theta) \tag{6.34}$$

$$m_1(\theta) - m_2(\theta) = 2e(\theta)\,. \tag{6.35}$$

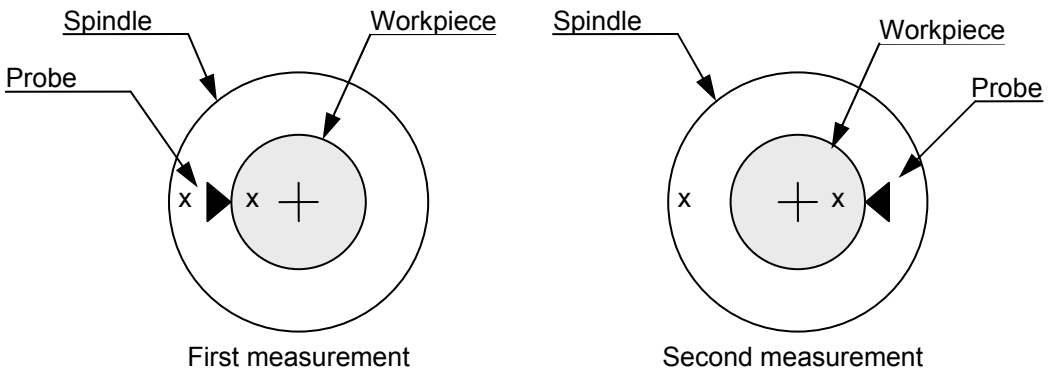

Figure 6-28: Reversal method

A variation of the reversal method that measures the spindle error directly with an additional probe can be found in Horikawa et al. [2001]. Whitehouse [1976] presented another variation called the double-orientation method. After the first measurement, only the workpiece is rotated by 180° with respect to the spindle while the probe remains at its original position (Figure 6-29) resulting in a simplified setup for the second measurement.

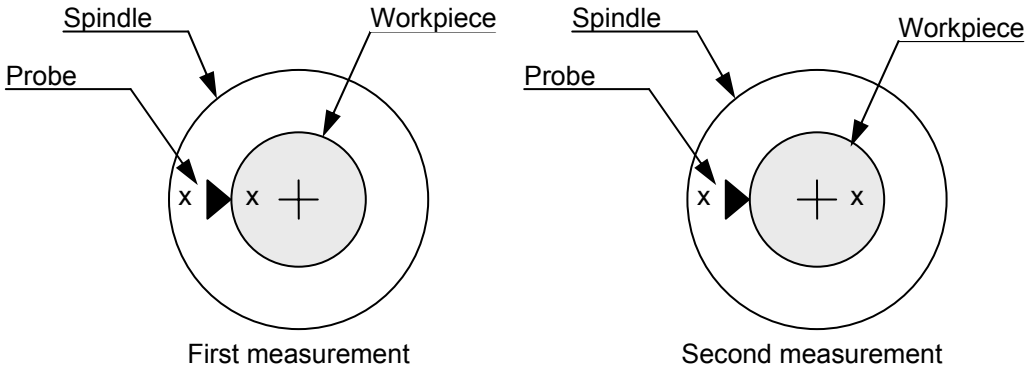

Figure 6-29: Double-orientation method

The probe signals of the first and second measurement are given by

$$m_1(\theta) = r(\theta) + e(\theta) \tag{6.36}$$

$$m_2(\theta) = r(\theta - \pi) + e(\theta), \tag{6.37}$$

respectively. To eliminate the spindle error, the measurements are combined by subtracting the two equations. The combined measurement $m_C(\theta)$ is

$$m_C(\theta) = m_1(\theta) - m_2(\theta) = r(\theta) - r(\theta - \pi). \tag{6.38}$$

Opposite to the reversal method, the profile is not readily available here anymore. Taking the Fourier transform of equation (6.38) yields

$$\begin{aligned} M_C(k) &= \mathcal{F}[m_1(\theta) - m_2(\theta)] \\ &= R(k) - R(k)e^{-jk\pi} \\ &= (1 - e^{-jk\pi})R(k) \\ &= M_W(k)R(k) \end{aligned}, \tag{6.39}$$

where $M_C(k)$ is the Fourier transform of the combined measurements, $k = 0,1,2,...$ the number of undulations per revolution, and $M_W(k) = (1 - e^{-jk\pi})$ a harmonic weighting function. It can be seen that for an odd number of undulations ($k = 1,3,5,...$) the weighting function $M_W(k)$ is 2. For even undulations ($k = 0,2,4,...$) the weighting functions is zero which means that after removal of the spindle error all information about the even harmonics in the profile is lost.

The double-orientation method can be generalized by rotating the workpiece by an arbitrary angle α between measurements. The weighting function then becomes

$$M_W(k) = (1 - e^{-jk\alpha}). \tag{6.40}$$

The new function has zeros only when

$$k\alpha = 2\pi n, \; n = 0,1,2,... \tag{6.41}$$

For the frequencies where the weighting function is nonzero, the Fourier transform of the true profile $R(k)$ can be restored from the combined measurements through division by the weighting function

$$R(k) = M_C(k) / M_W(k)\,,\; M_W(k) \neq 0\,. \tag{6.42}$$

A similar method that uses Prony spectrum is presented in [Sun 1996]. Even if the weighting function is nonzero but very small, restoration of the profile may be difficult in practical applications. In this case, noise inherent in the measurement is amplified by the reciprocal of the weighting function.

The number of zeros of the weighting function can be reduced if more than two measurements are taken. The multi-step method uses N_m measurements with different orientations. The orientations are spaced by angle increments of $\Delta\alpha = 2\pi / N_m$ and complete a full circle [Whitehouse 1976], [Chetwynd, Siddall 1976]. If the roundness error of the workpiece is the desired quantity, the orientation of the spindle with respect to the workpiece and the probe is changed with every step. If the spindle error is to be measured, the orientation of the workpiece with respect to the spindle and the probe is varied. After completion of the N_m measurements, the average is calculated

$$\overline{m}(\theta) = \frac{1}{N_m} \sum_{i=1}^{N_m} m_i(\theta) \tag{6.43}$$

to yield the desired quantity. Due to the high number of measurements, the multi-step method provides excellent random noise rejection capabilities. The multi-step method is capable of separating the desired quantity from the disturbance except for harmonics that are a multiple of the number of measurements, i.e. if the roundness error of the workpiece

is the desired quantity, $\bar{m}(\theta)$ will contain the kN_m harmonics ($k = 1,2,3,...$) of the spindle error [Cao 1989], [Estler et al. 1997], [Neugebauer 2001]. This problem can be overcome if the multi-step method is applied several times with different numbers of orientations per pass $N_{m1}, N_{m2}, ...$ [Tan et al. 1991]. For a suitably chosen number of orientations in the passes, error separation is possible up to high frequencies [Cao et al. 1992]. A disadvantage is that a high number of measurements have to be taken for one profile.

6.6.3 Multi-Probe Methods

Multi-orientation methods require that the error is repeatable with every revolution. Non-repeatable, time-dependent components (variable components) of the error cannot be removed. Multi-probe methods overcome this problem by utilizing two or more probes to acquire multiple measurements simultaneously. Thus, any time-dependent error is contained in all measurements.

The simplest multi-probe method consists of two coplanar probes that are placed opposite to each other [Whitehouse 1976], as displayed in Figure 6-30.

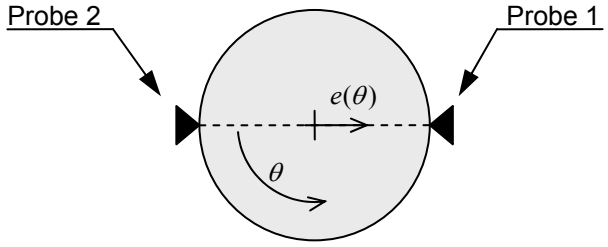

Figure 6-30: Two-point method

The probe signals of the first and second measurement are given by

$$m_1(\theta) = r(\theta) + e(\theta) \tag{6.44}$$

$$m_2(\theta) = r(\theta - \pi) - e(\theta)\,, \tag{6.45}$$

respectively. The error is removed by adding the two measurements. Taking the Fourier transform of the sum of the measurements yields

$$\begin{aligned} M_C(k) &= \mathcal{F}[m_1(\theta) + m_2(\theta)] \\ &= R(k) + R(k)e^{-jk\pi} \\ &= (1 + e^{-jk\pi})R(k) \\ &= M_W(k)R(k) \end{aligned} \,. \tag{6.46}$$

The harmonic weighting function

$$M_W(k) = (1 + e^{-jk\pi}) \tag{6.47}$$

is now 2 for an even number of undulations ($k = 0,1,2,...$) and zero for an odd number of undulations ($k = 1,3,5,...$). Odd harmonics can therefore not be restored. The geometric interpretation is that with the given configuration only diameter information can be retrieved after removal of the error motion [Whitehouse 1976].

Besides Fourier synthesis, the problem of reconstructing the original profile can be expressed as a set of linear equations [Whitehouse 1976], [Urban, Urban 1979]. Assuming $2N_S$ samples are taken around the complete circumference of the part, let r_i be the radius at the *i*-th part position and e_i the error movement at the *i*-th position with $i = 0, 1, 2, ..., 2N_S - 1$. The measurements acquired with the first and second probe are given by

$$m_{1i} = r_i + e_i \,,\; i = 0, 1, 2, ..., 2N_S - 1 \tag{6.48}$$

$$m_{2i} = \begin{cases} r_{i+N_S} - e_i & \text{for } i < N_S \\ r_{i-N_S} - e_i & \text{for } i \geq N_S \end{cases},\; i = 0, 1, 2, ..., 2N_S - 1\,, \tag{6.49}$$

respectively. The error movement is again eliminated by adding the equations which yields the following $2N_S$ equations with the $2N_S$ unknowns r_i

$$\begin{aligned} m_{1i} + m_{2i} &= r_i + r_{i+N_S} \quad \text{for } i = 0, 1, 2, ..., N_S - 1 \\ m_{1i} + m_{2i} &= r_i + r_{i-N_S} \quad \text{for } i = N_S, N_S + 1, N_S + 2, ..., 2N_S - 1 \end{aligned}. \tag{6.50}$$

Introducing the column vectors

$$\mathbf{m} = \left[m_{11} + m_{21}, m_{12} + m_{22}, ..., m_{1(2N_S)} + m_{2(2N_S)} \right]^T \tag{6.51}$$

$$\mathbf{r} = \left[r_1, r_2, ..., r_{(2N_S)} \right]^T \tag{6.52}$$

for the measurements and the radii, the $2N_S$ equations in (6.50) can be written in matrix notation

$$\mathbf{m} = \mathbf{A}\mathbf{r}\,. \tag{6.53}$$

The matrix **A** is a $2N_S \times 2N_S$ matrix, but has a rank of only N_S. To determine the radii vector **r**, N_S radii values have to be specified. The matrix equation therefore does not allow reconstructing more information about the profile than the Fourier synthesis.

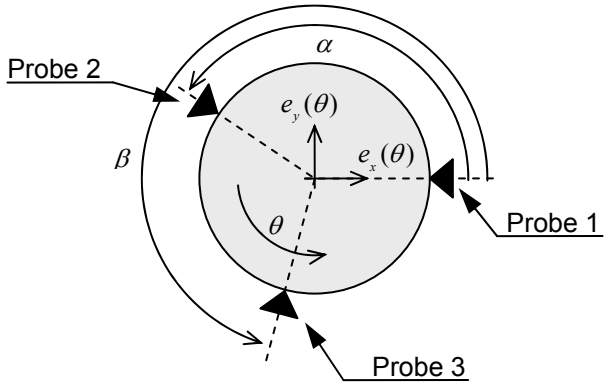

Figure 6-31: Three-point method

To retain information about the odd harmonics in the profile, configurations with three or more probes are successfully employed in the literature [Whitehouse 1976], [Lu, Zhang 1986], [Shinno et al. 1987], [Zhang et al. 1990]. The general setup for the three-point method is displayed in Figure 6-31. The measurement directions of the probes intersect in one point. Since the probes are not aligned on a single axis anymore, the error motion as a function of the workpiece rotation θ has to be expressed by two components $e_x(\theta)$ and $e_y(\theta)$. The probe signals are

$$m_1(\theta) = r(\theta) + e_x(\theta) \tag{6.54}$$

$$m_2(\theta) = r(\theta - \alpha) + e_x(\theta)\cos\alpha + e_y(\theta)\sin\alpha \tag{6.55}$$

$$m_3(\theta) = r(\theta - \beta) + e_x(\theta)\cos\beta + e_y(\theta)\sin\beta\,. \tag{6.56}$$

A weighted average $m_C(\theta)$ of the three measurements with the respective weights 1, w_2, w_3 can be calculated by

$$\begin{aligned} m_C(\theta) &= m_1(\theta) + w_2 m_2(\theta) + w_3 m_3(\theta) \\ &= r(\theta) + e_x(\theta) + w_2 r(\theta-\alpha) + w_2 e_x(\theta)\cos\alpha + w_2 e_y(\theta)\sin\alpha \\ &\quad + w_3 r(\theta-\beta) + w_3 e_x(\theta)\cos\beta + w_3 e_y(\theta)\sin\beta \end{aligned} . \tag{6.57}$$

The weights w_2 and w_3 are arbitrary parameters. If they are chosen such that

$$\begin{aligned} 1 + w_2\cos\alpha + w_3\cos\beta &= 0 \\ w_2\sin\alpha + w_3\sin\beta &= 0 \end{aligned} , \tag{6.58}$$

which is the case if

$$\begin{aligned} w_2 &= \frac{\sin\beta}{\sin(\alpha-\beta)} \\ w_3 &= -\frac{\sin\alpha}{\sin(\alpha-\beta)} \end{aligned} , \ \alpha-\beta \neq n\pi , \ n = 0, \pm 1, \pm 2, ... \tag{6.59}$$

the error movements $e_x(\theta)$ and $e_y(\theta)$ cancel in equation (6.57) so that the combined measurement becomes

$$m_C(\theta) = r(\theta) + w_2 r(\theta-\alpha) + w_3 r(\theta-\beta) . \tag{6.60}$$

Taking the Fourier transform of the combined measurement yields

$$\begin{aligned} M_C(k) &= \mathcal{F}[r(\theta) + w_2 r(\theta-\alpha) + w_3 r(\theta-\beta)] \\ &= R(k) + w_2 R(k) e^{-jk\alpha} + w_3 R(k) e^{-jk\beta} \\ &= (1 + w_2 e^{-jk\alpha} + w_3 e^{-jk\beta}) R(k) \\ &= M_W(k) R(k) \end{aligned} , \tag{6.61}$$

where the harmonic weighting function is given by

$$M_W(k) = 1 + w_2 e^{-jk\alpha} + w_3 e^{-jk\beta} . \tag{6.62}$$

Its amplitude becomes

$$\left|M_W(k)\right| = \sqrt{\left(1 + w_2\cos(k\alpha) + w_3\cos(k\beta)\right)^2 + \left(w_2\sin(k\alpha) + w_3\sin(k\beta)\right)^2}\,. \qquad (6.63)$$

In combination with the constraints for the weights w_2 and w_3 defined in equation (6.58), the amplitude of the weighting function becomes zero for the first harmonic, that is

$$\left|M_W(1)\right| = 0\,. \qquad (6.64)$$

Therefore, complete removal of the error motion also causes loss of the eccentricity information about the workpiece [Whitehouse 1976].

The amplitude of the weighting function as expressed in equation (6.63) includes the probe angles α and β as parameters. They can be chosen in a manner to reduce the undesirable attenuation of harmonics by the weighting function. A configuration where the probes are equally spaced around the full circumference of the workpiece ($\alpha = 120°$, $\beta = -120°$) is highly undesirable since it cancels a large portion of the harmonics from the spectrum and, in addition, hinders loading and unloading of the workpiece. In general, configurations with asymmetrically spaced probes are preferable [Moore 1989]. In the literature, several setups with different probe angles are discussed. In most cases, the angle combination is sought for by trial and error until an appropriate configuration for the given application is found. Gleason and Schwenke [1998] compared configurations with symmetrically ($\alpha = 60°$, $\beta = -60°$) and asymmetrically ($\alpha = 60°, \beta = -45°$) spaced probes. With the symmetric configuration, the first zero in the amplitude after the 1 UPR harmonic occurs at 5 UPR, whereas with the asymmetric configuration the minimum amplitude was 0.75 from 2 to 22 UPR with the first zero occurring at 23 UPR. Kakino and Kitazawa [1978] used a setup with $\alpha = 50°$ and $\beta = -40°$ which yields an amplitude of at least 0.7 for the range of 2 to 34 UPR. Moore [1989] used $\alpha = 28.125°$,

$\beta = -39.375°$ and obtained an amplitude of at least 0.5 for the range of 2 to 62 UPR. In Mitsui [1982], a configuration with $\alpha = 133.5°$ and $\beta = -120.8°$ is utilized. The feasible frequency range for error separation with this configuration is not investigated further since the employed sensor system is not capable of measuring the higher harmonics. A more systematic approach for the determination of the probe angles is presented in [Kato et al. 1991]. Assuming a standard deviation of the error in the combined measurement, the error in the restored profile is calculated on the basis of the error propagation law. The probe angles are determined by minimizing a performance index that consists of the weighted sum of the errors for all harmonics. For a frequency range from 2 to 15 UPR, the optimal angles based on this method were $\alpha = 38°$ and $\beta = 67°$.

Although adequate results were reported with the three-point method, it fails to separate the error movement from the profile for higher harmonics. Moore [1989] concluded that regardless of the finger angles for harmonics up to 125 UPR at least one harmonic will always be attenuated. Several different approaches are explained in the literature to overcome this difficulty. Kato et al. [1990] repeated the three-point method five times with different angular configurations to prevent the unwanted attenuation of harmonics. Since the method is a combination of multi-probe methods and multi-orientation methods, it requires the error movement to be fully repeatable. Moore [1989] suggested adding a fourth measurement probe to the system for full error suppression. The redundant probe information can also be used for self-monitoring and detection of probe malfunctions. The specific setup used probe angle of 21°, 29°, and 47°. Zhang and Wang [1993] also employed a four-probe setup. Through computer simulation, they found that the four point method is capable of separating harmonics up to 480 UPR. The

general case of an *m*-probe system is treated in [Jansen et al. 2001]. The composition of the probe signals from the profile and the error motion is expressed through a matrix relationship using a matrix **A** that describes the configuration of the probes. The probe angles are selected by minimizing the condition number of **A**. Gao et al. [1996] solves the problem of harmonic suppression by combining displacement sensors with angle sensors which is referred to as the mixed method. A configuration with one displacement sensor and one angle sensor provides good preservation of higher frequency harmonics. More mixed probe configurations are discussed in [Gao et al. 1997].

6.6.4 Sources of Errors

The equations for vibration separation stated above are an idealization. Practical applications are prone to several errors. One important assumption of the equations above is that both fingers measure the same part profile $r(\theta)$ except for a certain phase shift. This requires that the workpiece is perfectly rigid and does not deform during the measurement. Calibration differences between the fingers or tracing on slightly different planes violate this assumption and prevent the complete cancellation of the vibration.

Another possible deficiency are the angles between the fingers [Zhang, Wang 1993]. The true value of the angles has to be repeatable and has to match the value assumed in the equations. With regard to potential flotation of the workpiece center in the centerless fixture and the fact that the gage head is retracted and reinserted after every measurement this may not be the case.

It should also be stated that the equations above are only first-order approximations of the true geometric relationship for the case that the error movements

e_x and e_y are small compared to the average radius of the workpiece. A more exact geometric model is presented by Tu et al. [1997]. However, using the exact equations for analysis is tedious. In most cases the error movements e_x and e_y can be assumed to be small without significant loss of accuracy.

6.6.5 Vibration Removal for Centrically Placed Fingers

Since the goal of this work is to measure waviness using the Marposs Thruvar 5 in-process gage, the following analysis focuses exclusively on two-point methods. Configurations with three or more simultaneously used probes are disregarded. This section derives a model where the fingers are placed centrically to the part, so that the connecting line between the contact points of the fingers pass through the workpiece center as shown in Figure 6-32.

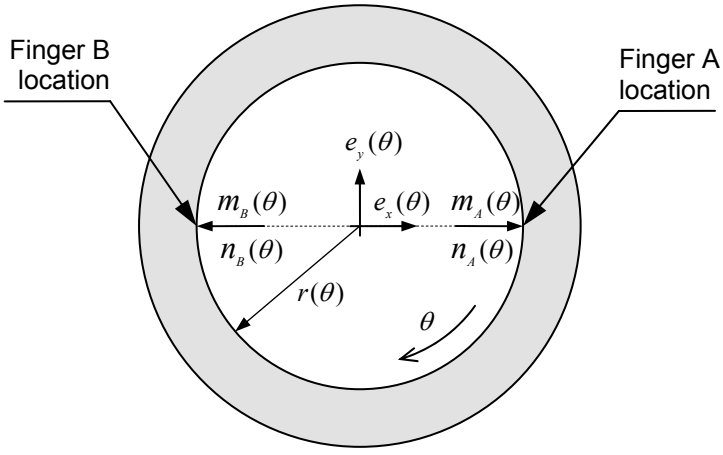

Figure 6-32: Configuration with centrically placed fingers

The model is a slightly extended version of the two-point method presented earlier. It is covered here in more depth for two reasons. Firstly, the centric finger placement is the standard configuration for two probe measurement systems and was employed for example in Chapter 5. Therefore, its further examination seems justified. Secondly, results from this model will be used for the parameter estimation to optimize the more advanced model presented in the next section.

The model uses as similar notation as in the previous section. The angular position of the part is denoted by θ. The part is rotated clockwise as in the post-process machine. The measurements at finger A and finger B are expressed by $m_A(\theta)$ and $m_B(\theta)$, respectively with the positive measurement direction pointing outward. Compared to the two-point method, the model is extended by taking random noise into account that affects the measurements at the fingers. For this purpose, two terms $n_A(\theta)$ and $n_B(\theta)$ are introduced for the two fingers. They are lumped values for noise that is not accounted for by any of the other parameters in this model. They include for example disturbances like electrical noise, potential deformation of the workpiece or differences in the measured profile due to slightly different axial positions of the finger.

To simplify the analysis, the following assumptions are made for this model:

1. The vertical error motion of the workpiece center $e_y(\theta)$ is small compared to the average value of the radius $\overline{r}$

$$e_y(\theta) \ll \overline{r}\,. \tag{6.65}$$

2. The error motions $e_x(\theta)$ and $e_y(\theta)$ and the noise $n_A(\theta)$ and $n_B(\theta)$ are random processes which are independent of each other, i.e. the covariance is zero for any two of them.

Assumption (1) can be verified by utilizing values from the previous chapters. In section 5.3 it was found that the motion of the workpiece in the vertical direction is 10.0 μm. Comparing this to the nominal workpiece radius of 5.38 mm, the radius is by a factor of 538 higher than the vertical error motion. Assumption (2) is harder to justify but seems to be a reasonable approximation since the error motions and the random noise terms are caused by different mechanisms.

As a result of assumption (1), the influence of vertical workpiece center movement $e_y(\theta)$ on the measurements at the fingers $m_A(\theta)$ and $m_B(\theta)$ is neglected. Likewise, the phase error that is introduced into the measurement because of the vertical motion is disregarded as well.

Under the assumptions stated above, the measurements $m_A(\theta)$ and $m_B(\theta)$ and their respective Fourier transforms are given by

$$m_A(\theta) = r(\theta) + e_x(\theta) + n_A(\theta) \tag{6.66}$$

$$m_B(\theta) = r(\theta - \pi) - e_x(\theta) + n_B(\theta) \tag{6.67}$$

$$M_A(k) = \mathcal{F}[m_A(\theta)] = R(k) + E_x(k) + N_A(k) \tag{6.68}$$

$$M_B(k) = \mathcal{F}[m_B(\theta)] = e^{-j\pi k} R(k) - E_x(k) + N_B(k)\,. \tag{6.69}$$

These equations are the same as (6.44) and (6.45) except for the additional noise terms. Adding the signals from finger A and B cancels the horizontal error motion $e_x(\theta)$

$$(m_A + m_B)(\theta) = r(\theta) + r(\theta - \pi) + n_A(\theta) + n_B(\theta) \tag{6.70}$$

$$\begin{aligned}(M_A + M_B)(k) &= \mathcal{F}[m_A(\theta) + m_B(\theta)] \\ &= (1 + e^{-j\pi k})R(k) + N_A(k) + N_B(k) \\ &= \begin{cases} 2R(k) + N_A(k) + N_B(k) & k = 0,2,4,... \\ N_A(k) + N_B(k) & k = 1,3,5,... \end{cases}\end{aligned} \tag{6.71}$$

Similar to the results in the previous section, the profile information is lost for the odd frequencies when the signals are added. The remainder is the sum of the random noise at both fingers. This can be utilized if the random noise has to be estimated. Subtracting the signals $m_A(\theta)$ and $m_B(\theta)$ yields

$$(m_A - m_B)(\theta) = r(\theta) - r(\theta - \pi) + 2e_x(\theta) + n_A(\theta) - n_B(\theta) \tag{6.72}$$

$$\begin{aligned}(M_A - M_B)(k) &= \mathcal{F}[m_A(\theta) - m_B(\theta)] \\ &= (1 - e^{-j\pi k})R(k) + 2E_x(k) + N_A(k) - N_B(k) \\ &= \begin{cases} 2E_x(k) + N_A(k) - N_B(k) & k = 0,2,4,... \\ 2R(k) + 2E_x(k) + N_A(k) - N_B(k) & k = 1,3,5,... \end{cases}\end{aligned} \tag{6.73}$$

For the even frequencies now the horizontal error motion is separated while for the odd frequencies sum of the radius, the error motion, and the random noise is retrieved. Phase shifting the signal of finger B by π and adding the signals leads to

$$m_A(\theta) + m_B(\theta + \pi) = 2r(\theta) + e_x(\theta) - e_x(\theta + \pi) + n_A(\theta) + n_B(\theta + \pi) \tag{6.74}$$

$$\begin{aligned}(M_A + e^{j\pi k} M_B)(k) &= \mathcal{F}[m_A(\theta) + m_B(\theta+\pi)] \\ &= 2R(k) + (1 - e^{j\pi k}) E_x(k) + N_A(k) + e^{j\pi k} N_B(k) \\ &= \begin{cases} 2R(k) + N_A(k) + N_B(k) & k = 0,2,4,... \\ 2R(k) + 2E_x(k) + N_A(k) - N_B(k) & k = 1,3,5,... \end{cases}\end{aligned} \quad . \tag{6.75}$$

This method has the advantage that the profile information is retained for both odd and even frequencies. Since error motion separation is not possible for the odd frequencies, the term $E_x(k)$ appears in the equation for $k = 1,3,5,...$. Phase shifting of signal B by π and subtracting the signals yields

$$m_A(\theta) - m_B(\theta+\pi) = e_x(\theta) + e_x(\theta+\pi) + n_A(\theta) - n_B(\theta+\pi) \tag{6.76}$$

$$\begin{aligned}(M_A - e^{j\pi k} M_B)(k) &= \mathcal{F}[m_A(\theta) - m_B(\theta+\pi)] \\ &= (1 + e^{j\pi k}) E_x(k) + N_A(k) - e^{j\pi k} N_B(k) \\ &= \begin{cases} 2E_x(k) + N_A(k) - N_B(k) & k = 0,2,4,... \\ N_A(k) + N_B(k) & k = 1,3,5,... \end{cases}\end{aligned} \quad . \tag{6.77}$$

Here, the profile information is completely removed and only the error motion and the random noise remain.

From a computational point of view, phase shift and addition as expressed in equation (6.74) is the most convenient way of vibration separation, since it retains the profile for both odd and even frequencies and removes the vibration for the even frequencies.

6.6.6 Vibration Removal for Eccentrically Placed Fingers

To overcome the deficiency of odd harmonic suppression with only two probes, a configuration with slightly eccentrically placed fingers as shown in Figure 6-33 is proposed. The amount of eccentricity is determined by the angle between the connection from the finger contact point to the workpiece center and the *x*-axis. It is mathematically convenient to denote this angle by $\varphi/2$. The angle between the fingers is then given by $\pi-\varphi$ and φ is the eccentricity angle that designates the deviation of the finger angle from π. The amount of eccentricity d_φ measured along the *y*-direction can be calculated by

$$d_\varphi = \bar{r}\sin(\varphi/2)\,. \tag{6.78}$$

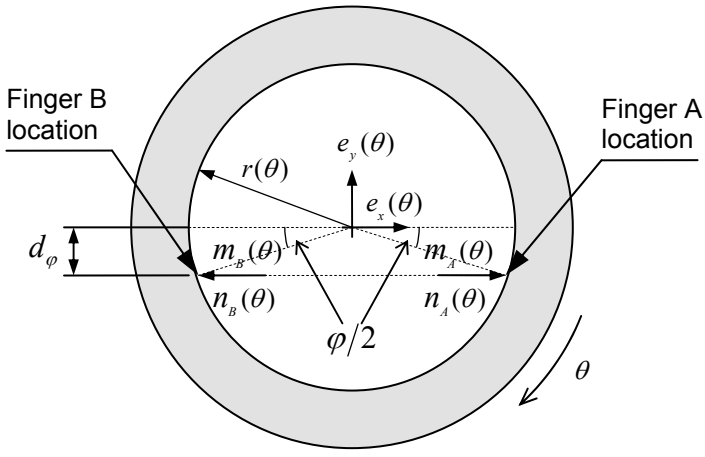

Figure 6-33: Configuration with eccentrically placed fingers

Besides the error motion in the *x*-direction $e_x(\theta)$, which is the quantity to be separated from the radius, the following three disturbances are considered in the model:

- Random noise affecting the fingers, $n_A(\theta)$ and $n_B(\theta)$
- The vertical error motion of the workpiece center $e_y(\theta)$
- Inaccuracies in the eccentricity angle φ

Similar to the model for centrically placed fingers, lumped noise terms $n_A(\theta)$ and $n_B(\theta)$ are added for the fingers. Depending on the value of the eccentricity angle φ, the vertical error motion $e_y(\theta)$ affects the measurements and therefore has to be included in the model. Since as stated in section 6.6.4, the vibration separation methods are prone to inaccuracies in the finger angle, variations in the eccentricity angle φ are incorporated into the model as well.

An important difference compared to the model for centrically placed fingers is that the fingers do not measure normal to the workpiece surface anymore. The radial variation of the profile and the resulting displacement of the fingers are not the same. Instead, the measurement at the fingers is given by

$$r(\theta)\cos(\varphi/2)\,. \tag{6.79}$$

Another consequence of the non-normal measuring direction is a small phase error. This error exists even in absence of any workpiece center motion and depends on the variation of the radius [Chetwynd 1987].

The following assumptions are made to simplify the analysis:

1. The vertical error motion of the workpiece center $e_y(\theta)$ is small compared to the average value of the radius $\overline{r}$

$$e_y(\theta) \ll \overline{r} \,. \tag{6.80}$$

2. The variation of the radius $r(\theta)$, i.e. the profile height, is small compared to the average value of the radius $\overline{r}$

$$r(\theta) \ll \overline{r} \,. \tag{6.81}$$

3. The angle of eccentricity φ is larger than zero, even in presence of the vertical error motion $e_y(\theta)$

$$\varphi > 0 \,. \tag{6.82}$$

4. The error motions $e_x(\theta)$ and $e_y(\theta)$ and the noise $n_A(\theta)$ and $n_B(\theta)$ are random processes which are independent to each other, i.e. the covariance is zero for any two of them.

Assumptions (1) and (4) were already justified in the previous section. Assumption (2) can be validated as well. The nominal value of the bore radius is 5.38 mm (section 3.5.1) and the largest profile height measured on the roundness machine was 3.71 µm (section 5.1.2). For assumption (3) to hold, the eccentricity d_φ of the fingers measured along the *y*-axis has to be larger than the vertical part motion

$$d_\varphi > \max(e_y(\theta)) \tag{6.83}$$

or using equation (6.78)

$$\sin(\varphi/2) > \frac{\max(e_y(\theta))}{\overline{r}}. \tag{6.84}$$

With the estimated vertical part motion of 10.0 µm from section 5.3 and the minimum bore radius of 5.38 mm, this yields a lower bound for the eccentricity angle φ

$$\varphi > 0.213°. \tag{6.85}$$

It should be emphasized that no assumption is made that the eccentricity angle φ is small compared to π. Practically however, φ has to be relatively small since otherwise stylus drag may occur. Similar to the model for centrically placed fingers, the phase error due to vertical workpiece motion can be dropped from the model under assumption (1). Owing to assumption (2), the phase error caused by eccentric finger placement and variations in the radius is disregarded as well.

The influence of the vertical motion $e_y(\theta)$ on the part measurement can be derived from Figure 6-34.

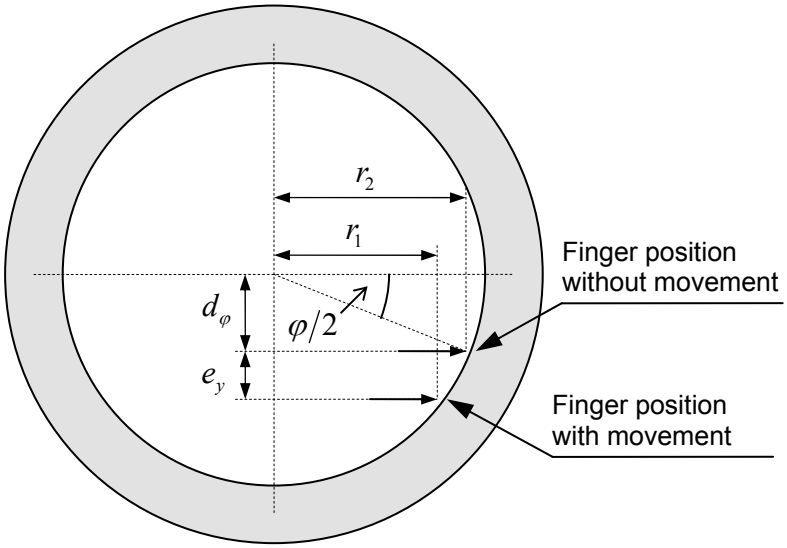

Figure 6-34: Derivation of the vertical motion on the measurement

The change of the radius Δr due to the movement e_y is given by

$$\Delta r = r_2 - r_1 . \tag{6.86}$$

Replacing r_1 and r_2 yields

$$\begin{aligned} \Delta r &= \sqrt{\overline{r}^2 - d_\varphi{}^2} - \sqrt{\overline{r}^2 - (e_y + d_\varphi)^2} \\ &= \sqrt{\overline{r}^2 - (\overline{r}\sin(\varphi/2))^2} - \sqrt{\overline{r}^2 - (e_y + \overline{r}\sin(\varphi/2))^2} \end{aligned} . \tag{6.87}$$

Δr can be regarded as a function of the movement e_y

$$\Delta r(e_y) = \sqrt{\overline{r}^2 - (\overline{r}\sin(\varphi/2))^2} - \sqrt{\overline{r}^2 - (e_y + \overline{r}\sin(\varphi/2))^2} . \tag{6.88}$$

To simplify (6.88), $\Delta r(e_y)$ is approximated by a Taylor series at the point 0 ignoring all second or higher order terms

$$\begin{aligned} \Delta r(e_y) &= \Delta r(0) + \Delta r'(0)(e_y - 0) + \frac{1}{2!}\Delta r''(0)(e_y - 0)^2 + \ldots \\ &\approx \Delta r(0) + \Delta r'(0) e_y \\ &= 0 - \frac{1}{2}\left(\overline{r}^2 - (e_y + \overline{r}\sin(\varphi/2))^2\right)^{-\frac{1}{2}}\left(-2(e_y + \overline{r}\sin(\varphi/2))\right)\Big|_{e_y=0} e_y \\ &= \frac{\overline{r}\sin(\varphi/2)}{\sqrt{\overline{r}^2 - (\overline{r}\sin(\varphi/2))^2}} e_y \\ &= \frac{\overline{r}\sin(\varphi/2)}{\overline{r}\cos(\varphi/2)} e_y \\ &= \tan(\varphi/2) e_y \end{aligned} \tag{6.89}$$

which yields a linearized version of the radius change. The measured signal at finger A and B and their respective Fourier transforms are then

$$m_A(\theta) = \cos(\varphi/2)\, r(\theta) + e_x(\theta) - \tan(\varphi/2)\, e_y(\theta) + n_A(\theta) \tag{6.90}$$

$$m_B(\theta) = \cos(\varphi/2) r(\theta - \pi + \varphi) - e_x(\theta) - \tan(\varphi/2) e_y(\theta) + n_B(\theta) \tag{6.91}$$

$$\begin{aligned} M_A(k) &= \mathcal{F}[m_A(\theta)] \\ &= \cos(\varphi/2)\, R(k) + E_x(k) - \tan(\varphi/2) E_y(k) + N_A(k) \end{aligned} \tag{6.92}$$

$$\begin{aligned} M_B(k) &= \mathcal{F}[m_B(\theta)] \\ &= e^{-j(\pi-\varphi)k} \cos(\varphi/2) R(k) - E_x(k) - \tan(\varphi/2) E_y(k) + N_B(k) \end{aligned} . \tag{6.93}$$

The horizontal workpiece center motion $e_x(\theta)$ can be eliminated completely by adding the signals for finger A and B

$$\begin{aligned} (m_A + m_B)(\theta) = \cos(\varphi/2)&(r(\theta) + r(\theta - \pi + \varphi)) \\ &-2\tan(\varphi/2)\, e_y(\theta) + n_A(\theta) + n_B(\theta) \end{aligned} \tag{6.94}$$

$$\begin{aligned} (M_A + M_B)(k) &= \mathcal{F}[m_A(\theta) + m_B(\theta)] \\ &= (1 + e^{-j(\pi-\varphi)k}) \cos(\varphi/2)\, R(k) \\ &\quad -2\tan(\varphi/2) E_y(k) + N_A(k) + N_B(k) \end{aligned} . \tag{6.95}$$

The harmonic weighting function $M_W(k)$ of the part profile is given by

$$M_W(k) = (1 + e^{-j(\pi-\varphi)k}) \cos(\varphi/2) . \tag{6.96}$$

Opposite to the centric finger placement, the odd harmonics do not cancel out completely. Instead, both odd and even harmonics are attenuated and phase shifted according to the harmonic weighting function $M_W(k)$. Since φ is a parameter of $M_W(k)$, the harmonic suppression depends on the eccentricity angle. Figure 6-35 and Figure 6-36 display the amplitude $|M_W(k)|$ for two configurations with $\varphi = 2°$ and $\varphi = 5°$. The amplitudes of the harmonic weighting function can be rewritten as (appendix B.1)

$$|M_W(k)| = \begin{cases} \sqrt{2\left(1+\cos(\varphi k)\right)}\cos(\varphi/2) & \text{for } k = 0,2,4,... \\ \sqrt{2\left(1-\cos(\varphi k)\right)}\cos(\varphi/2) & \text{for } k = 1,3,5,... \end{cases}. \tag{6.97}$$

Treating the amplitudes of the even and odd frequencies as a continuous functions of the variable *k*, the zeros are located at

$$k = \begin{cases} \dfrac{(2n+1)\pi}{\varphi} & \text{for even frequencies} \\ \dfrac{2n\pi}{\varphi} & \text{for odd frequencies} \end{cases} \qquad n = 0,1,2,.... \tag{6.98}$$

Decreasing the eccentricity angle φ therefore shifts the zeros to higher frequencies, increasing the angle shifts them to lower frequencies. This can also be observed in Figure 6-35 and Figure 6-36.

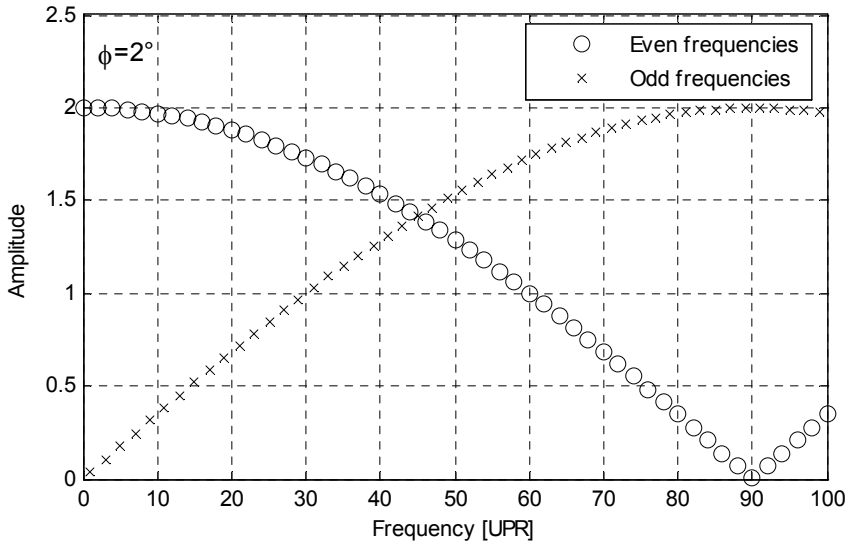

Figure 6-35: Amplitude of the signal sum for φ = 2°

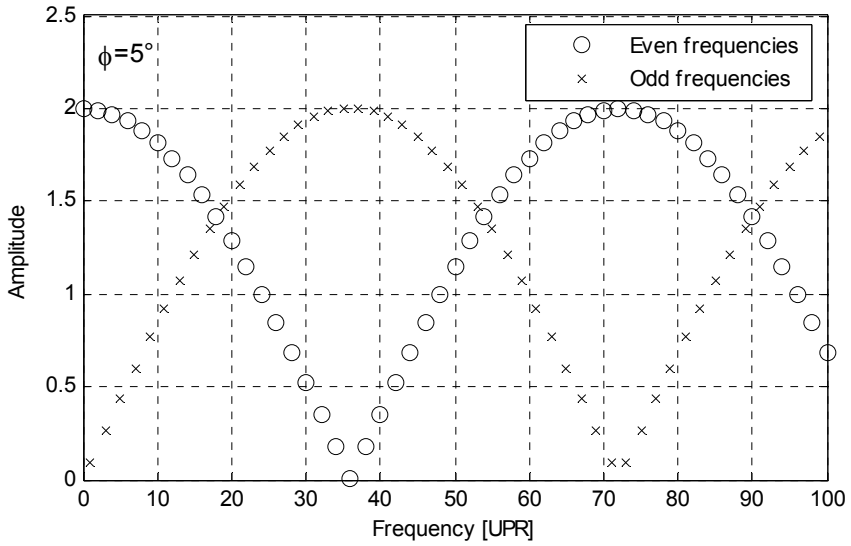

Figure 6-36: Amplitude of the signal sum for φ = 5°

Whether exact zeros occur, depends on whether the solutions to equation (6.98) are exact even or odd numbers. For even frequencies, exact zeros occur if the ratio π/φ is an even number. This is the case in Figure 6-35 and Figure 6-36 where the first zeros for the even frequencies occur at 90 UPR and 36 UPR respectively. For odd frequencies, exact zeros occur for example if the ratio $2\pi/\varphi$ is an odd number. Theoretically, it is therefore possible for certain non-integer values of the ratio π/φ to prevent zeros in the harmonic weighting function. However, although no exact zeros exist, the amplitudes of some frequencies will be almost zero, which limits the practical use. It is more practical to identify a certain range of frequencies for a given eccentricity angle φ where the amplitude attenuation is not too severe and where vibration separation is possible. For the eccentricity angle of $\varphi = 2°$ in Figure 6-35, a reasonable frequency range would be 10-80 UPR, for $\varphi = 5°$ in Figure 6-36 it would be 5-32 UPR. Since the eccentricity angle can be chosen arbitrarily during the setup of the gage, it can be selected so that vibration

separation is possible for the frequency range where the highest vibration amplitudes are expected.

Similar to the other multi-probe methods discussed in section 6.6.3, the eccentric configuration is capable of separating the DC component (0 UPR frequency) of the profile from vibration, since

$$\left|M_W(0)\right| = 2\cos(\varphi/2)\,. \tag{6.99}$$

A difference to the three-point method exists in that the 1 UPR frequency is non-zero

$$\left|M_W(1)\right| = \sqrt{2\left(1-\cos\varphi\right)}\cos(\varphi/2)\,. \tag{6.100}$$

Since in most cases however the eccentricity angle will be small, the amplitude of the 1 UPR frequency is highly attenuated and the restored amplitude highly noisy.

Different information can be retrieved with the same finger configuration by subtracting the signals

$$\begin{aligned}(m_A - m_B)(\theta) = {} & \cos(\varphi/2)(r(\theta) - r(\theta-\pi+\varphi)) \\ & + 2e_x(\theta) + n_A(\theta) - n_B(\theta)\end{aligned} \tag{6.101}$$

$$\begin{aligned}(M_A - M_B)(k) &= \mathcal{F}[m_A(\theta) - m_B(\theta)] \\ &= (1-e^{-j(\pi-\varphi)k})\cos(\varphi/2)\,R(k)\,. \\ &\quad + 2E_x(k) + N_A(k) - N_B(k)\end{aligned} \tag{6.102}$$

Subtraction cancels the vertical workpiece center motion $e_y(\theta)$ but the horizontal motion $e_x(\theta)$ remains in the equations. The harmonic weighting function of the radius becomes

$$M_W(k) = (1-e^{-j(\pi-\varphi)k})\cos(\varphi/2)\,. \tag{6.103}$$

A plot of the amplitudes $|M_W(k)|$ for $\varphi = 5°$ is given in Figure 6-37. The amplitudes have the same shape as for the summation except that they are switched for even and odd frequencies.

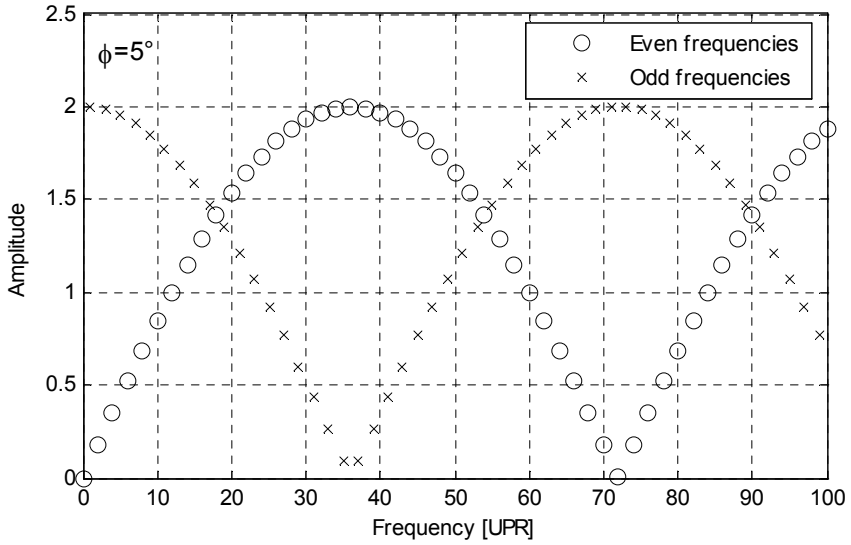

Figure 6-37: Amplitude of the signal difference for φ = 5°

The advantage of subtracting the signals is that the harmonic weighting function is high for the frequencies where the weighting function for the addition of the signals is low, therefore yielding a good signal-to-noise ratio wherever the addition yields a poor ratio and vice versa. The subtraction however has the drawback that it is susceptible to horizontal motion since $E_x(k)$ is included with a factor of 2 in the equation.

Phase shifting signal B by $\pi - \alpha$ and adding the signals yields

$$\begin{aligned} m_A(\theta) + m_B(\theta + \pi - \alpha) = \cos(\varphi/2)(r(\theta) + r(\theta + \varphi - \alpha) \\ + e_x(\theta) - e_x(\theta + \pi - \alpha) \\ - \tan(\varphi/2)(e_y(\theta) + e_y(\theta + \pi - \alpha)) \\ + n_A(\theta) + n_B(\theta + \pi - \alpha) \end{aligned} \tag{6.104}$$

$$\begin{aligned} (M_A + e^{j(\pi-\alpha)k} M_B)(k) &= \mathcal{F}[m_A(\theta) - m_B(\theta)] \\ &= (1 + e^{j(\varphi-\alpha)k})\cos(\varphi/2)R(k) \\ &\quad + (1 - e^{j(\pi-\alpha)k})E_x(k) \\ &\quad - (1 + e^{j(\pi-\alpha)k})\tan(\varphi/2)E_y(k) \\ &\quad + N_A(k) + e^{j(\pi-\alpha)k} N_B(k) \end{aligned} \tag{6.105}$$

If α is exactly equal to the eccentricity angle φ, then the above equations simplify to

$$\begin{aligned} m_A(\theta) + m_B(\theta + \pi - \varphi) = 2\cos(\varphi/2)r(\theta) \\ + e_x(\theta) - e_x(\theta + \pi - \varphi) \\ - \tan(\varphi/2)(e_y(\theta) + e_y(\theta + \pi - \varphi)) \\ + n_A(\theta) + n_B(\theta + \pi - \varphi) \end{aligned} \tag{6.106}$$

$$\begin{aligned} (M_A + e^{j(\pi-\varphi)k} M_B)(k) &= \mathcal{F}[m_A(\theta) - m_B(\theta)] \\ &= 2\cos(\varphi/2)R(k) \\ &\quad + (1 - e^{j(\pi-\varphi)k})E_x(k) \\ &\quad - (1 + e^{j(\pi-\varphi)k})\tan(\varphi/2)E_y(k) \\ &\quad + N_A(k) + e^{j(\pi-\varphi)k} N_B(k) \end{aligned} \quad . \tag{6.107}$$

In this case, the amplitudes of the radius have a constant harmonic weighting function

$$M_W(k) = 2\cos(\varphi/2)\,, \tag{6.108}$$

which is independent from the frequency *k* and the undesirable attenuation is avoided. As a disadvantage, both the horizontal and vertical motion with respective weighting functions are present in the equation. Therefore, phase shift and addition is susceptible to horizontal and vertical motion to a certain degree. Opposite to the radius information,

small values of the weighting function are desired for the error motions. The weighting function for the horizontal motion is given by

$$M_{W,E_x}(k) = 1 - e^{j(\pi-\varphi)k} . \tag{6.109}$$

A plot of $\left|M_{W,E_x}(k)\right|$ is shown in Figure 6-38. The weighting function of the vertical error motion is

$$M_{W,E_y}(k) = (1 + e^{j(\pi-\varphi)k}) \tan(\varphi/2) . \tag{6.110}$$

$\left|M_{W,E_y}(k)\right|$ is plotted in Figure 6-39. Due to the factor $\tan(\varphi/2)$, the amplitudes are significantly attenuated.

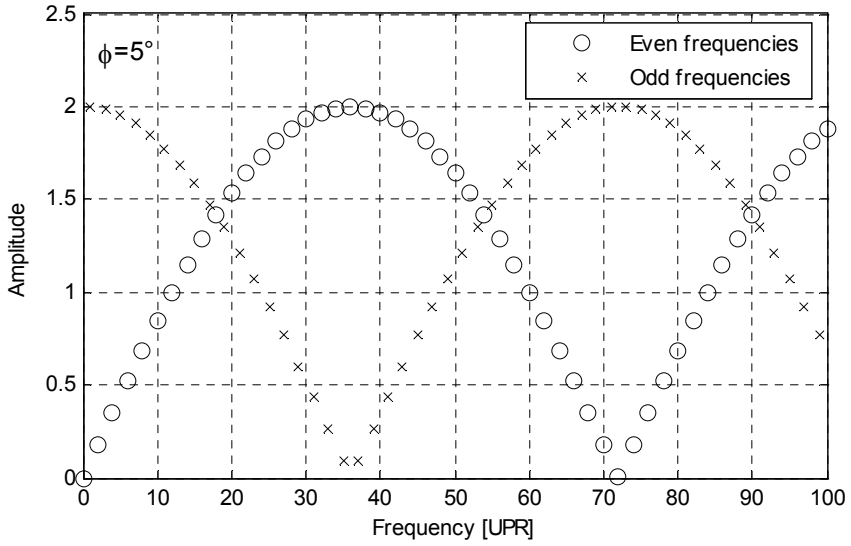

Figure 6-38: Amplitude of the horizontal error motion for φ = 5°

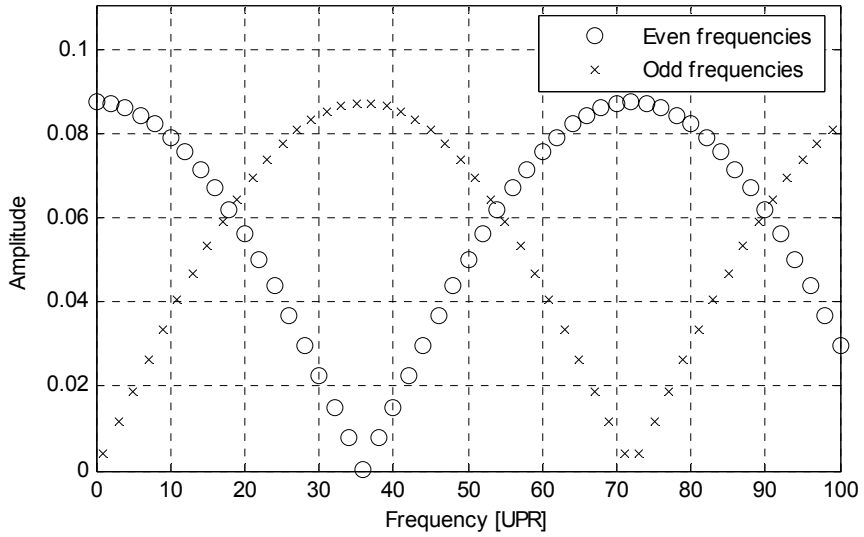

Figure 6-39: Amplitude of the vertical error motion for φ = 5°

Phase shifting signal B by $\pi - \varphi$ and subtracting the signals yields

$$\begin{aligned} m_A(\theta) - m_B(\theta + \pi - \varphi) = e_x(\theta) + e_x(\theta + \pi - \varphi) \\ + n_A(\theta) - n_B(\theta + \pi - \varphi) \end{aligned} \tag{6.111}$$

$$\begin{aligned} (M_A - e^{j(\pi-\varphi)k} M_B)(k) &= \mathcal{F}[m_A(\theta) - m_B(\theta)] \\ &= (1 + e^{j(\pi-\varphi)k}) E_x(k) \\ &\quad + N_A(k) - e^{j(\pi-\varphi)k} N_B(k) \end{aligned} \quad . \tag{6.112}$$

Here, any radius information is lost and only the horizontal motion and the random noise remain.

Therefore, for retrieval of the radius information, three different arithmetic operations for combining the signals of the two fingers are available (addition, subtraction, phase shift and addition). Each of them is prone to the disturbances in a different way. Knowledge of the disturbances is therefore required to decide which method of combination is most suitable. In addition to the method of combination, the

eccentricity angle is of importance, since it determines the amplitude attenuation and amplification of the radius and the disturbances. Within a certain range, the angle can be chosen arbitrarily during the setup of the gage head. The remainder of section 6.6 is therefore structured in the following way: section 6.6.7 introduces a simple disturbance model to quantify the effect of the individual disturbances on the restored radius. The following section describes methods to estimate the disturbances from the measurement data. Section 6.6.9 presents and discusses the decision rule to retrieve the radius from the different combinations of the signal. Section 6.6.10 derives an equation for the optimal finger angle based on the disturbance data. In section 6.6.11, a simple heuristic is explained that allows radius estimation without knowledge of the disturbances.

6.6.7 Modeling of the Disturbances

To model the disturbances, the harmonics of the horizontal and vertical error motions $E_x(k)$ and $E_y(k)$ and the random noise $N_A(k)$ and $N_B(k)$ are replaced by complex random variables $\boldsymbol{\mathcal{E}}_x(k)$, $\boldsymbol{\mathcal{E}}_y(k)$, $\boldsymbol{\mathcal{N}}_A(k)$, and $\boldsymbol{\mathcal{N}}_B(k)$, respectively. $E_x(k)$, $E_y(k)$, $N_A(k)$, and $N_B(k)$ are then regarded as a specific outcome of $\boldsymbol{\mathcal{E}}_x(k)$, $\boldsymbol{\mathcal{E}}_y(k)$, $\boldsymbol{\mathcal{N}}_A(k)$, and $\boldsymbol{\mathcal{N}}_B(k)$, respectively. For two real random variables X and Y, the complex random variable Z is defined as [Papoulis 1991]

$$Z = X + jY\,. \tag{6.113}$$

The expected value, variance, and covariance of a complex random variable are defined as

$$\mu_Z = \mathrm{E}[Z] = \mathrm{E}[X + jY] = \mathrm{E}[X] + j\,\mathrm{E}[Y] = \mu_X + j\mu_Y \tag{6.114}$$

$$\mathrm{Var}(Z) = \mathrm{E}\left[\,|\,Z - \mu_Z\,|^2\,\right] = \mathrm{E}\left[(Z-\mu_Z)(Z-\mu_Z)^*\right] = \mathrm{E}\left[\,|\,Z\,|^2\,\right] - \left|\mathrm{E}[Z]\right|^2 \tag{6.115}$$

$$\mathrm{Cov}(Z_1, Z_2) = \mathrm{E}\left[(Z_1-\mu_{Z_1})(Z_2-\mu_{Z_2})^*\right] = \mathrm{E}\left[Z_1 Z_2^*\right] - \mu_{Z_1}\mu_{Z_2}^*, \tag{6.116}$$

where * denotes the complex conjugate. The expected value and the variance of complex random variables have similar properties as their counterpart for real random variables. Some of these properties are listed here, since they will be used in the following analysis. The expected value of a linear combination of N complex random variables $Z_1, Z_2, ..., Z_N$ is given by

$$\mathrm{E}\left[a_1 Z_1 + a_2 Z_2 + ... + a_N Z_N\right] = a_1 Z_1 + a_2 Z_2 + ... + a_N Z_N\,. \tag{6.117}$$

The expected value of a product of two complex random variables can be calculated by

$$\mathrm{E}\left[Z_1 Z_2\right] = \mu_{Z_1}\mu_{Z_2} + \mathrm{Cov}(Z_1, Z_2^*), \tag{6.118}$$

which follows directly from (6.116). If N complex random variables are independent, the variance of a linear combination becomes

$$\mathrm{Var}(a_1 Z_1 + a_2 Z_2 + \ldots + a_N Z_N) = a_1^2\sigma_{Z_1}^2 + a_2^2\sigma_{Z_2}^2 + \ldots + a_N^2\sigma_{Z_N}^2. \tag{6.119}$$

It is assumed that the random variables of the disturbances have an expected value of zero, i.e.

$$\mathrm{E}\left[\boldsymbol{\mathcal{E}}_x(k)\right] = \mu_{\mathcal{E}_x} = 0 \tag{6.120}$$

$$\mathrm{E}\left[\boldsymbol{\mathcal{E}}_y(k)\right] = \mu_{\mathcal{E}_y} = 0 \tag{6.121}$$

$$\mathrm{E}\left[\boldsymbol{\mathcal{N}}_A(k)\right] = \mu_{\mathcal{N}_A} = 0 \tag{6.122}$$

$$\mathrm{E}\left[\boldsymbol{\mathcal{N}}_B(k)\right] = \mu_{\mathcal{N}_B} = 0 \tag{6.123}$$

and the variances are given by

$$\mathrm{Var}(\boldsymbol{\mathcal{E}}_x(k)) = \sigma_{\mathcal{E}_x}^2(k) \tag{6.124}$$

$$\mathrm{Var}(\boldsymbol{\mathcal{E}}_y(k)) = \sigma_{\mathcal{E}_y}^2(k) \tag{6.125}$$

$$\mathrm{Var}(\boldsymbol{\mathcal{N}}_A(k)) = \sigma_{\mathcal{N}_A}^2(k) \tag{6.126}$$

$$\mathrm{Var}(\boldsymbol{\mathcal{N}}_B(k)) = \sigma_{\mathcal{N}_B}^2(k). \tag{6.127}$$

For the eccentricity angle φ, a real random variable Φ is introduced. φ is then one specific outcome of Φ. The expected value and variance of Φ are

$$\mathrm{E}[\Phi] = \mu_{\Phi} \tag{6.128}$$

$$\mathrm{Var}(\Phi) = \sigma_{\Phi}{}^{2}. \tag{6.129}$$

It is assumed that all random variables are independent and the covariance between any two of them is zero. As a result of defining these random variables, the measurements at finger A and B $M_A(k)$ and $M_B(k)$ become the random variables $\boldsymbol{\mathcal{M}}_A(k)$ and $\boldsymbol{\mathcal{M}}_B(k)$.

The equations for combining the two finger signals from the previous section allow determining estimates $\tilde{R}(k)$ of the radius harmonics. Using sum of the signals and replacing all variables by their respective random variables

$$\begin{aligned}(\boldsymbol{\mathcal{M}}_A + \boldsymbol{\mathcal{M}}_B)(k) = {} & (1+e^{-j(\pi-\Phi)k})\cos(\Phi/2)\,R(k) \\ & -2\tan(\Phi/2)\boldsymbol{\mathcal{E}}_y(k) + \boldsymbol{\mathcal{N}}_A(k) + \boldsymbol{\mathcal{N}}_B(k)\end{aligned} \tag{6.130}$$

an estimate of the radius harmonics can be defined by

$$\tilde{R}_S(k) = \frac{(\boldsymbol{\mathcal{M}}_A + \boldsymbol{\mathcal{M}}_B)(k)}{(1+e^{-j(\pi-\mu_{\Phi})k})\cos(\mu_{\Phi}/2)}. \tag{6.131}$$

The expected value of $\tilde{R}_S(k)$ can be calculated by

$$\mathrm{E}\left[\tilde{R}_S(k)\right] = \mathrm{E}\left[\frac{(\boldsymbol{\mathcal{M}}_A + \boldsymbol{\mathcal{M}}_B)(k)}{(1+e^{-j(\pi-\mu_{\Phi})k})\cos(\mu_{\Phi}/2)}\right]. \tag{6.132}$$

Substituting (6.130) into (6.132) yields

$$\begin{aligned}\mathrm{E}\left[\tilde{R}_S(k)\right] = {} & \frac{1}{(1+e^{-j(\pi-\mu_{\Phi})k})\cos(\mu_{\Phi}/2)} \\ & \Big(\mathrm{E}\left[(1+e^{-j(\pi-\Phi)k})\cos(\Phi/2)\,R(k)\right] \\ & -2\,\mathrm{E}\left[\tan(\Phi/2)\boldsymbol{\mathcal{E}}_y(k)\right] + \mathrm{E}\left[\boldsymbol{\mathcal{N}}_A(k)\right] + \mathrm{E}\left[\boldsymbol{\mathcal{N}}_B(k)\right]\Big)\end{aligned} \tag{6.133}$$

With (6.122), (6.123), and the fact that $\mathrm{Cov}(\Phi, \mathcal{E}_y(k)) = 0$ this simplifies to

$$\begin{aligned} \mathrm{E}\left[\tilde{R}_S(k)\right] = & \frac{1}{(1+e^{-j(\pi-\mu_\Phi)k})\cos(\mu_\Phi/2)} \\ & \left(R(k)\,\mathrm{E}\left[(1+e^{-j(\pi-\Phi)k})\cos(\Phi/2)\right]\right. \\ & \left.-2\,\mathrm{E}\left[\tan(\Phi/2)\right]\mathrm{E}\left[\mathcal{E}_y(k)\right]\right) \end{aligned} \tag{6.134}$$

and with (6.121) to

$$\mathrm{E}\left[\tilde{R}_S(k)\right] = \frac{\mathrm{E}\left[(1+e^{-j(\pi-\Phi)k})\cos(\Phi/2)\right]}{(1+e^{-j(\pi-\mu_\Phi)k})\cos(\mu_\Phi/2)} R(k). \tag{6.135}$$

To simplify the expected value further, a function $g(\Phi)$ is defined

$$g(\varphi) = (1+e^{-j(\pi-\varphi)k})\cos(\varphi/2) \tag{6.136}$$

so that

$$\mathrm{E}\left[\tilde{R}_S(k)\right] = \frac{\mathrm{E}\left[g(\Phi)\right]}{(1+e^{-j(\pi-\mu_\Phi)k})\cos(\mu_\Phi/2)} R(k). \tag{6.137}$$

The expected value of $g(\Phi)$ is defined as [Devore 1995]

$$\mathrm{E}\left[g(\Phi)\right] = \int_{-\infty}^{\infty} g(\varphi) f(\varphi) d\varphi, \tag{6.138}$$

where $f(\varphi)$ is the probability density function of Φ. Approximating $g(\varphi)$ by a Taylor series at the expected value μ_Φ yields

$$\begin{aligned} g(\varphi) \simeq & g(\mu_\Phi) + g'(\mu_\Phi)(\varphi-\mu_\Phi) + g''(\mu_\Phi)\frac{(\varphi-\mu_\Phi)^2}{2} + \ldots \\ & + g^{(n)}(\mu_\Phi)\frac{(\varphi-\mu_\Phi)^n}{n!} \end{aligned}. \tag{6.139}$$

Inserting into (6.138) gives the expected value of $g(\Phi)$ as a linear combination of the central moments of Φ

$$\mathrm{E}\left[g(\Phi)\right] \simeq g(\mu_\Phi) + g'(\mu_\Phi)\mu_1 + g''(\mu_\Phi)\frac{\mu_2}{2} + \ldots + g^{(n)}(\mu_\Phi)\frac{\mu_n}{n!}, \tag{6.140}$$

where the *n*-th central moment μ_n is defined as [Papoulis 1991]

$$\mu_n = \mathrm{E}\left[(\varphi - \mu_\Phi)^n\right] = \int_{-\infty}^{\infty} (\varphi - \mu_\Phi)^n f(\varphi) d\varphi . \tag{6.141}$$

In particular, the first and the second central moment are

$$\mu_1 = 0 \tag{6.142}$$

$$\mu_2 = \sigma^2 \tag{6.143}$$

so that the expected value of $g(\Phi)$ becomes

$$\mathrm{E}\left[g(\Phi)\right] \simeq g(\mu_\Phi) + g''(\mu_\Phi)\frac{\sigma^2}{2} + \ldots + g^{(n)}(\mu_\Phi)\frac{\mu_n}{n!} . \tag{6.144}$$

Assuming that the variance of Φ is small and that $g(\Phi)$ can be approximated by a linear function in the vicinity of μ_Φ this results in

$$\mathrm{E}\left[g(\Phi)\right] \simeq g(\mu_\Phi) . \tag{6.145}$$

Using this result in (6.135) leads to

$$\mathrm{E}\left[\tilde{R}_S(k)\right] \simeq R(k) . \tag{6.146}$$

The expected value of the estimated radius harmonic $\tilde{R}_S(k)$ is the true harmonic of the radius. $\tilde{R}_S(k)$ is therefore an unbiased estimation. Similarly to $\tilde{R}_S(k)$, an estimation based on the difference of the signals

$$\begin{aligned}(\boldsymbol{\mathcal{M}}_A - \boldsymbol{\mathcal{M}}_B)(k) = (1 - e^{-j(\pi-\Phi)k})\cos(\Phi/2)\,R(k) \\ + 2\boldsymbol{\mathcal{E}}_x(k) + \boldsymbol{\mathcal{N}}_A(k) - \boldsymbol{\mathcal{N}}_B(k)\end{aligned} \tag{6.147}$$

can be defined by

$$\tilde{R}_D(k) = \frac{(\boldsymbol{\mathcal{M}}_A - \boldsymbol{\mathcal{M}}_B)(k)}{(1 - e^{-j(\pi-\mu_\Phi)k})\cos(\mu_\Phi/2)} \tag{6.148}$$

or based on the phase shifted sum with a phase shift of $\pi - \mu_\varphi$

$$\begin{aligned}(\boldsymbol{\mathcal{M}}_A + e^{j(\pi-\mu_\varphi)k}\boldsymbol{\mathcal{M}}_B)(k) = (1 + e^{j(\Phi-\mu_\varphi)k})\cos(\Phi/2)R(k) \\ + (1 - e^{j(\pi-\mu_\varphi)k})\boldsymbol{\mathcal{E}}_x(k) \\ - (1 + e^{j(\pi-\mu_\varphi)k})\tan(\Phi/2)\boldsymbol{\mathcal{E}}_y(k) \\ + \boldsymbol{\mathcal{N}}_A(k) + e^{j(\pi-\mu_\varphi)k}\boldsymbol{\mathcal{N}}_B(k)\end{aligned} \tag{6.149}$$

by

$$\tilde{R}_{PS}(k) = \frac{(\boldsymbol{\mathcal{M}}_A + e^{j(\pi-\mu_\Phi)k}\boldsymbol{\mathcal{M}}_B)(k)}{2\cos(\mu_\Phi/2)}\,. \tag{6.150}$$

In the same manner as it was shown for $\tilde{R}_S(k)$, it can be shown that the estimates $\tilde{R}_D(k)$ and $\tilde{R}_{PS}(k)$ are unbiased as well.

Besides the expected value, the variance of the estimate is of importance. For the sum of the signals

$$\begin{aligned}(\boldsymbol{\mathcal{M}}_A + \boldsymbol{\mathcal{M}}_B)(k) = (1 + e^{-j(\pi-\Phi)k})\cos(\Phi/2)\,R(k) \\ - 2\tan(\Phi/2)\boldsymbol{\mathcal{E}}_y(k) + \boldsymbol{\mathcal{N}}_A(k) + \boldsymbol{\mathcal{N}}_B(k)\end{aligned}\,, \tag{6.151}$$

the variance of $\tilde{R}_S(k)$ is given by

$$\mathrm{Var}\left(\tilde{R}_S(k)\right) = \mathrm{Var}\left(\frac{(\boldsymbol{\mathcal{M}}_A + \boldsymbol{\mathcal{M}}_B)(k)}{(1+e^{-j(\pi-\mu_\Phi)k})\cos(\mu_\Phi/2)}\right). \tag{6.152}$$

Substituting (6.151) into (6.152) results in

$$\begin{aligned}\mathrm{Var}\left(\tilde{R}_S(k)\right) = \mathrm{Var}\Big(&(1+e^{-j(\pi-\Phi)k})\cos(\Phi/2)\,R(k)\\ &-2\tan(\Phi/2)\boldsymbol{\mathcal{E}}_y(k)+\boldsymbol{\mathcal{N}}_A(k)+\boldsymbol{\mathcal{N}}_B(k)\Big).\\ &\Big/(1+e^{-j(\pi-\mu_\Phi)k})\cos(\mu_\Phi/2)\end{aligned} \tag{6.153}$$

Since all random variables are assumed to be independent and with the additional assumption that the variances are small, the error propagation law can be applied [Deming 1943]

$$\mathrm{Var}\left(\tilde{R}_S(k)\right) \approx \left|\frac{\partial\tilde{R}_S(k)}{\partial\Phi}\right|^2 \sigma_\Phi{}^2 + \left|\frac{\partial\tilde{R}_S(k)}{\partial\boldsymbol{\mathcal{E}}_y}\right|^2 \sigma_{\mathcal{E}_y}{}^2 + \left|\frac{\partial\tilde{R}_S(k)}{\partial\boldsymbol{\mathcal{N}}_A}\right|^2 \sigma_{\mathcal{N}_A}{}^2 + \left|\frac{\partial\tilde{R}_S(k)}{\partial\boldsymbol{\mathcal{N}}_B}\right|^2 \sigma_{\mathcal{N}_B}{}^2. \tag{6.154}$$

The squared absolute partial derivatives act as weights of the four disturbance variances, determining to what extent each disturbance contributes to the overall variance. They are given by (Appendix B.2)

$$\left|\frac{\partial\tilde{R}_S(k)}{\partial\Phi}\right|^2 \approx \frac{\left(\frac{k^2}{2}+\frac{1}{4}+\left(\frac{k^2}{2}-\frac{1}{4}\right)\cos(\mu_\varphi)\right)\left|R(k)\right|^2}{\left(1+(-1)^k\cos(\mu_\Phi k)\right)\left(1+\cos(\mu_\varphi)\right)} \tag{6.155}$$

$$\left|\frac{\partial\tilde{R}_S(k)}{\partial\boldsymbol{\mathcal{E}}_y}\right|^2 = \frac{4\tan^2(\frac{1}{2}\mu_\varphi)}{\left(1+(-1)^k\cos(\mu_\Phi k)\right)\left(1+\cos(\mu_\varphi)\right)} \tag{6.156}$$

$$\left|\frac{\partial\tilde{R}_S(k)}{\partial\boldsymbol{\mathcal{N}}_A}\right|^2 = \frac{1}{\left(1+(-1)^k\cos(\mu_\Phi k)\right)\left(1+\cos(\mu_\varphi)\right)} \tag{6.157}$$

$$\left|\frac{\partial \tilde{R}_S(k)}{\partial \mathcal{N}_B}\right|^2 = \frac{1}{\left(1+(-1)^k \cos(\mu_\Phi k)\right)\left(1+\cos(\mu_\varphi)\right)}. \tag{6.158}$$

The variance of $\tilde{R}_D(k)$ is given by

$$\mathrm{Var}\left(\tilde{R}_D(k)\right) \approx \left|\frac{\partial \tilde{R}_D(k)}{\partial \Phi}\right|^2 {\sigma_\Phi}^2 + \left|\frac{\partial \tilde{R}_D(k)}{\partial \mathcal{E}_x}\right|^2 {\sigma_{\mathcal{E}_x}}^2 + \left|\frac{\partial \tilde{R}_D(k)}{\partial \mathcal{N}_A}\right|^2 {\sigma_{\mathcal{N}_A}}^2 + \left|\frac{\partial \tilde{R}_D(k)}{\partial \mathcal{N}_B}\right|^2 {\sigma_{\mathcal{N}_B}}^2. \tag{6.159}$$

The squared partial derivatives can be obtained in the same way (Appendix B.3)

$$\left|\frac{\partial \tilde{R}_D(k)}{\partial \Phi}\right|^2 \approx \frac{\left(\frac{k^2}{2}+\frac{1}{4}+\left(\frac{k^2}{2}-\frac{1}{4}\right)\cos(\mu_\varphi)\right)\left|R(k)\right|^2}{\left(1+(-1)^{k+1}\cos(\mu_\Phi k)\right)\left(1+\cos(\mu_\varphi)\right)} \tag{6.160}$$

$$\left|\frac{\partial \tilde{R}_D(k)}{\partial \mathcal{E}_x}\right|^2 = \frac{4}{\left(1+(-1)^{k+1}\cos(\mu_\Phi k)\right)\left(1+\cos(\mu_\varphi)\right)} \tag{6.161}$$

$$\left|\frac{\partial \tilde{R}_D(k)}{\partial \mathcal{N}_A}\right|^2 = \frac{1}{\left(1+(-1)^{k+1}\cos(\mu_\Phi k)\right)\left(1+\cos(\mu_\varphi)\right)} \tag{6.162}$$

$$\left|\frac{\partial \tilde{R}_D(k)}{\partial \mathcal{N}_B}\right|^2 = \frac{1}{\left(1+(-1)^{k+1}\cos(\mu_\Phi k)\right)\left(1+\cos(\mu_\varphi)\right)}. \tag{6.163}$$

The variance of $\tilde{R}_{PS}(k)$ is (Appendix B.4)

$$\begin{aligned}\mathrm{Var}\left(\tilde{R}_{PS}(k)\right) \approx & \left|\frac{\partial \tilde{R}_{PS}(k)}{\partial \Phi}\right|^2 {\sigma_\Phi}^2 + \left|\frac{\partial \tilde{R}_{PS}(k)}{\partial \mathcal{E}_x}\right|^2 {\sigma_{\mathcal{E}_x}}^2 + \left|\frac{\partial \tilde{R}_{PS}(k)}{\partial \mathcal{E}_y}\right|^2 {\sigma_{\mathcal{E}_y}}^2 \\ & + \left|\frac{\partial \tilde{R}_{PS}(k)}{\partial \mathcal{N}_A}\right|^2 {\sigma_{\mathcal{N}_A}}^2 + \left|\frac{\partial \tilde{R}_{PS}(k)}{\partial \mathcal{N}_B}\right|^2 {\sigma_{\mathcal{N}_B}}^2\end{aligned} \tag{6.164}$$

with the squared partial derivatives

$$\left|\frac{\partial \tilde{R}_{PS}(k)}{\partial \Phi}\right|^2 = \frac{\left(\frac{k^2}{2}+\frac{1}{2}+(\frac{k^2}{2}-\frac{1}{2})\cos(\mu_\varphi)\right)\left|R(k)\right|^2}{2\left(1+\cos(\mu_\varphi)\right)} \tag{6.165}$$

$$\left|\frac{\partial \tilde{R}_{PS}(k)}{\partial \boldsymbol{\mathcal{E}}_x}\right|^2 = \frac{2\left(1-(-1)^k\cos(\mu_\varphi k)\right)}{2\left(1+\cos(\mu_\varphi)\right)} \tag{6.166}$$

$$\left|\frac{\partial \tilde{R}_{PS}(k)}{\partial \boldsymbol{\mathcal{E}}_y}\right|^2 = \frac{2\tan^2(\mu_\varphi/2)\left(1+(-1)^k\cos(\mu_\varphi k)\right)}{2\left(1+\cos(\mu_\varphi)\right)} \tag{6.167}$$

$$\left|\frac{\partial \tilde{R}_{PS}(k)}{\partial \boldsymbol{\mathcal{N}}_A}\right|^2 = \frac{1}{2\left(1+\cos(\mu_\varphi)\right)} \tag{6.168}$$

$$\left|\frac{\partial \tilde{R}_{PS}(k)}{\partial \boldsymbol{\mathcal{N}}_B}\right|^2 = \frac{1}{2\left(1+\cos(\mu_\varphi)\right)}\,. \tag{6.169}$$

6.6.8 Disturbance Variances Estimation

To calculate the variances of $\tilde{R}_S(k)$, $\tilde{R}_D(k)$, and $\tilde{R}_{PS}(k)$ using equations (6.154), (6.159), and (6.164), respectively, the variances of the individual disturbances $\sigma_{\varepsilon_x}{}^2(k)$, $\sigma_{\varepsilon_y}{}^2(k)$, $\sigma_{N_A}{}^2(k)$, $\sigma_{N_B}{}^2(k)$, and $\sigma_{\Phi}{}^2$ need to be known. Determination of their exact value is not possible, but they can be estimated from a measurement series. Unless major hardware changes are made, it can be assumed that the variances of the disturbances remain approximately constant from measurement series to measurement series.

In addition to the disturbance variances, the Fourier transform of the radius $R(k)$ appears in the equation, which is the quantity that is actually to be estimated. An estimate of $R(k)$ is therefore also calculated from a measurement series. The data taken with the roundness machine is used for this purpose. Figure 6-40 shows the values of $|R(k)|$. For each frequency *k*, the values of $|R(k)|$ are averaged over all parts and all measurements per part.

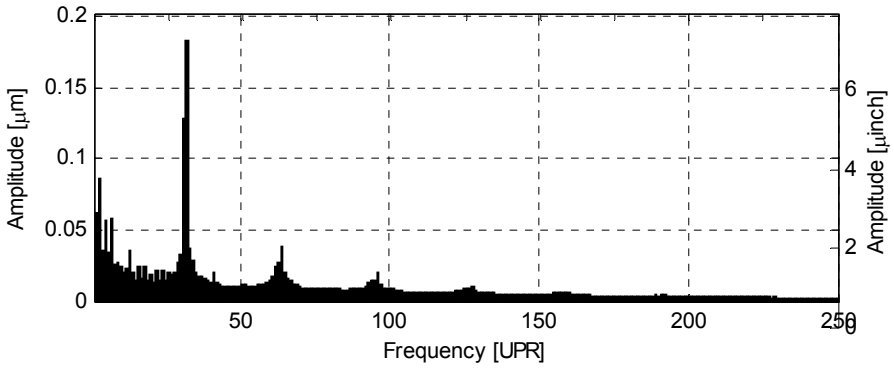

Figure 6-40: Spectrum of the roundness machine averaged over all parts and measurements

The variances $\sigma_{\mathcal{N}_A}{}^2(k)$ and $\sigma_{\mathcal{N}_B}{}^2(k)$ of the random noise can be estimated with the post-process machine with centrically placed fingers. Addition of the measurements of finger A and B in the frequency domain yields

$$(\mathcal{M}_A + \mathcal{M}_B)(k) = \begin{cases} 2R(k) + \mathcal{N}_A(k) + \mathcal{N}_B(k) & k = 0,2,4,... \\ \mathcal{N}_A(k) + \mathcal{N}_B(k) & k = 1,3,5,... \end{cases}. \tag{6.170}$$

For odd frequencies $k = 1,3,5,...$, the following equation holds for the variance

$$\mathrm{Var}\big((\mathcal{M}_A + \mathcal{M}_B)(k)\big) = \sigma_{\mathcal{N}_A}{}^2(k) + \sigma_{\mathcal{N}_B}{}^2(k). \tag{6.171}$$

Assuming that $\sigma_{\mathcal{N}_A}{}^2(k) = \sigma_{\mathcal{N}_B}{}^2(k)$

$$\sigma_{\mathcal{N}_A}{}^2(k) = \sigma_{\mathcal{N}_B}{}^2(k) = \tfrac{1}{2}\mathrm{Var}\big((\mathcal{M}_A + \mathcal{M}_B)(k)\big). \tag{6.172}$$

The variance values for the even frequencies are linearly interpolated from the two adjacent odd frequencies. The variance values are therefore given by

$$\sigma_{\mathcal{N}_A}{}^2(k) = \sigma_{\mathcal{N}_B}{}^2(k) = \begin{cases} \tfrac{1}{4}\mathrm{Var}\big((\mathcal{M}_A + \mathcal{M}_B)(k-1)\big) & \\ \quad + \tfrac{1}{4}\mathrm{Var}\big((\mathcal{M}_A + \mathcal{M}_B)(k+1)\big) & k = 2,4,6,... \\ \tfrac{1}{2}\mathrm{Var}\big((\mathcal{M}_A + \mathcal{M}_B)(k)\big) & k = 1,3,5,.. \end{cases}. \tag{6.173}$$

$\mathrm{Var}((\mathcal{M}_A + \mathcal{M}_B)(k))$ for a specific frequency k is estimated by calculating the sample variance using $(M_A + M_B)(k)$ for all parts and all measurements. Figure 6-41 shows the results using the measurement data from section 5.2 as an example. The plot shows the estimated values for the standard deviation $\sigma_{\mathcal{N}_A}(k)$ and $\sigma_{\mathcal{N}_B}(k)$ instead of the variance, since the unit of the standard deviation is easier to interpret.

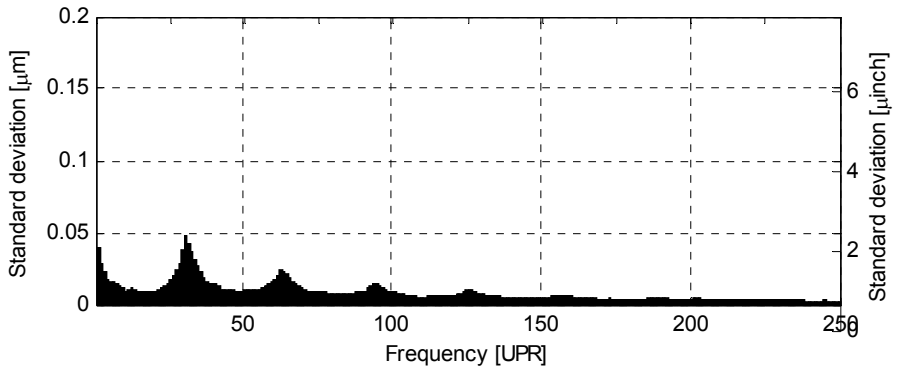

Figure 6-41: Standard deviation of the random noise

To determine an estimate for the variance $\sigma_{\varepsilon_x}{}^2(k)$ of the error motion in the *x*-direction, the same measurement series is used. Here, the difference of the measurements at finger A and B is computed.

$$(\mathcal{M}_A - \mathcal{M}_B)(k) = \begin{cases} 2\mathcal{E}_x(k) + \mathcal{N}_A(k) - \mathcal{N}_B(k) & k = 0,2,4,... \\ 2R(k) + 2\mathcal{E}_x(k) + \mathcal{N}_A(k) - \mathcal{N}_B(k) & k = 1,3,5,... \end{cases}. \tag{6.174}$$

For even frequencies $k = 0,2,4,...$, the following equation holds for the variance

$$\mathrm{Var}((\mathcal{M}_A - \mathcal{M}_B)(k)) = 4\sigma_{\varepsilon_x}{}^2(k) + \sigma_{\mathcal{N}_A}{}^2(k) + \sigma_{\mathcal{N}_B}{}^2(k). \tag{6.175}$$

Solving for $\sigma_{\varepsilon_x}{}^2(k)$ yields

$$\sigma_{\varepsilon_x}{}^2(k) = \tfrac{1}{4}\mathrm{Var}((\mathcal{M}_A - \mathcal{M}_B)(k)) - \tfrac{1}{2}\sigma_{\mathcal{N}_A}{}^2(k). \tag{6.176}$$

Using this equation for the even frequencies and interpolating linearly for the odd frequencies yields

$$\sigma_{\varepsilon_x}{}^2(k) = \begin{cases} \tfrac{1}{4}\mathrm{Var}\big((\mathcal{M}_A - \mathcal{M}_B)(k)\big) - \tfrac{1}{2}\sigma_{\mathcal{N}_A}{}^2(k) & k = 0,2,4,... \\ \tfrac{1}{8}\mathrm{Var}\big((\mathcal{M}_A - \mathcal{M}_B)(k-1)\big) - \tfrac{1}{4}\sigma_{\mathcal{N}_A}{}^2(k-1) & \\ \quad + \tfrac{1}{8}\mathrm{Var}\big((\mathcal{M}_A - \mathcal{M}_B)(k+1)\big) - \tfrac{1}{4}\sigma_{\mathcal{N}_A}{}^2(k+1) & k = 1,3,5,.. \end{cases}, \tag{6.177}$$

where $\sigma_{N_A}(k)$ is obtained from equation (6.173). Var($(\mathcal{M}_A - \mathcal{M}_B)(k)$) for a specific frequency *k* is estimated by calculating the sample variance using $(M_A - M_B)(k)$ for all parts and all measurements. The results expressed again as the standard deviation $\sigma_{\varepsilon_x}(k)$ using the data from section 5.2 are shown in Figure 6-42.

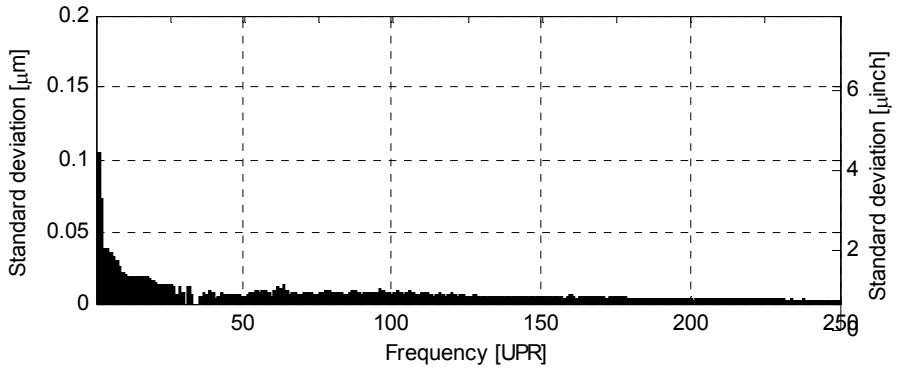

Figure 6-42: Standard deviation of the error motion in the *x*-direction

To estimate the variance of the error motion in *y*-direction, the same procedure is used as for the *x*-direction except that a configuration with vertically placed fingers at the 12 o'clock and 6 o'clock position has to be used. The variance is then estimated by

$$\sigma_{\varepsilon_y}{}^2(k) = \begin{cases} \frac{1}{4}\mathrm{Var}\left((\mathcal{M}_A - \mathcal{M}_B)(k)\right) - \frac{1}{2}\sigma_{N_A}{}^2(k) & k = 0,2,4,... \\ \frac{1}{8}\mathrm{Var}\left((\mathcal{M}_A - \mathcal{M}_B)(k-1)\right) - \frac{1}{4}\sigma_{N_A}{}^2(k-1) & \\ \quad + \frac{1}{8}\mathrm{Var}\left((\mathcal{M}_A - \mathcal{M}_B)(k+1)\right) - \frac{1}{4}\sigma_{N_A}{}^2(k+1) & k = 1,3,5,.. \end{cases} . \qquad (6.178)$$

A plot of the resulting standard deviation $\sigma_{\varepsilon_y}(k)$ is shown in Figure 6-43. To obtain the plot, the measurement series from section 5.3 with vertically placed fingers was used. As expected, the standard deviation $\sigma_{\varepsilon_y}(k)$ is much higher than $\sigma_{\varepsilon_x}{}^2(k)$.

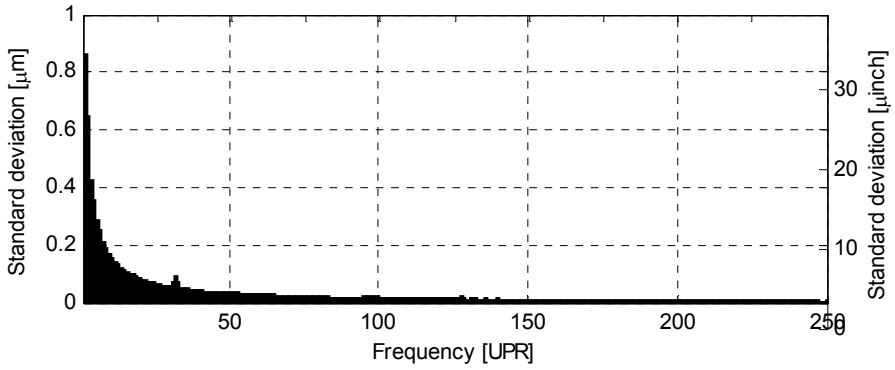

Figure 6-43: Standard deviation of the error motion in the *y*-direction

For the estimation of the finger angle variance σ_{Φ}^{2}, a measurement series is conducted with parts that contain a notch on the surface in the axial direction. The notch appears as a sharp peak in the measurement. To account for the variation of the finger angle due to differences in the outer diameters of the parts, 11 notched parts were used for the measurements. Figure 6-44 shows the measured profile of one of these parts. Each part is measured for 100 revolutions. For each part, the beginning of the notch and its approximate length in data points is identified manually. The reoccurrence is then sought for by using the AMDF for shape comparison similar to the profile length estimation in section 6.2.3. Using notched parts instead of arbitrary test parts as in section 6.2.3 has the advantage that the finger angle variation is estimated more accurately since the shape of the notch can be reliably recognized by the AMDF.

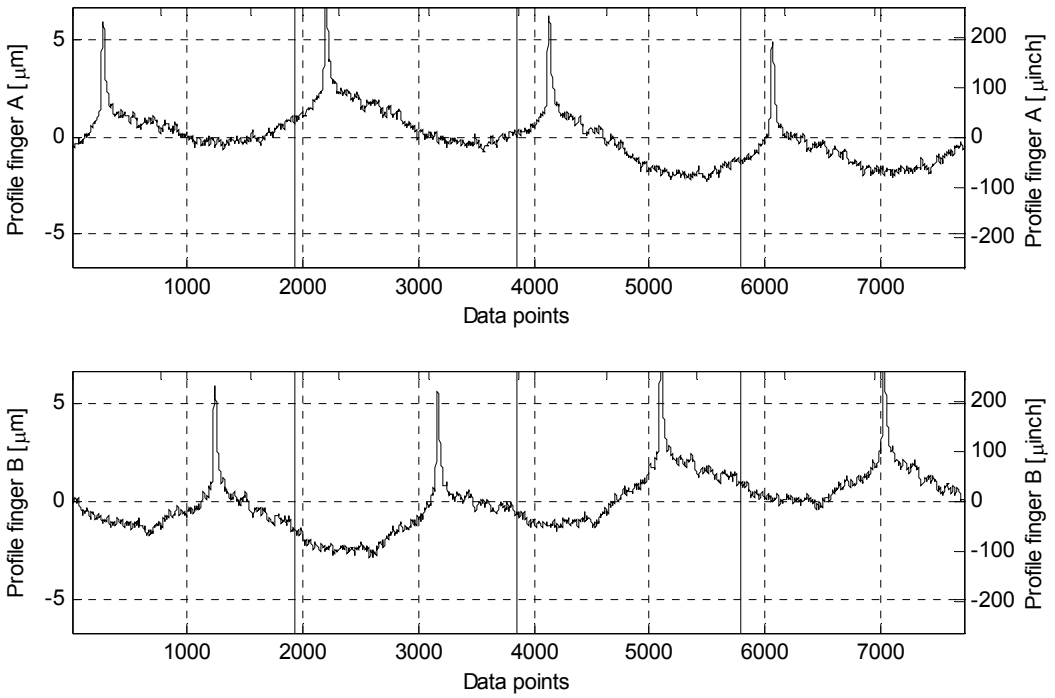

Figure 6-44: Profile of a part with a notch

If $N_R(k)$ denotes the number of data points between adjacent occurrences of the notch and $\bar{N}_R$ denotes the average of $N_R(k)$ across all revolutions and all parts, then the deviation of the finger angle in degrees is calculated by

$$\Delta\varphi = \frac{N_R(k) - \bar{N}_R}{\bar{N}_R} \cdot 360° . \tag{6.179}$$

Using the results from the 11 notched test parts yielded a standard deviation of the finger angle of $\sigma_\Phi = 0.213°$.

6.6.9 Final Radius Estimate

With $\tilde{R}_S(k)$, $\tilde{R}_D(k)$, and $\tilde{R}_{PS}(k)$ three radius estimates are available. With the variance equations from section 6.6.7 and the disturbance estimates of section 6.6.8, the variances of the radius estimates are available. Therefore, to determine a final radius estimate, for each individual frequency *k* the radius estimate with the lowest variance is picked

$$\tilde{R}(k) = \begin{cases} \tilde{R}_S(k) & \text{if } \min\left[\mathrm{Var}(\tilde{R}_S(k)), \mathrm{Var}(\tilde{R}_D(k)), \mathrm{Var}(\tilde{R}_{PS}(k))\right] = \mathrm{Var}(\tilde{R}_S(k)) \\ \tilde{R}_D(k) & \text{if } \min\left[\mathrm{Var}(\tilde{R}_S(k)), \mathrm{Var}(\tilde{R}_D(k)), \mathrm{Var}(\tilde{R}_{PS}(k))\right] = \mathrm{Var}(\tilde{R}_D(k)) \\ \tilde{R}_{PS}(k) & \text{if } \min\left[\mathrm{Var}(\tilde{R}_S(k)), \mathrm{Var}(\tilde{R}_D(k)), \mathrm{Var}(\tilde{R}_{PS}(k))\right] = \mathrm{Var}(\tilde{R}_{PS}(k)) \end{cases} . \quad (6.180)$$

The variance of $\tilde{R}(k)$ is then

$$\tilde{R}(k) = \min\left[\mathrm{Var}(\tilde{R}_S(k)), \mathrm{Var}(\tilde{R}_D(k)), \mathrm{Var}(\tilde{R}_{PS}(k))\right]. \quad (6.181)$$

It is expected that when comparing the variances of $\tilde{R}_S(k)$, $\tilde{R}_D(k)$, and $\tilde{R}_{PS}(k)$ for a specific frequency *k*, in most cases one of them will clearly have the lowest value. Therefore, small deviations in the disturbance variances will not alter the outcome of the comparison. Choosing the estimate with the lowest variance is therefore robust against small errors in the disturbance variances as they were estimated in section 6.6.8.

6.6.10 Determination of the Optimal Eccentricity Angle

It is desirable to keep the variance of the final estimate $\tilde{R}(k)$ small to obtain an estimate as close to the true value as possible. The expected value of the finger eccentricity angle μ_Φ is a setup parameter that unlike the error variances can be chosen arbitrarily. Its optimal value is the value that minimizes the variance of $\tilde{R}(k)$. To find this value, a performance index $T(\mu_\Phi)$ as a function of μ_Φ is defined. The performance index is the sum of the variances of $\tilde{R}(k)$ for all harmonics ranging from 1 UPR to infinity

$$\begin{aligned} T(\mu_\Phi) &= \sum_{k=1}^{\infty} w_k \operatorname{Var}(\tilde{R}(k)) \\ &= \sum_{k=1}^{\infty} w_k \min\left[\operatorname{Var}(\tilde{R}_S(k)), \operatorname{Var}(\tilde{R}_D(k)), \operatorname{Var}(\tilde{R}_{PS}(k))\right] \end{aligned} . \tag{6.182}$$

Each variance $\operatorname{Var}(\tilde{R}_S(k))$ is multiplied by a weight w_k in the summation. The weights allow optimizing the eccentricity angle for vibration separation at certain frequencies. In practical applications, the desired radius information is confined to a certain frequency band. In this case, the weights outside the frequency band can be set to zero or a very small value.

The performance index $T(\mu_\Phi)$ is a function that can have several minima. Numerical minimization methods may therefore not yield the global minimum. It is more appropriate to evaluate $T(\mu_\Phi)$ for a range of angles with small increments and choose the angle that yields the lowest value of $T(\mu_\Phi)$. Practically, the precision with which the eccentricity angle can be adjusted in a machine is limited so that it is not necessary to

have a very precise value of the optimal angle. In section 6.6.6 it was found that the lower boundary for the preset eccentricity angle μ_Φ is 0.213° to ensure that $\varphi > 0$ even in presence of vertical part motion. The upper boundary is given by the requirement to prevent stylus drag. A reasonable value is 5°. The performance index is therefore calculated for the interval

$$\mu_\Phi = [0.2°, 0.25°, 0.3°..., 5°] \tag{6.183}$$

and the value of μ_Φ yielding the lowest performance index is chosen.

6.6.11 Radius Estimate without Disturbance Information

In the previous two sections, methods were presented to estimate the radius and to determine a finger eccentricity angle. While the radius estimate and the eccentricity angle are optimal for the given disturbance estimates, they require the measurement of the disturbance standard deviations as described in section 6.6.8. The measurement procedure is time consuming since measurements with special test parts have to be performed and both the horizontal and vertical finger configuration has to be used, which requires changing the setup.

This section introduces a simple heuristic that attempts to estimate the radius without knowledge of the variances. The heuristic uses only the radius estimate based on the sum $\tilde{R}_S(k)$

$$\tilde{R}_S(k) = \frac{(\boldsymbol{M}_A + \boldsymbol{M}_B)(k)}{(1 + e^{-j(\pi - \mu_\Phi)k})\cos(\mu_\Phi/2)} \tag{6.184}$$

and on the phase shifted sum $\tilde{R}_{PS}(k)$

$$\tilde{R}_{PS}(k) = \frac{(\boldsymbol{\mathcal{M}}_A + e^{j(\pi-\mu_\Phi)k}\boldsymbol{\mathcal{M}}_B)(k)}{2\cos(\mu_\Phi/2)}. \tag{6.185}$$

The radius estimate based on the difference of the signals $\tilde{R}_D(k)$ is disregarded since it does not reject the error motion in the *x*-direction. The estimate $\tilde{R}_S(k)$ has the advantage that it eliminates the *x*-error motion but also amplifies the random noise significantly for certain frequencies when the denominator in equation (6.184) becomes small. $\tilde{R}_{PS}(k)$ does not suffer from the random noise amplification, since its denominator is constant. On the other hand, it only attenuates the error motions in the *x*- and *y*-direction but does not eliminate them completely. The amount of attenuation varies for different frequencies. The decision rule for choosing between the estimator $\tilde{R}_S(k)$ and $\tilde{R}_{PS}(k)$ is therefore to pick $\tilde{R}_S(k)$ whenever the amplification of $\boldsymbol{\mathcal{M}}_A + \boldsymbol{\mathcal{M}}_B$ due to a small denominator is below a critical amplification value κ_C and to pick $\tilde{R}_{PS}(k)$ otherwise

$$\tilde{R}_H(k) = \begin{cases} \tilde{R}_S(k) & \text{if } \dfrac{1}{\left|(1+e^{-j(\pi-\mu_\Phi)k})\cos(\mu_\Phi/2)\right|} \le \kappa_C \\ \tilde{R}_{PS}(k) & \text{otherwise} \end{cases}. \tag{6.186}$$

The value of κ_C determines which of the two estimators $\tilde{R}_S(k)$ and $\tilde{R}_{PS}(k)$ is given preference. κ_C is the largest amplification of the sum of the measurements $\boldsymbol{\mathcal{M}}_A + \boldsymbol{\mathcal{M}}_B$ and therefore also of the random noise $\boldsymbol{\mathcal{N}}_A$ and $\boldsymbol{\mathcal{N}}_B$, for which the estimator $\tilde{R}_S(k)$ is still chosen over the estimator $\tilde{R}_{PS}(k)$. It depends on the disturbances which value yields the best results. If the vibration is large compared to the random noise, a large value of κ_C should be chosen. If the vibration on the other hand is small compared to the random

noise, a small value of κ_C is more suitable. For practical applications, values of κ_C between 2 and 10 are reasonable.

From the heuristic, a method can be derived to determine the optimal finger eccentricity angle for vibration separation. The optimal angle for vibration separation is the angle that minimizes the following performance index

$$T_H(\mu_\varphi) = \sum_{k=1}^{\infty} w'_k \frac{1}{\left|(1+e^{-j(\pi-\mu_\Phi)k})\cos(\mu_\Phi/2)\right|}. \tag{6.187}$$

For each frequency *k*, a weight w'_k is defined that denotes the importance of the vibration separation for this particular frequency. The weights w'_k therefore have a different meaning than the weights w_k from section 6.6.10. The weights w_k in the previous section denote the relative importance of a low standard deviation for the individual frequencies. The values of w_k are therefore chosen based on for which frequencies information is desired. Opposite to that, the weights w'_k in equation (6.187) characterize the relative importance of vibration separation for individual frequencies. Their values are therefore chosen based on for what frequencies vibration is expected.

The minimum of the performance index $T_H(\mu_\varphi)$ can be determined numerically following the same procedure as outlined in section 6.6.10.

CHAPTER 7 – POST-PROCESS MACHINE MEASUREMENTS

7.1 Reference Measurements with the Roundness Machine

As reference measurements, the same data set is used that was acquired in section 5.1 with the roundness machine. In the following, the results from section 5.1.2 are extended by using the maximum profile amplitude and the profile difference as additional performance criteria.

The maximum profile amplitude obtained from the *m*-th measurement of the *n*-th part is denoted by $A_R(n,m)$ with $n = 1,2,...,126$ and $m = 1,...,5$. Similar to the profile height $h_R(n,m)$ in section 5.1.2, the maximum profile amplitude $A_R(n,m)$ can be used to classify the parts into the categories "good," "bad," and "good/bad" depending on the outcome of the five measurements. The critical maximum profile amplitude A_{crit} is set to 191 nm (7.5 µinch) as it was chosen in section 6.4.2. The results of the classification are shown in Table 7-1 along with the classification using the profile height for comparison.

Table 7-1: Classification of parts obtained from the roundness machine

Roundness Machine				
	Profile height h_R		Maximum profile amplitude A_R	
Classification	Quantity	Percentage	Quantity	Percentage
Good	44	(35%)	52	(41%)
Good/bad	34	(27%)	5	(4%)
Bad	48	(38%)	69	(55%)
Sum	126	(100%)	126	(100%)

The table demonstrates that by using the maximum profile amplitude as a criterion, the number of parts with inconsistent results in the five measurements is reduced from 34 to 5. This supports the earlier assumption that the maximum profile amplitude is the more robust criterion of the two.

From the individual five measurements $A_R(n,m)$, the average maximum profile amplitude $\overline{A}_R(n)$ is computed

$$\overline{A}_R(n) = \sum_{m=1}^{5} A_R(n,m), \quad n = 1,2,...,126. \tag{7.1}$$

$\overline{A}_R(n)$ is used as the reference value against which all other measurements are compared to. To assess the variability of the maximum profile amplitude, the distribution of the maximum profile amplitude error $\Delta A_R(n,m)$ defined as the difference between the maximum amplitude of the individual measurements from the average maximum amplitude

$$\Delta A_R(n,m) = A_R(n,m) - \overline{A}_R(n), \quad n = 1,2,...,126, \; m = 1,...,5 \tag{7.2}$$

is shown in Figure 7-1. The distribution mean is zero due to the definition of $\overline{A}_R(n)$ in equation (7.1). The standard deviation is 30.5 nm (1.202 μinch).

To calculate the profile difference, the five profile measurements are aligned as outlined in section 6.4.1 and the average profile $\overline{x}_R(n,k)$ for the *n*-th part is calculated from the five profiles by

$$\overline{x}_R(n,k) = \sum_{m=1}^{5} x_R(n,m,k), \quad n = 1,2,...,126, \; k = 0,...,N-1, \tag{7.3}$$

with N being the number of data points of the profile. The average profile $\overline{x}_R(n,k)$ is used as the reference profile against which all other measurements are compared to.

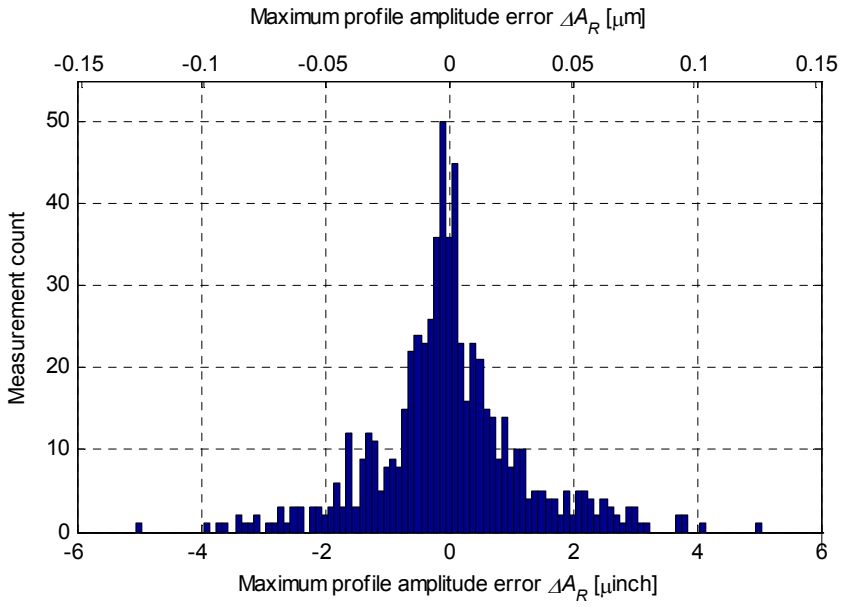

Figure 7-1: Distribution of the maximum profile amplitude error of the roundness machine

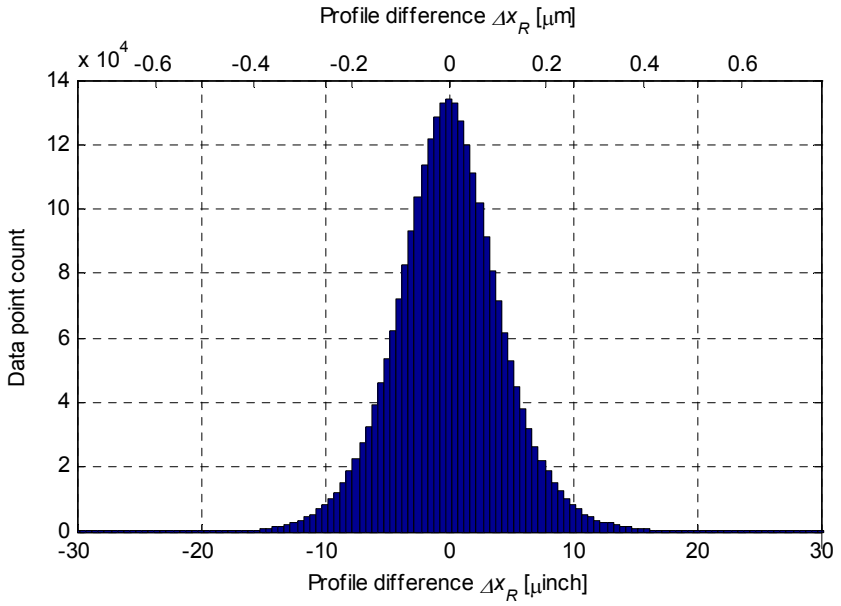

Figure 7-2: Distribution of the profile difference of the roundness machine

The profile difference $\Delta x_R(n,m,k)$ of the roundness machine is then given by

$$\Delta x_R(n,m,k) = x_R(n,m,k) - \bar{x}_R(n,k), \quad \begin{matrix} n = 1,2,...,126, \;\; m = 1,...,5, \\ k = 0,...,N-1 \end{matrix}. \tag{7.4}$$

Figure 7-2 displays the distribution of $\Delta x_R(n,m,k)$. Since an estimate of the profile difference is obtained for every data point, the number of estimates is very large and, as a result, the histogram clearly reveals the bell-shaped distribution of the profile difference. The mean is zero because of the definition of the average profile in (7.3). The standard deviation is 111.8 nm (4.403 μinch).

7.2 Measurements at Low Speed

7.2.1 Methodology

The reference measurements of the roundness machine are first compared with the post-process machine measurements from section 5.2. The parts were rotated with a speed of 0.9 rev/s (54 RPM) during the measurements. The results from section 5.2.2 are extended by using the maximum profile amplitude and the profile difference as additional criteria.

7.2.2 Results without Analytical Methods

The maximum profile amplitude of the measurements taken with the post-process machine is denoted by $A_P(n,m)$ with $n = 1,2,...,126$ and $m = 1,2$. The individual values for A_P from the two fingers are combined into one value by using the average of the two. The classification of the parts into "good," "bad," and "good/bad" using the maximum profile amplitude is shown in Table 7-2. The classification based on the profile height is listed for comparison as well.

It can be seen that the agreement between the two machines is better when the maximum profile amplitude is used. 100 % of all parts that were measured consistently as either "good" or "bad" on the roundness machine were also measured as "good" or "bad" respectively on the post-process machine. However, with the measurement series used here, the profile height yielded a good agreement between the machines as well, so that difference between the criteria is fairly small.

Table 7-2: Classification of the parts obtained from the post-process machine

	Roundness Machine		Post-process machine		
			Good	Good/Bad	Bad
Criterion	Classification	Quantity	Quantity	Quantity	Quantity
Profile height h_R, h_P	Good	44 (100%)	43 (97.7%)	0 (0.0%)	1 (2.3%)
	Good/bad	34 (100%)	10 (29.4%)	4 (11.8%)	20 (58.8%)
	Bad	48 (100%)	0 (0.0%)	0 (0.0%)	48 (100%)
Max. profile amplitude A_R, A_P	Good	52 (100%)	52 (100%)	0 (0.0%)	0 (0.0%)
	Good/bad	5 (100%)	2 (40.0%)	1 (20.0%)	2 (40.0%)
	Bad	69 (100%)	0 (0.0%)	0 (0.0%)	69 (100%)

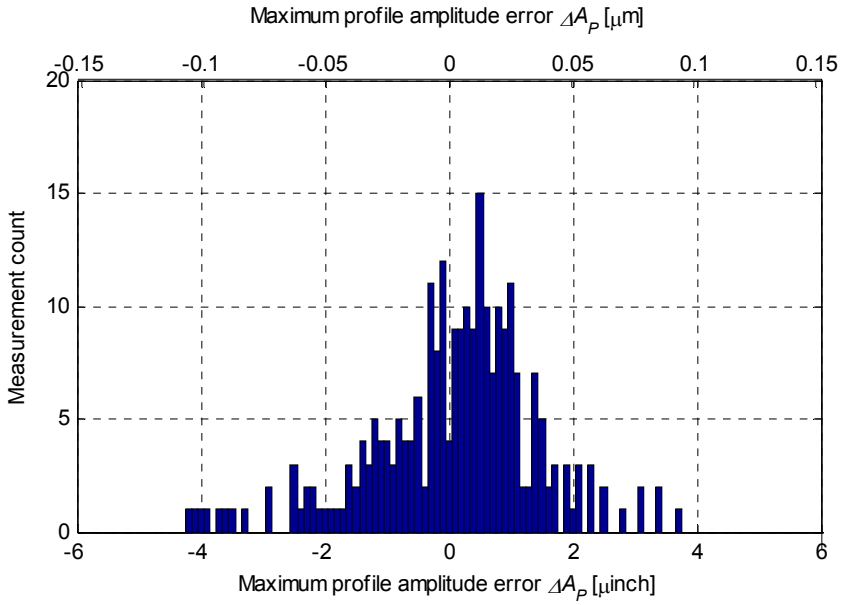

Figure 7-3: Distribution of maximum profile amplitude error of the post-process machine

The maximum profile amplitude error $\Delta A_p(n,m)$ for the post-process machine is defined by

$$\Delta A_P(n,m) = A_P(n,m) - \bar{A}_R(n), \quad n = 1,2,...,126, \quad m = 1,...,5. \tag{7.5}$$

Its distribution is plotted in Figure 7-3. The mean of the distribution is 2.1 nm (0.082 μinch) and the standard deviation is 34.4 nm (1.354 μinch).

The profile difference $\Delta x_P(n,m,k)$ is defined as the deviation of the profile data points from reference profile data points $\bar{x}_R(n,k)$

$$\Delta x_P(n,m,k) = x_P(n,m,k) - \bar{x}_R(n,k), \quad \begin{matrix} n = 1,2,...,126, \;\; m = 1,...,5, \\ k = 0,...,N-1 \end{matrix}. \tag{7.6}$$

The corresponding distribution is shown in Figure 7-4. The mean of the distribution is zero, since as mentioned in section 6.4.1, the means of all profiles are removed before the computation of the profile difference. The standard deviation of the distribution is 161.0 nm (6.339 μinch). The mean and the standard deviations for all three comparison criteria are summarized in Table 7-4.

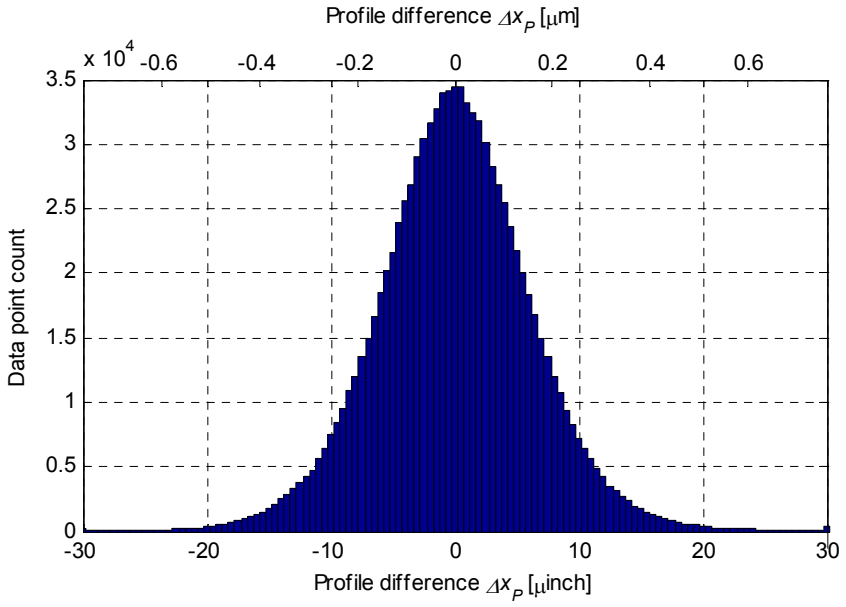

Figure 7-4: Distribution of the profile difference of the post-process machine

Table 7-3: Comparison between the roundness machine and the post-process machine

	Roundness machine		Post-process machine			
	Standard dev. / repeatability		Mean / bias		Standard dev. / repeatability	
Criterion	nm	(μinch)	nm	(μinch)	nm	(μinch)
Profile height error	176.4	(6.943)	75.7	(2.979)	156.0	(6.140)
Max. profile amplitude error	30.5	(1.202)	2.1	(0.082)	34.4	(1.354)
Profile difference	111.8	(4.403)			161.0	(6.339)

7.2.3 Results Using Analytical Methods

This section investigates if the measurement results can be improved by applying the analytical methods developed in Chapter 6. No major improvements are expected though, since the measurement data from the post-process machine is already in close agreement with the data acquired with the roundness machine.

First, the compensation of the gage transfer function is applied to the data. Although the parts were rotated slow enough so that the desired profile information is below the cutoff frequency of the gage head, compensating the transfer function may a lead to a small improvement since the frequency response is not constant below the cutoff frequency. The resulting classification of the parts into “good,” “bad,” “good/bad” is the same as in Table 7-1. The performance criteria for transfer function compensated measurements are listed in Table 7-3. Comparing the values with Table 7-3, it can be seen that a small improvement is achieved. The bias of the profile height decreases from 75.7 nm to 15.4 nm, the bias of the maximum profile amplitude from 2.1 nm to –0.8 nm. The standard deviation of the profile difference, which is the most reliable performance

criterion of the three, is reduced from 161.0 nm to 154.5 nm, which is equivalent to a 4 % reduction.

Table 7-4: Comparison using the transfer function compensation

	Roundness machine		Post-process machine			
	Standard dev. / repeatability		Mean / bias		Standard dev. / repeatability	
Criterion	nm	(µinch)	nm	(µinch)	nm	(µinch)
Profile height error	176.4	(6.943)	15.4	(0.605)	157.1	(6.185)
Max. profile amplitude error	30.5	(1.202)	–0.8	(–0.032)	35.3	(1.390)
Profile difference	111.8	(4.403)			154.5	(6.082)

Although the measurement system was not exposed to any severe vibration during the measurement series, the effect of the vibration separation methods on the measurement data is examined. Since the fingers were placed centrically in the setup, the corresponding separation model for centrically placed finger from section 6.6.5 has to be used. The most suitable way of removing the vibration is to shift the profile of finger B by 180° and then add the signals as expressed in equation (6.74). The resulting part classification is listed in Table 7-5 and is very similar to the classification without vibration separation. Using the profile height criterion, now all "good" parts are also detected as "good" with the post-process machine. This includes the part that was measured previously as "bad" due to a movement of the workpiece center. This indicates that the vibration separation filtered out the workpiece center motion. On the other hand, it can also be seen that one of the "bad" parts passed as "good" in one of the measurements.

Table 7-5: Part classification using the vibration separation

	Roundness Machine		Post-process machine		
			Good	Good/Bad	Bad
Criterion	Classification	Quantity	Quantity	Quantity	Quantity
Profile height h_R, h_P	Good	44 (100%)	44 (100%)	0 (0.0%)	0 (0.0%)
	Good/bad	34 (100%)	27 (79.4%)	1 (2.9%)	6 (17.6%)
	Bad	48 (100%)	0 (0.0%)	1 (2.1%)	47 (97.9%)
Max. profile amplitude A_R, A_P	Good	52 (100%)	52 (100%)	0 (0.0%)	0 (0.0%)
	Good/bad	5 (100%)	3 (60.0%)	0 (0.0%)	2 (40.0%)
	Bad	69 (100%)	0 (0.0%)	0 (0.0%)	69 (100%)

The remaining performance criteria are given in Table 7-6. It can be seen that both the profile height and the maximum profile amplitude tend to be lower than the corresponding values measured with the roundness machine which is indicated by the negative means. With vibration separation, the post-process machine therefore tends to shift from overpicking (rejecting "good" parts) to underpicking (passing "bad" parts), i.e. the type 1 error decreases while the type 2 error slightly increases. However, as it can be seen from Table 7-5, the underpicking is not severe. The standard deviation of the profile difference is smaller than without vibration separation. This suggests that the overall agreement between the post-process machine and the roundness machine is improved by the vibration separation.

Last, the effect of averaging over multiple revolutions is tested. The data set allows taking the average of up to 10 measurements. To account for the varying number of data points, the profile length is corrected for each measurement. The possible profile length is confined to the range of 1930 ± 20 data points. The window size is set to 100 data points. The performance criteria as a function of the number of averaged

measurements are shown in Figure 7-5. The profile height, the maximum profile amplitude, and the profile difference are averaged over all parts and measurements. The corresponding values of the roundness machine without averaging are plotted as well for comparison.

Table 7-6: Effect of the vibration separation

	Roundness machine		Post-process machine			
	Standard dev. / repeatability		Mean / bias		Standard dev. / repeatability	
Criterion	nm	(μinch)	nm	(μinch)	nm	(μinch)
Profile height error	176.4	(6.943)	–121.7	(–4.790)	159.4	(6.278)
Max. profile amplitude error	30.5	(1.202)	–1.3	(–0.052)	34.1	(1.341)
Profile difference	111.8	(4.403)			131.7	(5.186)

The graphs show that the profile heights h_P and the maximum profile amplitude A_P approach the corresponding values h_R and A_R of the roundness machine as the number of averaged measurements increases. The profile difference Δx_P decreases as well, indicating a better agreement between the profiles measured with the post-process machine and the roundness machine. It can be seen that the profile height and the maximum profile amplitude seem to converge against a value which would be the value in absence of random noise.

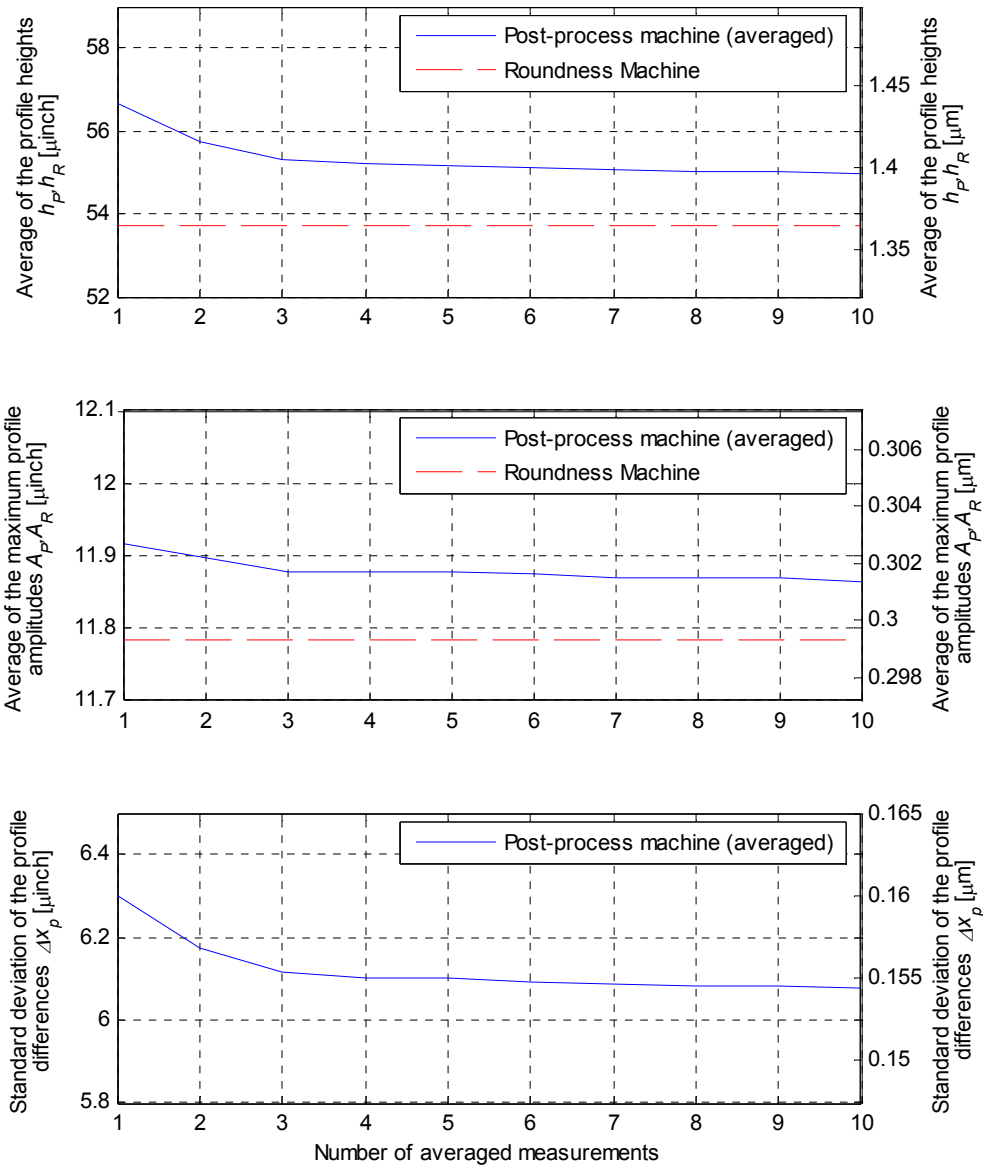

Figure 7-5: Effect of averaging on the performance criteria

The graphs also show that for the given data set, averaging more than 4 measurements yields only marginal improvements. In most cases, the small gain in accuracy does not justify the additional time for taking more measurements.

7.3 Measurements at High Speed

7.3.1 Methodology

In the previous section, the parts were rotated at 0.9 rev/s to ensure that the 250 UPR frequency remains below the natural frequency of the gage head. In a grinding machine, the parts are rotated at a much higher speed of 12.5–13.3 rev/s (750–800 RPM). This scenario is therefore tested with the post-process machine. In its original configuration, the maximum part speed of the post-process machine is approximately 5 rev/s (300 RPM). To achieve a higher speed, the pulleys of the roll drive train were replaced from a set with 60 and 60 grooves to a set with 120 and 40 grooves, yielding a gear ratio of 3. This allows parts speeds up to 15 rev/s (900 RPM) and covers the speed range of a grinding machine. A disadvantage of the different gear ratio is that the number of encoder pulses per part revolution is reduced by a factor of 3 to 644.

The cutoff frequency of the anti-aliasing filter was set to 1 kHz for the measurements series. The rotational speed of the part was approximately 14 rev/s (840 RPM). Every part was measured for slightly more than 20 revolutions until it was ejected to have sufficient data for averaging. Unlike the previous measurement series, all parts were loaded only once into the post-process machine.

7.3.2 Results

The effect of the high rotational speed on the measurement and the compensation of the gage transfer function are exemplified for a specific part in Figure 7-6 to Figure 7-9. Figure 7-6 displays the spectrum of a part when it was measured at the normal speed

of the post-process machine of 0.9 rev/s. In the spectrum, a dominant harmonic at 32 UPR with an amplitude of 1.24 µm is clearly visible. In addition, harmonics at multiples of 32 UPR, i.e. 64, 96, and 128 UPR can be seen as well. Rotating the same part at a speed of 14 rev/s significantly decreases the amplitudes in the spectrum due to the cutoff frequency of the gage head. The amplitude of the 32 UPR harmonic is reduced to 0.50 µm. The peaks at multiples of 32 UPR are completely erased. Above 64 UPR, the amplitudes seem to be zero. This is the result of the two low-pass filter with 1 kHz cutoff frequency, which corresponds to 72 UPR at the given part speed. Applying the transfer function compensation to the measurement yields the spectrum in Figure 7-8. As mentioned in section 6.5, the transfer function is compensated only up to 1 kHz since the attenuation above this frequency is to large. The compensation algorithm therefore leaves all harmonics above 72 UPR unchanged. Figure 7-8 shows that the amplitude of the 32 UPR harmonic is restored to its original value. The amplitude of the 64 UPR harmonic is visible again as well. However, the spectrum also shows several erroneous harmonic that stem from amplified noise, e.g. a peak with a large amplitude at 57 UPR. This noise amplification is unavoidable. The only way to lower its effect is to average several measurements. This is depicted in Figure 7-9 where 10 measurements are averaged. The harmonics of the noise are reduced and only the peaks at 32 and 64 UPR remain. The noise levels are almost the same as for the measurement at low speed with the only difference that the spectrum is virtually cut off above 72 UPR. It should be mentioned that the total time for 10 measurements at high speed is still lower than for the single measurements at low speed.

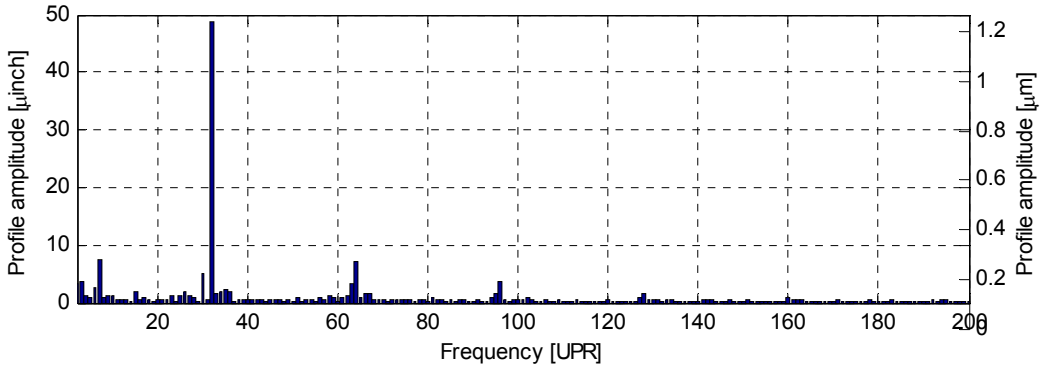

Figure 7-6: Spectrum of a part measured at 0.9 rev/s

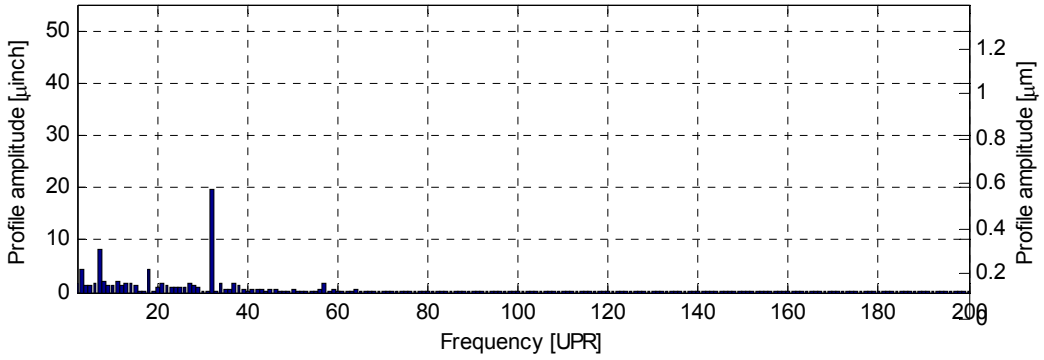

Figure 7-7: Spectrum of a part measured at 14 rev/s

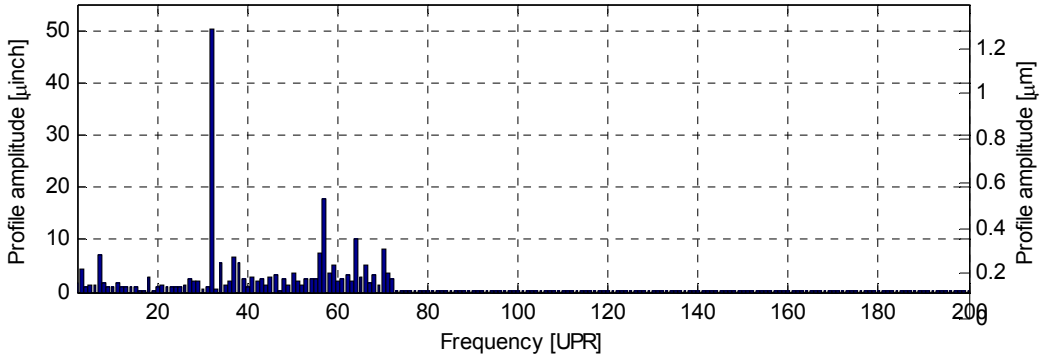

Figure 7-8: Spectrum of a part measured at 14 rev/s, compensated

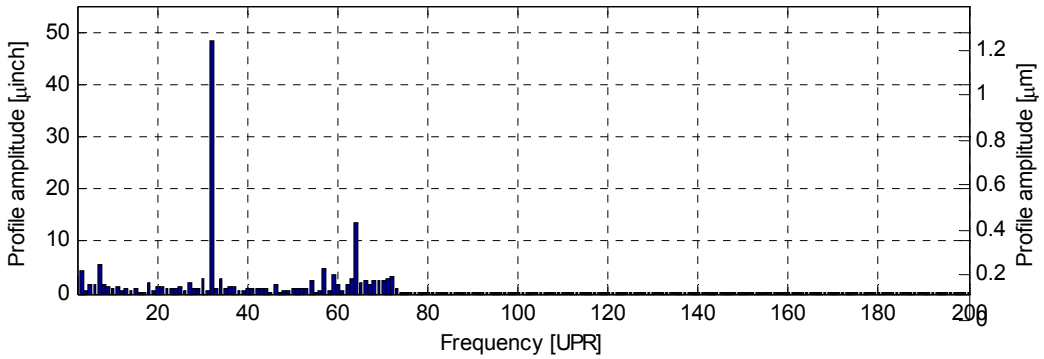

Figure 7-9: Spectrum of a part, average of 10 measurements

Figure 7-10 shows the effect of the transfer function compensation and of the averaging on the performance criteria using all test parts. The first bar in the graphs represents the corresponding value obtained with the roundness machine. The remaining bars refer to measurements with the post-process. The graphs exhibit a behavior that is in accordance with the spectra in Figure 7-6 to Figure 7-9. For uncompensated measurements, the profile heights h_P and the maximum amplitudes A_P are lower than the respective values of the roundness due to the attenuation of the gage head. After the transfer function compensation, they are higher since all random noise is amplified. The percent deviation from the roundness machine values is higher for the profile height than for the maximum amplitude again supporting the earlier observation that A_P is more robust against noise than h_P. Averaging several measurements improves the performance again. When averaging 20 measurements, the profile heights h_P and maximum profile amplitudes A_P were at the same level as for the roundness machine. A good agreement was already achieved with the average of 10 measurements.

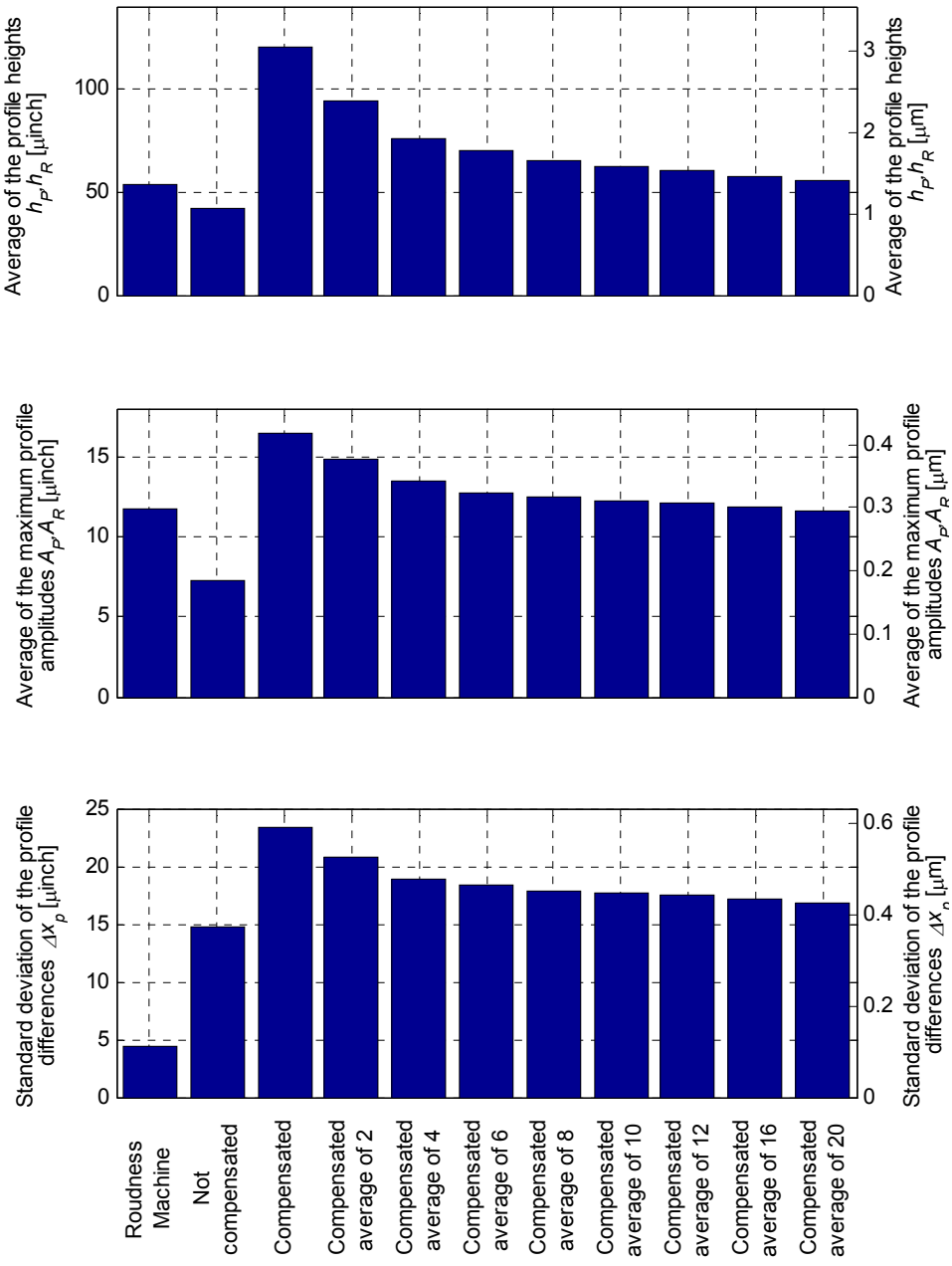

Figure 7-10: Effect of transfer function compensation and averaging

The standard deviation of the profile differences remains at a much higher level than for the measurements at low speed (Table 7-3), even when 20 measurements are averaged. This can be explained by the fact that the spectrum is virtually cut off at 72 UPR which is not improved by the averaging.

Table 7-7: Part classification for high speed measurements

	Roundness Machine		Post-process machine		
			Good	Good/Bad	Bad
Criterion	Classification	Quantity	Quantity	Quantity	Quantity
Profile height h_R, h_P	Good	44 (100%)	41 (93.2%)	0 (0.0%)	3 (6.8%)
	Good/bad	34 (100%)	7 (20.6%)	0 (0.0%)	27 (79.4%)
	Bad	48 (100%)	0 (0.0%)	0 (0.0%)	48 (100%)
Max. profile amplitude A_R, A_P	Good	52 (100%)	49 (94.2%)	0 (0.0%)	3 (5.8%)
	Good/bad	5 (100%)	2 (40.0%)	0 (0.0%)	4 (60.0%)
	Bad	69 (100%)	1 (1.4%)	0 (0.0%)	68 (98.6%)

Table 7-7 shows the part classification for the high speed measurements series using the transfer function compensation and averaging over 10 measurements. The results are close to the ones obtained at low speed.

7.4 Measurements with Forced Vibration

7.4.1 Methodology

To test the vibration separation algorithms, a test series was conducted under artificially introduced vibration. For this purpose, a vibration exciter was attached to the bracket of the gage head as shown in Figure 7-11. The exciter was made by Brüel & Kjær and is driven by a power amplifier from the same manufacturer. A Tektronix signal generator is used to generate the excitation signal. With the aid of a force transducer, which is mounted between the shaker and the gage bracket, the excitation can be monitored.

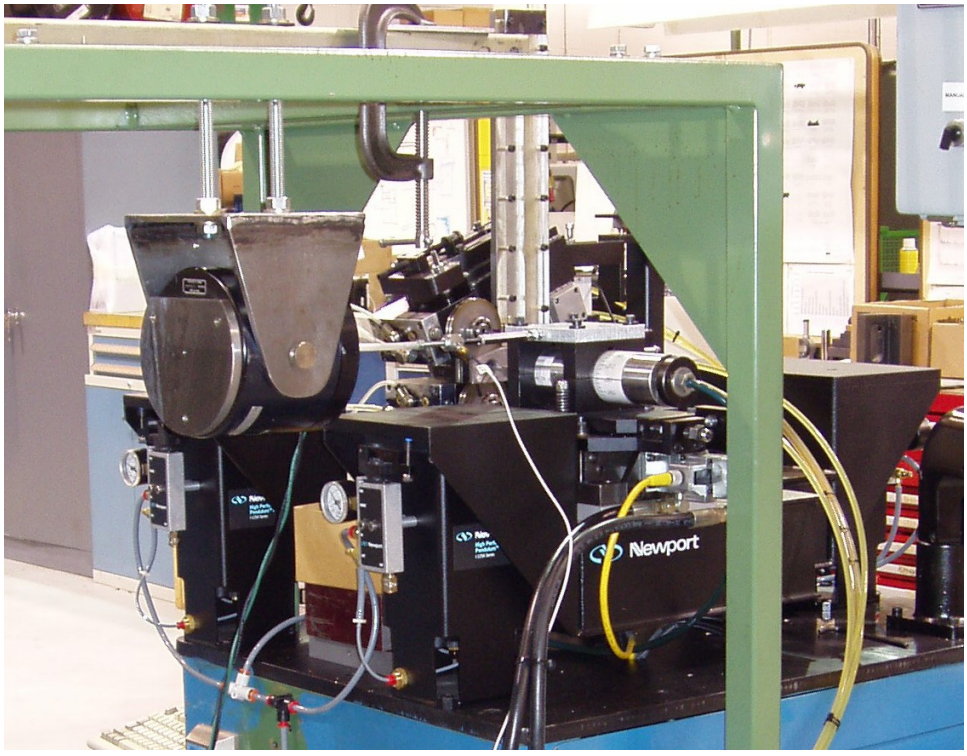

Figure 7-11: Configuration with shaker attached to the gage bracket

The rotational speed was approximately 0.9 rev/s during the measurements. The capabilities of the vibration separation algorithms can be tested best if the energy of the forced vibration is distributed over a frequency band. For this reason, the signal generator was set to linear sweep mode. The waveform was a sinusoid with frequencies ranging approximately from 40 to 90 Hz. Taking the part speed into account, this corresponds to a frequency range of 30 to 80 UPR. The sweep duration was chosen to be approximately 1 s so that the signal generator sweeps through the full frequency range during a part measurement. The spectrum of the force measured for one complete part revolution with this setup is displayed in Figure 7-12.

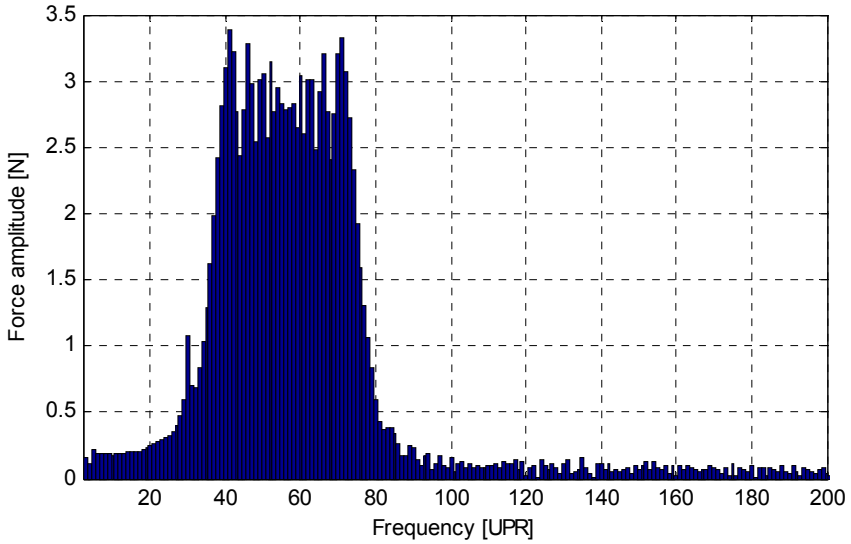

Figure 7-12: Force spectrum of the vibration

7.4.2 Determination of the Finger Eccentricity Angle

To determine the optimal finger eccentricity angle, the variances of the disturbances have to be estimated again since the scenario changed due to the induced vibration. For this purpose, tests series were conducted with horizontally and vertically placed fingers. In both setups, the fingers were placed centrically. The same procedure as outlined in section 6.6.8 was followed for the estimation of the disturbances. Figure 7-13 to Figure 7-15 show the standard deviation of the random noise, of the error motion in the *x*-direction and of the error motion in the *y*-direction. For the variation of the radius and of the eccentricity angle, the same values as the ones determined in section 6.6.8 are used.

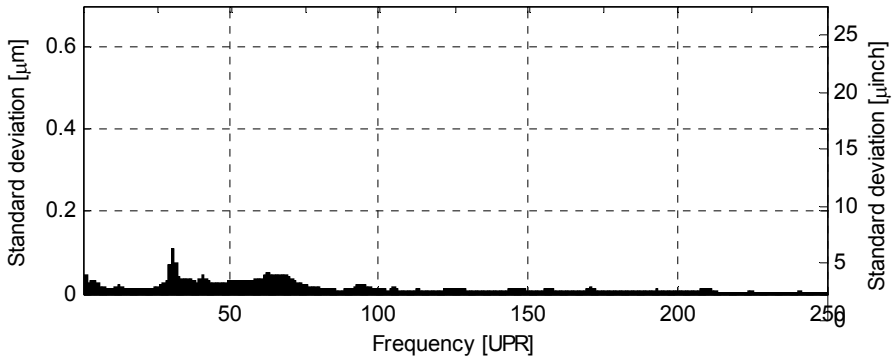

Figure 7-13: Standard deviation of the random noise

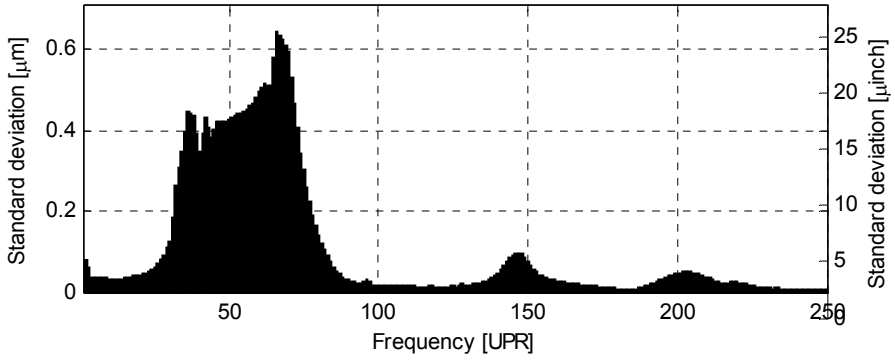

Figure 7-14: Standard deviation of the error motion in the *x*-direction

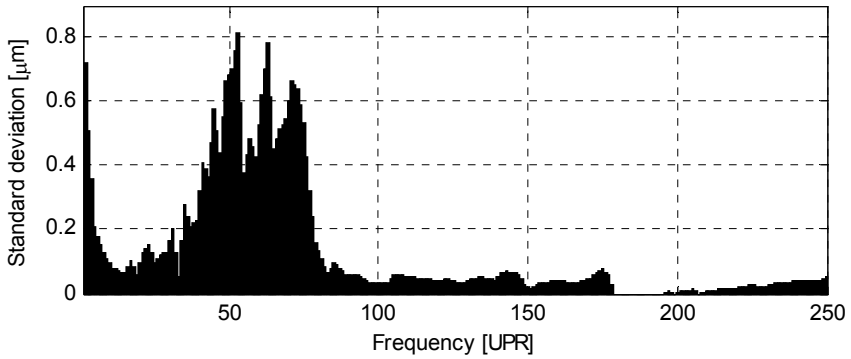

Figure 7-15: Standard deviation of the error motion in the *y*-direction

With the variances of the disturbances, the performance index $T(\mu_\Phi)$ can be calculated. The weights w_k where set to 1 inside the frequency band from 10 to 250 UPR and to 0 everywhere else

$$w_k = \begin{cases} 1 & 10 \le k \le 250 \\ 0 & \text{otherwise} \end{cases}. \tag{7.7}$$

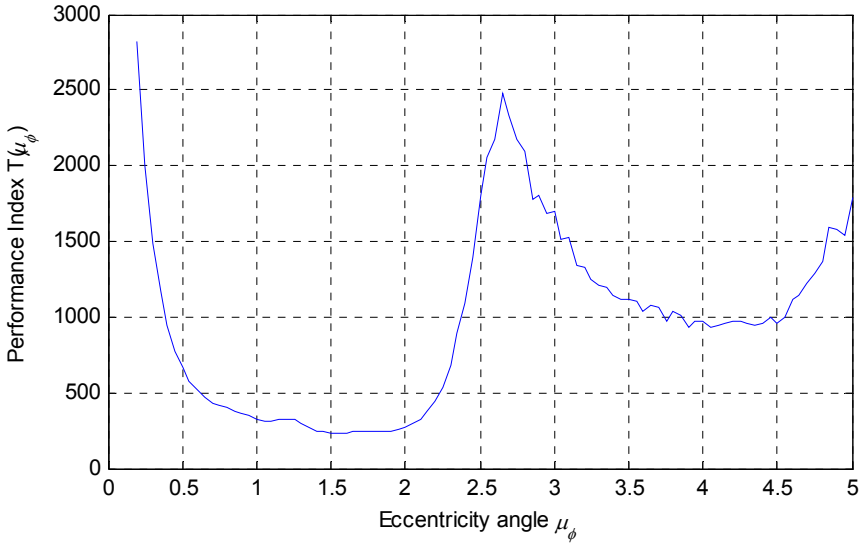

Figure 7-16: Performance index as a function of the eccentricity angle

Figure 7-16 shows the values of the performance index $T(\mu_\Phi)$ for eccentricity angles ranging from 0.2° to 5°. The minimum was found at 1.55°. To adjust the eccentricity angle of the gage head, a part with a notch was inserted and measured for several revolutions. The occurrence of the notch in the profile for the two fingers was determined using the AMDF and an eccentricity angle is calculated similar to the procedure outlined in section 6.6.8. The procedure has to be repeated until the measured eccentricity angle is close enough to the desired value. For the setup considered here, the procedure was stopped when an angle of 1.477° was measured. This value was then used as the expected value of the eccentricity angle μ_Φ. For the measurement series with eccentrically placed fingers, all 126 test parts were inserted once and measured for slightly more than 10 revolutions.

7.4.3 Results

The effect of the vibration separation can be seen in Figure 7-17 to Figure 7-20. Figure 7-17 shows the spectrum of a part without vibration. The part profile contains waviness around 32 UPR. A second harmonic at 64 UPR is visible as well. In Figure 7-18 the same part is shown in presence of vibration. The graph clearly shows the distortion of the spectrum in the range from 30 to 80 UPR. The peak at 32 UPR is still visible but its amplitude is distorted. The second harmonic at 64 UPR completely disappears within the vibration. The spectrum of the part after vibration separation is plotted in Figure 7-19. The frequency band of the vibration is removed. The amplitude of the 32 UPR harmonic is approximately restored to its original value. The 64 UPR harmonic becomes visible again as well. Its amplitude is slightly higher than in the original profile. It can also be

seen that the noise floor for the vibration separated profile is higher than for the profile in absence of vibration. Combining the vibration separation with averaging improves this. This is shown in Figure 7-20 where 10 measurements are averaged. The profile lengths are not corrected prior to the averaging since the raw signal is seriously distorted by the vibration. The length correction algorithm is therefore not capable of detecting the profile ends correctly. After averaging the noise went down to a level similar to the measurement without vibration.

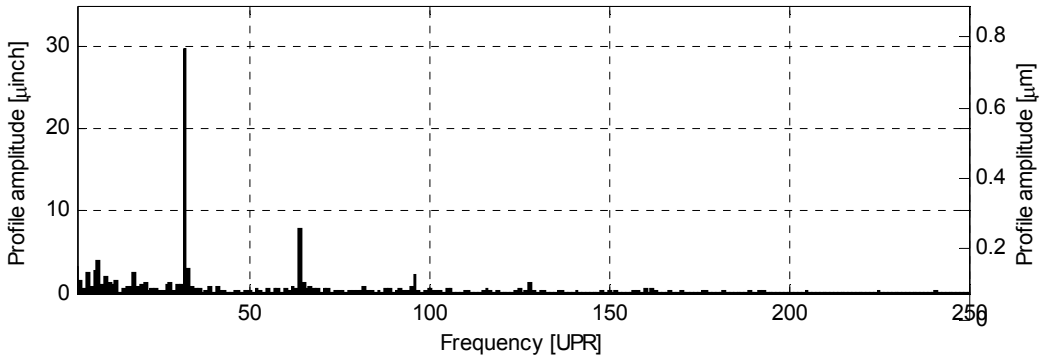

Figure 7-17: Spectrum of the part without vibration

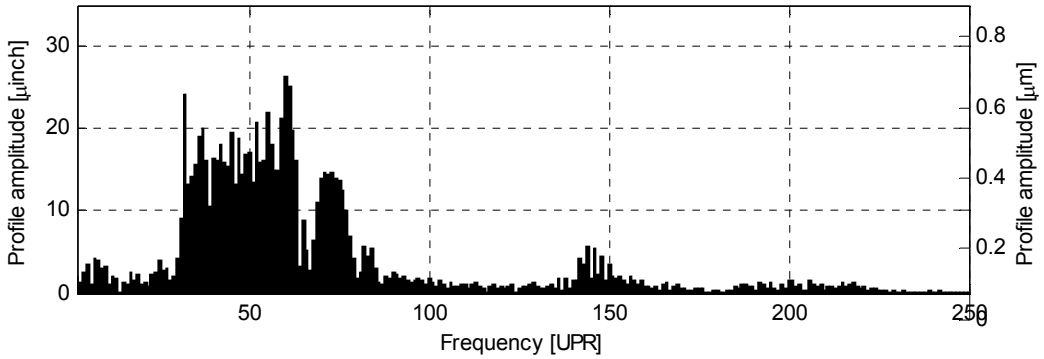

Figure 7-18: Spectrum of the part with forced vibration

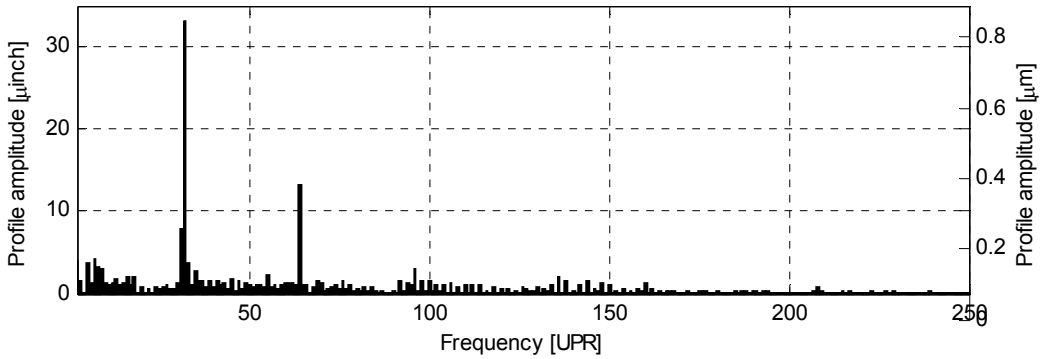

Figure 7-19: Spectrum of the part after vibration separation

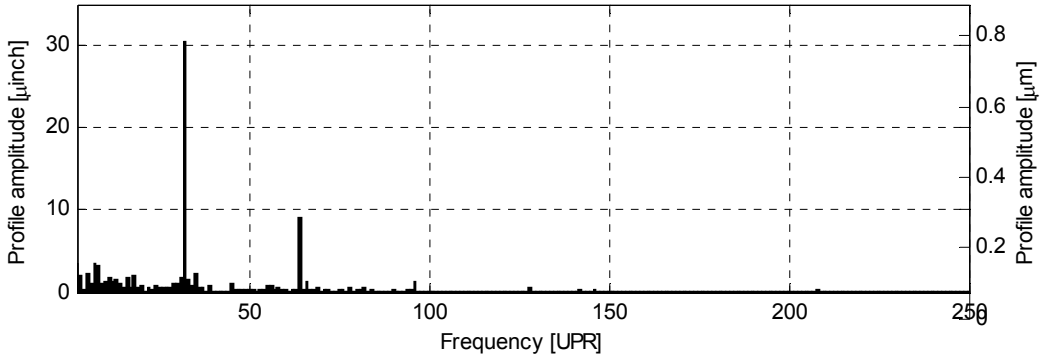

Figure 7-20: Spectrum after vibration separation and averaging of 10 measurements

To demonstrate that the vibration separation algorithm with eccentrically placed fingers is able to separate vibration for odd and even frequencies, Figure 7-21 to Figure 7-24 show the same graphs as above for a part with waviness at 31 UPR. In the measurement with vibration, the peak completely disappears in the frequency band of the vibration. After separation of the vibration is it visible again.

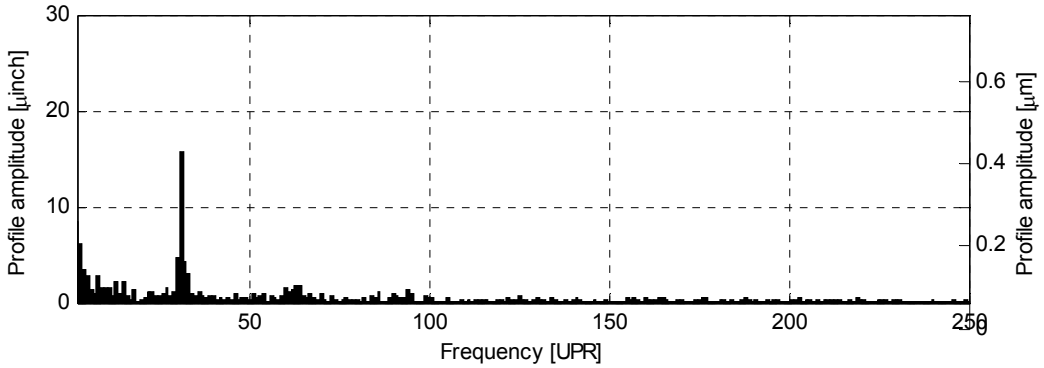

Figure 7-21: Spectrum of the part without vibration

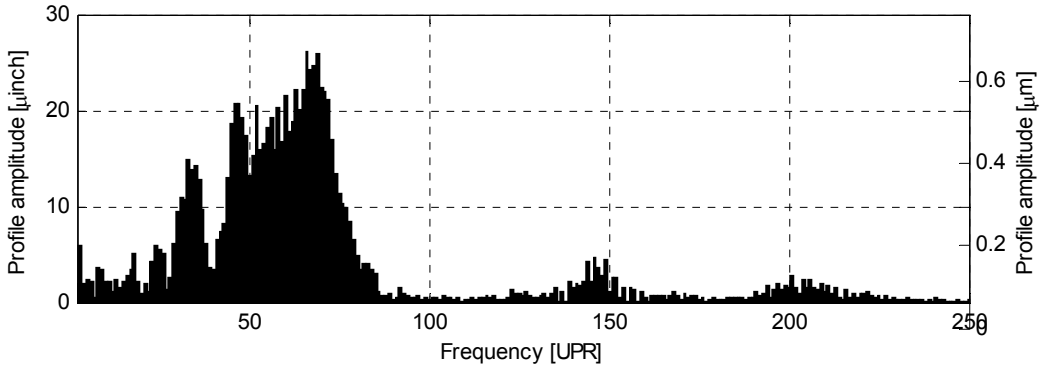

Figure 7-22: Spectrum of the part with forced vibration

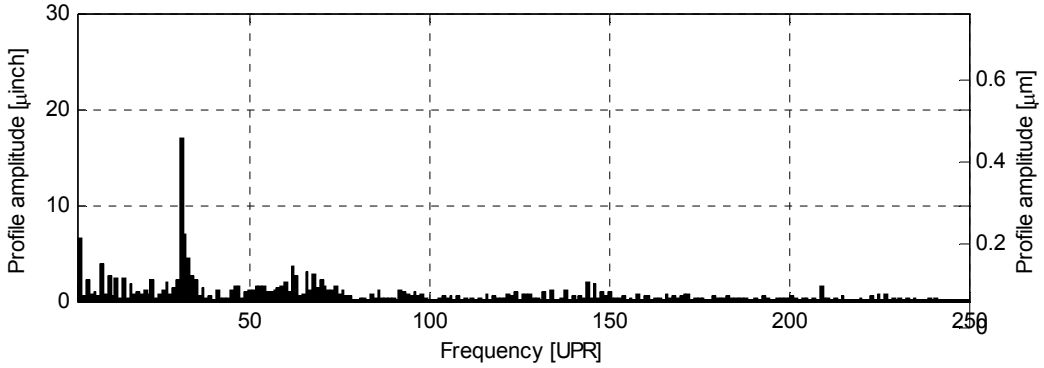

Figure 7-23: Spectrum of the part after vibration separation

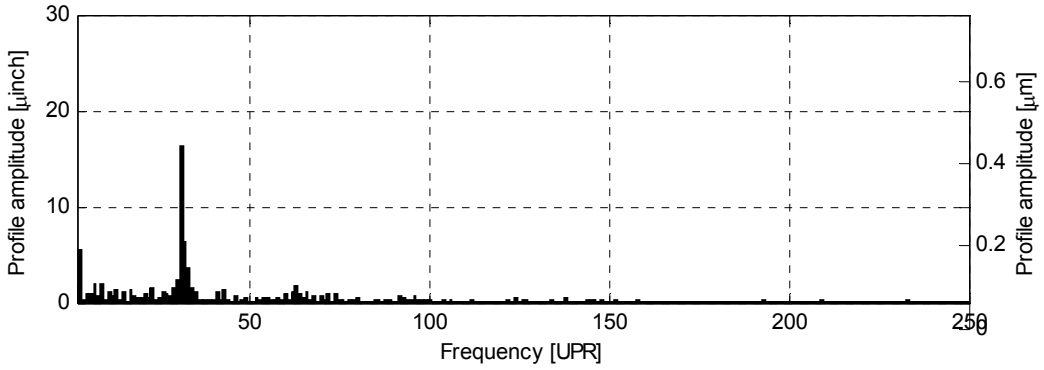

Figure 7-24: Spectrum after vibration separation and averaging of 10 measurements

Figure 7-25 shows the performance criteria for the complete measurement series of 126 parts. The first bar in the graphs represents the values obtained with the roundness machine for comparison. The remaining bars refer to the post-process machine. The second bar shows the values of the performance criteria in presence of vibration. The profile heights h_P are more severely affected than the maximum amplitudes A_P. Applying the vibration separation algorithm to the measurements restores their values close to the original value. Averaging several measurements improves the results. With seven averaged measurements, good agreement between the machines is obtained. Using more measurements yields only marginal improvements. This can also be seen from the classification of the parts in Table 7-8. The classification is made averaging seven measurements. With this configuration, 100 % of the "good" parts were detected as "good" and 100 % of the "bad" parts were recognized as "bad" with the post-process machine. This result is better than the measurement series taken in Chapter 5 at low speed without vibration since one "good" part with a defect in the outer diameter was mistakenly detected as "bad." The interpretation is that besides the forced vibration, the

vibration separation algorithm also removed the workpiece center movement of the part with an OD defect so that it was recognized correctly as a "good" part.

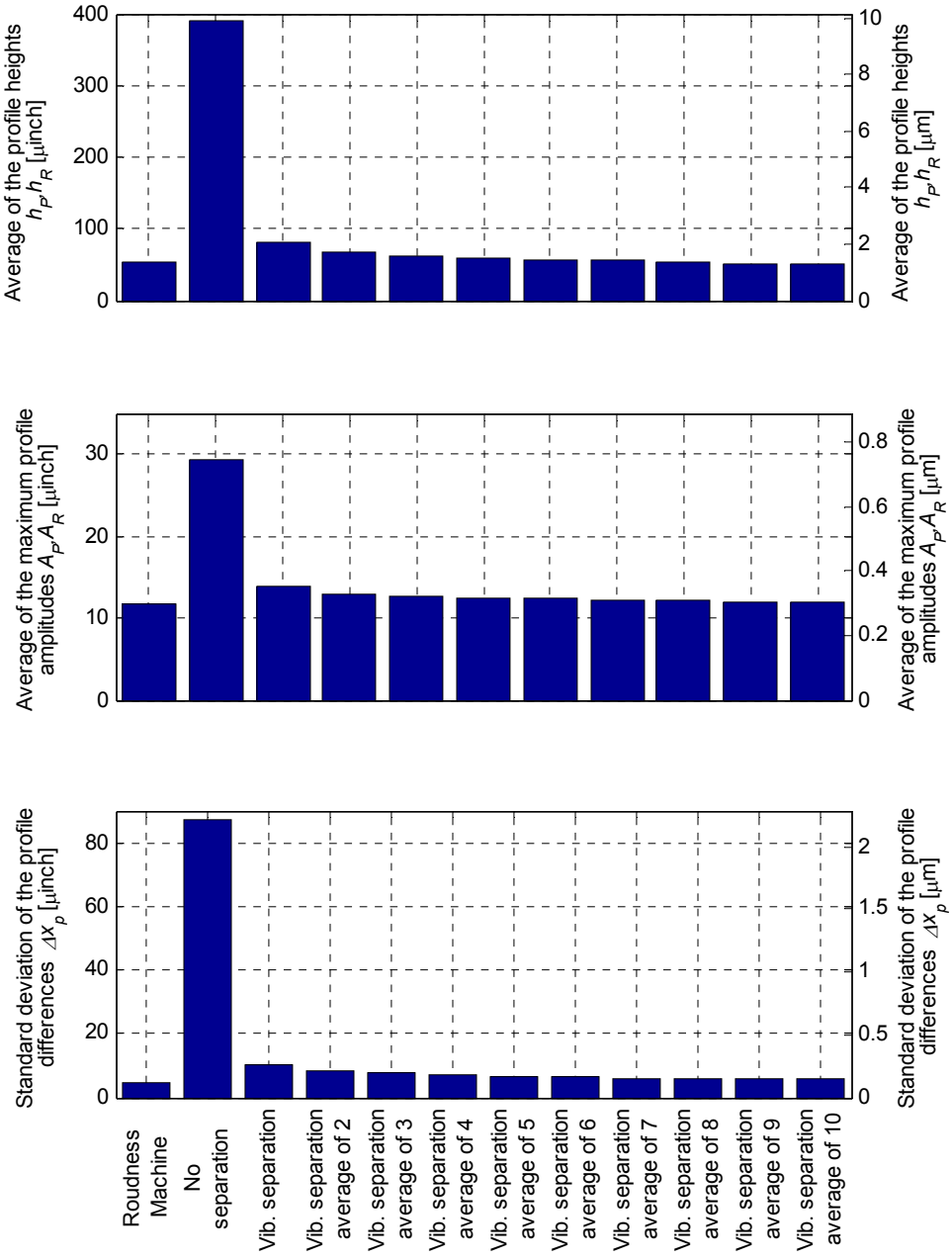

Figure 7-25: Effect of the vibration separation and averaging

Table 7-8: Part classification with vibration separation and averaging of 7 measurements

	Roundness Machine		Post-process machine		
			Good	Good/Bad	Bad
Criterion	Classification	Quantity	Quantity	Quantity	Quantity
Profile height h_R, h_P	Good	44 (100%)	44 (100%)	0 (0.0%)	0 (0.0%)
	Good/bad	34 (100%)	19 (55.9%)	0 (0.0%)	15 (44.1%)
	Bad	48 (100%)	0 (0.0%)	0 (0.0%)	48 (100%)
Max. profile amplitude A_R, A_P	Good	52 (100%)	49 (94.2%)	0 (0.0%)	3 (5.8%)
	Good/bad	5 (100%)	3 (60.0%)	0 (0.0%)	2 (40.0%)
	Bad	69 (100%)	0 (0.0%)	0 (0.0%)	69 (100%)

The performance of the vibration separation algorithm based on the minimum variance is compared to the heuristic approach explained in section 6.6.11. The same data set with the same eccentricity angle is used for better comparison of the two methods. Figure 7-26 shows the effect of the critical amplification value κ_C on the performance criteria for one revolution without using averaging. For $\kappa_C = 0$, the heuristic always prefers the estimator $\tilde{R}_{PS}$ over $\tilde{R}_S$. Since $\tilde{R}_{PS}$ does only partly reject vibration, the performance criteria deviate considerably from the reference values obtained with the roundness machine. For $\kappa_C = 0.5$, the heuristics starts to use $\tilde{R}_S$ instead of $\tilde{R}_{PS}$ for certain frequencies. As a result, the performance criteria drop and approach the reference values. If κ_C is chosen to be approximately 2, the performance criteria are closest to the reference values from the roundness machine indicating that the best balance between using $\tilde{R}_S$ and $\tilde{R}_{PS}$ is found. As the value of κ_C increases, the heuristic starts preferring $\tilde{R}_S$ over $\tilde{R}_{PS}$. Simultaneously, the performance criteria deteriorate again since $\tilde{R}_S$ amplifies the random noise.

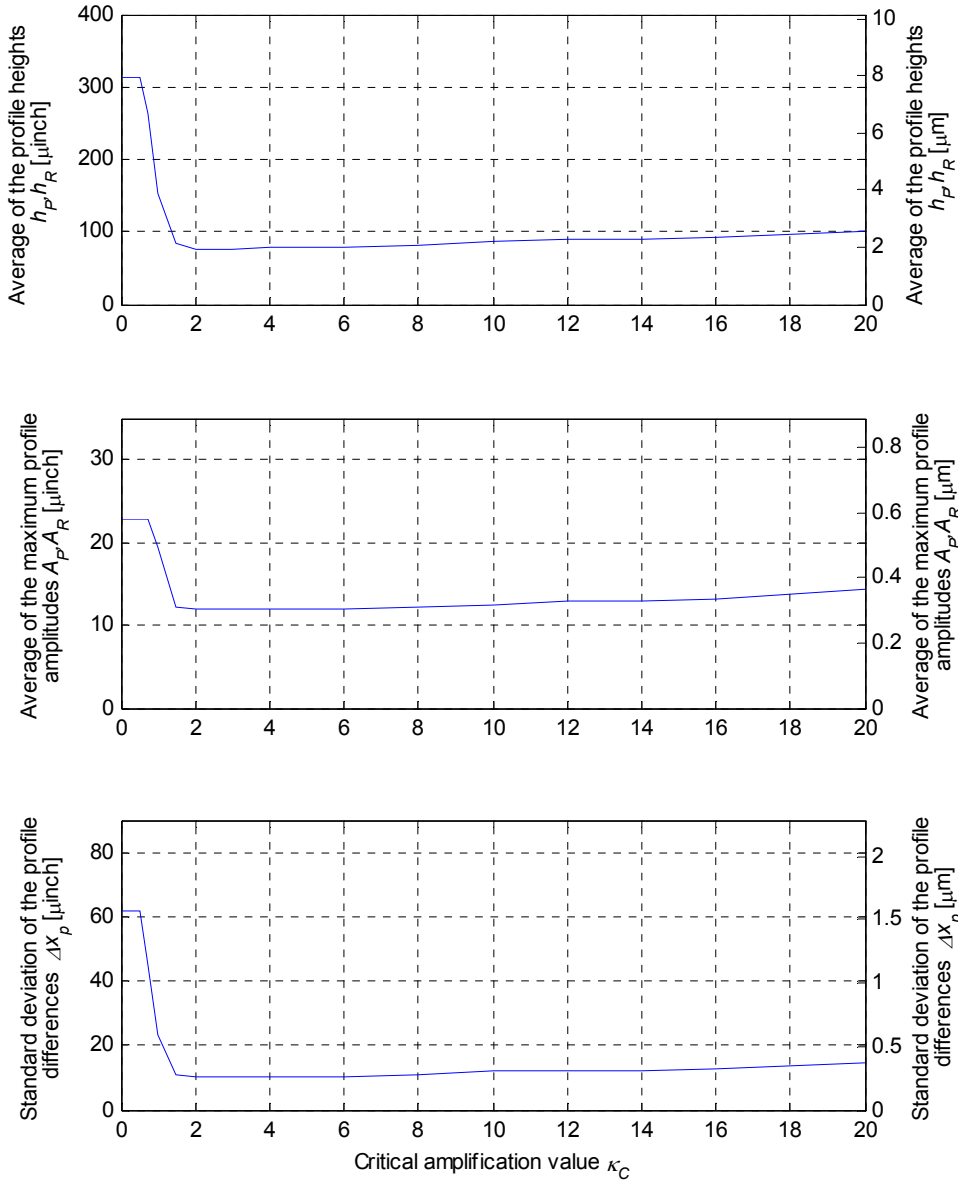

Figure 7-26: Effect of the critical amplification value

The graphs also show that for the range of κ_C between 2 and 6 the performance criteria remain relatively constant. The heuristic is therefore insensitive to small deviations of κ_C from its optimal value. For practical applications, it is therefore sufficient to choose κ_C somewhat arbitrarily within this range. For the data set given here, κ_C is chosen to be 2.5.

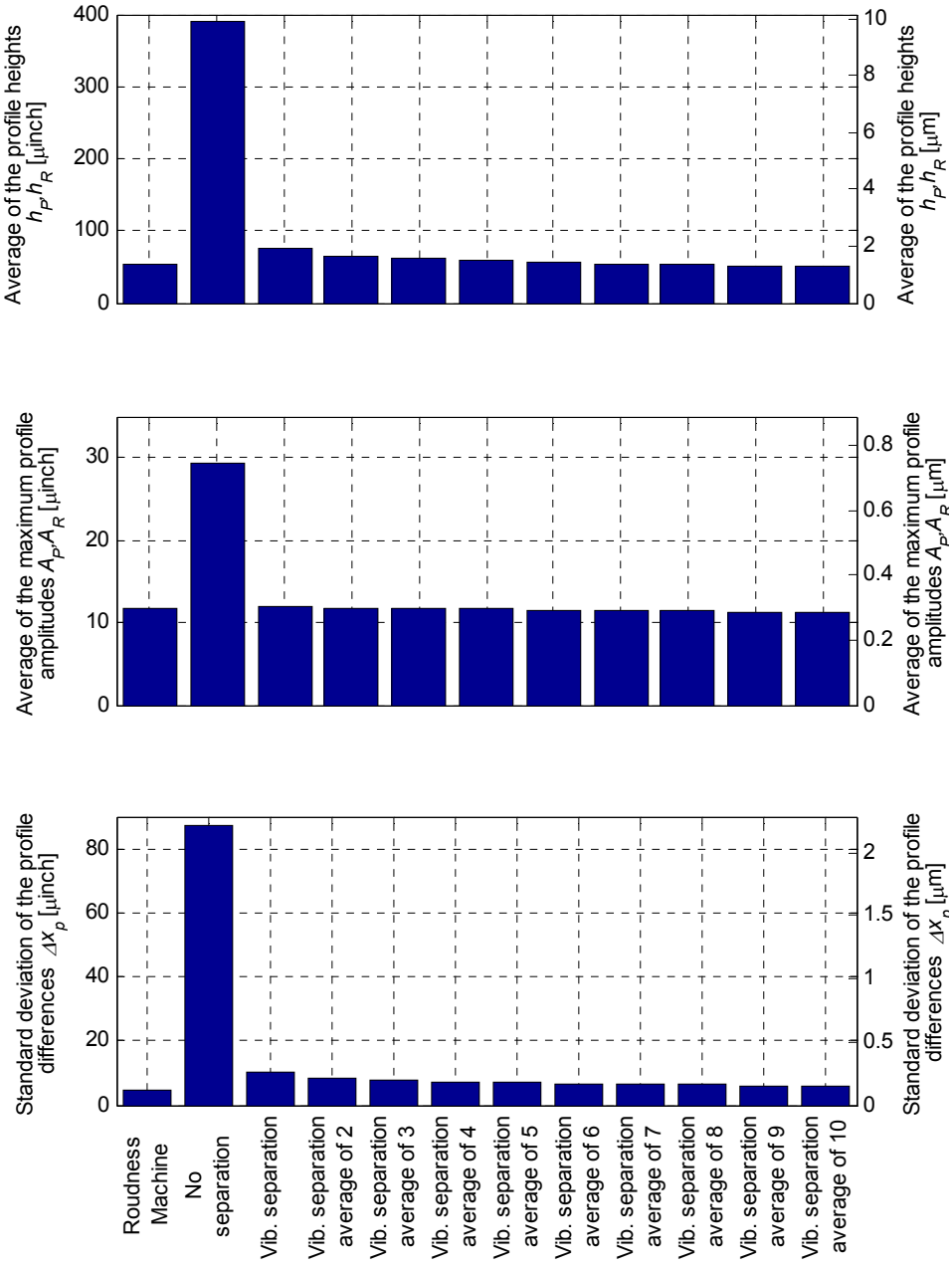

Figure 7-27: Effect of vibration separation using the heuristic and averaging

Figure 7-27 shows the performance criteria if the vibration separation is combined with averaging. As expected, the performance criteria converge to the values obtained with the roundness machine. The part classification resulting from the heuristic vibration separation and averaging of seven measurements is shown in Table 7-9.

Table 7-9: Part classification with heuristic vibration separation and averaging of 7 measurements

	Roundness Machine		Post-process machine		
			Good	Good/Bad	Bad
Criterion	Classification	Quantity	Quantity	Quantity	Quantity
Profile height h_R, h_P	Good	44 (100%)	43 (97.7%)	0 (0.0%)	1 (2.3%)
	Good/bad	34 (100%)	20 (58.8%)	0 (0.0%)	14 (41.2%)
	Bad	48 (100%)	0 (0.0%)	0 (0.0%)	48 (100%)
Max. profile amplitude A_R, A_P	Good	52 (100%)	49 (94.2%)	0 (0.0%)	3 (5.8%)
	Good/bad	5 (100%)	3 (60.0%)	0 (0.0%)	2 (40.0%)
	Bad	69 (100%)	1 (1.4%)	0 (0.0%)	68 (98.6%)

Comparing the performance of the variance based vibration separation method with the heuristic method, it can be stated that both methods perform approximately equally well. The variance based method yields a slightly better part classification when seven averages are used. Without averaging on the other hand, slightly better results are achieved with the heuristic method. This is surprising since the variance based method estimates the radius harmonics with minimum variance. It has to be considered though that the method is only as good as the variance estimates of the disturbances. The fact that the heuristic method can outperform the variance based method in certain cases may indicate that the variance estimates of the disturbances are not accurate enough.

CHAPTER 8 – GRINDING MACHINE MEASUREMENTS

8.1 Setup of the Grinding Machine

This chapter presents the results of measurements taken with the grinding machine described in section 3.1. Two different measurement setups are considered. In section 8.2, a measurement series is conducted with the parts rotating at their normal speed but with the grinding wheel retracted and turned off. In section 8.3, the grinding wheel is turned on but not in contact with the part. These two configurations represent intermediate steps towards full in-process implementation. Due to limited availability of the grinding machine, in-process measurements where the geometry is measured during the grinding process were not considered here.

8.1.1 Setup of the Measurement System

The setup of the measurement system in the grinding machine is shown in Figure 8-1. The measurement system uses the gage head and the signal conditioning card from the grinding machine. The circuits in the grinding machine are left unchanged. The only modification is that the signal conditioning card output is in addition to being connected to the controller of the grinding machine also connected to the data acquisition system of the post-process machine. This setup allows taking measurements without interfering with the control of the grinding machine.

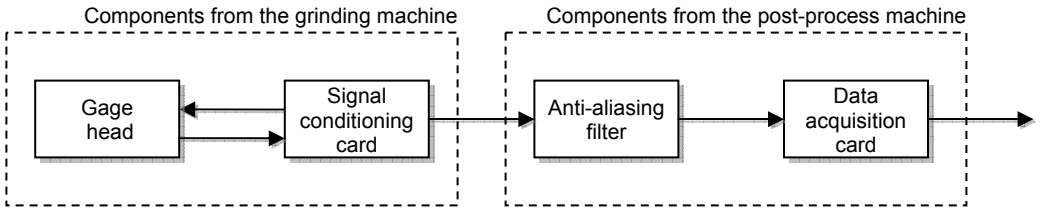

Figure 8-1: Setup of the measurement system in the grinding machine

The gains and the zero adjust of the gage head and the signal conditioning card were left unchanged as well. The fingers were calibrated with a micrometer head following the same procedure as explained in section 4.4.3 for the post-process machine. The resulting calibration data is shown in Table 8-1.

Table 8-1: Calibration data for the grinding machine

	Finger A	Finger B
Slope	32.36 μm/V	32.23 μm/V
Measurement range	647.3 μm	644.6 μm
Resolution	9.877 nm	9.836 nm

Since no encoder is available in the grinding machine to trigger the data acquisition, the measurement signal is acquired at a constant frequency of 40 kHz. The cutoff frequency of the anti-aliasing filter was set to 16 kHz. The workpiece was rotated at approximately 13.5 rev/s (810 RPM). This speed and sampling frequency resulted in approximately 2960 data points per revolution.

8.1.2 Electrical Noise

As a next step, the electrical noise in the measurement system is measured. Since the original purpose of the measurement system in the grinding machine is to measure only the average diameter, it is not necessarily designed to yield a low-noise signal. To measure the electrical noise, the fingers are inserted into a part that is loaded in the fixture. The resulting signal is sampled for 10 s with a sampling frequency of 40 kHz. The acquired data is divided into 10 non-overlapping ensembles. The overall standard deviation is calculated as the mean of the standard deviation of the individual ensembles using equation (4.5) from section 4.2. Table 8-2 shows the resulting standard deviations for finger A and B when the electrical components of the grinding machine are successively turned on. The belt that drives the lower and upper roll was removed so that the part in the fixture did not rotate when roll motor was turned on. The table shows that the noise increases as the components are turned on.

Table 8-2: Electrical noise in the grinding machine

Hydraulics	Servos	Roll motor	Grinding wheel	Standard deviation			
				Finger A		Finger B	
				[mV]	[nm]	[mV]	[nm]
off	off	off	off	2.969	96.09	2.861	92.20
on	off	off	off	3.551	114.9	2.842	91.60
on	on	off	off	5.274	170.7	4.656	150.1
on	on	on	off	6.000	194.2	5.289	170.4
on	on	on	on	8.025	258.7	6.302	204.0

The spectrum of the fingers when all components are turned on is shown in Figure 8-2. Electrical noise at multiples of the 60 Hz power frequency can be clearly seen. Since

reduction of the electrical noise through revision of the circuits is time consuming, it is decided to remove the electrical noise by applying a notch filter. The notch filter is applied at the 60 first multiples of the 60 Hz power frequency, i.e. it is applied at 60, 120, …, 3600 Hz. For the given part speed, frequencies above 3600 Hz are not inside the 10-250 UPR frequency band anymore so that their removal is not necessary.

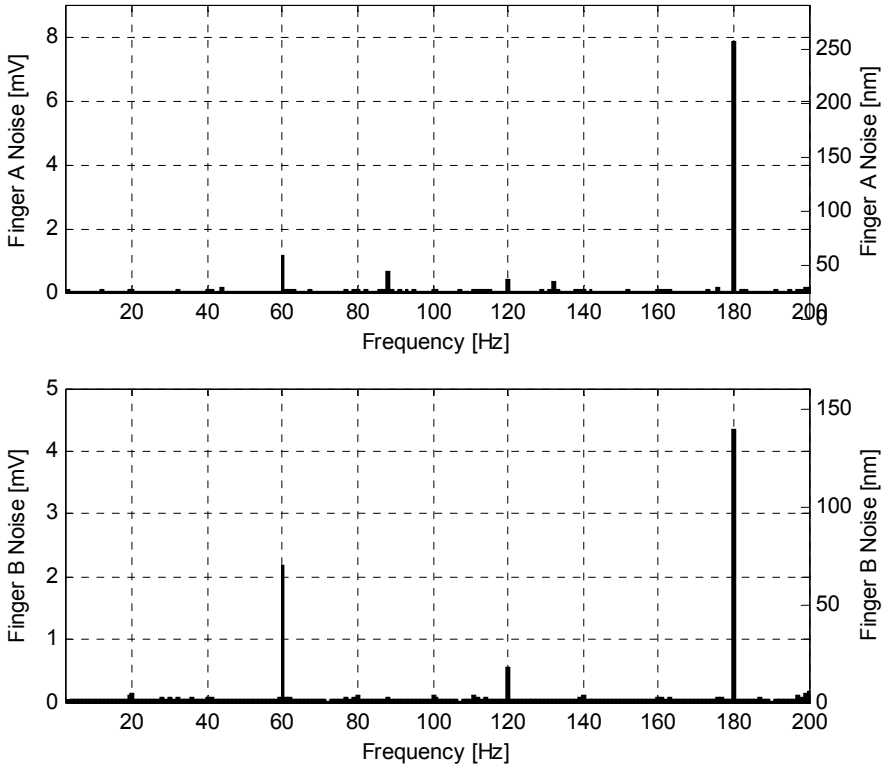

Figure 8-2: Spectrum of the electrical noise in the grinding machine

In addition to the harmonics at multiples of 60 Hz, high frequency ripple occurs periodically for a short duration. This is shown in Figure 8-3 where three of these wave trains are shown. The ripple affects both fingers simultaneously. It has a duration of approximately 1.25 ms and occurs approximately 120 times per second. It is caused by

the servos and the roll motor. Due to its sharp peaks, it is expected that the ripple has a significant impact on the profile height.

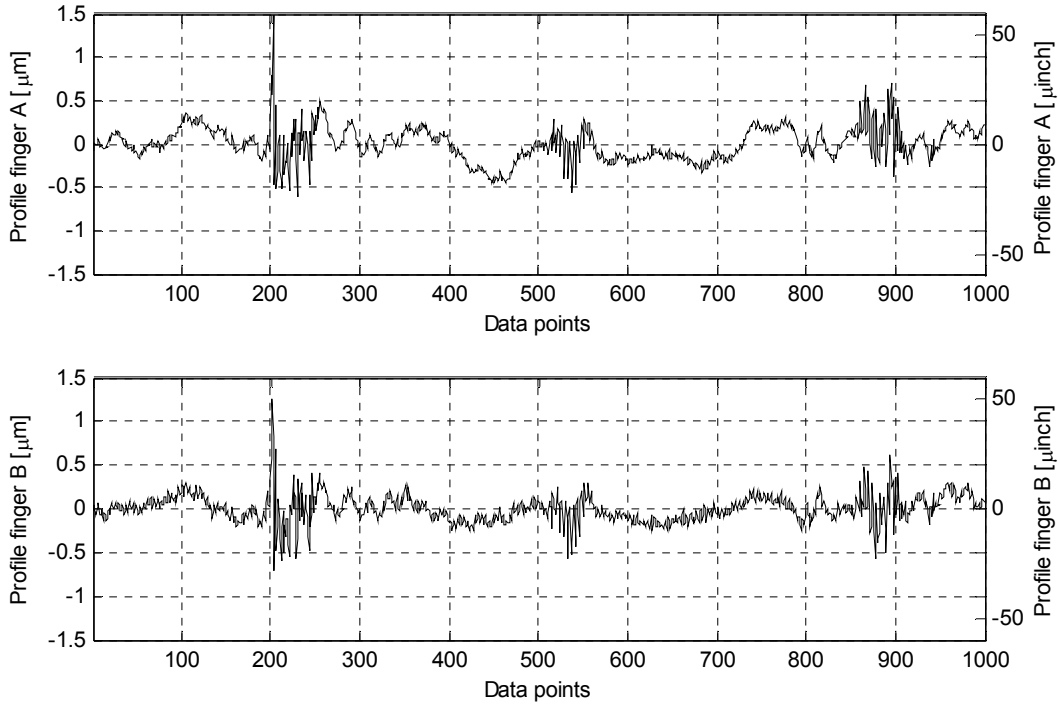

Figure 8-3: High frequency ripple in the electrical signal

8.1.3 Number of Data Points per Revolution

Determining the number of data points per revolution is critical since no encoder is available that sends pulses at constant angular increments of the workpiece rotation. The roll motor is therefore set to the same predefined speed for all measurements. To estimate the resulting number of data points at this speed, the same procedure is used as in section 6.6.8 for the estimation of the finger angle standard deviation. 11 test parts with a notch on the surface in the axial direction are measured for 50 revolutions. The beginning and the length of the notch in data points are identified manually for each part.

Using the AMDF, the reoccurrence of the notch in the measurement is then sought for. The possible length of one workpiece revolution was confined to a range of 3000 ± 200 data points. The resulting distribution of the number of data points per revolution is shown in Figure 8-4. The average value is 3011.3 and the standard deviation is 12.0 data points. The average workpiece speed was therefore 13.28 rev/s (797 RPM).

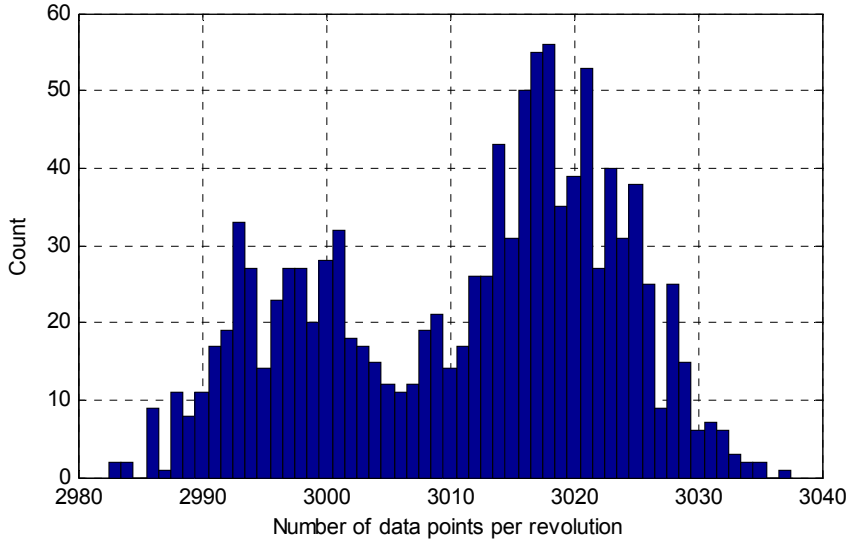

Figure 8-4: Distribution of the number of data points in the grinding machine

8.1.4 Measurement of the System Transfer Function

The measurement system in the grinding machine uses different components than the post-process machine. The biggest difference is the use of the Mini Thruvar 5 gage head as opposed to the Thruvar 5 head in the post-process machine. It is therefore expected that the measurement system in the grinding machine has a different frequency response than the one in the post-process machine. Because of that, the system transfer function has to be measured again. Since the grinding machine uses different control

hardware than the post-process machine, it was not possible to implement the automatic procedure for the transfer function measurement from section 6.5.3 easily. Due to time constraints, a manual procedure was used. The manual procedure measures only the amplitude attenuation but not the phase shift. Therefore, only the amplitude error of the gage head can be corrected but not the phase error. This has to be taken into account when evaluating the measurement results.

To measure the amplitude of the transfer function, a part with a strong 32 UPR harmonic with an amplitude of approximately 1.5 μm was inserted into the machine. The part was rotated a different speeds and the measured signal of both fingers was recorded. The difficulty of determining the transfer function from the measurements is that both the number of data points per revolution and also the exact rotational speed of the workpiece are unknown. It is only known that the part profile contains exactly 32 undulations per revolution. This information can be used to determine the number of data points per revolution. To find the true profile length, the spectrum is calculated assuming different profile lengths. For the true profile length, the amplitude of the 32 UPR harmonic will assume its maximum. If the profile length is slightly to short or to long, the amplitude of the 32 UPR will be lower as it leaks into the adjacent frequencies. Therefore, the number of data points is used as the true number of data points that maximizes the amplitude of the 32 UPR harmonic. Knowing that the data points are sampled at a constant frequency of 40 kHz, the rotational speed of the part and the corresponding frequency in Hertz can be calculated. The resulting amplitude curve of the transfer function is shown in Figure 8-5. The curve reveals that the gage head exhibits an underdamped response.

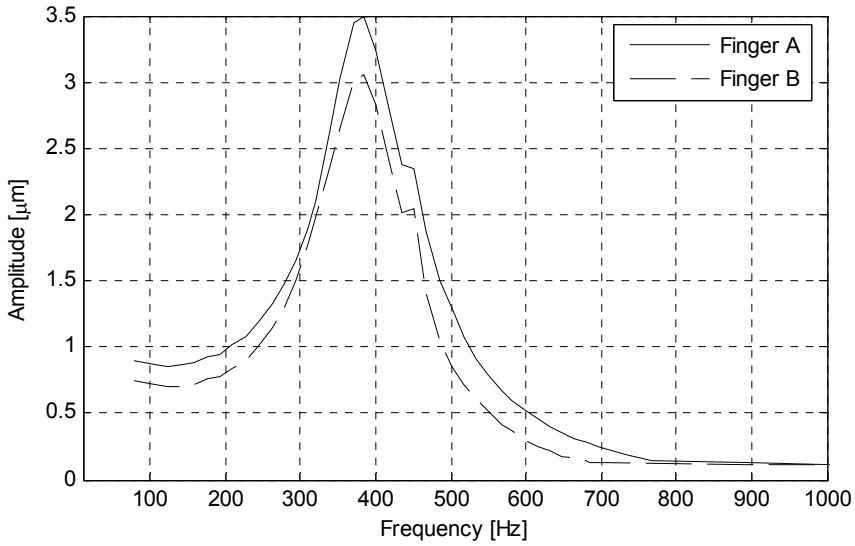

Figure 8-5: Amplitude as function of the frequency in the grinding machine

8.2 Measurements with the Grinding Wheel Turned Off

8.2.1 Methodology for Centrically Placed Fingers

As the first setup, the configuration with centrically placed fingers was tested. The fingers were placed vertically at the 12 o'clock and 6 o'clock position as it is required in the grinding machine. Due to technical limitations, the parts could not be measured in their dead center. This has to be taken into account when comparing the measurements to the ones obtained by the roundness machine.

All 126 test parts were loaded once and each of them was measured for slightly more than 20 revolutions. The parts were rotated at the standard roll speed that was found to be 13.28 rev/s in section 8.1.3. The grinding wheel was turned off during the measurements.

8.2.2 Results for Centrically Placed Fingers

Prior to analyzing the measurements, several filters had to be applied. As mentioned in section 8.1.2, a notch filter was used to remove multiples of the 60 Hz power frequency. Since it is expected that the roll motor speed fluctuates slightly, the profile length correction was applied as well. In section 8.1.3, the average profile length was determined to be approximately 3011 data points per revolution. The possible range was therefore limited to 3011 ± 50 data points. For the 126 test parts, this resulted in a standard deviation of the profile length of 19.27. This is higher than the standard deviation that was measured with the notched parts and much higher than the standard deviation obtained with the post-process machine. It is believed that this is not only caused by the fluctuation of the roll motor speed but also by erroneous results of the profile length correction. In the grinding machine, the noise is significantly higher than in the post-process machine. Especially the ripple in the signal that was found in section 8.1.2, seriously distorts the signal and impedes correct detection of the profile length.

Since the parts were rotated at a high speed, the transfer function compensation had to be used. The amplitudes were corrected up to 1 kHz, which corresponds to 75 UPR at the given part speed. As it was already mentioned for the post-process machine, the transfer function compensation amplifies noise for the higher frequencies. This is more severe in the grinding machine as the noise levels are higher. Therefore, the transfer function compensation has to be combined with averaging over multiple measurements. The three performance criteria that were used for the post-process machine are shown in Figure 8-6. They are denoted here by h_G, A_G, and Δx_G to indicate that they refer to the grinding machine. The first bar in every graph shows the value obtained with the

roundness machine. The corresponding value measured with the grinding machine without transfer function compensation is represented by the second bar and the value with transfer function compensation by the third bar. The remaining bars characterize the performance criteria when the average over different numbers of measurements is calculated.

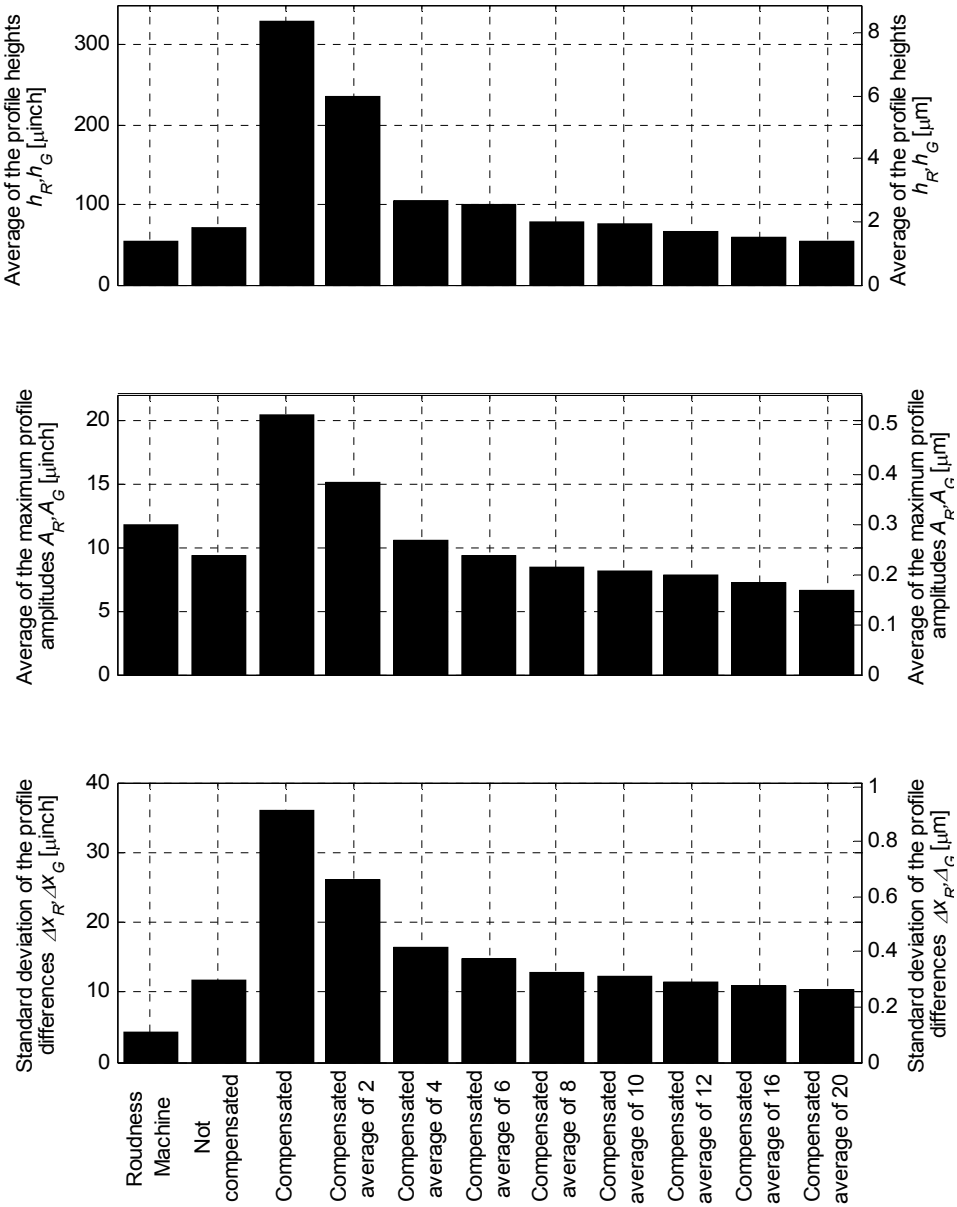

Figure 8-6: Performance criteria for the grinding machine

The plots reveal that compensating the transfer function significantly amplifies the noise in the measurement. Averaging several measurements reduces the noise again. The profile height h_G reaches approximately the same value as the roundness machine when 20 measurements are averaged. The maximum profile amplitude shows good agreement between the two machines for only 4 averaged measurements. However, when a higher number of measurements are averaged, the value of the grinding machine drops below the value of the roundness machine. After a certain point, averaging more and more measurements therefore leads to a poorer agreement between the machines. This indicates a problem with the averaging algorithm. Its cause is the imperfect profile length correction. Due to misalignment of the individual measurements, the harmonics leak into the adjacent frequencies and the amplitude at the original frequency is distributed over several frequencies.

To summarize the observations, it can be stated that the transfer function compensation introduces a high amount of noise into the measurements. Averaging reduces this noise considerably but on the other hand also tends to erase a small portion of the profile information due to the misalignment of the measurements.

The resulting part classification for 8 and 20 averaged measurements are shown in Table 8-3 and Table 8-4. The table for 8 averaged measurements shows that although the maximum profile amplitude A_G is affected by the misalignment of the averaging algorithm, it is more robust against noise than the profile height h_G. While the profile height h_G rejects all test parts as bad, the maximum profile amplitude A_G is able classify the majority of the part correctly.

Table 8-3: Part classification for the grinding machine averaging 8 measurements

	Roundness Machine		Grinding machine		
			Good	Good/Bad	Bad
Criterion	Classification	Quantity	Quantity	Quantity	Quantity
Profile height h_R, h_G	Good	44 (100%)	0 (0.0%)	0 (0.0%)	44 (100%)
	Good/bad	34 (100%)	0 (0.0%)	0 (0.0%)	34 (100%)
	Bad	48 (100%)	0 (0.0%)	0 (0.0%)	48 (100%)
Max. profile amplitude A_R, A_G	Good	52 (100%)	46 (88.5%)	0 (0.0%)	6 (11.5%)
	Good/bad	5 (100%)	4 (80.0%)	0 (0.0%)	1 (20.0%)
	Bad	69 (100%)	28 (40.6%)	0 (0.0%)	41 (59.4%)

Table 8-4: Part classification for the grinding machine averaging 20 measurements

	Roundness Machine		Grinding machine		
			Good	Good/Bad	Bad
Criterion	Classification	Quantity	Quantity	Quantity	Quantity
Profile height h_R, h_G	Good	44 (100%)	39 (88.6%)	0 (0.0%)	5 (11.4%)
	Good/bad	34 (100%)	19 (55.9%)	0 (0.0%)	15 (44.1%)
	Bad	48 (100%)	7 (14.6%)	0 (0.0%)	41 (85.4%)
Max. profile amplitude A_R, A_G	Good	52 (100%)	52 (100%)	0 (0.0%)	0 (0.0%)
	Good/bad	5 (100%)	5 (100%)	0 (0.0%)	0 (0.0%)
	Bad	69 (100%)	39 (56.5%)	0 (0.0%)	30 (43.5%)

When 20 measurements are averaged, the maximum profile amplitude criterion passes the majority of the "bad" parts due to the alignment errors. Using the profile height as a criterion however yields acceptable results with 11.4 % classification error for the "good" parts and 14.6 % for the "bad" parts.

8.2.3 Methodology for Eccentrically Placed Fingers

As the next step, a configuration with the fingers placed eccentrically is tested since it allows rejecting vibration in the system. To determine the optimal finger angle, the standard deviations of the disturbances are estimated first. Their knowledge also gives evidence about the amount of vibration that is present in the system.

For the variation of the radius, the same values are used as in section 6.6.8. The standard deviation of the random noise and the error motions in the *x*- and *y*-direction are shown in Figure 8-7 to Figure 8-9. The standard deviations are calculated following the procedure described in section 6.6.8 and using the data sets from the previous section for centrically placed fingers. The transfer function of the gage was compensated prior to the computation of the standard deviations. To estimate the standard deviation for the error motion in the *x*-direction, measurements were taken with the fingers placed horizontally.

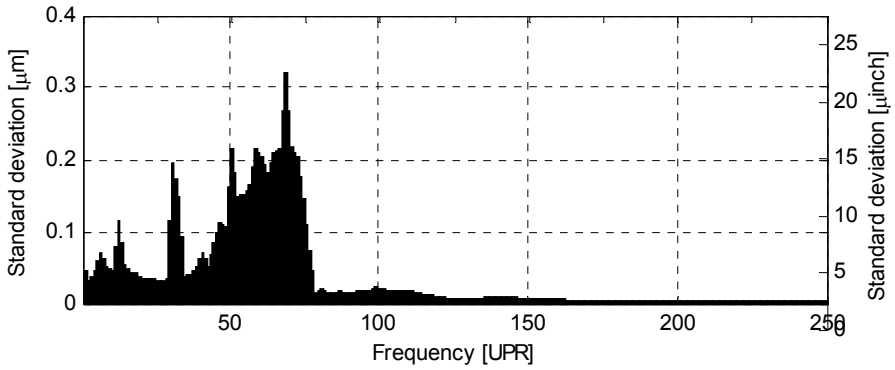

Figure 8-7: Standard deviation of the random noise in the grinding machine

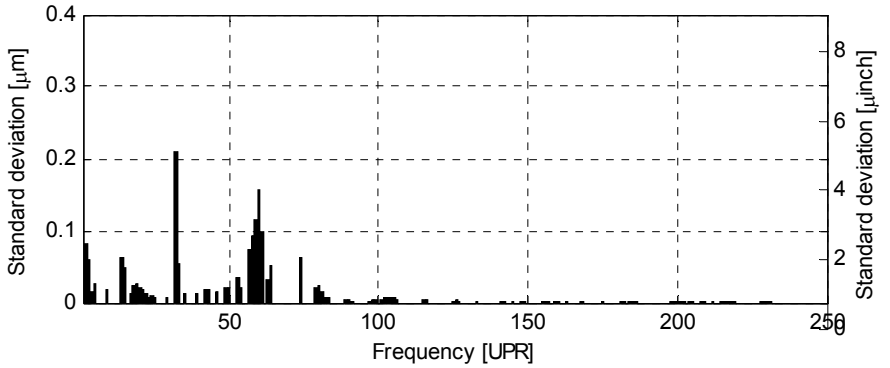

Figure 8-8: Standard deviation of the error motion in the x-direction

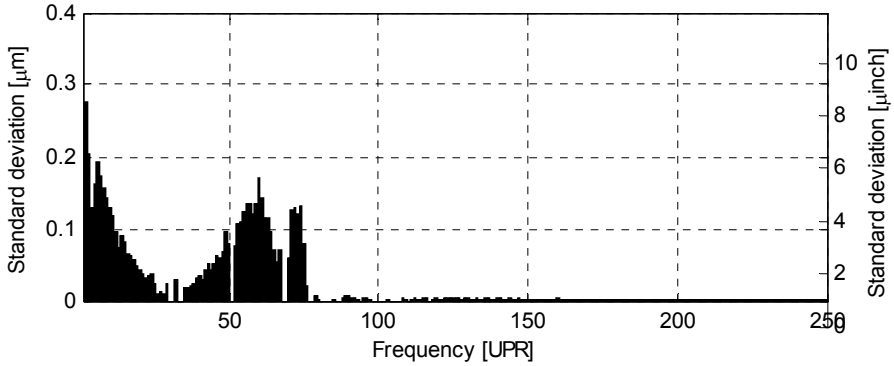

Figure 8-9: Standard deviation of the error motion in the y-direction

The plots show a general increase of the amplitudes towards 75 UPR. This is caused by the amplification of the transfer function compensation. The standard deviation of the error motion in the *x*-direction is lower than the one in the *y*-direction because of the roundness error of the rolls. Comparing the error motions to the random noise it can be stated that the error motions are lower than the random noise.

A potential problem for the vibration separation and for the estimation of the random noise exists because of the nature of the random noise at the two fingers. In the grinding machine, the random noise consists to a large extend of electrical noise. Figure 8-3 shows that the periodically occurring ripple affects both fingers at the same time and

has the same shape. This violates the assumption that the random noise at finger A and B are independent random processes with a covariance of zero. As a consequence, while the vibration separation may still provide good vibration rejection capabilities, its performance is not optimal anymore. This problem did not exist with the post-process machine since with this setup the electrical noise consisted mainly of white noise which is independent for the two fingers.

The optimal finger eccentricity angle for the measured disturbance variances was 2.17°. The measured finger angle after the adjustment of the gage head was 2.08°, which was considered to be close enough to the optimal value.

8.2.4 Results for Eccentrically Placed Fingers

The performance of the vibration separation algorithm can be assessed with the graphs in Figure 8-10. The first bar in each of the three plots represents the value of the performance criteria obtained from the roundness machine. The remaining bars correspond to the performance criteria measured with the grinding machine averaging over different numbers of measurements. The black bars characterize the value of the performance criteria without vibration separation and the grey bars with vibration separation. For both, the results with and without vibration separation, the data set with eccentrically placed fingers was used.

It can be seen that especially for a low number of averaged measurements, the vibration separation provides some improvement. The performance criteria for vibration separated measurements reach the reference values of the roundness machine faster, but then drop below them due to the misalignment of the profiles and the resulting averaging

error. This behavior is more obvious for the maximum profile amplitude than for the profile height.

The improvement of the measurement results by the vibration separation is limited by the fact that the workpiece center motion is not the largest disturbance. As it was found in the previous section, the remaining noise besides vibration still contributes the most to the distortion of the measurement signal.

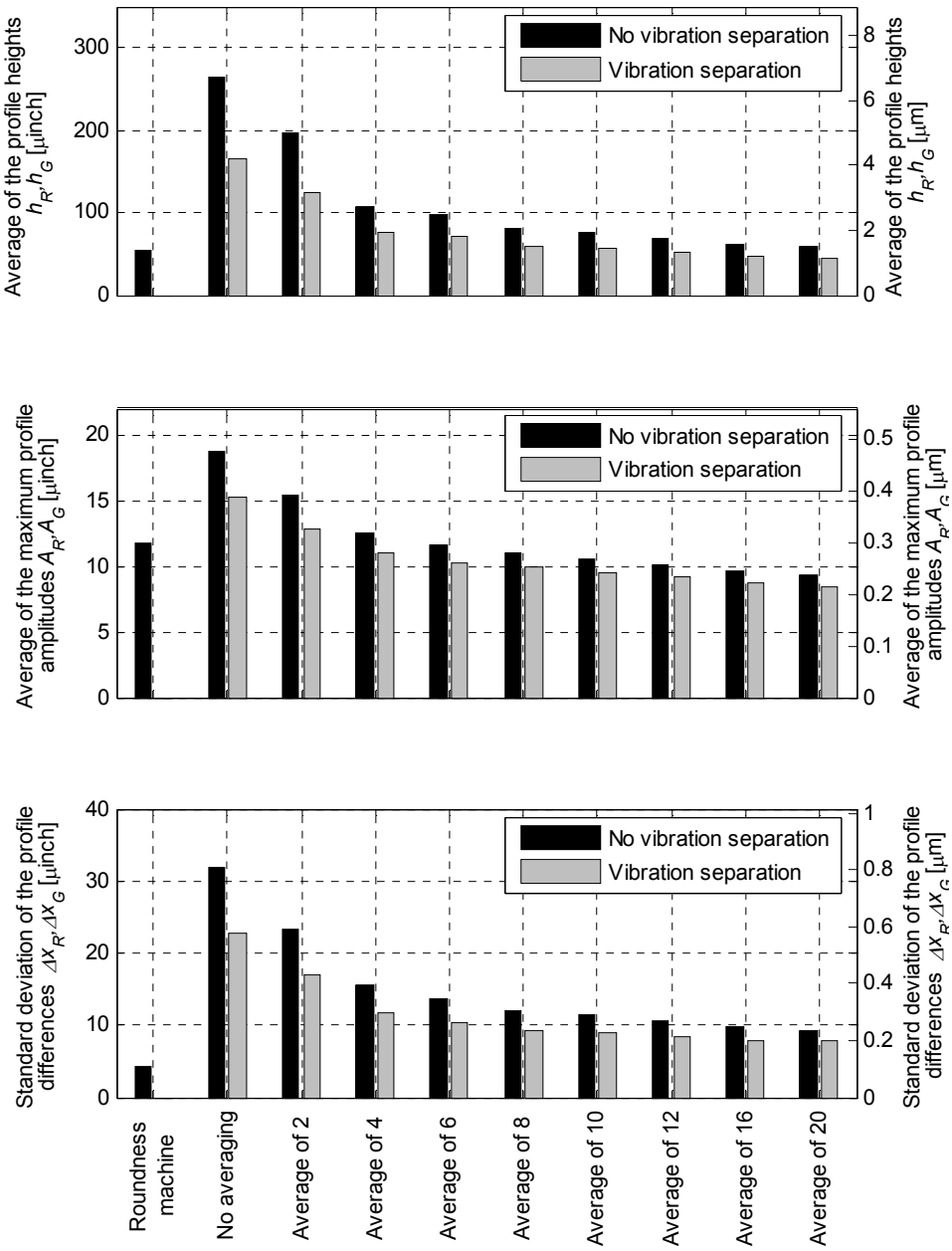

Figure 8-10: Effect of vibration separation in the grinding machine

8.3 Measurement with the Grinding Wheel Running

8.3.1 Methodology

To analyze the effect of running the grinding wheel in the machine without cutting the part, measurements are performed with a set of test parts. To reduce the measurement time, only 10 test parts where used, consisting of 5 “good” parts and 5 “bad” parts. For comparison, every part was first measured with the spindle turned off and then with the spindle turned on. The spindle speed was set to 65000 RPM or 1083 rev/s during the measurements. In the grinding machine, the spindle speed varies between 65000 and 90000 RPM depending on the wear of the grinding wheel. It is expected that due to the high spindle speed, any spindle induced vibration falls also in the high frequency range and will be partly above the 1 kHz cutoff frequency of the low-pass filter in the measurement system. It is therefore assumed that the minimum spindle speed is more critical for the measurement accuracy than higher spindle speeds.

8.3.2 Results

The results of the measurements are shown in Figure 8-11. The graphs display the performance criteria of the 10 parts. The black bars correspond to the measurements with the spindle turned off and the grey bars to the measurements with the spindle turned on.

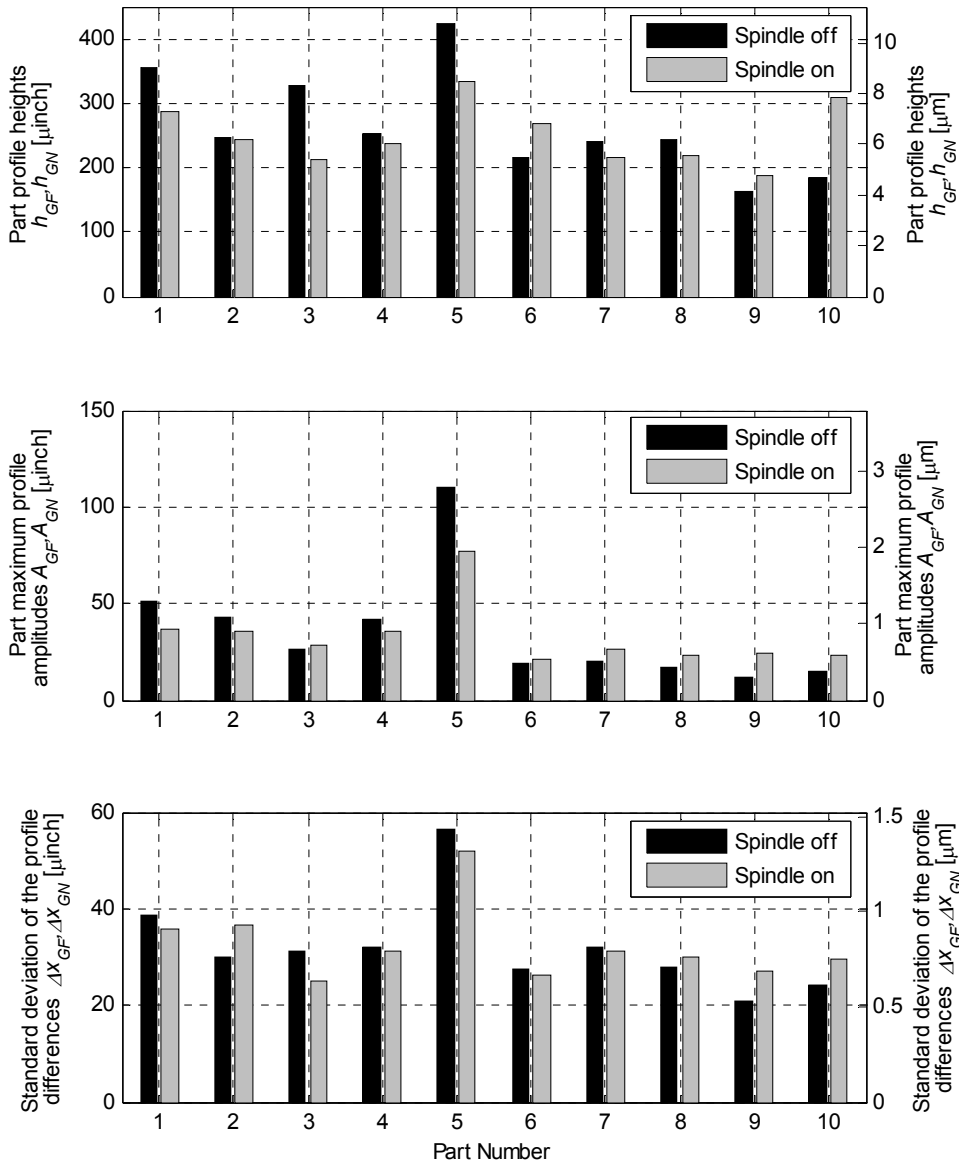

Figure 8-11: Effect of the spindle on the measurements

Based on visual observations alone, it is not clear whether the spindle has an effect on the measurements. Therefore, formal t-tests for each of the three performance criteria are conducted. The criteria for the spindle turned off are denoted by $h_{GF}(n)$, $A_{GF}(n)$, and $\Delta x_{GF}(n)$ and for the spindle turned on by $h_{GN}(n)$, $A_{GN}(n)$, and $\Delta x_{GN}(n)$, where $n = 1,2,...,10$ denotes the part number. The quantities considered are the differences

between the configurations with the spindle turned on and spindle turned off $h_{GN}(n)-h_{GF}(n)$, $A_{GN}(n)-A_{GF}(n)$, $\Delta x_{GN}(n)-\Delta x_{GF}(n)$. For the profile heights, the following null hypothesis H_0 is tested against the alternative hypothesis H_a

$$H_0 : \mu_{h_{GN}-h_{GF}} = 0 \text{ (spindle is not significant)} \tag{8.1}$$

$$H_a : \mu_{h_{GN}-h_{GF}} \neq 0 \text{ (spindle is significant).} \tag{8.2}$$

Under the assumption that $h_{GN}(n)-h_{GF}(n)$ is normal distributed, the test statistic is given by

$$T = \frac{\overline{x}}{s/\sqrt{N_S}}, \tag{8.3}$$

where $\overline{x}$ is the arithmetic sample

$$\overline{x} = \frac{1}{N_S}\sum_{n=1}^{N_S} h_{GN}(n)-h_{GF}(n), \tag{8.4}$$

s the sample standard deviation

$$s = \sqrt{\frac{1}{N_S-1}\sum_{n=1}^{N_S}\left(h_{GN}(n)-h_{GF}(n)-\overline{x}\right)^2}, \tag{8.5}$$

and $N_S = 10$ the number of samples. The t-tests for the maximum profile amplitudes $A_{GN}(n)-A_{GF}(n)$ and the profile difference $\Delta x_{GN}(n)-\Delta x_{GF}(n)$ are performed similarly. The results of the t-tests are shown in Table 8-5. The null hypothesis, i.e. the assumption that the spindle is not significant, cannot be rejected at the 5 % significance. The high P-values indicate that this is also the case for much higher significance levels.

Table 8-5: Results of the t-test for spindle effect

Criterion	Test result at the 5% significance level	P-value
Profile height $h_{GN}(n) - h_{GF}(n)$	$\mu_{h_{GN}-h_{GF}} = 0$ cannot be rejected	0.5445
Max. profile amplitude $A_{GN}(n) - A_{GF}(n)$	$\mu_{A_{GN}-A_{GF}} = 0$ cannot be rejected	0.6059
Profile difference $\Delta x_{GN}(n) - \Delta x_{GF}(n)$	$\mu_{\Delta x_{GN}-\Delta x_{GF}} = 0$ cannot be rejected	0.8157

It is therefore concluded that running the spindle without grinding does not affect the measurements. This is explainable by the high spindle speed. Any harmonic vibration related to the rotation of the spindle will occur at multiples of the rotational frequency which in this case was 1083 Hz. Since this is above the cutoff frequency of the analog low-pass filters, the measurement is not affected by it.

CHAPTER 9 – CONCLUSIONS AND FUTURE WORK

9.1 Summary and Conclusions

This research addressed the problem of fast automatic bore waviness measurement of small parts. A post-process machine was developed to fulfill this task. In addition, possibilities for implementing the measurement in a commercial grinding machine were investigated.

The post-process machine was built as a partial replication of a grinding machine by using a roll-shoe centerless fixture for part rotation and an in-process gage head for the measurement. Since the gage head uses LVDTs to convert the displacement into a voltage, its resolution is theoretically infinite. Through reduction of electrical noise it was possible to improve the accuracy of the measurement system compared to a grinding machine. The signal conditioning card was found to be a major noise source since it exhibited a high susceptibility to magnetic fields. After shielding the card, the noise level was significantly reduced. The improved measurement system was capable of detecting waviness up to a high number of undulations if the parts were rotated slowly enough. In experiments, waviness as high as 128 UPR was detected. It is expected that the system can detect even higher undulations but due to a lack of appropriate test parts this could not be verified.

The roll-shoe centerless fixture proved to offer a precise enough rotation of the part while keeping the loading and unloading time short. A potential problem is the roundness error of the rolls. The result is a motion of the workpiece center during the measurement which is superimposed on the workpiece profile. Since the roll error can be

several times larger than the actual roundness error of the part, this leads to a serious distortion of the measurement. If the roll error cannot be reduced, the fingers should be placed so that the measurement direction points against the stationary shoe of the fixture.

A measurement series with 126 test parts proved that the post-process machine is able to achieve accuracies similar to a roundness machine. It detected all parts that based on measurements with the roundness machine did not meet the specifications. This indicates that the in-process gage head and the roll-shoe centerless fixture are suitable for high precision measurement. A potential problem can be irregularities in the outer diameter of the part. They can cause a motion of the workpiece center similar to the roll error and therefore affect the measurement.

The cycle time of the post-process machine was 4 s which corresponds to a throughput of 15 parts/min. Most of the time is used for loading and unloading parts. Through minor technical modifications, reduction of the cycle time to 2 s is feasible. As a comparison, the total time to measure a part on the roundness machine is approximately 3 min.

During the development and testing of the post-process machine, several disturbances were noticed. By revising the design of the machine, the detrimental effect of most of them could be reduced to a minimum. In the grinding machine, the disturbances were more severe. The possibilities for their reduction through technical methods were limited since modifications of the grinding machine have to be kept at a minimum to avoid interference with its primary purpose of grinding precision parts. A set of analytical methods was therefore developed to alleviate the effect of the disturbances on the measurement.

To reduce random noise in the measurements, a method was presented to calculate an average profile from several individual profiles. A difficulty is the slight variation in the number of data points that constitute a full 360° revolution of the part. In the post-process machine, the encoder that triggers the data acquisition is mounted on the motor spindle instead of the roll spindle. Elasticity of the belt between the motor and rolls causes variation of the angular part movement between encoder pulses. In the grinding machine, the problem is more serious, since no encoder exists and therefore time based sampling has to be used. Here, fluctuations in the roll motor speed are the reason for a variation of the number of data points per revolution. An algorithm was therefore developed to detect the end of a full revolution by searching for the reoccurrence of the beginning of the profile. The algorithm uses the average magnitude difference function (AMDF) for comparing different segments of the profile. The AMDF can tolerate a certain level of noise while also being computationally efficient. To average the individual measurements with different numbers of data points, they have to be interpolated to the same number. This is accomplished by zero-padding in the frequency domain which is fast and free of interpolation errors for bandlimited signals.

The low natural frequency of the gage head was found to be an important limitation of the measurement system. To avoid amplitude and phase distortion of the measurement, it has to be ensured that the highest frequency to be measured remains below the natural frequency of the gage head. This imposes an upper limit on the rotational speed of the part. To overcome this, a procedure was developed to automatically measure the transfer function of the gage with the aid of a test part. By going through a series of acceleration and deceleration cycles, the procedure is able to

measure both amplitude and phase of the transfer function. Knowledge of the transfer function allows restoring the original amplitude and phase of the profile. In experiments at high part speeds, it was verified that the proposed method is capable of restoring the amplitude for frequencies more than twice the natural frequency of the gage head thus extending its usable frequency range. A weakness however exists for the higher frequency ranges. Since their amplitudes are significantly attenuated by the transfer function, the compensation algorithm has to amplify them to their original value. In the same manner as the profile information is amplified, the noise floor is amplified as well resulting in a highly noisy measurement. Combining the transfer function compensation with the averaging over several revolutions reduces the noise again and allows achieving accuracies similar to the measurements taken at low part speed.

Another disturbance originates from the workpiece center motion relative to the gage head. Besides the roundness error of the rolls or the part outer diameter, it can be caused by vibrations in the system. A method was developed to separate the profile from the error motion by combining the measurements of the two fingers in an appropriate way. In the literature, models can be found that are capable of separating the vibration for even but not for odd frequencies when only two fingers are used simultaneously. For full separation of all frequencies, three or more probes are usually employed. Since the task here was to use the existing two-probe gage head, a method was developed to separate vibration for even and odd frequencies for a certain range with only two fingers. This was accomplished by placing the fingers slightly eccentric with respect to the part. The model takes several disturbances into account. Besides the error motions in the x- and the y-direction, these include lumped noise terms that comprises all additional noise for each

finger. Opposite to the existing literature, the model also accounts for inaccuracies in the angle between the fingers. Deviation of the true finger angle from the ideal angle can have a big impact on the recovery of certain frequencies in the spectrum. Given statistical information about the error motions, the random noise, and the variation of the finger angle, the model allows determination of the optimal finger angle and can recover the profile with optimal noise and error motion rejection. Experimental tests on the roundness machine with artificially introduced vibration showed that the proposed method is able to recover the profile even when it is completely swamped in vibration. This was verified for both even and odd frequencies. For the case that no statistical information about the error motions and the random noise is available, a vibration separation method based on a heuristic was presented. During experimental verification, the heuristic based method yielded results similar to the statistics based method.

In the grinding machine, two different scenarios were tested besides full in-process measurement. The tested configurations were measurement with the grinding wheel turned off and measurement with the grinding wheel running but not inserted into the part. Due to limited availability of the grinding machine, measurements during the grinding operation could not be performed. During the setup of the grinding machine, several deficiencies were noticed. The electrical noise in the measurement system was considerably higher than in the post-process machine. It is characterized mainly as harmonics at multiples of the 60 Hz power frequency and as periodically occurring ripple. Since revising the electrical circuits was too time consuming, the harmonics at the power frequencies were eliminated with the aid of a notch filter. This however did not remove the ripple. Another problem was the lack of a rotary encoder for the roll rotation. The

time based sampling resulted in a fluctuation of the number of data points per revolution. The profile length correction was used to compensate for this. However, it was found that the high noise level had a detrimental effect on the accuracy of the profile length correction.

To compensate for the frequency response of the gage head, its transfer function was measured in the grinding machine. The automatic procedure for amplitude and phase measurement was not implemented in the control software of the grinding machine since it was considered to be too time consuming. Instead, a simplified approach was used that measured only the amplitude but not the phase of the transfer function. Thus, correction of the phase was not possible. The amplitude correction also amplified the already very high noise for the higher frequencies. Therefore, several measurements had to be averaged to obtain acceptable results. Averaging a high number of measurements however was also found to introduce an error. This stems from the imperfect profile alignment. Besides the random noise, small portions of the profile cancelled out as well. Applying the vibration separation algorithm to the measurements improved the results, but did not yield any major accuracy gain since vibration was not the main disturbance. Achieving the same accuracy with the grinding machine as with the post-process machine was therefore not possible. With the grinding wheel turned off, a classification error of approximately 15 % was obtained. Tests revealed that turning on the grinding wheel without actually grinding the part does not affect the measurements. Thus, a similar result is expected with the wheel rotating.

For comparing the measurements of the roundness machine, the post-process machine, and the grinding machine, different criteria were used. The profile height is

commonly used to assess the geometry deviations of a part. It is defined as the radial distance between the highest peak and the lowest valley in the profile. While it is probably the best test criterion to ensure the reliability of the final bearing, it was found that its measurement is usually less accurate than other criteria regardless of what machine is used for the measurement. With the roundness machine, measurements were taken at 5 slightly different axial positions of the part with 0.3 mm spacing between the positions. Based on these measurements, 27 % of the 126 test parts yielded contradictory results, i.e. the profile height was below a critical value in at least one of the 5 measurements and above the critical value in at least one measurement. The high variability in the measurements stems from the fact that the profile height is calculated from only two points in the profile.

As an alternative criterion, the maximum profile amplitude was introduced, which is the value of the largest amplitude in the spectrum within the frequency range of interest. Opposite to the profile height, the maximum profile amplitude is calculated from all points in the profile. As a result, it is more robust and usually has a lower variability. Using the maximum profile amplitude as a test criterion, only 4 % of the 126 test parts yielded contradictory results. In addition to that, when comparing the measurements of different machines, the agreement was usually higher than with the profile height. A disadvantage of the maximum profile amplitude is that it can only detect waviness in the profile. The profile height on the other hand, detects any defect including flat spots or small notches.

The main conclusion and contributions of this research are also summarized in Table 9-1.

Table 9-1: Summary of the main conclusions and contributions

- The in-process gage head is capable of measuring waviness up to a high number of undulations.
- The roll-shoe centerless fixture can provide precise rotation of the parts.
- The in-process gage head in combination with roll-shoe centerless fixture can achieve accuracy comparable to a roundness machine.
- The cycle time of the post-process machine was 4 s, which can be reduced further to 2 s.
- An averaging algorithm was developed that can detect and compensate varying numbers of data points per revolution.
- Through compensation of the gage transfer function, the usable frequency range of the gage head can be extended beyond its natural frequency.
- A procedure for automatic in-machine measurement of the complex transfer function was developed and implemented in the post-process machine.
- A model was presented that can remove vibration from the profile for odd and even frequencies by using only two fingers.
- The vibration separation model is capable of taking disturbances such as random noise and variations of the finger angle into account.
- The measurement accuracy of the grinding machine was lower than that of the post-process machine with a part classification error of approximately 15 %.
- Running the grinding wheel without grinding parts does not affect the measurement.
- The electrical noise in the grinding machine was considerably higher than in the post-process machine.
- The profile length correction algorithm yielded less accurate results due to the higher noise levels in the grinding machine.
- The vibration separation algorithm yielded noticeable but no major improvements since vibration was not the largest disturbance.

9.2 Recommendations for Future Work

While this research covered many aspects of the problem addressed, possibilities for improvement and future work were realized.

The developed post-process machine showed good performance in experiments with respect to both accuracy and speed. Nevertheless, some potential for improvement exists. Cross talk between the two probes of the gage head was detected but its reduction was not addressed. By modeling the cross talk, a method for its compensation can be developed. This will require simultaneous calibration of the two fingers which is more time consuming than independent calibration but can lead to accuracy improvements since the cross talk was found to be in the order of 5 %.

The rotational speed of the part of 0.9 rev/s was chosen as a conservative value to prevent amplitude and phase distortion due to the transfer function of the gage. Higher rotational speeds are desirable since they reduce cycle time and increase throughput. More exhaustive tests at different speeds should be done to determine how far the speed can be increased without significant impact on the measurement accuracy. Analytical compensation of the gage transfer function and averaging across several measurements may be used to improve the results.

The transfer function compensation algorithm has the weakness of serious random noise amplification for higher frequencies. Because of this, it can only be used in combination with the averaging algorithm which requires several measurements. The random noise amplification can be reduced if a nonlinear approach is used that takes information about the noise floor into account. Instead of amplifying the amplitude of

every frequency by the inverse of the transfer function, only the component of the amplitude above the noise floor is amplified. This approach however requires statistical modeling of the noise floor.

While the disturbances were fairly well understood for the post-process machine, this was not the case for the grinding machine due to time constraints and limited availability of the machine. For systematic accuracy improvement, a detailed analysis of the noise budget should be performed. This research gave an approximate direction for improvements by pointing out the electrical noise and the lack of a rotary encoder for the rolls as weaknesses. As long as parts were not ground, vibration, although it existed, was not a major concern and was adequately handled by the vibration separation algorithm.

The mechanisms that cause electrical noise are the same as for the post-process machine. Therefore, the methods for its reduction are the same as well. They are mainly comprised of shielding and proper grounding of components. In the same manner as the electrical noise was reduced in the post-process machine, its reduction should also be feasible in the grinding machine. In the grinding machine, this however presents a bigger challenge than in the post-process machine due to the larger number of electrical components and the higher power levels. The general concepts outlined in section 4.3 can be used as guidelines for noise reduction.

A rotary encoder should be installed in the roll drive train as a trigger for the data acquisition. It is expected that this significantly reduces the error introduced by the averaging algorithm. The procedure for automatic measurement of amplitude and phase of the gage transfer function should be implemented in the grinding controller. The benefit is that both the amplitude and phase error of the gage head can be compensated.

Implementing these recommendations allows achieving an accuracy that is similar to the post-process. It requires however, that the grinding wheel is retracted from the part. The measurement time for a part is expected to be approximately 1 s. This procedure can therefore be used for part checks in certain intervals for example during the dressing of the grinding wheel.

For true in-process measurement during the grinding operation, more substantial technical modifications have to be made. One of the most important modifications is to replace the gage head by one with a higher usable frequency range. Using the transfer function compensation may still be beneficial since most gages do not have an ideal frequency behavior. The possibility of measuring the profile with three instead of two fingers simultaneously should also be considered. Three fingers offer better rejection capabilities for both vibration and random noise. The literature review on vibration separation methods in section 6.6.3 revealed that the vibration separation is most successful if the fingers encompass a total arc of 120°. With the current two finger configuration, the fingers are placed opposite to each other, therefore encompassing 180°. Due to the smaller arc for the three finger configuration, additional space is available for the grinding wheel (Figure 9-1).

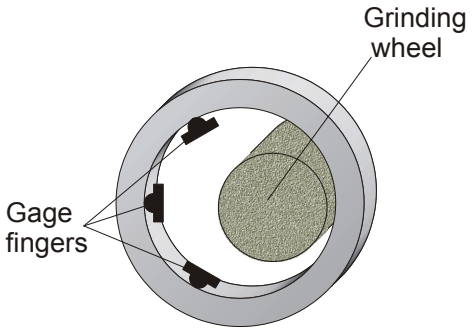

Figure 9-1: Proposed three-finger configuration in the grinding machine

The main focus of this research was the improvement of the part measurement. The models developed here allow determining additional information about the machine such as the workpiece center motion or the random noise present in the measurement system. This information can be utilized for self-monitoring capabilities or for fault detection.

The main recommendations structured into recommendations for the post-process machine, in-machine and in-process implementation for the grinding machine are summarized in Table 9-2.

Table 9-2: Recommendations for future work

Post-process machine	▪ Simultaneous calibration of the two fingers to reduce cross talk ▪ More exhaustive tests to determine possibility of measuring at higher speeds
In-machine implementation	▪ Electrical noise reduction ▪ Mounting of a rotary encoder on the rolls ▪ Implementation of automatic transfer function measurement
In-process implementation	▪ Replacement of the gage head by one with higher useable frequency range ▪ Simultaneous measurement of the part with three fingers instead of two

APPENDIX A – TECHNICAL DATA OF MACHINE COMPONENTS

A.1 Measurement System

Gage Head

Manufacturer:	Marposs
Model:	Thruvar 5
Number of transducers:	2
Type of Transducer:	Linear Variable Differential Transformer (LVDT)
Cutoff Frequency:	approx. 250 Hz
Finger positioning:	through built-in motor

Signal Conditioning Card

Manufacturer:	Solartron
Model:	CAH-8D
Part number:	911001-8DT
Number of channels:	2
Transducer drive:	5 V RMS at 5 or 10 kHz
Transducer sensitivity:	selectable between 0.5 and 750 mV/V
Outputs:	A, B, A+B, A–B, (A+B)/2, (A–B)/2
Output voltage:	± 10 V
Output impedance:	< 1 Ω
Output ripple:	≤ 5 mV peak to peak at 10 kHz
Output filter:	-3 dB cutoff frequency at 500 Hz or 1 kHz
Non-linearity:	< 0.02 %
Temperature coefficient	
Zero:	< ± 0.01 %/°C
Gain:	< ± 0.01 %/°C

Low-Pass Filter

Manufacturer:	Krohn-Hite
Model:	3384
Number of channels:	4
Filter mode:	Low-pass or high-pass
Filter type:	8 pole Butterworth or Bessel
Cutoff frequency range:	0.1 Hz to 200 kHz
Cutoff frequency accuracy:	±3 %
Gain at cutoff frequency:	
Butterworth:	–3 dB
Bessel:	–12.6 dB
Input voltage:	±10 V
Output voltage:	±10 V
Wideband noise:	< 400 μV RMS

Data Acquisition Card

Manufacturer:	National Instruments
Model:	NI PCI-6031E
Analog input	
Mode:	differential or single-ended
Number of channels:	64 (differential), 32 (single-ended)
Resolution:	16 bit
Max. sampling rate:	100 kS/s
Input range:	0.1 to 10 V unipolar or bipolar
Relative accuracy:	±0.75 LSB typical, ±1 LSB max.
Analog output	
Number of channels:	2
Resolution:	16 bit
Max update rate:	100 kS/s
Output voltage:	±10 V
Relative accuracy:	±0. 5 LSB typical, ±1 LSB max.
Digital input/output	
Number of channels:	8
Max transfer rate:	50 kwords/s

A.2 Mechanical Components

Roll Motor

Manufacturer:	Bodine
Model No.:	6542
Product No.:	33A5BEPM-5F
Type:	Right angle DC gear motor
Max voltage:	130 V
Gear ratio:	20
Motor spindle speed:	2500 RPM
Output spindle speed:	125 RPM
Rated torque:	4.2 Nm
Peak torque:	9.4 Nm
Power:	0.093 kW (0.127 HP)

Vibration Isolation System

Manufacturer:	Newport
Model:	I-125A-4
Number of isolators:	4
Max load per isolator:	60 kg
Vertical Isolation	
Resonance frequency:	1.8 Hz
Amplification at res.:	9 dB
Isolation at 5 Hz:	85 %
Isolation at 10 Hz:	95 %
Horizontal Isolation	
Resonance frequency:	1.3 Hz
Amplification at res.:	13 dB
Isolation at 5 Hz:	86 %
Isolation at 10 Hz:	96 %

A.3 Electrical Components

Main transformer

Manufacturer:	Square D
Model:	1.5S1F
Type:	Single phase general purpose transformer
Power:	1.5 kVA
Primary:	240 X 480 V, 60 Hz
Secondary:	120/240 V, 60 Hz

Power supply 1

Manufacturer:	Astec
Model:	24N4.8
Input:	120 V
Output:	24 V, 4.8 A

Power supply 2

Manufacturer:	Condor
Model:	HTAA-16W-A+
Input:	120 V
Output:	+5 V, 2 A
	+15 V, 0.2 A
	–15 V, 0.2 A

PLC

Manufacturer:	GE Fanuc
Model	
Power supply:	IC693PWR321
CPU module:	IC693CPU331
Communications module:	IC693CMM311
5 VDC input module:	IC693MDL654
24 VDC input module:	IC693MDL645
24 VDC output module:	IC693MDL740

Roll Motor Drive

Manufacturer:	KB Electronics
Model:	KBWS-22D
Part number:	9492
Input voltage:	115 V
Motor voltage range:	0 V to 130 V
Maximum power:	0.25 kW (0.33 HP)
Switching frequency:	> 16 kHz

A.4 Hydraulic Components

Hydraulic Unit

Manufacturer:	Hydropa
Pump 1	
Model:	Hydropa Typ 2 ISP 5.5 CR/S
Type:	Gear pump, 12 teeth
Max pressure:	210 bar
Max flow rate:	9.2 L/min, 5.5 cm^3/rev
Pump 2	
Model:	Hydropa Typ 1 ISP 3 GF/S
Type:	Gear pump, 9 teeth
Max pressure:	180 bar
Max flow rate:	5 L/min, 3 cm^3/rev
Motor	
Manufacturer:	Leroy-Somer
Model:	Typ LSE100L
Type:	Synchron-Motor
Power:	2.5 kW
Speed:	1715 RPM

Accumulators

Manufacturer:	Hydac
Model:	SB210P-0.32E1/112S-210CI
Product No:	02102633
Type:	Welded Diaphragm
Gas volume:	0.32 L
Gas pressure:	20 bar

A.5 Equipment for Vibration Measurement

Signal Generator

Manufacturer:	Tektronix
Model:	FG 504
Output voltage	30 V peak-to-peak
Output waveform	Sine-wave, square-wave, and triangle
Frequency range:	0.001 Hz to 40 MHz
Frequency resolution:	0.01 % of full range

Vibration Exciter

Manufacturer:	Brüel & Kjær
Model:	Type 4809
Maximum input current:	5 A RMS
Maximum displacement:	8 mm peak-to-peak
Force range:	±44.5 N
Frequency range:	10 Hz to 20 kHz
Resonant frequency:	20 kHz

Vibration Exciter Power Amplifier

Manufacturer:	Brüel & Kjær
Model:	Type 2706

Force Transducer

Manufacturer:	PCB Piezotronics
Model:	208A02
Output voltage range:	±5 V
Force range:	±445 N
Sensitivity:	11.24 mV/N
Resonant frequency:	70 kHz
Discharge time constant:	500 s

Charge Amplifier

Manufacturer:	PCB Piezotronics
Model:	480A

APPENDIX B – VIBRATION SEPARATION

B.1 Harmonic Weighting Function

The harmonic weighting function $M_W(k)$ for the sum of two centrically placed fingers can be simplified to

$$\begin{aligned}
\left|M_W(k)\right| &= \left|(1+e^{-j(\pi-\varphi)k})\cos(\varphi/2)\right| \\
&= \left|1+e^{-j\pi k}e^{j\varphi k}\right|\cos(\varphi/2) \\
&= \left|1+(-1)^k e^{j\varphi k}\right|\cos(\varphi/2) \\
&= \left|1+(-1)^k\cos(\varphi k)+j(-1)^k\sin(\varphi k)\right|\cos(\varphi/2) \\
&= \sqrt{\left(1+(-1)^k\cos(\varphi k)\right)^2+\left((-1)^k\sin(\varphi k)\right)^2}\cos(\varphi/2) \\
&= \sqrt{1+2(-1)^k\cos(\varphi k)+(-1)^{2k}\cos^2(\varphi k)+(-1)^{2k}\sin^2(\varphi k)}\cos(\varphi/2) \\
&= \sqrt{2\left(1+(-1)^k\cos(\varphi k)\right)}\cos(\varphi/2)
\end{aligned} \quad . \qquad \text{(B.1)}$$

Distinguishing between even and odd frequencies yields

$$\left|M_W(k)\right| = \begin{cases} \sqrt{2\left(1+\cos(\varphi k)\right)}\cos(\varphi/2) & \text{for } k=0,2,4,... \\ \sqrt{2\left(1-\cos(\varphi k)\right)}\cos(\varphi/2) & \text{for } k=1,3,5,... \end{cases} . \qquad \text{(B.2)}$$

Thus, for even frequencies ($k=0,2,4,...$), the harmonic weighting function becomes zero if

$$\cos(\varphi k) = -1 \text{ or} \qquad \text{(B.3)}$$

$$k = \frac{(1+2n)\pi}{\varphi}, \quad n=0,1,2,.... \qquad \text{(B.4)}$$

For odd frequencies ($k=1,3,5,...$), the zeros are located at

$$\cos(\varphi k) = 1 \text{ or} \qquad \text{(B.5)}$$

$$k = \frac{2n\pi}{\varphi},\ n = 0, 1, 2, \ldots. \tag{B.6}$$

B.2 Variance of the Sum of the Signals

The harmonics estimated from the sum of the signals are given by

$$\tilde{R}_S(k) = \Big((1+e^{-j(\pi-\Phi)k}) \cos(\Phi/2)\, R(k) - 2\tan(\Phi/2) \boldsymbol{\mathcal{E}}_y(k) + \boldsymbol{\mathcal{N}}_A(k) + \boldsymbol{\mathcal{N}}_B(k) \Big) \Big/ (1+e^{-j(\pi-\mu_\Phi)k}) \cos(\mu_\Phi/2) \,. \tag{B.7}$$

Using the error propagation law, the variance of $\tilde{R}_S(k)$ can be approximated by

$$\mathrm{Var}\big(\tilde{R}_S(k)\big) \approx \left|\frac{\partial \tilde{R}_S(k)}{\partial \Phi}\right|^2 \sigma_\Phi{}^2 + \left|\frac{\partial \tilde{R}_S(k)}{\partial \boldsymbol{\mathcal{E}}_y}\right|^2 \sigma_{\mathcal{E}_y}{}^2 + \left|\frac{\partial \tilde{R}_S(k)}{\partial \boldsymbol{\mathcal{N}}_A}\right|^2 \sigma_{\mathcal{N}_A}{}^2 + \left|\frac{\partial \tilde{R}_S(k)}{\partial \boldsymbol{\mathcal{N}}_B}\right|^2 \sigma_{\mathcal{N}_B}{}^2 . \tag{B.8}$$

Subsequently, the four partial derivatives are calculated. They are evaluated at $\Phi = \mu_\varphi$, $\boldsymbol{\mathcal{E}}_y = \mu_{\mathcal{E}_y} = 0$, $\boldsymbol{\mathcal{N}}_A = \mu_{\mathcal{N}_A} = 0$, $\boldsymbol{\mathcal{N}}_B = \mu_{\mathcal{N}_B} = 0$. The squared absolute partial derivative of $\tilde{R}_S(k)$ with respect to Φ is

$$\left|\frac{\partial \tilde{R}_S(k)}{\partial \Phi}\right|^2 = \Big| \Big((jke^{-j(\pi-\mu_\varphi)k}) \cos(\mu_\varphi/2) R(k) - \tfrac{1}{2}(1+e^{-j(\pi-\mu_\varphi)k}) \sin(\mu_\varphi/2) R(k) - \big(1+\tan^2(\mu_\varphi/2)\big) \mu_{\mathcal{E}_y} \Big) \Big/ \Big((1+e^{-j(\pi-\mu_\Phi)k}) \cos(\mu_\Phi/2) \Big) \Big|^2 \,. \tag{B.9}$$

Since $\mu_{\mathcal{E}_y} = 0$, this simplifies to

$$\left|\frac{\partial \tilde{R}_S(k)}{\partial \Phi}\right|^2 = \left| \frac{(jke^{-j(\pi-\mu_\varphi)k}) \cos(\tfrac{1}{2}\mu_\varphi) R(k) - \tfrac{1}{2}(1+e^{-j(\pi-\mu_\varphi)k}) \sin(\tfrac{1}{2}\mu_\varphi) R(k)}{(1+e^{-j(\pi-\mu_\Phi)k}) \cos(\tfrac{1}{2}\mu_\varphi)} \right|^2 \tag{B.10}$$

$$= \frac{\left| (jke^{-j(\pi-\mu_\varphi)k}) \cos(\tfrac{1}{2}\mu_\varphi) R(k) - \tfrac{1}{2}(1+e^{-j(\pi-\mu_\varphi)k}) \sin(\tfrac{1}{2}\mu_\varphi) R(k) \right|^2}{\left| (1+e^{-j(\pi-\mu_\Phi)k}) \cos(\tfrac{1}{2}\mu_\varphi) \right|^2} \tag{B.11}$$

$$=: \frac{N_S}{D_S} \,, \tag{B.12}$$

where N_S and D_S are the numerator and denominator of the equation. Expanding the numerator yields

$$N_S = \left|(jke^{-j(\pi-\mu_\varphi)k})\cos(\tfrac{1}{2}\mu_\varphi) - \tfrac{1}{2}(1+e^{-j(\pi-\mu_\varphi)k})\sin(\tfrac{1}{2}\mu_\varphi)\right|^2 \left|R(k)\right|^2. \tag{B.13}$$

Defining $\alpha_k = (\pi - \mu_\varphi)k$, this can be rewritten as

$$N_S = \left|(jke^{-j\alpha_k})\cos(\tfrac{1}{2}\mu_\varphi) - \tfrac{1}{2}(1+e^{-j\alpha_k})\sin(\tfrac{1}{2}\mu_\varphi)\right|^2 \left|R(k)\right|^2 \tag{B.14}$$

$$\begin{aligned} &= \Big|(jk\cos(-\alpha_k)\cos(\tfrac{1}{2}\mu_\varphi) - k\sin(-\alpha_k)\cos(\tfrac{1}{2}\mu_\varphi) \\ &\quad -\tfrac{1}{2}\sin(\tfrac{1}{2}\mu_\varphi) - \tfrac{1}{2}\cos(-\alpha_k)\sin(\tfrac{1}{2}\mu_\varphi) + \tfrac{1}{2}j\sin(-\alpha_k)\sin(\tfrac{1}{2}\mu_\varphi)\Big|^2 \left|R(k)\right|^2 \end{aligned} \tag{B.15}$$

$$\begin{aligned} &= \Big|\Big(k\cos(\alpha_k)\cos(\tfrac{1}{2}\mu_\varphi) + \tfrac{1}{2}\sin(\alpha_k)\sin(\tfrac{1}{2}\mu_\varphi)\Big)j \\ &\quad +\Big(-\tfrac{1}{2}\sin(\tfrac{1}{2}\mu_\varphi) + k\sin(\alpha_k)\cos(\tfrac{1}{2}\mu_\varphi) - \tfrac{1}{2}\cos(\alpha_k)\sin(\tfrac{1}{2}\mu_\varphi)\Big)\Big|^2 \left|R(k)\right|^2. \end{aligned} \tag{B.16}$$

Computation of the squared absolute value of the complex expression yields

$$\begin{aligned} N_S = \Big[&\Big(k\cos(\alpha_k)\cos(\tfrac{1}{2}\mu_\varphi) + \tfrac{1}{2}\sin(\alpha_k)\sin(\tfrac{1}{2}\mu_\varphi)\Big)^2 \\ &+\Big(-\tfrac{1}{2}\sin(\tfrac{1}{2}\mu_\varphi) + k\sin(\alpha_k)\cos(\tfrac{1}{2}\mu_\varphi) - \tfrac{1}{2}\cos(\alpha_k)\sin(\tfrac{1}{2}\mu_\varphi)\Big)^2\Big]\left|R(k)\right|^2 \end{aligned}. \tag{B.17}$$

Expanding the powers

$$\begin{aligned} N_S = \Big[&k^2\cos^2(\alpha_k)\cos^2(\tfrac{1}{2}\mu_\varphi) + \tfrac{1}{4}\sin^2(\alpha_k)\sin^2(\tfrac{1}{2}\mu_\varphi) \\ &+k\cos(\alpha_k)\sin(\alpha_k)\cos(\tfrac{1}{2}\mu_\varphi)\sin(\tfrac{1}{2}\mu_\varphi) \\ &+\tfrac{1}{4}\sin^2(\tfrac{1}{2}\mu_\varphi) + k^2\sin^2(\alpha_k)\cos^2(\tfrac{1}{2}\mu_\varphi) + \tfrac{1}{4}\cos^2(\alpha_k)\sin^2(\tfrac{1}{2}\mu_\varphi) \\ &-k\sin(\alpha_k)\cos(\tfrac{1}{2}\mu_\varphi)\sin(\tfrac{1}{2}\mu_\varphi) + \tfrac{1}{2}\cos(\alpha_k)\sin^2(\tfrac{1}{2}\mu_\varphi) \\ &-k\cos(\alpha_k)\sin(\alpha_k)\cos(\tfrac{1}{2}\mu_\varphi)\sin(\tfrac{1}{2}\mu_\varphi)\Big]\left|R(k)\right|^2 \end{aligned} \tag{B.18}$$

and collecting terms yields

$$N_S = \Big[k^2 \cos^2(\tfrac{1}{2}\mu_\varphi) + \tfrac{1}{2}\sin^2(\tfrac{1}{2}\mu_\varphi) + \tfrac{1}{2}\cos(\alpha_k)\sin^2(\tfrac{1}{2}\mu_\varphi) - k\sin(\alpha_k)\cos(\tfrac{1}{2}\mu_\varphi)\sin(\tfrac{1}{2}\mu_\varphi)\Big] \big|R(k)\big|^2 \quad . \tag{B.19}$$

Using the following trigonometric formulas

$$\begin{aligned} \cos(\alpha_k) &= \cos\Big((\pi - \mu_\varphi)k\Big) \\ &= \cos(\pi k)\cos(\mu_\varphi k) + \sin(\pi k)\sin(\mu_\varphi k) \\ &= (-1)^k \cos(\mu_\varphi k) \end{aligned} \tag{B.20}$$

$$\begin{aligned} \sin(\alpha_k) &= \sin\Big((\pi - \mu_\varphi)k\Big) \\ &= \sin(\pi k)\cos(\mu_\varphi k) - \cos(\pi k)\sin(\mu_\varphi k) \\ &= (-1)^{k+1} \sin(\mu_\varphi k) \end{aligned} \tag{B.21}$$

$$\begin{aligned} \cos^2(\tfrac{1}{2}\mu_\varphi) &= \Big(\sqrt{\tfrac{1}{2}(1+\cos(\mu_\varphi))}\Big)^2 \\ &= \tfrac{1}{2} + \tfrac{1}{2}\cos(\mu_\varphi) \end{aligned} \tag{B.22}$$

$$\begin{aligned} \sin^2(\tfrac{1}{2}\mu_\varphi) &= \Big(\sqrt{\tfrac{1}{2}(1-\cos(\mu_\varphi))}\Big)^2 \\ &= \tfrac{1}{2} - \tfrac{1}{2}\cos(\mu_\varphi) \end{aligned} \tag{B.23}$$

$$\begin{aligned} \cos(\alpha_k)\sin^2(\tfrac{1}{2}\mu_\varphi) &= \cos(\alpha_k)\tfrac{1}{2}\Big(1-\cos(\mu_\varphi)\Big) \\ &= \tfrac{1}{2}\cos(\alpha_k) - \tfrac{1}{4}\cos(\alpha_k)\cos(\mu_\varphi) \\ &= \tfrac{1}{2}(-1)^k \cos(\mu_\varphi k) - \tfrac{1}{2}(-1)^k \cos(\mu_\varphi k)\cos(\mu_\varphi) \\ &= \tfrac{1}{2}(-1)^k \cos(\mu_\varphi k) - \tfrac{1}{4}(-1)^k \Big(\cos(\mu_\varphi(k-1)) + \cos(\mu_\varphi(k+1))\Big) \end{aligned} \tag{B.24}$$

$$\begin{aligned} \sin(\alpha_k)\cos(\tfrac{1}{2}\mu_\varphi)\sin(\tfrac{1}{2}\mu_\varphi) &= \tfrac{1}{2}\sin(\alpha_k)\sin(\mu_\varphi) \\ &= \tfrac{1}{2}(-1)^{k+1} \sin(\mu_\varphi k)\sin(\mu_\varphi) \\ &= \tfrac{1}{4}(-1)^k \Big(-\cos(\mu_\varphi(k-1)) + \cos(\mu_\varphi(k+1))\Big) \end{aligned} \quad , \tag{B.25}$$

the numerator can be simplified further

$$\begin{aligned} N_S = &\left(\tfrac{k^2}{2}+\tfrac{1}{4}+\left(\tfrac{k^2}{2}-\tfrac{1}{4}\right)\cos(\mu_\varphi)\right. \\ &+(-1)^k\left((\tfrac{k}{4}-\tfrac{1}{8})\cos(\mu_\varphi(k-1))\right. \\ &\left.\left.+\tfrac{1}{4}\cos(\mu_\varphi k)+(-\tfrac{k}{4}-\tfrac{1}{8})\cos(\mu_\varphi(k+1))\right)\right)\left|R(k)\right|^2 \end{aligned} . \tag{B.26}$$

For small values of the expected eccentricity angle μ_φ

$$\cos((\mu_\varphi(k-1)) \approx \cos(\mu_\varphi k) \approx \cos((\mu_\varphi(k+1)) \tag{B.27}$$

and therefore

$$N_S \approx \left(\tfrac{k^2}{2}+\tfrac{1}{4}+\left(\tfrac{k^2}{2}-\tfrac{1}{4}\right)\cos(\mu_\varphi)\right)\left|R(k)\right|^2 . \tag{B.28}$$

Expanding the denominator D_S yields

$$\begin{aligned} D_S &= \left|(1+e^{-j(\pi-\mu_\Phi)k})\cos(\tfrac{1}{2}\mu_\varphi)\right|^2 \\ &= \left|\left(1+\cos((\pi-\mu_\Phi)k)\right)+\left(-\sin((\pi-\mu_\Phi)k)\right)j\right|^2\left|\cos(\tfrac{1}{2}\mu_\varphi)\right|^2 \end{aligned} . \tag{B.29}$$

Calculation of the absolute value results in

$$D_S = \left(\left(1+\cos((\pi-\mu_\Phi)k)\right)^2+\left(\sin((\pi-\mu_\Phi)k)\right)^2\right)\cos^2(\tfrac{1}{2}\mu_\varphi) \tag{B.30}$$

$$\begin{aligned} &= \left(1+\cos^2((\pi-\mu_\Phi)k)+2\cos((\pi-\mu_\Phi)k)\right. \\ &\quad \left.+\sin^2((\pi-\mu_\Phi)k)\right)\cos^2(\tfrac{1}{2}\mu_\varphi) \end{aligned} \tag{B.31}$$

$$= \left(1+\cos((\pi-\mu_\Phi)k)\right)2\cos^2(\tfrac{1}{2}\mu_\varphi) . \tag{B.32}$$

Using the trigonometric relations (B.20) and (B.22), the denominator can be written as

$$D_S = \left(1+(-1)^k\cos(\mu_\Phi k)\right)\left(1+\cos(\mu_\varphi)\right) . \tag{B.33}$$

The squared absolute partial derivative of $\tilde{R}_S(k)$ with respect to Φ is therefore given by

$$\left|\frac{\partial \tilde{R}_S(k)}{\partial \Phi}\right|^2 \approx \frac{\left(\frac{k^2}{2}+\frac{1}{4}+\left(\frac{k^2}{2}-\frac{1}{4}\right)\cos(\mu_\varphi)\right)\left|R(k)\right|^2}{\left(1+(-1)^k\cos(\mu_\Phi k)\right)\left(1+\cos(\mu_\varphi)\right)}. \tag{B.34}$$

The squared absolute partial derivative of $\tilde{R}_S(k)$ with respect to $\boldsymbol{\varepsilon}_y$ is

$$\begin{aligned}\left|\frac{\partial \tilde{R}_S(k)}{\partial \boldsymbol{\varepsilon}_y}\right|^2 &= \left|\frac{-2\tan(\frac{1}{2}\mu_\varphi)}{(1+e^{-j(\pi-\mu_\Phi)k})\cos(\frac{1}{2}\mu_\varphi)}\right|^2 \\ &= \frac{\left|-2\tan(\frac{1}{2}\mu_\varphi)\right|^2}{\left|(1+e^{-j(\pi-\mu_\Phi)k})\cos(\frac{1}{2}\mu_\varphi)\right|^2} \\ &= \frac{4\tan^2(\frac{1}{2}\mu_\varphi)}{\left(1+(-1)^k\cos(\mu_\Phi k)\right)\left(1+\cos(\mu_\varphi)\right)}\end{aligned} \tag{B.35}$$

and the squared absolute partial derivatives of $\tilde{R}_S(k)$ with respect to $\boldsymbol{\mathcal{N}}_A$ and $\boldsymbol{\mathcal{N}}_B$ are

$$\begin{aligned}\left|\frac{\partial \tilde{R}_S(k)}{\partial \boldsymbol{\mathcal{N}}_A}\right|^2 &= \left|\frac{1}{(1+e^{-j(\pi-\mu_\Phi)k})\cos(\frac{1}{2}\mu_\varphi)}\right|^2 \\ &= \frac{1}{\left(1+(-1)^k\cos(\mu_\Phi k)\right)\left(1+\cos(\mu_\varphi)\right)}\end{aligned} \tag{B.36}$$

and

$$\left|\frac{\partial \tilde{R}_S(k)}{\partial \boldsymbol{\mathcal{N}}_B}\right|^2 = \frac{1}{\left(1+(-1)^k\cos(\mu_\Phi k)\right)\left(1+\cos(\mu_\varphi)\right)}. \tag{B.37}$$

B.3 Variance of the Difference of the Signals

The harmonics estimated from the difference of the signals are given by

$$\tilde{R}_D(k) = \Big((1-e^{-j(\pi-\Phi)k})\cos(\Phi/2)\,R(k) - 2\boldsymbol{\mathcal{E}}_x(k) + \boldsymbol{\mathcal{N}}_A(k) - \boldsymbol{\mathcal{N}}_B(k)\Big) \Big/ (1-e^{-j(\pi-\mu_\Phi)k})\cos(\mu_\Phi/2) \tag{B.38}$$

Using the error propagation law, the variance of $\tilde{R}_D(k)$ can be approximated by

$$\mathrm{Var}\Big(\tilde{R}_D(k)\Big) \approx \left|\frac{\partial \tilde{R}_D(k)}{\partial \Phi}\right|^2 \sigma_\Phi{}^2 + \left|\frac{\partial \tilde{R}_D(k)}{\partial \boldsymbol{\mathcal{E}}_x}\right|^2 \sigma_{\boldsymbol{\mathcal{E}}_x}{}^2 + \left|\frac{\partial \tilde{R}_D(k)}{\partial \boldsymbol{\mathcal{N}}_A}\right|^2 \sigma_{\boldsymbol{\mathcal{N}}_A}{}^2 + \left|\frac{\partial \tilde{R}_D(k)}{\partial \boldsymbol{\mathcal{N}}_B}\right|^2 \sigma_{\boldsymbol{\mathcal{N}}_B}{}^2. \tag{B.39}$$

Subsequently, the four partial derivatives are calculated. They are evaluated at $\Phi = \mu_\varphi$, $\boldsymbol{\mathcal{E}}_x = \mu_{\boldsymbol{\mathcal{E}}_x} = 0$, $\boldsymbol{\mathcal{N}}_A = \mu_{\boldsymbol{\mathcal{N}}_A} = 0$, $\boldsymbol{\mathcal{N}}_B = \mu_{\boldsymbol{\mathcal{N}}_B} = 0$. The squared absolute partial derivative of $\tilde{R}_D(k)$ with respect to Φ is

$$\left|\frac{\partial \tilde{R}_D(k)}{\partial \Phi}\right|^2 = \left|\frac{(-jke^{-j(\pi-\mu_\varphi)k})\cos(\tfrac{1}{2}\mu_\varphi)R(k) - \tfrac{1}{2}(1-e^{-j(\pi-\mu_\varphi)k})\sin(\tfrac{1}{2}\mu_\varphi)R(k)}{(1-e^{-j(\pi-\mu_\Phi)k})\cos(\tfrac{1}{2}\mu_\varphi)}\right|^2 \tag{B.40}$$

$$=: \frac{N_D}{D_D}, \tag{B.41}$$

where N_D and D_D are the numerator and denominator of the equation. Expanding the numerator yields

$$N_D = \left|(-jke^{-j(\pi-\mu_\varphi)k})\cos(\tfrac{1}{2}\mu_\varphi) - \tfrac{1}{2}(1-e^{-j(\pi-\mu_\varphi)k})\sin(\tfrac{1}{2}\mu_\varphi)\right|^2 \left|R(k)\right|^2. \tag{B.42}$$

Defining $\alpha_k = (\pi - \mu_\varphi)k$, this can be rewritten as

$$N_D = \left|(-jke^{-j\alpha_k})\cos(\tfrac{1}{2}\mu_\varphi) - \tfrac{1}{2}(1-e^{-j\alpha_k})\sin(\tfrac{1}{2}\mu_\varphi)\right|^2 \left|R(k)\right|^2 \tag{B.43}$$

$$= \left| (-jk\cos(-\alpha_k)\cos(\tfrac{1}{2}\mu_\varphi) + k\sin(-\alpha_k)\cos(\tfrac{1}{2}\mu_\varphi) \right.$$
$$\left. -\tfrac{1}{2}\sin(\tfrac{1}{2}\mu_\varphi) + \tfrac{1}{2}\cos(-\alpha_k)\sin(\tfrac{1}{2}\mu_\varphi) + \tfrac{1}{2}j\sin(-\alpha_k)\sin(\tfrac{1}{2}\mu_\varphi) \right|^2 |R(k)|^2 \quad \text{(B.44)}$$

$$= \left| \left(-k\cos(\alpha_k)\cos(\tfrac{1}{2}\mu_\varphi) - \tfrac{1}{2}\sin(\alpha_k)\sin(\tfrac{1}{2}\mu_\varphi)\right) j \right.$$
$$\left. +\left(-\tfrac{1}{2}\sin(\tfrac{1}{2}\mu_\varphi) - k\sin(\alpha_k)\cos(\tfrac{1}{2}\mu_\varphi) + \tfrac{1}{2}\cos(\alpha_k)\sin(\tfrac{1}{2}\mu_\varphi)\right) \right|^2 |R(k)|^2 . \quad \text{(B.45)}$$

Computation of the squared absolute value of the complex expression yields

$$N_D = \left[\left(k\cos(\alpha_k)\cos(\tfrac{1}{2}\mu_\varphi) + \tfrac{1}{2}\sin(\alpha_k)\sin(\tfrac{1}{2}\mu_\varphi)\right)^2 \right.$$
$$\left. +\left(-\tfrac{1}{2}\sin(\tfrac{1}{2}\mu_\varphi) - k\sin(\alpha_k)\cos(\tfrac{1}{2}\mu_\varphi) + \tfrac{1}{2}\cos(\alpha_k)\sin(\tfrac{1}{2}\mu_\varphi)\right)^2 \right] |R(k)|^2 . \quad \text{(B.46)}$$

Expanding the powers

$$\begin{aligned} N_D = \Big[& k^2\cos^2(\alpha_k)\cos^2(\tfrac{1}{2}\mu_\varphi) + \tfrac{1}{4}\sin^2(\alpha_k)\sin^2(\tfrac{1}{2}\mu_\varphi) \\ & + k\cos(\alpha_k)\sin(\alpha_k)\cos(\tfrac{1}{2}\mu_\varphi)\sin(\tfrac{1}{2}\mu_\varphi) \\ & + \tfrac{1}{4}\sin^2(\tfrac{1}{2}\mu_\varphi) + k^2\sin^2(\alpha_k)\cos^2(\tfrac{1}{2}\mu_\varphi) + \tfrac{1}{4}\cos^2(\alpha_k)\sin^2(\tfrac{1}{2}\mu_\varphi) \\ & + k\sin(\alpha_k)\cos(\tfrac{1}{2}\mu_\varphi)\sin(\tfrac{1}{2}\mu_\varphi) - \tfrac{1}{2}\cos(\alpha_k)\sin^2(\tfrac{1}{2}\mu_\varphi) \\ & - k\cos(\alpha_k)\sin(\alpha_k)\cos(\tfrac{1}{2}\mu_\varphi)\sin(\tfrac{1}{2}\mu_\varphi) \Big] |R(k)|^2 \end{aligned} \quad \text{(B.47)}$$

and collecting terms yields

$$\begin{aligned} N_D = \Big[& k^2\cos^2(\tfrac{1}{2}\mu_\varphi) + \tfrac{1}{2}\sin^2(\tfrac{1}{2}\mu_\varphi) - \tfrac{1}{2}\cos(\alpha_k)\sin^2(\tfrac{1}{2}\mu_\varphi) \\ & + k\sin(\alpha_k)\cos(\tfrac{1}{2}\mu_\varphi)\sin(\tfrac{1}{2}\mu_\varphi) \Big] |R(k)|^2 \end{aligned} . \quad \text{(B.48)}$$

Using the following trigonometric formulas

$$\begin{aligned} \cos(\alpha_k) &= \cos\left((\pi - \mu_\varphi)k\right) \\ &= \cos(\pi k)\cos(\mu_\varphi k) + \sin(\pi k)\sin(\mu_\varphi k) \\ &= (-1)^k \cos(\mu_\varphi k) \end{aligned} \quad \text{(B.49)}$$

$$\begin{aligned}\sin(\alpha_k) &= \sin\left((\pi-\mu_\varphi)k\right)\\ &= \sin(\pi k)\cos(\mu_\varphi k)-\cos(\pi k)\sin(\mu_\varphi k)\\ &= (-1)^{k+1}\sin(\mu_\varphi k)\end{aligned} \tag{B.50}$$

$$\begin{aligned}\cos^2(\tfrac{1}{2}\mu_\varphi) &= \left(\sqrt{\tfrac{1}{2}(1+\cos(\mu_\varphi))}\right)^2\\ &= \tfrac{1}{2}+\tfrac{1}{2}\cos(\mu_\varphi)\end{aligned} \tag{B.51}$$

$$\begin{aligned}\sin^2(\tfrac{1}{2}\mu_\varphi) &= \left(\sqrt{\tfrac{1}{2}(1-\cos(\mu_\varphi))}\right)^2\\ &= \tfrac{1}{2}-\tfrac{1}{2}\cos(\mu_\varphi)\end{aligned} \tag{B.52}$$

$$\begin{aligned}\cos(\alpha_k)\sin^2(\tfrac{1}{2}\mu_\varphi) &= \cos(\alpha_k)\tfrac{1}{2}\left(1-\cos(\mu_\varphi)\right)\\ &= \tfrac{1}{2}\cos(\alpha_k)-\tfrac{1}{4}\cos(\alpha_k)\cos(\mu_\varphi)\\ &= \tfrac{1}{2}(-1)^k\cos(\mu_\varphi k)-\tfrac{1}{2}(-1)^k\cos(\mu_\varphi k)\cos(\mu_\varphi)\\ &= \tfrac{1}{2}(-1)^k\cos(\mu_\varphi k)-\tfrac{1}{4}(-1)^k\left(\cos(\mu_\varphi(k-1))+\cos(\mu_\varphi(k+1))\right)\end{aligned} \tag{B.53}$$

$$\begin{aligned}\sin(\alpha_k)\cos(\tfrac{1}{2}\mu_\varphi)\sin(\tfrac{1}{2}\mu_\varphi) &= \tfrac{1}{2}\sin(\alpha_k)\sin(\mu_\varphi)\\ &= \tfrac{1}{2}(-1)^{k+1}\sin(\mu_\varphi k)\sin(\mu_\varphi)\\ &= \tfrac{1}{4}(-1)^k\left(-\cos(\mu_\varphi(k-1))+\cos(\mu_\varphi(k+1))\right)\end{aligned} \quad , \tag{B.54}$$

the numerator can be simplified further

$$\begin{aligned}N_D = &\left(\tfrac{k^2}{2}+\tfrac{1}{4}+\left(\tfrac{k^2}{2}-\tfrac{1}{4}\right)\cos(\mu_\varphi)\right.\\ &+(-1)^{k+1}\left((\tfrac{k}{4}-\tfrac{1}{8})\cos(\mu_\varphi(k-1))\right.\\ &\left.\left.+\tfrac{1}{4}\cos(\mu_\varphi k)+(-\tfrac{k}{4}-\tfrac{1}{8})\cos(\mu_\varphi(k+1))\right)\right)\left|R(k)\right|^2\end{aligned} \quad . \tag{B.55}$$

For small values of the expected eccentricity angle μ_φ

$$\cos((\mu_\varphi(k-1)) \approx \cos(\mu_\varphi k) \approx \cos((\mu_\varphi(k+1)) \tag{B.56}$$

and therefore

$$N_D \approx \left(\tfrac{k^2}{2}+\tfrac{1}{4}+\left(\tfrac{k^2}{2}-\tfrac{1}{4}\right)\cos(\mu_\varphi)\right)\left|R(k)\right|^2 . \tag{B.57}$$

Expanding the denominator D_D yields

$$\begin{aligned} D_D &= \left|(1-e^{-j(\pi-\mu_\Phi)k})\cos(\tfrac{1}{2}\mu_\varphi)\right|^2 \\ &= \left|\left(1-\cos((\pi-\mu_\Phi)k)\right)+\left(\sin((\pi-\mu_\Phi)k)\right)j\right|^2 \left|\cos(\tfrac{1}{2}\mu_\varphi)\right|^2 . \end{aligned} \tag{B.58}$$

Calculation of the absolute value results in

$$D_D = \left(\left(1-\cos((\pi-\mu_\Phi)k)\right)^2+\left(\sin((\pi-\mu_\Phi)k)\right)^2\right)\cos^2(\tfrac{1}{2}\mu_\varphi) \tag{B.59}$$

$$\begin{aligned} &= \left(1+\cos^2((\pi-\mu_\Phi)k)-2\cos((\pi-\mu_\Phi)k)\right. \\ &\quad \left.+\sin^2((\pi-\mu_\Phi)k)\right)\cos^2(\tfrac{1}{2}\mu_\varphi) \end{aligned} \tag{B.60}$$

$$= \left(1-\cos((\pi-\mu_\Phi)k)\right)2\cos^2(\tfrac{1}{2}\mu_\varphi) . \tag{B.61}$$

Using the trigonometric relations (B.20) and (B.22), the denominator can be written as

$$D_D = \left(1+(-1)^{k+1}\cos(\mu_\Phi k)\right)\left(1+\cos(\mu_\varphi)\right). \tag{B.62}$$

The squared absolute partial derivative of $\tilde{R}_D(k)$ with respect to Φ is therefore given by

$$\left|\frac{\partial\tilde{R}_D(k)}{\partial\Phi}\right|^2 \approx \frac{\left(\tfrac{k^2}{2}+\tfrac{1}{4}+\left(\tfrac{k^2}{2}-\tfrac{1}{4}\right)\cos(\mu_\varphi)\right)\left|R(k)\right|^2}{\left(1+(-1)^{k+1}\cos(\mu_\Phi k)\right)\left(1+\cos(\mu_\varphi)\right)} . \tag{B.63}$$

The squared absolute partial derivative of $\tilde{R}_D(k)$ with respect to ε_x is

$$\begin{aligned}\left|\frac{\partial \tilde{R}_D(k)}{\partial \boldsymbol{\mathcal{E}}_x}\right|^2 &= \left|\frac{-2}{(1-e^{-j(\pi-\mu_\Phi)k})\cos(\frac{1}{2}\mu_\varphi)}\right|^2 \\ &= \frac{\left|-2\right|^2}{\left|(1-e^{-j(\pi-\mu_\Phi)k})\cos(\frac{1}{2}\mu_\varphi)\right|^2} \\ &= \frac{4}{\left(1+(-1)^{k+1}\cos(\mu_\Phi k)\right)\left(1+\cos(\mu_\varphi)\right)}\end{aligned} \tag{B.64}$$

and the squared absolute partial derivatives of $\tilde{R}_D(k)$ with respect to $\boldsymbol{\mathcal{N}}_A$ and $\boldsymbol{\mathcal{N}}_B$ are

$$\begin{aligned}\left|\frac{\partial \tilde{R}_D(k)}{\partial \boldsymbol{\mathcal{N}}_A}\right|^2 &= \left|\frac{1}{(1-e^{-j(\pi-\mu_\Phi)k})\cos(\frac{1}{2}\mu_\varphi)}\right|^2 \\ &= \frac{1}{\left(1+(-1)^{k+1}\cos(\mu_\Phi k)\right)\left(1+\cos(\mu_\varphi)\right)}\end{aligned} \tag{B.65}$$

and

$$\left|\frac{\partial \tilde{R}_D(k)}{\partial \boldsymbol{\mathcal{N}}_B}\right|^2 = \frac{1}{\left(1+(-1)^{k+1}\cos(\mu_\Phi k)\right)\left(1+\cos(\mu_\varphi)\right)}. \tag{B.66}$$

B.4 Variance of the Phase Shifted Sum of the Signals

The harmonics estimated from the phase shifted sum of the signals with the phase shift angle α are given by

$$\begin{aligned}\tilde{R}_{PS}(k) = \Big(& (1+e^{j(\Phi-\alpha)k})\cos(\Phi/2)\,R(k) + (1-e^{j(\pi-\alpha)k})\boldsymbol{\mathcal{E}}_x(k) \\ & -(1+e^{j(\pi-\alpha)k})\tan(\Phi/2)\boldsymbol{\mathcal{E}}_y(k) + \boldsymbol{\mathcal{N}}_A(k) + e^{j(\pi-\alpha)k}\boldsymbol{\mathcal{N}}_B(k)\Big). \\ & /2\cos(\mu_\Phi/2)\end{aligned} \tag{B.67}$$

Using the error propagation law, the variance of $\tilde{R}_{PS}(k)$ can be approximated by

$$\begin{aligned}\mathrm{Var}\left(\tilde{R}_{PS}(k)\right) \approx & \left|\frac{\partial\tilde{R}_{PS}(k)}{\partial\Phi}\right|^2 \sigma_\Phi{}^2 + \left|\frac{\partial\tilde{R}_{PS}(k)}{\partial\boldsymbol{\mathcal{E}}_x}\right|^2 \sigma_{\mathcal{E}_x}{}^2 + \left|\frac{\partial\tilde{R}_{PS}(k)}{\partial\boldsymbol{\mathcal{E}}_y}\right|^2 \sigma_{\mathcal{E}_y}{}^2 \\ & + \left|\frac{\partial\tilde{R}_{PS}(k)}{\partial\boldsymbol{\mathcal{N}}_A}\right|^2 \sigma_{\mathcal{N}_A}{}^2 + \left|\frac{\partial\tilde{R}_{PS}(k)}{\partial\boldsymbol{\mathcal{N}}_B}\right|^2 \sigma_{\mathcal{N}_B}{}^2\end{aligned} . \tag{B.68}$$

Subsequently, the four partial derivatives are calculated. They are evaluated at $\Phi = \mu_\varphi$, $\boldsymbol{\mathcal{E}}_x = \mu_{\mathcal{E}_x} = 0$, $\boldsymbol{\mathcal{E}}_y = \mu_{\mathcal{E}_y} = 0$, $\boldsymbol{\mathcal{N}}_A = \mu_{\mathcal{N}_A} = 0$, $\boldsymbol{\mathcal{N}}_B = \mu_{\mathcal{N}_B} = 0$. The squared absolute partial derivative of $\tilde{R}_{PS}(k)$ with respect to Φ is

$$\begin{aligned}\left|\frac{\partial\tilde{R}_{PS}(k)}{\partial\Phi}\right|^2 = & \Big|\Big((jke^{j(\mu_\varphi-\alpha)k})\cos(\mu_\varphi/2)R(k) - \tfrac{1}{2}(1+e^{j(\mu_\varphi-\alpha)k})\sin(\mu_\varphi/2)R(k) \\ & -\left(1+e^{j(\pi-\alpha)k}\right)\left(1+\tan^2(\mu_\varphi/2)\right)\mu_{\mathcal{E}_y}\Big)\Big/\left(2\cos(\mu_\Phi/2)\right)\Big|^2\end{aligned} . \tag{B.69}$$

With $\alpha = \mu_{\mathcal{E}_y}$, this simplifies to

$$\begin{aligned}\left|\frac{\partial\tilde{R}_{PS}(k)}{\partial\Phi}\right|^2 = & \Big|\Big(jk\cos(\mu_\varphi/2)R(k) - \sin(\mu_\varphi/2)R(k) \\ & -2\left(1+\tan^2(\mu_\varphi/2)\right)\mu_{\mathcal{E}_y}\Big)\Big/\left(2\cos(\mu_\Phi/2)\right)\Big|^2\end{aligned} \tag{B.70}$$

and since $\mu_{\varepsilon_y} = 0$

$$\left|\frac{\partial \tilde{R}_{PS}(k)}{\partial \Phi}\right|^2 = \left|\frac{jk\cos(\tfrac{1}{2}\mu_\varphi)R(k) - \sin(\tfrac{1}{2}\mu_\varphi)R(k)}{2\cos(\tfrac{1}{2}\mu_\varphi)}\right|^2 \tag{B.71}$$

$$= \frac{\left|jk\cos(\tfrac{1}{2}\mu_\varphi)R(k) - \sin(\tfrac{1}{2}\mu_\varphi)R(k)\right|^2}{\left|2\cos(\tfrac{1}{2}\mu_\varphi)\right|^2} \tag{B.72}$$

$$=: \frac{N_{PS}}{D_{PS}}, \tag{B.73}$$

where N_{PS} and D_{PS} are the numerator and denominator of the equation. Expanding the numerator yields

$$N_{PS} = \left|jk\cos(\tfrac{1}{2}\mu_\varphi) - \sin(\tfrac{1}{2}\mu_\varphi)\right|^2 \left|R(k)\right|^2 \tag{B.74}$$

$$= \left[k^2\cos^2(\tfrac{1}{2}\mu_\varphi) + \sin^2(\tfrac{1}{2}\mu_\varphi)\right]\left|R(k)\right|^2 \tag{B.75}$$

$$= \left[1 + (k^2 - 1)\cos^2(\tfrac{1}{2}\mu_\varphi)\right]\left|R(k)\right|^2. \tag{B.76}$$

Using the trigonometric formula

$$\begin{aligned}\cos^2(\tfrac{1}{2}\mu_\varphi) &= \left(\sqrt{\tfrac{1}{2}(1+\cos(\mu_\varphi))}\right)^2 \\ &= \tfrac{1}{2} + \tfrac{1}{2}\cos(\mu_\varphi)\end{aligned}, \tag{B.77}$$

the numerator can be simplified further

$$N_{PS} = \left(\tfrac{k^2}{2} + \tfrac{1}{2} + \left(\tfrac{k^2}{2} - \tfrac{1}{2}\right)\right)\cos(\mu_\varphi). \tag{B.78}$$

Expanding the denominator D_{PS} yields

$$\begin{aligned} D_{PS} &= \left|2\cos(\tfrac{1}{2}\mu_\varphi)\right|^2 \\ &= 4\cos^2(\tfrac{1}{2}\mu_\varphi) \end{aligned} . \tag{B.79}$$

Using the trigonometric relations (B.77), the denominator can be written as

$$D_{PS} = 2\left(1+\cos(\mu_\varphi)\right). \tag{B.80}$$

The squared absolute partial derivative of $\tilde{R}_{PS}(k)$ with respect to Φ is therefore given by

$$\left|\frac{\partial\tilde{R}_{PS}(k)}{\partial\Phi}\right|^2 \approx \frac{\left(\frac{k^2}{2}+\frac{1}{2}+\left(\frac{k^2}{2}-\frac{1}{2}\right)\cos(\mu_\varphi)\right)\left|R(k)\right|^2}{2\left(1+\cos(\mu_\varphi)\right)}. \tag{B.81}$$

The squared absolute partial derivative of $\tilde{R}_{PS}(k)$ with respect to ε_x is

$$\begin{aligned} \left|\frac{\partial\tilde{R}_{PS}(k)}{\partial\varepsilon_x}\right|^2 &= \left|\frac{(1-e^{j(\pi-\alpha)k})}{2\cos(\frac{1}{2}\mu_\varphi)}\right|^2 \\ &= \frac{\left|(1-e^{j(\pi-\mu_\varphi)k})\right|^2}{\left|2\cos(\frac{1}{2}\mu_\varphi)\right|^2} \\ &= \frac{\left|1-\cos\left((\pi-\mu_\varphi)k\right)-j\sin\left((\pi-\mu_\varphi)k\right)\right|^2}{\left|2\cos(\frac{1}{2}\mu_\varphi)\right|^2} \\ &= \frac{\left(1-\cos\left((\pi-\mu_\varphi)k\right)\right)^2+\left(\sin\left((\pi-\mu_\varphi)k\right)\right)^2}{2\left(1+\cos(\mu_\varphi)\right)} \\ &= \frac{2+2\cos\left((\pi-\mu_\varphi)k\right)}{2\left(1+\cos(\mu_\varphi)\right)} \end{aligned} . \tag{B.82}$$

Using the trigonometric formula

$$\begin{aligned} \cos\left((\pi-\mu_\varphi)k\right) &= \cos(\pi k)\cos(\mu_\varphi k)+\sin(\pi k)\sin(\mu_\varphi k) \\ &= (-1)^k\cos(\mu_\varphi k) \end{aligned} , \tag{B.83}$$

this simplifies to

$$\left|\frac{\partial \tilde{R}_{PS}(k)}{\partial \boldsymbol{\varepsilon}_x}\right|^2 = \frac{2\left(1-(-1)^k \cos(\mu_\varphi k)\right)}{2\left(1+\cos(\mu_\varphi)\right)}. \tag{B.84}$$

The squared absolute partial derivatives of $\tilde{R}_{PS}(k)$ with respect to $\boldsymbol{\mathcal{N}}_A$ and $\boldsymbol{\mathcal{N}}_B$ are

$$\begin{aligned}\left|\frac{\partial \tilde{R}_{PS}(k)}{\partial \boldsymbol{\mathcal{N}}_A}\right|^2 &= \left|\frac{1}{2\cos(\frac{1}{2}\mu_\varphi)}\right|^2 \\ &= \frac{1}{2\left(1+\cos(\mu_\varphi)\right)}\end{aligned} \tag{B.85}$$

and

$$\left|\frac{\partial \tilde{R}_{PS}(k)}{\partial \boldsymbol{\mathcal{N}}_B}\right|^2 = \frac{1}{2\left(1+\cos(\mu_\varphi)\right)}. \tag{B.86}$$

BIBLIOGRAPHY

ARA, K. (1972). *A Differential Transformer with Temperature and Excitation Independent Output*. IEEE Transaction on Instrumentation and Measurement, Vol. 21, August 1972, pp. 249–255.

ARANTES, A. A., DA CUNHA, P. M. R. (1970). *Two* Cases *of Forced Vibrations in Grinding Machines*. Annals of the CIRP, Vol. 18, 1970, pp. 425–434.

BARNES, J. R. (1987). *Electronic System Design: Interference and Noise Control Techniques*. Prentice Hall, Englewood Cliffs, N.J.

BAZARAA, M. S., SHERALI, H. D., SHETTY, C. M. (1993). Nonlinear Programming: Theory and Algorithms. 2nd edition, John Wiley & Sons, New York.

BENDAT, J. S., PIERSOL, A. G. (1986). *Random Data: Analysis and Measurement Procedures*. 2nd edition, John Wiley & Sons, New York.

BENDAT, J. S., PIERSOL, A. G. (1993). *Engineering Applications of Correlation and Spectral Analysis*. 2nd edition, John Wiley & Sons, New York.

BEUTLER, F. J. (1966). *Error-Free Recovery of Signals from Irregularly Spaced Samples*. SIAM Review, Vol. 8, No. 3, July 1966, pp. 328–335.

BEUTLER, F. J. (1970). *Alias-Free Randomly Timed Sampling of Stochastic Processes*. IEEE Transactions on Information Theory, Vol. 16, No. 2, March 1970, pp. 147–152.

BLANKINSHIP, W. A. (1974). *Note on Computing Autocorrelations*. IEEE Transactions on Acoustics, Speech, and Signal Processing, Vol. 22, No. 1, February 1974, pp. 76–77.

BOHMANN, J., MEYR, H., PETERS, R., SPIES, G. (1984). *A Signal Processor for a Noncontact Speed Measurement System*. IEEE Transactions on Vehicular Technology, Vol. VT-33, No. 1, February 1984, pp. 14–22.

BRAULT, J. W. (1996). *New approach to high-precision Fourier transform spectrometer design*. Applied Optics, Vol. 35, No. 16, June 1996, pp. 2891–2896.

BRIGHAM, E. O. (1988). *The fast Fourier transform and its applications*. Prentice Hall, Englewood Cliffs, N.J.

BRODMANN, R., GAST, T., THURN, G. (1984). *An Optical Instrument for Measuring the Surface Roughness in Production Control*. Annals of the CIRP, Vol. 33, No. 1, 1984, pp. 403–406.

BRODMANN, R., PAISDZIOR, H., RAU, H., HÜBNER, G. (1986). *Rauheit und Welligkeit feinbearbeiteter Oberflächen optisch messen*. Werkstatt und Betrieb, Vol. 119, No. 10, 1986, pp. 849–852.

BRYAN, J., CLOUSER, R., HOLLAND, E. (1967). *Spindle Accuracy*. American Machinist, Technical Report No. 612, December 4, 1967, pp. 149–164.

CAO, L. (1989). *The measuring accuracy of the multistep method in the error separation technique*. Journal of Physics E: Scientific Instruments, Vol. 22, 1989, pp. 903–906.

CAO, L., WANG, H., LI, X., SHEN, Q. (1992). *Full-harmonic error separation technique*. Measurement Science and Technology, Vol. 3, 1992, pp. 1129–1132.

CHARPENTIER, F. J. (1986). *Pitch Detection Using the Short-Term Phase Spectrum*. Proceedings of the IEEE International Conference on Acoustics, Speech and Signal Processing (ICASSP), 1986, pp. 113–116.

CARROLL, R. J., RUPPERT, D. (1988). *Transformation and Weighting in Regression – Monographs on statistics and applied probability*. Chapman and Hall, London.

CAVICCHI, T. J. (1992). *DFT time-domain interpolation*. IEE Proceedings F: Radar and Signal Processing, Vol. 139, No. 3, June 1992, pp. 207–211.

CHEN, X., ROWE, W. B., LI, Y., MILLS, B. (1996). *Grinding vibration detection using a neural network*. Proceedings of the Institution of Mechanical Engineers, Part B: Journal of Engineering Manufacture, Vol. 210, 1996, pp. 349–352.

CHETWYND, D. G. (1987). *High-precision measurement of small balls*. Journal of Physics E: Scientific Instruments, Vol. 20, 1987, pp. 1179–1187.

CHETWYND, D. G., SIDDALL, G. J. (1976). *Improving the accuracy of roundness measurement*. Journal of Physics E: Scientific Instruments, Vol. 9, 1976, pp. 537–544.

CHRISTENSEN, R. (1996). *Analysis of Variance, Design and Regression*. Chapmen & Hall, London.

COOLEY, J. W., TUKEY, J. W. (1965). *An Algorithm for the Machine Calculation of Complex Fourier Series*. Mathematics of Computation, Vol. 19, No. 90, April 1965, pp. 297–301.

CRESCINI, D., FLAMMINI, A., MARIOLI, D., TARONI, A. (1998). *Application of an FFT-Based Algorithm to Signal Processing of LVDT Position Sensors*. IEEE Transactions on Instrumentation and Measurement, Vol. 47, No. 5, October 1998, pp. 1119–1123.

DAMIR, M. H. H. (1973). *Error in the Measurement due to Stylus Kinematics*. Wear, Vol. 26, 1973, pp. 219–227.

DAVIDSON, J. J. (1961). *Average vs. RMS Meters for Measuring Noise*. IRE Transactions on Audio, Vol. 9, No. 4, July-August 1961, pp. 108–111.

DAVIS, P. J. (1975). *Interpolation and Approximation*. Dover Publications, New York.

DE BOOR, C. (2001). *A pratical guide to splines*. Applied mathematical series, Vol. 27, Spring Verlag, New York.

DEMING, W. E. (1943). *Statistical Adjustment of Data*. John Wiley & Sons, New York.

DEVORE, J. L. (1995). *Probability and Statistics for Engineering and the Sciences*. 4th edition, Duxbury Press, New York.

DIN 4760 (1982). *Gestaltabweichungen: Begriffe, Ordnungssystem*. Deutsches Institut für Normung.

DONALDSON, R. R. (1972). *A simple method for Separating Spindle Error from Test Ball Roundness Error*. Annals of the CIRP, Vol. 21, No. 1, 1972, pp. 125–126.

DREW, S. J., MANNAN, M. A., ONG, K. L., STONE, B. J. (1999). *An investigation of in-process measurement of ground surface in the presence of vibration*. International Journal of Machine Tools and Manufacture, Vol. 39, 1999, pp. 1841–1861.

DUBNOWSKI, J. J., SCHAFER, R. W., RABINER, L. R. (1976). *Real-Time Digital Hardware Pitch Detector*. IEEE Transactions on Acoustics, Speech, and Signal Processing, Vol. 24, No. 1, February 1976, pp. 2–8.

DURING, C. (1997). *Recursive versus Nonrecursive Correlation for Real-Time Peak Detection and Tracking*. IEEE Transactions on Signal Processing, Vol. 45, No. 3, March 1997, pp. 781–785.

EL-WARDANI, T., SADEK, M. M., YOUNIS, M. A. (1987). *Theoretical Analysis of Grinding Chatter*. Transactions of the ASME, Journal of Engineering for Industry, Vol. 109, November 1987, pp. 314–320.

ESTLER, W. T., EVANS, C. J., SHAO. L. Z. (1997). *Uncertainty estimation for multiposition form error metrology*. Precision Engineering, Vol. 21, 1997, pp. 72–82.

FEICHTINGER, H. G., GRÖCHENING, K., STROHMER, T. (1995). *Efficient numerical methods in non-uniform sampling theory*. Numerische Mathematik, Vol. 69, 1995, pp. 423–440.

FERTNER, A., SJÖLUND, A. (1986). *Comparison of Various Time Delay Estimation Methods by Computer Simulation*. IEEE Transactions on Acoustics, Speech, and Signal Processing, Vol. ASSP-34, No. 5, October 1986, pp. 1329–1330.

FETTE, N., GIBSON, R., GREENWOOD, E. (1980). *Windowing Function for the Average Magnitude Difference Function Pitch Extractor*. IEEE International Conference on Acoustics, Speech & Signal Processing, Vol. 1, April 1980, pp. 49–52.

FORD, R. M., WEISSBACH, R. S., LOKER, D. R. (2000). *A DSP-Based Modified Costas Receiver for LVDT Position Sensors*. IEEE Instrumentation and Measurement Technology Conference, Vol. 3, 2000, pp. 1448–1452.

FORD, R. M., WEISSBACH, R. S., LOKER, D. R. (2001). *A Novel DSP-Based LVDT Signal Conditioner*. IEEE Transactions on Instrumentation and Measurement, Vol. 50, No. 3, June 2001, pp. 768–773.

FOTH, M. (1989). *Erkennen und Mindern von Werkstückwelligkeiten während des Außenrundschleifens*. Fortschritt-Berichte VDI, Reihe 2, Nr. 173, VDI Verlag Düsseldorf 1989.

FRASER, D. (1989). *Interpolation by the FFT Revisited – An Experimental Investigation*. IEEE Transactions on Acoustics, Speech, and Signal Processing, Vol. 37, No. 5, May 1989, pp. 665–675.

FRITSCHE, R., MESCH, F. (1973). *Vergleich von Ortsfrequenzfilterung und Korrelationsverfahren zur berührungslosen Geschwindigkeitsmessung*. : Proceedings of the 6th Congress of the International Measurement Confederation, IMEKO 1973, pp. 579–589.

FU, J. C., MORI, K., YOKOMICHI, M. (1994). *Application of entropy functions in on-line vibration classification for cylindrical plunge grinding*. International Journal of Production Research, Vol. 32, No. 6, 1994, pp. 1477–1487.

FU, J. C., TROY, C. A., MORI, K. (1996). *Chatter classification by entropy functions and morphological processing in cylindrical traverse grinding*. Precision Engineering, Vol. 18, No. 2/3, April/May 1996, pp. 110–117.

FURUI, S. (2001). *Digital Speech Processing, Synthesis and Recognition*. 2nd edition, Marcel Dekker Inc., New York.

FURUKAWA, Y., MIYASHITA, M., SHIOZAKI, S. (1970). *Chatter Vibration in Centerless Grinding*. Bulletin of the Japan Society of Mechanical Engineers, Vol. 13, No. 64, 1970, pp. 1274–1283.

GABRIEL, K. J. (1983). *Comparison of Three Correlation Coefficient Estimators for Gaussian Stationary Processes*. IEEE Transactions on Acoustics, Speech, and Signal Processing, Vol. ASSP-31, No. 4, August 1983, pp. 1023–1025.

GAO, Y., JONES B. (1992). *An Integrated Sensor System for Size and Roundness Control in Plunge Grinding*. International Journal of Machine Tools and Manufacture, Vol. 32, No. 3, 1992, pp. 281–290.

GAO, W., KIYONO, S. NOMURA, T. (1996). *A new multiprobe method of roundness measurements*. Precision Engineering, Vol. 19, 1996, pp. 37–45.

GAO, W., KIYONO, S., SUGAWARA, T. (1997). *High-accuracy roundness measurement by a new error separation method*. Precision Engineering, Vol. 21, 1997, pp. 123–133.

GLEASON, E., SCHWENKE, H. (1998). *A spindleless instrument for the roundness measurement of precision spheres*. Precision Engineering, Vol. 22, 1998, pp. 37–42.

GOLD, B., RABINER, L. (1969). *Parallel Processing Techniques for Estimating Pitch Periods of Speech in the Time Domain*. Journal of the Acoustical Society of America, Vol. 46, No. 2, August 1969, pp. 442–448.

GOVEKAR, E., BAUS, A., GRADIŠEK, J., KLOCKE, F., GRABEC, I. (2002). *A New Method for Chatter Detection in Grinding*. Annals of the CIRP, Vol. 51, No. 1, 2002, pp. 267–270.

GRADIŠEK, J., BAUS, A., GOVEKAR, E., KLOCKE, F., GRABEC, I. (2003). *Automatic chatter detection in grinding*. International Journal of Machine Tools and Manufacture, Vol. 43, 2003, pp. 1397–1403.

GRAY, N. C. (1987). *Simplifying LVDT Signal Conditioning*. Machine Design, Vol. 59, No. 10, May 7, 1987, pp. 103–106.

GRAZEN, A. E. (1983). *Wheel Design Can Stop Chatter Vibrations*. Industrial Diamond Review, Vol. 42, No. 4, 1983, pp. 198–199.

HAHN, R. S. (1954). *On the Theory of Regenerative Chatter in Precision-Grinding Operations*. Transactions of the ASME, Vol. 76, March 1954, pp. 593–597.

HAHN, R. S., LINDSAY, R. P. (1971a). *Principles of Grinding: Part 1. Basic Relationship in Precision Grinding*. Machinery, July 1971, pp. 55–62.

HAHN, R. S., LINDSAY, R. P. (1971b). *Principles of Grinding: Part 2. Basic Relationship in Precision Grinding*. Machinery, August 1971, pp. 33–39.

HASAN, K., SHANAZ, C., FATATH, S. A. (2003). *Determination of Pitch of Noisy Speech Using Dominant Harmonic Frequency*. Proceedings of the 2003 IEEE International Symposium on Circuits and Systems, Vol. 2, 2003, pp. 556–559.

HASHIMOTO, F., KANAI, A., MIYASHTIA, M. (1984). *Growing Mechanism of Chatter Vibrations in Grinding Processes and Chatter Stabilization Index of Grinding Wheel*. Annals of the CIRP, Vol. 33, No. 1, 1984, pp. 259–263.

HASHIMOTO, F., YOSHIOKA, J., MIYASHITA, M. (1985). *Sequential Estimation of Growth Rate of Chatter Vibrations in Grinding Processes*. Annals of the CIRP, Vol. 34, No. 1, 1985, pp. 271–275.

HASHIMOTO, F., ZHOU, S. S., LAHOTI, G. D., MIYASHITA, M. (2000). *Stability Diagram for Chatter Free Centerless Grinding and its Application in Machine Development*. Annals of the CIRP, Vol. 49, No. 1, 2000, pp. 225–230.

HERCEG, E. E. (1972). *Handbook of Measurement and Control*. Schaevitz Engineering, Pennsauken, N.J.

HERTZ, D. (1982). *A Fast Digital Method of Estimating the Autocorrelation of a Gaussian Stationary Process*. IEEE Transactions on Acoustics, Speech, and Signal Processing, Vol. ASSP-30, No. 2, April 1982, pp. 329.

HIGGINS, J. R. (1996). *Sampling Theory in Fourier and Signal Analysis – Foundations*. Clarendon Press, Oxford.

HOLM, S. (1987). *FFT Pruning Applied to Time Domain Interpolation and Peak Localization*. IEEE Transactions on Acoustics, Speech, and Signal Processing, Vol. 35, No. 12, December 1987, pp. 1776–1778.

HORIKAWA, O., MARUYAMA, N., SHIMADA, M. (2001). *A low cost, high accuracy roundness measuring system*. Precision Engineering, Vol. 25, 2001, pp. 200–205.

HSU, C. Y., LIN, T. P. (1988). *Novel Approach to Discrete Interpolation using the Subsequence FHT*. Electronics Letters, Vol. 24, No. 4, February 1988, pp. 223–224.

INASAKI, I. (1985a). *Monitoring of Dressing and Grinding Processes with Acoustic Emission Signals*. Annals of the CIRP, Vol. 34, No. 1, 1985, pp. 277–280.

INASAKI, I. (1985b). *In-process measurement of surface roughness during cylindrical grinding process*. Precision Engineering, Vol. 7, No. 2, April 1985, pp. 73–76.

INASAKI, I. (1991). *Monitoring and Optimization of Internal Grinding Process*. Annals of the CIRP, Vol. 40, No. 1, 1991, pp. 359–362.

INASAKI, I. (1997). *Monitoring Technology for Achieving Intelligent Grinding System*. ASME Paper, MED-Vol. 6-1, Manufacturing Science and Technology, 1997, pp. 75–81.

INASAKI, I. (1999). *Sensor Fusion for Monitoring and Controlling Grinding Processes*. International Journal of Advanced Manufacturing Technology, Vol. 15, 1999, pp. 730–736.

INASAKI, I. (2001). *Grinding Chatter – Origin and Suppression*. Annals of the CIRP, Vol. 50, No. 2, 2001, pp. 515–534.

JACOVITTI, G., SCARANO, G. (1993). *Discrete Time Techniques for Time Delay Estimation*. IEEE Transactions on Signal Processing, Vol. 41, No. 2, February 1993, pp. 525–533.

JANSEN, M. J., SCHELLEKENS, P. H. J., DE VEER, B. (2001). *Advanced Spindle Runout-Roundness Separation Method*. Advanced Mathematical and Computational Tools in Metrology V, World Scientific Publishing Company.

JESPERS, P., CHU, P. T., FETTWEIS, A. (1962). *A New Method to Compute Correlation Functions*. IEEE Transactions on Information Theory, Vol. 8, No. 5, September 1962, pp. 106–107.

JOHNSON, J. B. (1928). *Thermal Agitation of Electricity in Conductors*. Physical Review, Vol. 32, July 1928, 97–109.

KAKINO, Y., KITAZAWA, J. (1978). *In Situ Measurement of Cylindricity*. Annals of the CIRP, Vol. 27, No. 1, 1978, pp. 371–375.

KALISZER, H., MISHINA, O., WEBSTER, J. (1979). *Adaptively Controlled Surface Roughness and Roundness During Grinding*. International Machine Tool Design and Research (MTDR) Conference, 1979, pp. 471–478.

KALISZER, H., WEBSTER, J. (1982). *Inprocess Measurement of Size, Shape and Surface Roughness*. Proceedings of the International Conference on Automated Inspection and Product Control, 1982, pp. 41–48.

KALISZER, H., WEBSTER, J., ZHAO, Y. W. (1986). *Dynamic Response of a Computer-Controlled In-Process Size and Roundness Measuring System*. SME Technical Paper IQ86-627.

KALLURI, C., RAO, S. S., RAO, N. S. (2001). *Using evolutionary programming for reconstruction of an irregularly sampled bandlimited sequence*. Proceedings of the SPIE – The International Society for Optical Engineering, Vol. 4479, 2001, pp. 177–185.

KARPUSCHEWSKI, B., WEHMEIER, M., INASAKI, I. (2000). *Grinding Monitoring System Based on Power and Acoustic Emission Sensors*. Annals of the CIRP, Vol. 49, No. 1, pp. 235–240.

KATO, H., NAKANO, Y., NOMURA, Y. (1990). *Development of In-Situ Measuring System of Circularity in Precision Cylindrical Grinding*. Bulletin of the Japan Society of Precision Engineering, Vol. 24, No. 2, June 1990, pp. 130–135.

KATO, H., SONE, R. Y., NOMURA, Y. (1991). *In-Situ Measuring System of Circularity Using an Industrial Robot and a Piezoactuator*. International Journal of the Japan Society of Precision Engineering, Vol. 25, No. 2, June 1991, pp. 130–135.

KEGG, R. L. (1983*). Industrial Problems in Grinding*. Annals of the CIRP, Vol. 32, No. 2, 1983, pp. 559–561.

KIM, H. Y., KIM, S. R., AHN, J. H., KIM, S. H. (2001). *Process monitoring of centerless grinding using acoustic emission*. Journal of Materials Processing Technology, Vol. 111, 2001, pp. 273–278.

KIM, J., SHIN, D., BAE, M. (2002). *A Study on the Improvement of Speaker Recognition System by Voiced Detection*. Proceedings of the 45th Midwest Symposium on Circuits and Systems, Vol. 3, August 2002, pp. 324–327.

KNYAZHITSKII, A. I., ETINGOF, M. I., KHASIN, I. A. (1989). *New Range of Automatic Instruments for Internal Grinding Machines*. Measurement Techniques, Vol. 32, No. 3, August 1989, 204–206.

KOBAYASHI, H., SHIMAMURA, T. (2000). *A Weighted Autocorrelation Method for Pitch Extraction of Noisy Speech*. Proceedings of the IEEE International Conference on Acoustics, Speech, and Signal Processing (ICASSP), Vol. 3, 2000, pp. 1307–1310.

KWAK, J. S., HA, M. K. (2004). *Neural network approach for diagnosis of grinding operation by acoustic emission and power signals*. Journal of Materials Processing Technology, Vol. 147, 2004, pp. 65–71.

KWAK, J. S., SONG, J. B. (2001). *Trouble Diagnosis of the grinding process by using acoustic emission signals*. International Journal of Machine Tools and Manufacture, Vol. 41, 2001, pp. 899–913.

LACEY, S. J. (1990a). *Vibration Monitoring of the internal centreless grinding process. Part 1: mathematical models*. Proceedings of the Institution of Mechanical Engineers, Part B: Journal of Engineering Manufacture, Vol. 204, 1990, pp. 119–128.

LACEY, S. J. (1990b). *Vibration Monitoring of the internal centreless grinding process. Part 2: experimental results*. Proceedings of the Institution of Mechanical Engineers, Part B: Journal of Engineering Manufacture, Vol. 204, 1990, pp. 129–142.

LA RIVIÈRE, P. J., PAN, X. (1998). *Mathematical equivalence if zero-padding interpolation and circular sampling theorem interpolation with implications for direct Fourier image reconstruction*. Proceedings of the SPIE – The International Society for Optical Engineering, Medical Imaging: Image Processing, Vol. 3339, February 1998, pp. 1117–1126.

LEARNER, R. C. M., THORNE, A. P., BRAULT, J. W. (1996). *Ghosts and artifacts in Fourier-transform spectrometry*. Applied Optics, Vol. 35, No. 16, June 1996, pp. 2947–2954.

LEE, J. N., BAE, J. I., LEE, S., LEE, M. H., LEE, J. M. (1997). *Development of Real Time and In-Process Gaging Technology for Grinding Process of Cylindrical Workpieces*. IEEE International Symposium on Industrial Electronics, Vol. 1, 1997, pp. 160–164.

LEE, M. H., BAE, J. I., YOON, K. S., HARASHIMA, F. (2000). *Real Time and an In-Process Measuring System for the Grinding Process Cylindrical Workpieces Using Kalman Filtering*. IEEE Transactions on Industrial Electronics, Vol. 47, No. 6, December 2000, pp. 1326–1333.

LEE, J. H., KIM, S. I., LEE, D. S. (1998). *Fast Cross-Correlation Method for Real Time Detection of Fetal Heart Rate*. Proceedings of the 20th Annual International Conference of the IEEE Engineering in Medicine and Biology Society, Vol. 20, No. 1, 1998, pp. 178–181.

LEE, C. S., KIM, S. W., YIM, D. Y. (1987). *An In-Process Measurement Technique Using Laser for Non-Contact Monitoring of Surface Roughness and Form Accuracy of Ground Surfaces*. Annals of the CIRP, Vol. 36, No. 1, 1987, pp. 425–428.

LEZANSKI, P., RAFALOWICZ, J. (1993). *An Intelligent Monitoring System for Cylindrical Grinding*. Annals of the CIRP, Vol. 42, No. 1, 1993.

LI, G. S., XUE, B. Y., HE, X. S., GU, K. Y. (1991). *In-Process Measurement and Compensatory Control of Cylindricity in External Cylindrical Grinding*. Proceedings of the 11th International Conference on Production Research (ICPR), 1991, pp. 773–776.

LOEWENSTEIN, E. B. (2000). *Reducing the Effects of Noise in a Data Acquisition System by Averaging*. National Instruments Application Note 152, April 2000.

LONGANBACH, D. M., KURFESS, T. R. (1998). *Real-Time Measurement for an Internal Grinding System*. SME Technical Paper MS98-261, 1998.

LONGANBACH, D. M., KURFESS, T. R. (2001). *In-process gage frequency response measurement*. Mechatronics, Vol. 11, 2001, pp. 745–757.

LU, D., ZHANG, Q. (1986). *High Accuracy Instrument for Roundness Measurement and Analysis with Three Displacement Sensors*. 5th International IMEKO Symposium on Intelligent Measurement, Jena, German Democratic Republic, June 10-14, 1986, pp. 357–360.

MAKSOUD, T. M. A., MOKBEL, A. A. (2002). *Suppression of chatter in grinding using high-viscosity coolants*. Proceedings of the Institution of Mechanical Engineers, Part B: Journal of Engineering Manufacture, Vol. 216, No. 1, 2002, pp. 113–123.

MALKIN, S. (1989). *Grinding Technology –Theory and Applications of Machining with Abrasives*. John Wiley & Sons, New York.

MARKEL, J. D. (1972). *The SIFT Algorithm for Fundamental Frequency Estimation*. IEEE Transactions on Audio and Electroacoustics, Vol. 20, No. 5, December 1972, pp. 367–377.

MARKS, R. J. (1993). *Advanced Topics in Shannon Sampling and Interpolation Theory*. Springer Verlag, New York.

MARVASTI, F. (1993). *Nonuniform Sampling*. In: MARKS, R. J. (1993). *Advanced Topics in Shannon Sampling and Interpolation Theory*. Springer Verlag, New York, pp. 121–156.

MARVASTI, F., ANALOUI. M., GAMSHADZAHI, M. (1991). *Recovery of Signals from Nonuniform Samples Using Iterative Methods*. IEEE Transactions on Signal Processing, Vol. 39, No. 4, April 1991, pp. 872–878.

MARVASTI, F. (1996). *Nonuniform Sampling Theorems for Bandpass Signals at or Below the Nyquist Density*. IEEE Transactions on Signal Processing, Vol. 44, No. 3, March 1996, pp. 572–576.

MARZILIANO, P., VETTERLI, M. (1999). *Irregular Sampling with Unknown Locations*. Proceedings of the IEEE International Conference on Acoustics, Speech, and Signal Processing, Phoenix, AZ, March 1999, pp. 1657–1660.

MARZILIANO, P., VETTERLI, M. (2000). *Reconstruction of Irregularly Sampled Discrete-Time Bandlimited Signals with Unknown Sampling Locations*. IEEE Transactions on Signal Processing, Vol. 48, No. 12, December 2000, pp. 3462–3471.

MASSEN, R. (1983). *Some Remarks on the Selection of Sensors for Correlation Velocity Measurement Systems*. Sensors and Actuators, Vol. 3, No. 3, May 1983, pp. 221–231.

MATSUMOTO, T., INASAKI, I., OGAWA, K. (1993). *Monitoring of Grinding Process with a Sensor Integrated CBN Wheel*. SME Technical Paper MR93-367, 1993.

MATSUO, T., TOUGE, M., IWASAKI, K. (1993). *In-Process Measurements of Progressive Variation of Grinding Characteristics in Constant-Load Heavy Grinding*. Annals of the CIRP, Vol. 42, No. 1, 1993, pp. 401–404.

MCCOOL, J. I. (1984). *Assessing the Effect of Stylus Tip Radius on Surface Topography Measurements*. Transactions of the ASME, Journal of Tribology, Vol. 106, April 1984, pp. 202–210.

MCFARLAND, D. M., BAILEY, G. E., HOWES, T. D. (1999). *The Design and Analysis of a Polypropylene Hub CBN Wheel to Suppress Grinding Chatter*. Transactions of the ASME, Journal of Manufacturing Science and Engineering, Vol. 121, February 1999, pp. 28–31.

MENDELEYEV, V. Y. (1997). *Dependence of measuring errors of rms roughness on stylus tip size for mechanical profilers*. Applied Optics, Vol. 36, No. 34, December 1997, pp. 9005–9009.

MILLER, N. J. (1975). *Pitch Detection by Data Reduction*. IEEE Transactions on Acoustics, Speech, and Signal Processing, Vol. 23, No. 1, February 1975, pp. 72–79.

MITSUI, K. (1982). *Development of a New Measuring Method for Spindle Rotation Accuracy by Three Points Method*. Proceedings of the 23rd International Machine Tool Design and Research Conference, 1982, pp. 115–121.

MOORE, D. (1989). *Design considerations in multiprobe roundness measurement*. Journal of Physics E: Scientific Instruments, Vol. 22, 1989, pp. 339–343.

MORI, K., KASASHIMA, N., YAMANE, T., NAKAI, T. (1992). *An Intelligent Vibration Diagnostic System for Cylindrical Grinding*. ASME Japan/USA Symposium on Flexible Automation, Vol. 2, 1992, pp. 1097–1100.

MORRISON, R. (1998). *Grounding and Shielding Techniques*. 4th edition, John Wiley & Sons, New York.

NAKANO, Y., KATO, H., LOW, S. K. (1986). *Chatter Marks due to Pulsation of Hydraulic Oil Pressure in Surface Grinding and its Suppression*. Bulletin of the Japan Society of Precision Engineering, Vol. 20, No. 1, March 1986, pp. 43–44.

NAKANO, Y., KATO, H., TOBITA, T., UETAKE, A., UNO, M. (1988). *Suppression of Chatter Marksin Surface Grinding by Using Dynamic Damper*. Bulletin of the Japan Society of Precision Engineering, Vol. 22, No. 1, March 1988, pp. 37–42.

NAKKEERAN, P. R., RADHAKRISHNAN, V. (1988). *A Strategy for Inprocess Control of Workpiece Quality in Centreless Grinding*. American Society of Mechanical Engineers, Production Engineering Division (PED), Vol. 29, 1988, pp. 65–73

NATIONAL INSTRUMENTS (2002). *PCI E Series User Manual*. National Instruments Product Manual, July 2002.

NAZRUL, N. I., SETU, M. T. H., HUSSAIN, S., HASAN, M. K. (2004). *An Effective Speech Preprocessing Technique for Normalized Cross-Correlation Pitch Extractor*. Proceedings of the 3rd IEEE International Symposium on Signal Processing and Information Technology, 2004, pp. 749–752.

NETER, J., KUTNER, M. H., WASSERMAN, W., NACHTSHEIM, C. J. (1996). *Applied Linear Statistical Models*. 4th edition, McGraw-Hill/Irwin, Chicago.

NEUGEBAUER, M. (2001). *Uncertainty analysis for roundness measurements by the example of measurements on a glass hemisphere*. Measurement Science and Technology, Vol. 12, 2001, pp. 68–76.

NEWPORT (2004). The Newport Resource. Newport Product Catalog, 2004.

NIKULKIN, B. I. (1970). *Effect of Wheel Imbalance on Diamond Grinding*. Machines & Tooling, Vol. 41, No. 12, 1970, pp. 49–50.

NOLL, A. M. (1967). *Cepstrum Pitch Detection*. The Journal of the Acoustical Society of America, Vol. 41, No. 2, 1967, pp. 293–309.

NOVAK, A. (1981). *Sensing of Workpiece Diameter, Vibration and Out-Off-Roundness by Laser – Way to Automate Quality Control*. Annals of the CIRP, Vol. 30, No. 1, 1981, pp. 473–476.

NYQUIST, H. (1928). *Thermal Agitation of Electric Charge in Conductors*. Physical Review, Vol. 32, July 1928, 110–113.

OSBORNE, J. R. (1993). *In-process gaging improves grinding quality*. Tooling & Production, Vol. 58, No. 12, March 1993, pp. 33–36.

OTT, H. W. (1988). *Noise Reduction Techniques in Electronic Systems*. 2nd edition, John Wiley & Sons, New York.

PALCHETTI, L., LASTRUCCI, D. (2001). *Spectral noise due to sampling errors in Fourier-transform spectroscopy*. Applied Optics, Vol. 40, No. 19, July 2001, pp. 3235–3243.

PAPOULIS, A. (1966). *Error analysis in sampling theory*. Proceedings of the IEEE, Vol. 54, No. 7, July 1966, pp. 947–955.

PAPOULIS, A. (1991). *Probability, Random Variables, and Stochastic Processes*. 3rd edition, McGraw-Hill, New York.

PARK, Y. C., LEE, K. Y., YOUN, D. H., KIM, N. H., KIM, W. K., PARK, S. H. (1992). *On Detecting the Presence of Fetal R-Wave Using the Moving Averaged Magnitude Difference Algorithm*. IEEE Transactions on Biomedical Engineering, Vol. 39, No. 8, August 1992, pp. 868–871.

PAWLUS, P. P. (2004). *Mechanical filtration of surface profiles*. Measurement, Vol. 35, 2004, pp. 325–341.

PETERS, J., VANHERCK, P. (1971). *The Unbalance of Electromotors and their Influence on the Surface Geometry in Surface Grinding*. Annals of the CIRP, Vol. 19, pp. 585–589.

PRASAD, K. P., SATYANARAYANA, P. (1986). *Fast Interpolation Algorithm Using FFT*. Electronics Letters, Vol. 22, No. 4, February 1986, pp. 185–186.

PREZAS, D. P., PICONE, J., THOMSON, D. L. (1986). *Fast and Accurate Pitch Detection Using Pattern Recognition and Adaptive Time-Domain Analysis*. Proceedings of the IEEE International Conference on Acoustics, Speech and Signal Processing, 1986, pp. 109–112.

RABINER, L. R. (1977). *On the Use of Autocorrelation Analysis for Pitch Detection*. IEEE Transactions on Acoustics, Speech, and Signal Processing, Vol. 25, No. 1, February 1977, pp. 24–33.

RABINER, L. R. (1978). *Digital Processing of Speech Signals*. Prentice-Hall, Englewood Cliffs, N.J.

RABINER, L. R., CHENG, M. J., ROSENBERG, A. E., MCGONEGAL, C. A. (1976). *A Comparative Performance Study of Several Pitch Detection Algorithms*. IEEE Transactions on Acoustics, Speech, and Signal Processing, Vol. 24, No. 5, October 1976, pp. 399–418.

RADHAKRISHNAN, V. (1970). *Effect of Stylus Radius on the Roughness Values Measured with Tracing Stylus Instruments*. Wear, Vol. 16, 1970, pp. 325–335.

RAWN, M. D. (1989). *A Stable Nonuniform Sampling Expansion Involving Derivatives*. IEEE Transactions on Information Theory, Vol. 35, No. 6, November 1989, pp. 1223–1227.

ROSS, M. J., SHAFFER, H. L., COHEN, A., FREUDBERG, R., MANLEY, H. J. (1974). *Average Magnitude Difference Function Pitch Extractor*. IEEE Transactions on Acoustics, Speech, and Signal Processing, Vol. ASSP-22, No. 5, October 1974, pp. 353–362.

RUBINCHIK, S. I., SOLOVEICHIK, A. S. (1970). *Effect of Grinding-Spindle Imbalance on Surface Waviness in Internal Grinding*. Machines & Tooling, Vol. 41, No. 2, pp. 7–10.

SALT, J. E., DAKU, B. L. F., WOOD, H. C. (1993). *Noncontact Velocity Measurement Using Time Delay Estimation Techniques*. IEEE Transactions on Signal Processing, Vol. 41, No. 1, January 1993, pp. 288–295.

SAXENA, S. C., SEKENSA, S. B. L. (1989). *A Self-Compensating Smart LVDT Transducer*. IEEE Transaction on Instrumentation and Measurement, Vol. 38, No. 3, June 1989, pp. 748–753.

SHAH, S. J. (2001). *Field Wiring and Noise Considerations for Analog Signals*. National Instruments Application Node 025, July 2001.

SHANNON, C. E. (1949). *Communications in the Presence of Noise*. Proceedings of the Institute of Radio Engineers, Vol. 37, No. 1, January 1949, pp. 10–21.

SHANNON, C. E. (1998). *Classic Paper: Communications in the Presence of Noise*. Proceedings of the IEEE, Vol. 86, No. 2, February 1998, pp. 447–457.

SCHAFER, R. W., RABINER, L. R. (1970). *System for Automatic Formant Analysis of Voiced Speech*. Journal of the Acoustical Society of America, Vol. 47, No. 2, February 1970, pp. 634–648.

SCHIMMEL, M. (1999). *Phase Cross-Correlations: Design. Comparisons, and Applications*. Bulletin of the Seismological Society of America, Vol. 89, No. 5, October 1999, pp. 1366–1378.

SCHIMMEL, M., PAULSSEN, H. (1997). *Noise reduction and detection of weak, coherent signals through phase-weighted stacks*. Geophysical Journal International, Vol. 130, No. 2, August 1997, pp. 497–505.

SCHOLZ, R. (2002). *Gaging Improves Automatic Grinder Control*. Quality, Vol. 41, No. 4, April 2002, pp. 33–35.

SCHOTTKY, W. (1918). *Über spontane Stromschwankungen in verschiedenen Elektrizitätsleitern*. Annalen der Physik, Vol. 57, 1918, pp. 541–567.

SCHOTTKY, W. (1922). *Zur Berechnung und Beurteilung des Schrotteffektes*. Annalen der Physik, Vol. 68, 1922, pp. 157–176.

SHIMAMURA, T., KOBAYASHI, H. (2001). *Weighted Autocorrelation for Pitch Extraction of Noisy Speech*. IEEE Transactions on Speech and Audio Processing, Vol. 9, No. 7, October 2001, pp. 727–730.

SHINNO, H., MITSUI, K., TATSUE, Y. (1987). *A New Method for Evaluating Error Motion of Ultra Precision Spindle*. Annals of the CIRP, Vol. 36, No. 1, 1987, pp. 381–384.

SONDHI, M. M. (1968). *New Methods of Pitch Extraction*. IEEE Transactions on Audio and Electroacoustics. Vol. 16, No. 2, June 1968, pp. 262–266.

SONG, J. F., VORBURGER, T. V. (1996). *Stylus Flight in Surface Profiling*. Journal of Manufacuring Science and Engineering, Vol. 118, May 1996, pp. 188–198.

STARK, H. (1979). *Sampling theorems in polar coordinates*. Journal of the Optical Society of America, Vol. 69, No. 11, November 1979, pp. 1519–1525.

SUN, T. (1996). *Two-step method without harmonics suppression in error separation*. Measurement Science & Technology, Vol. 7, No. 11, 1996, pp. 1563–1568.

SUSIČ, E., GRABEC, I. (2000). *Characterization of the grinding process by acoustic emission*. International Journal of Machine Tools and Manufacture, Vol. 40, 2000, pp. 225–238.

SUZUKI, S. (1984). *In Process Measurement by Hydrostatic Micrometer with Soluble Type Grinding Fluid*. Proceedings of the 1st International Machine Tool Conference, June 1984 , Birmingham, UK, pp. 299–306.

SYLVAN, J. (1990). *ICs Simplify LVDT Interface*. Machine Design, Vol. 62, No. 2, January 25, 1990, pp. 84–87.

TAN, J., LI, D., QIANG, X., YONG, W. (1993). *Applying the Nanometer Degree Capacitance Sensor to the Super-High-Precision Measurement of Roundness*. Proceedings of the IECON '93, International Conference on Industrial Electronics, Control, and Instrumentation, Vol. 3, 1993, pp 1932–1936.

TAN, J., QIANG, X., DING, X. (1991). *A Superprecision Measuring Method and the Corresponding Measuring System for Error Movement of Instrument Spindles*. Proceedings of IECON ’91, International Conference on Industrial Electronics, Control and Instrumentation, Vol. 3, 1991, pp. 2449–2454.

TANAKA, Y., YANO, A., HIGUCHI, M. (1975). *Die elastische Verformung an der Kontaktzone bei der Umfangsschleifschiebe*. Annals of the CIRP, Vol. 24, No. 1, 1975, pp. 249–252.

TIAN, J. (2004). *Reconstruction of Irregularly Sampled Interferograms in Imaging Fourier Transform Spectrometry*. PhD Thesis, Georgia Institute of Technology, Atlanta, 2004.

TOBIAS, S. A. (1961). *Schwingungen an Werkzeugmaschinen*. Carl Hander Verlag, München.

TÖNSHOFF, H. K., CHEN, Y. (1989). *Schwingungen und Welligkeiten beim Schleifen*. VDI-Z, Vol. 131, No. 10, October 1989, pp. 35–41.

TÖNSHOFF, H. K., FRIEMUTH, T., BECKER, J. C. (2002). *Process Monitoring in Grinding*. Annals of the CIRP, Vol. 51, No. 2, 2002, pp. 551–571.

TÖNSHOFF, H. K., KUHFUß, B., PAN, G. (1985). *Dynamische Schnittkraft und Welligkeit beim Schleifen*. VDI-Z, Vol. 127, No. 10, May 1985, pp. 377–382.

TÖNSHOFF, H. K., ROHR, G., ALTHAUS, P. G. (1980). *Process Control in Internal Grinding*. Annals of the CIRP, Vol. 29, No. 1, 1980, pp. 207–211.

TP (1978). *Jump-on gage for grinding*. Tooling & Production, Vol. 44, No. 3, 1978.

TRETTER, S. A. (1976). *Introduction to Discrete-Time Signal Processing*. John Wiley & Sons, New York.

TRUMPOLD, H., MACK, R. (1975). *Meßsystem für die adaptive Regelung der Formabweichung vom Kreis beim Aussenrund-Einstechschleifen*. Annals of the CIRP, Vol. 24, No. 1, 1975, pp. 383–386.

TU, J. F., BOSSMANNS, B., HUNG, S. C. C. (1997). *Modeling and error analysis for assessing spindle radial error motions*. Precision Engineering, Vol. 21, No. 2/3, September/December 1997, pp. 90–101.

UDUPA, H. G. S., SHUNMUGAM, M. S., RADHKRISHNAN, V. (1988). *Workpiece Movement in Centerless Grinding and Its Influence on Quality of the Ground Part*. Transactions of the ASME, Journal of Engineering for Industry, Vol. 110, May 1988, pp. 179–186.

UN, C. K., YANG, S. C. (1977). *A Pitch Extraction Algorithm Based on LPC Inverse Filtering and AMDF*. IEEE Transactions on Acoustics, Speech, and Signal Processing, Vol. ASSP-25, No. 6, December 1977, pp. 565–572.

URBAN E., URBAN D. (1979). *Fehlertrennverfahren – angewendet auf Rundheitsmessungen*. Feingerätetechnik, Vol. 28, March 1979, pp. 122–125.

YANG, Y., ZHANG, B., WANG, J. (1999). *Vacuum-Preloaded Hydrostatic Shoe for Centerless Grinding*. Annals of the CIRP, Vol. 48, No. 1, 1999, pp. 269–272.

YASSA, F. F., GARVERICK, S. L. (1990). *A Multichannel Digital Demodulator for LVDT/RVDT Position Sensors*. IEEE Journal of Solid-State Circuits, Vol. 25, No. 2, April 1990, pp. 441–450.

YING, S., JAMIESON, L. H., MICHELL, C. D. (1996). *A Probabilistic Approach to AMDF Pitch Detection*. Proceedings of the International Conference on Spoken Language Processing (ICSLP), Vol. 2, October 1996, pp. 1201–1204.

VIOLA, F., WALKER, W. F. (2003). *A Comparison of the Performance of Time-Delay Estimators in Medical Ultrasound*. IEEE Transactions on Ultrasonics, Ferroelectrics, and Frequency Control, Vol. 50, No. 4, April 2003, pp. 392–401.

WANG, Z. (1990). *Interpolation using Type I Discrete Cosine Transform*. Electronics Letters, Vol. 26, No. 15, July 1990, pp. 1170–1171.

WANG, Z. (1993). *Interpolation using Type I Discrete Cosine Transform: Reconsideration*. Electronics Letters, Vol. 29, No. 2, January 1993, pp. 198–199.

WEBSTER, J., MARINESCU, I., BENNETT, R. (1994). *Acoustic Emission for Process Control and Monitoring of Surface Integrity during Grinding*. Annals of the CIRP, Vol. 43, No. 1, 1994, pp. 299–304.

WEBSTER, J., DONG, W. P., LINDSAY, R. (1996). *Raw Acoustic Emission Signal Analysis of Grinding Process*. Annals of the CIRP, Vol. 45, No. 1, 1996, pp. 335–340.

WEISSBACH, R.S., LOKER D. R., FORD, R. M. (2000). *Test and Comparison of LVDT Signal Conditioner Performance*. IEEE Instrumentation and Measurement Technology Conference, Vol. 2, 2000, pp. 1143–1146.

WHITEHOUSE, D. J. (1976). *Some theoretical aspects of error separation techniques in surface metrology*. Journal of Physics E: Scientific Instruments, Vol. 9, 1976, pp. 531–536.

WHITEHOUSE, D. J. (1994). *Handbook of Surface Metrology*. Institute of Physics Publication, Bristol.

WHITTAKER, E. T. (1915). *On the functions which are represented by the expansion of interpolating theory*. Proceedings of the Royal Society of Edinburgh, Vol. 35, 1915, pp. 181–194.

WHITTAKER, J. M. (1935). *Interpolatory function theory*. Cambridge tracts in mathematics and mathematical physics, No. 33, Cambridge University Press.

WMSW (1969). *Continuous In-Process Gaging Improves Match Grinding*. Western Machinery and Steel World, Vol. 60, No. 7, July 1969, pp. 26–27.

WOLFF, S. S., THOMAS, J. B., WILLIAMS, T. R. (1962). *The Polarity-Coincidence Correlator: A Nonparametric Detection Device*. IEEE Transactions on Information Theory, Vol. 8, No. 1, January 1962, pp. 5–9.

WU, J. J. (1999). *Spectral analysis for the effect of stylus tip curvature on measuring rough profiles*. Wear, Vol. 230, 1999, pp. 194–200.

ZHANG, H., YUN, H., LI, J. (1990). *An On-line Measuring Method of Workpiece Diameter Based on the Principle of 3-Sensor Error Separation*. IEEE Proceedings of the National Aerospace and Electronics Conference, Vol. 3, 1990, pp. 1308–1312.

ZHANG, G. X., WANG, R. K. (1993). *Four-Point Method of Roundness and Spindle Error Measurements*. Annals of the CIRP, Vol. 42, No. 1, 1993, pp. 593–596.

ZHOU, S. S. (1996). *Characteristics of Work-Regenerative Chatter in Centerless Grinding*. ASME, Materials Division MD, Vol. 74, Advanced Materials: Development, Characterization, Processing, and Mechanical Behavior, pp. 133–134.

ZIMMER, C., RYSER H., MEYR, H. (1976). *An Instrument for Non-Contact Speed Measurement by Image Correlation*. Proceedings of the 7th Congress of the International Measurement Confederation, IMEKO 1976, pp. 117–129.